NASA TECHNICAL MEMORANDUM

NASA TM X-3511

NASA TM X-3511

REPORTS OF PLANETARY GEOLOGY PROGRAM, 1976-1977

Compiled by Raymond Arvidson and Russell Wahmann

Office of Space Science
NASA Headquarters

NATIONAL AERONAUTICS AND SPACE ADMINISTRATION • WASHINGTON, D. C. • MAY 1977

1. Report No.	2. Government Accession No.	3. Recipient's Catalog No.
TM X 3511		

4. Title and Subtitle	5. Report Date
REPORTS OF PLANETARY GEOLOGY PROGRAM, 1976-1977	May 1977
	6. Performing Organization Code: SL

7. Author(s)	8. Performing Organization Report No.
Compiled by Raymond Arvidson and Russell Wahmann	
	10. Work Unit No.
9. Performing Organization Name and Address	
Office of Space Science Lunar and Planetary Programs Planetary Geology Program	11. Contract or Grant No.
	13. Type of Report and Period Covered: Technical Memorandum
12. Sponsoring Agency Name and Address	
National Aeronautics and Space Administration Washington, D.C. 20546	14. Sponsoring Agency Code

15. Supplementary Notes

16. Abstract

A compilation of abstracts of reports which summarizes work conducted by Principal Investigators. Full reports of these abstracts were presented to the annual meeting of Planetary Geology Principal Investigators and their associates at Washington University, St. Louis, Missouri, May 23-26, 1977.

17. Key Words (Suggested by Author(s))	18. Distribution Statement
Planetary geology Solar system evolution Planetary geological mapping Instrument development	Unclassified–Unlimited

19. Security Classif. (of this report)	20. Security Classif. (of this page)	21. No. of Pages	22. Price*
Unclassified	Unclassified	294	$9.25

* For sale by the National Technical Information Service, Springfield, Virginia 22161

FOREWORD

This is a compilation of abstracts of reports from Principal Investigators of NASA's Office of Space Science, Division of Lunar and Planetary Programs Planetary Geology Program.

The purpose is to provide a document which succinctly summarizes work conducted in this program. Each report reflects significant accomplishments within the area of the author's funded grant or contract.

No attempt has been made to introduce editorial or stylistic uniformity; on the contrary, the style of each report is that of the Principal Investigator and may best portray his research. Bibliography information will be included in a separately published document.

Full reports of selected abstracts were presented to the annual meeting of Planetary Geology Principal Investigators at Washington University, St. Louis, Missouri, May 23-26, 1977.

S. E. Dwornik
Chief
Planetary Geology Program

R. Wahmann
Staff Scientist
Planetary Geology Program

CONTENTS

Chapter 1

CONSTRAINTS ON SOLAR SYSTEM FORMATION

The Formation of the Planetary System. H. Alfven and D.A. Mendis, University of California, San Diego, La Jolla, California 92093

Abstract

During the last several years we have made a systematic effort to reconstruct the origin and evolutionary history of the planetary system. We have pointed out that the formation of satellite systems around planets and the formation of planets around the sun proceeded along the same lines. Consequently, our approach has been to study the formation of companion bodies around a parent body characterized only by a mass, spin, and a minimum magnetic moment. We have stressed the important role played by electromagnetic forces firstly in the ionization,emplacement and differentiation of circumsolar and circumplanetary gases and secondly in the transfer of angular momentum from the central body to the surrounding plasma. Strong evidence in support of these early processes is reflected in the dynamical fine structure of the asteroidal belt and Saturnian ring system which have not undergone the final step in the evolutionary process into a single consolidated body due to different reasons, and therefore act as time capsules containing vital clues about the state of the plasma from which they condensed.

This work has been summarized in the publication last year of the NASA monograph Evolution of the Solar System.

Within the last year we have started on several new projects in order to clarify (1) the formation of jet streams, (2) collision processes

in the asteroidal belt, (3) acquirement of spin angular momentum of giant planets, and (4) the bombardment of planets and asteroids in the early history of the solar system. Following is a brief summary of preliminary results from these studies:

(1) We have developed a Monte Carlo model to simulate the orbital evolution of a stream of almost co-orbital colliding particles ("jet-stream"). Most of the important features of Trulsen's calculations of a "deterministic model" are essentially confirmed by our method which requires only a small fraction of the machine time needed by Trulsen. The colliding particles evolve into a flat-disk like structure with only a limited radial focussing. Several trial runs have been made to investigate the effect of continuous capture of stray bodies into the disk; the results are not yet clear enough to tell what initial conditions are required for strong orbital focussing. However, general considerations indicate that if the particles are continuously perturbed into eccentric orbits, such a focussing will result.

(2) Using a realistic model, the values of collision probability, impact velocity and probability of destructive collision in the asteroidal belt are estimated. It is found that orbits with large eccentricity would be less stable against catastrophic collision. Also, objects at a smaller solar distance would be affected by collision effect more severely. These could be relevant to the orbital structure and chemical composition of the asteroids.

(3) We have further considered the development of the spin momentum of Jupiter by searching for the bands of trajectories responsible for imparting the spin to it. This leads to an upper limit to the original size of the proto-planet by virtue of the fact that the bands of particles which contribute most significantly to the prograde angular momentum of the proto-planet should not have aphelia intercepting Saturn's orbit. We expect that the continuation of this line of study will lead not only to a better understanding of the origin of the direct spin of the giant planets, but will also furnish us with information on the initial conditions relevant to the environment of satellite formation. Already it is clear that proto-Jupiter was never much larger than its present size contrary to some theories of its origin.

(4) Finally it is seen that proto-Jupiter can perturb some particles into highly eccentric orbits. We are in the process of studying the bombardment effects of this population of particles on the terrestrial planets and asteroids. The bombardment effects by the planetesimals scattered from the terrestrial planets are also under study. We expect that this study will further contribute to our understanding of the late bombardment history of terrestrial planets and the asteroids.

Computer Simulations of Planetary Accretion Dynamics: Sensitivity to Initial Conditions. Richard Isaacman, National Astronomy and Ionosphere Center, Carl Sagan, Laboratory for Planetary Studies, Cornell University, Ithaca, NY., 14853

We have tested the implications and limitations of Program ACRETE, a scheme based on Newtonian Physics and accretion with unit sticking efficiency, devised by Dole (1) to simulate the origin of the planets. The dependence of the results on a variety of radial and vertical density distribution laws, on the ratio of gas to dust in the solar nebula, on the total nebular mass, and on the orbital eccentricity, ε, of the accreting grains are explored. Only for a small subset of conceivable cases are planetary systems closely like our own generated. Many models have tendencies towards one of two preferred configurations: multiple star systems, or planetary systems in which jovian planets either have substantially smaller masses than in our system or are absent altogether. But for a wide range of cases recognizable planetary systems are generated -- ranging from multiple star systems with accompanying planets, to systems with jovian planets at several hundred AU, to single stars surrounded only by asteroids. No terrestrial planets were generated more massive than 5 Earth masses. The number of planets per system is for most cases of order 10, and, roughly, inversely proportional to ε. All systems generated obey a relation of the Titius-Bode variety for relative planetary spacing. The ease with which planetary systems are generated, using such elementary physical assumptions, supports the idea of abundant and morphologically diverse planetary systems throughout the Galaxy.

(1) Dole, S. H. (1970). Formation of planetary systems by aggregation: A computer simulation. Icarus 13, 494-508.

Composition of the Terrestrial Planets. Kenneth A. Goettel
Dept. of Earth and Planetary Sciences, McDonnell Center for the Space Sciences
Washington University, St. Louis, Missouri 63130

Progress in understanding the process of condensation in the solar nebula, and recent data from space missions and Earth-based observations have necessitated a critical review of models for the origin and composition of the terrestrial planets. A quantitative model for the composition of each of the terrestrial planets is presented in Table 1. These calculated compositions are based on: a) the chemical equilibrium model for condensation in the solar nebula, b) the solar proportions of rock-forming elements, and c) several simplifying assumptions about the accretion of planets. Variations in the Fe/Si ratio in different regions of the nebula, or other fractionation processes are not required to explain the observed differences in mean density and composition among the terrestrial planets.

The model for the terrestrial planets presented below is based directly on the equilibrium condensation calculations of Lewis (1) and Grossman (2). The primary result of these condensation sequence calculations is the composition of condensed material, as a function of temperature and pressure in the nebula. Compositions of the terrestrial planets have been derived by: a) assigning a formation temperature-pressure to each planet (1), b) determining the phases condensed in the nebula in that temperature-pressure region (1,2), and c) calculating the composition of this condensed material using the solar proportions of rock-forming elements (3). The assumptions, implications, and limitations inherent in the above procedure have been discussed in detail by Goettel and Barshay (4). The principle limitations appear to be: a) the extent to which equilibrium was maintained during condensation in the nebula, and b) the uncertainties in the solar proportions of rock-forming elements. A variety of evidence, notably the ubiquitous presence of FeS in meteorites and the presence of substantial amounts of FeO in silicates in the Earth and in ordinary chondrites, suggests that equilibrium was probably closely approached, at least in the region of the nebula in which the terrestrial planets were formed (4).

The eight most abundant rock-forming elements (Mg,Si,Fe,S,Al,Ca,Na,Ni), with combined oxygen, constitute about 99 weight percent of the total rock-forming material in the solar nebula. Therefore, the bulk compositions and densities of the terrestrial planets are dominated by these most-abundant elements. The calculated planetary compositions presented in Table 1 include these eight elements, plus the heat-producing elements K, U, and Th. The relative abundances of these elements in the solar nebula (Table 2) were taken from Cameron (3), with the exceptions of Fe and S. Cameron's estimate of the Fe/Si ratio is .83. The value adopted for the present work is .90, which is in good agreement with the estimate of .89 by (5), and with the value of .901 reported for C1 meteorites (6). Cameron's estimate for the S/Si ratio is .50. The value adopted for the present work is .25. Direct observations of the sun and studies of cosmic rays give S/Si ratios from .146 to .400 (7,8). Cameron relied heavily on the S abundances reported for C1 meteorites. However, recent petrographic observations suggest that S may have been added to C1 meteorites by hydrothermal veins (9). Thus, Cameron's S abundance estimate appears to be too high. The Fe and S abundances adopted for the present work are within the present uncertainty range, and also result in compositions for the terrestrial planets which match the observed densities.

Several simplifying assumptions were made to derive planetary compositions from the chemical equilibrium condensation sequence. First, it was assumed that planets accreted material only from a narrow region of the nebula; thus, each planet accreted material with a narrow range of composition, with the composition determined by temperature and pressure in the nebula. Second, possible effects of mixing and/or fractionation processes were not considered.

Third, planets were assumed to accrete homogeneously, and subsequently to be fully differentiated into mantles and cores. Fourth, accretion of planets was assumed to be slow, so that initial compositions were not modified by volatilization from accretional heating. The validity and limitations of these assumptions have recently been discussed (4).

Mercury has an Fe-Ni core which constitutes nearly 2/3 of the planet's mass. The mantle is enriched in refractory condensates, including CaO and Al_2O_3; forsterite (Mg_2SiO_4) is the major magnesium silicate phase. Mercury is enriched in U and Th by a factor of about two above the solar proportions, due to incomplete condensation of MgO and SiO_2. Mercury is essentially void, in the simple model, of FeO, Na, K, S, and H_2O. Despite the U and Th enrichment, the absence of K in Mercury results in a total radiogenic heat production per gram which is less than any of the other terrestrial planets. This calculated composition for Mercury is consistent with the conclusions drawn about Mercury's surface by Adams and McCord (10) from spectral reflectivity data: a) absence of pyroxene, b) absence ($<6\%$) of FeO, and c) presence of an anorthositic crust. Various fractionation processes could have modified the simple model for the composition of Mercury presented in Table 1. The aerodynamic fractionation mechanism suggested by Weidenschilling (11) may be the most likely fractionation process to have affected Mercury (4). If this mechanism has been important, then some or perhaps much of the silicate fraction of Mercury could have initially condensed further out in the nebula. This would result in addition of enstatite ($MgSiO_3$), Na and K to Mercury, with a resulting decrease in the proportions of Mg_2SiO_4, Al_2O_3, CaO, U, and Th. However, even with this possible addition of some K to Mercury, the resulting heat production in Mercury would still be substantially lower than in the other terrestrial planets. The predicted lower internal heat production, and Mercury's low mass which reduces the effect of heating by retention of gravitational potential energy during accretion, suggest the reason for the apparent lack of global tectonic activity on Mercury.

Venus is also predicted to have an Fe-Ni core, which constitutes nearly 1/3 of the planet's mass. The mantle of Venus is dominated by magnesium silicates (largely $MgSiO_3$). Venus is predicted to contain very little FeO, S, or H_2O. The total radiogenic heat production per gram in Venus is larger than that of any other terrestrial planet. Venus, Earth, and Mars all have the same ratios of K, U, and Th relative to Fe, Si, and Mg, but the radiogenic heat sources in Earth and Mars are diluted by retention of S, oxidation of Fe to FeO, and retention of volatiles. Thus, due to its high content of radiogenic heat sources, and rather large mass, Venus may exhibit global tectonic activity.

Earth is predicted to have an Fe-Ni-S core and a mantle dominated by ferro-magnesium silicates (pyroxene and olivine). The Earth model presented in Table 1 is in rather good agreement with present data on the constitution of the mantle and core. The calculated core/mantle ratio is slightly too low. This discrepancy would be somewhat reduced if minor siderophile elements were included in the calculation. Increasing the Fe/Si ratio in the nebula from .90 to .92 or .93 would raise the core mass to match present geophysical data. Such an Fe/Si ratio is certainly within the uncertainty limits of present knowledge of solar composition. The high total K content calculated for Earth suggests that a significant fraction of the Earth's total K must be either in the core or sequestered in the lower mantle (12-14). Decay of ^{40}K in the core may provide an energy source for core and mantle convection, and thus provide the energy to maintain the geomagnetic field and to drive plate tectonics.

Mars is postulated to be composed of material in which essentially all of the Fe is oxidized to FeS or FeO. The FeS-NiS core of Mars constitutes only about 12% of the planet's mass. In Table 1, all of the Ni in Mars was

assumed to be in the core as NiS. However, given the predicted oxidation state of Mars, some or perhaps much of the Ni in Mars may have been incorporated into mantle silicates. The mantle of Mars is very high in FeO; the major mantle mineral is FeO-rich olivine. For comparison with the other planets, the composition of Mars has been presented in Table 1 on a water-free basis. However, as a result of its low formation temperature, Mars is predicted (1) to contain about 0.3% water (several times the water content of the Earth!). Thus, the chemical equilibrium condensation model for Mars correctly predicts the substantial amounts of water on Mars indicated by the photogeologic evidence for melting of subsurface ice on Mars. At present, the water on Mars must be retained as subsurface ice and in hydrated silicate phases, rather than as liquid water. The calculated low viscosities of Martian lavas (15) result directly from the high abundance of FeO, relatively low Al_2O_3, and very high content of water and other volatiles in the Martian mantle. The high Fe_2O_3 content of the Martian surface may be explained by differentiation of the very FeO-rich mantle. The total content of radiogenic heat sources in Mars is rather high: global tectonic activity may have been possible in the past, if not at the present time.

The simple model presented above for the terrestrial planets appears to be a viable, albeit oversimplified, working model. Extension of this model to include additional minor and trace elements, to consider the possible effects of mixing and/or fractionation, and to explore the thermal evolution and differentiation history implications is essential. However, in light of the apparent success of the simple model, more complex models invoking multi-stage evolution of planets or complex fractionation processes appear to be less viable.

References

(1) J.S. Lewis, Earth Planet. Sci. Lett. 15, 286 (1972).
(2) L. Grossman, Geochim. Cosmochim. Acta 36, 597 (1972).
(3) A.G.W. Cameron, Space Sci. Rev. 15, 121 (1973).
(4) K.A. Goettel and S.S. Barshay, in S. Dermott (ed.) The Origin of the Solar System, (1977) in press.
(5) R. Ganapathy and E. Anders, Proc. Fifth Lunar Science Conf. 2, 1181 (1974)
(6) B. Mason, in B. Mason (ed.) Handbook of Elemental Abundances in Meteorites p. 209 (1971).
(7) V. Trimble, Rev. Mod. Phys. 47, 877 (1975).
(8) B.E.J. Pagel, Space Sci. Rev. 15, 1 (1973).
(9) S.M. Richardson, EOS 57, 277 (1976).
(10) J.B. Adams and T.B. McCord, abstract, Conference on Comparisons of Mercury and the Moon. Houston, Texas. 15-17 November 1976.
(11) S.J. Weidenschilling, Mon. Not. Roy. Astron. Soc. (1977) submitted.
(12) J.S. Lewis, Earth Planet. Sci. Lett. 11, 130 (1971).
(13) H.T. Hall and V.R. Murthy, Earth Planet. Sci. Lett. 11, 239 (1971).
(14) K.A. Goettel, Geophys. Surv. 2, 369 (1976).
(15) E. Schonfeld, EOS 57, 948 (1976).

TABLE 1
Calculated Compositions of the Terrestrial Planets (wt. %)

	MERCURY		VENUS		EARTH		MARS	
component	bulk	mantle	bulk	mantle	bulk	mantle	bulk	mantle
MgO	12.83	36.89	25.74	37.82	24.25	34.79	23.07	26.20
SiO_2	11.67	33.53	36.16	53.13	34.06	48.88	32.41	36.80
Al_2O_3	5.32	15.30	2.61	3.83	2.46	3.53	2.34	2.65
CaO	4.97	14.28	2.43	3.58	2.29	3.29	2.18	2.48
Na_2O	0	0	1.12	1.64	1.05	1.51	1.00	1.14
FeO	0	0	0	0	5.58	8.00	27.06	30.72
mantle	34.79	100.00	68.06	100.00	69.69	100.00	88.07	99.99
		core		core		core		core
Fe	61.75	94.69	30.25	94.69	24.16	79.73	6.09	51.01
Ni	3.46	5.31	1.70	5.31	1.60	5.27	1.52	12.74
S	0	0	0	0	4.54	15.00	4.32	36.25
core	65.21	100.00	31.94	100.00	30.31	100.00	11.93	100.00
K(ppm)	0		990		930		890	
U(ppb)	77		37		35		34	
Th(ppb)	165		81		76		73	

TABLE 2
Solar Proportions of Rock-Forming Elements[1]

Mg	1.061×10^6	Na	6.0×10^4
Si	1.0×10^6	Ni	4.80×10^4
Fe	9.0×10^5	K	4200
S	2.5×10^5	U[2]	0.0262
Al	8.5×10^4	Th[2]	0.058
Ca	7.21×10^4		

[1]Atomic proportions relative to Si = 1.0×10^6. From Cameron (3), except Fe and S (see text).

[2]Initial value, not present value.

The role of pre-solar grains in the early Solar System. C. Federico, Istituto di Geologia, Università di Perugia, 06100 Perugia (Italy), A. Coradini and G. Magni, Laboratorio di Astrofisica Spaziale del CNR P.B. 67, 00044 Frascati (Italy)
Italian Consortium for Planetary Studies

In order to follow a series of stages during the development of the S.S. to the present condition, it has been suggested that planetesimals have to appear in some way. So the basic assumptions to obtain planetesimals is an accretion growth of condensed grains moving through a gaseous medium. By clarying the accretional processes we described the evolution of the primordial grains population. This evolution depends on the mutual interaction among gas and dust, and on the assumed model of the collapsing nebula. The different parameters reflecting the subsequent stages of the collapse have been selected among those pubblished by various Authors (1,2,3).

Briefly the protosolar nebula, during its gravitational collapse experiences firstly an isothermal phase, then an adiabatic one and after 10^6 yr, reaches a centrally condensed flat configuration. During this last phase, we have assumed a power law for the temperature and pressure radial distribution (3).

The characteristic dissipation time of the disk has been estimated to be of the order of $10^3 - 10^4$ yr, at a distance of about 1A.U. (1,4). The nebula is fully turbulent during the first two phases of the collapse (5) and the distribution function of grains velocity depends on the interaction among dust and gaseous material. The particles, at the beginning have in fact mass of the order of $10^{-13} - 10^{-12}$ g (typical interstellar grains) and their velocity is affected only by the gas and not by the other particles.

Some mechanisms which are expected to produce the growth of dusty grains have been studied during the isothermal and the adiabatic phase.

Owing to the low sticking efficiency in the grain-grain collisions and also to the impossibility of gas capture by solid particles in the physical environment considered, we have shown (6) that the main result is the production in about a million years of a set of particles similar in mass. The obtained mass limit($10^{-8} - 10^{-9}$ g) depends on the physical properties of the grains and seems to be independent of the turbulence model used.

These calculation has been performed in the outer regions of the Solar Nebula where solid material can survive to the increase of temperature due to the evolution of the gravitational collapse.

Our conclusion disagrees with the hypothesis of planetesimals formation in the external regions of the Nebula; whereas agglomerates similar to those foreseen theoretically, have been

identified as inclusions in meteorites (for example magnetite spheroids included in Orgueil meteorite) (7).

However, since experimental evidences - untill recently - suggest that in the region of terrestrial planets the grains have been vaporized or melted, we are now studying the accretion processes during the high temperature phases. In fact during the last stage of the adiabatic collapse in the inner region of the nebula, the temperature increases up to the melting temperature of the grains. Afterwards, during the disk configuration the gas temperature decreases again. The melted grains can grow by the following mechanisms :

-condensation as consequence of vapour-liquid phase transition;

-accretion by collisions among liquid particles.

Preliminary results, considering only the latter mechanism show that the accretion time for liquid drops is shorter than for solid one if the collision velocity is relatively small (10 - 100 cm/sec). The velocity distribution and the life time of particles in the disk configuration have been computed balancing newtonian forces and drag viscosity, because the turbulence rapidly decays.

So we suspect that the newly solidified grains before the dissipation of the disk can reaches a mass value some order of magnitude larger than the previous one.

References

1. A.G.W.Cameron, Icarus 18,407 (1973)
2. R.B.Larson, Fundaments of Cosmic Physics 1, 1 (1973)
3. S.J.Weidenschilling,Mon.Not.Roy.Astr.Soc.(in press)(1976)
4. P.Goldreich and W.R.Ward, Ap.J. 183, 1051 (1973)
5. A.Carusi,A.Coradini,C.Federico,M.Fulchignoni,G.Magni,Astroph. and Space Sci.,33,369 (1975)
6. A.Coradini,C.Federico,G.Magni,ibid.(in press) (1977)
7. J.Jedwab, Icarus 15, 319 (1971)

Ice Grains in Space. R. Smoluchowski, Materials Laboratory, Princeton University, Princeton, N. J., 08540.

Many properties of the interstellar medium can be explained by assuming the existence of grains of various solids such as graphite and water ice and a great deal of research has been devoted to this topic. These considerations are usually based on the assumption that the materials are simply small grains of the common terrestrial solids. Within the last few years, however, great progress has been made -- both in theory and in experiment -- concerning the physics and chemistry of small grains and of solids formed by slow condensation at low temperatures. Inasmuch as some of their properties differ considerably from those of the normal bulk solids they may play a significant role in the interpretation of astrophysical observations. Admittedly not all of the recent research deals specifically with ice but many conclusions can be based on analogies with other solids and with theoretical models.

Table 1 indicates the kinds of ices that could be formed during slow deposition in interstellar space. The considerable variation of the observed temperature limits are usually due to different rates of deposition. The range of temperatures in Table 1 encompasses those assumed to exist in various parts of space where grains are formed or exist. Since in a dust cloud the temperatures may vary by a factor of ten between the center and the outer layers (1) one may expect a radial gradient of ice grains (or ice covered grains) of different structures and properties.

In parallel with the variation of structure one expects a considerable variation in the average binding energy of an H_2O molecule to the grain. One expects the amorphous ice I_{A2} to have up to 25 per cent fewer hydrogen bonds (2) than the crystalline form and thus a correspondingly weaker binding. On the other hand the I_{A1} because of its higher density should have a binding which is stronger by a comparable amount. These differences will affect for instance the rates of growth and of sublimation of these grains.

It is known that slow growth of a cluster of atoms can lead to a progressively looser structure so that the number of nearest neighbors, the binding and the density can be lower by as much as 40 or 50 per cent near the outside than in the center. These effects can influence the sticking coefficient S that is the fraction of incident atoms which becomes thermalized and permanently attached to the grain and the accommodation coefficient α, that is the fraction of the energy of the atom transferred to the grain (3). As shown in Table 1 in the range of existence of ice I_{A1} the coefficients S and α would be higher than for the normal ice I_h: by a few per cent below 10°K, by 12 per cent near 20°K and by 50 per cent near 50°K. For ice I_{A2} these coefficients would be lower by similar amounts. No major differences would be expected for ices I_c and I_h. The effect of the amorphous surfaces and in particular of the altered coefficients S and α on the rates of formation (4) of interstellar H_2 molecules on the surfaces of grains is being investigated.

Interstellar flux of ultraviolet photons leads to photoionization of grains which become positively charged. This charge increases the probability of capturing a neutral atom and decreases this probability for a positive ion so that it plays an important role in the formation of various molecules (5). The emission of photoelectrons is also an important mechanism for giving the grains momentum and thus for heating the dust cloud. Normally photoionization of ice grains is considered unimportant (6) because the ionization threshold lies close to 13.5 eV which happens to coincide with the drop of intensity of the interstellar spectrum. It is known that amorphous solids have a narrower band gap and a band edge which is shifted to lower frequencies than crystalline solids; it follows that their photoionization threshold should lie at lower photon energies. Thus contrary to earlier conclusions amorphous ice grains

will be easily ionized by the abundant ultraviolet flux in the 10-13.5 eV range. This will be particularly true for ice I_{A1}. It follows that the nature of the ice grains should play a significant fole in the processes here mentioned. (More details and full references are given in a paper which is to appear in the proceedings of the IAU Colloquium #39).

Table 1: Water Ices

	Amorph.1	Amorph. 2	Cubic	Hexag.
Stability	Meta	Meta	Meta	Stab.
Existence (°K)	<77	77-140	140-200	0-273
Density (g cm^{-3})	1.2	0.93	0.92	1.00
Binding	+25%	-25%	Normal ?	Normal
Stick. coeff. S	+(T)	-(T)	Normal ?	Normal
Accom. coeff. A	+(T)	-(T)	Normal ?	Normal
UV ioniz. ($\sim\nu^{-1}$)	V.strong	Strong	?	Weak

$\Delta S = \Delta A = 4\%(T<10K), \quad 12\%(T = 20K), \quad 50\%(T = 50K)$

References:

1. Leung, C. M. Ap. J. 199, 340 (1975).
2. Briant, C. L. and Burton, J. J. J. Chem. Phys., 63, 3327 (1975).
3. Hollenbach, D. and Salpeter, E. E. J.Chem. Phys., 53, 79 (1970).
4. Hollenbach, D. and Salpeter, E. E. Ap. J., 163, 155 (1971).
5. Field, G. B., Highlights of Astronomy, 3, 37 (1974).
6. Watson, W. D., Ap. J., 176, 103 (1972).

Chapter 2

CONSTRAINTS ON PLANETARY INTERIORS

PROPERTIES OF GIANT GASEOUS PROTOPLANETS. A.G.W. Cameron,
Harvard College Observatory, Cambridge, MA 02138

In my report for a year ago (NASA TM X/3364) I described some calculations on evolutionary sequences of models of the primitive solar nebula which were then in progress, and some conclusions which had been derived from these calculations and from previous steady-flow calculations carried out the preceding fall. The computations on the evolution of the primitive solar nebula were carried on through the first half of 1976, some five different cases being studied with different combinations of input parameters. However, already early in the year an unexpected major conclusion had been drawn about the behavior of the primitive solar nebula.

In the course of the evolutionary calculations, quantities were recorded which formed criteria for local and global instabilities which might be associated with the primitive solar nebula. The local instability criterion measured the tendency of a local patch within the nebular disk to become unstable against gravitational contraction upon itself. Local instability was approached but never quite achieved within the disk during the course of the evolutionary calculations. The global instability criterion measured the tendency of a finite width of material within the primitive solar nebula to become gravitationally unstable against contraction to form a ring centered upon the rotational spin axis. It was found that every portion of the primitive solar nebula would become unstable against ring formation at some point within its evolutionary history; the critical mass within the finite range of radius at which instability would occur was exceeded by a factor of ten or more in all cases. The instability would first occur for the innermost portions of the primitive solar nebula, and would subsequently occur at larger and larger radii. This result was of such a large magnitude that I felt there was no escape from the conclusion that the primitive solar nebula had to become repeatedly unstable against the formation of rings. The subsequent work which has been carried out has been aimed at understanding this phenomenon.

It can be expected that, upon contraction, a ring should break up into a number of fluid blobs distributed around a circle. This aspect of the behavior is beyond my present capability for numerical simulation, although recent analytical work by W. Press has shown that the number of blobs that should result from this type of process is probably greater than four. A program has been written which follows the dynamical behavior of a ring of blobs formed by such process. Only a few representative cases will be run with this program in the near future, since greater insight is desired into the temporal behavior of the radius of a blob as a function of time after its formation. This is important for knowing when two blobs will collide and merge together.

The amount of mass participating in such a ring instability may approach a few per cent of that of the sun. Hence it is necessary to study the properties of the evolutionary behavior of gaseous protoplanets with masses ranging from about that of Jupiter to as much as twenty or thirty times that of Jupiter.

An early crude study was carried out to determine the probable gross characteristics of such protoplanets. Typical thermodynamic conditions in the primitive solar nebula at the time of formation of one of the inner rings were utilized in the construction of a table of gas properties corresponding to the adiabatic compression of such material. A series of models of giant gaseous protoplanets was then constructed corresponding to material lying on this adiabat, but with differing central pressures. This showed that the protoplanets should have radii of the order of an astronomical unit or greater, temperatures throughout the interior less than about 2,000 K, and

masses of the order of 10 Jupiter masses. These large radii are not an embarrassment for formation of protoplanets in the inner solar system; such protoplanets should be formed early in the evolution of the primitive solar nebula, when there is not much mass present near the center of the nebula, and consequently gravitational forces are weak and distances between objects are large.

In the course of its evolution, a giant gaeous protoplanet can be expected to lose energy, so that it will contract and its central regions will become hotter. When a sufficient number of the hydrogen molecules in the central regions of the giant gaseous protoplanet are dissociated, the protoplanet becomes unstable against gravitational collapse. A study of these evolutionary phases of giant gaseous protoplanets is currently under way, being carried out by Dr. Wayne Slattery, who joined me at Harvard College Observatory at the beginning of September.

Some aspects of these evolutionary calculations promise to be very exciting in terms of planetary formation. In collaboration with Dr. M. Herndon, at the University of California at San Diego, I have examined the thermodynamic behavior to be expected near the center of a giant gaseous protoplanet. As the central density and temperature increase in the course of evolution, the temperature will become high enough to evaporate solids in the central regions of the protoplanet. Such solids should be in finely divided form; they should be derived from the cores of interstellar grains brought in with the gas of the protoplanet during the collapse of an interstellar cloud to form the primitive solar nebula. When the temperature rises high enough to evaporate metallic iron from these grain cores, the opacity in the interior of the protoplanet would fall by several orders of magnitude. This allows radiant heat in the interior of the protoplanet to stream freely forth toward large radii, thereby cooling the inner regions of the protoplanet, and preserving much of the iron in the central regions in condensed form in the grain cores. This leads one to expect that the inner portions of the protoplanet will evolve so that the central regions lie along a saturated iron vapor pressure curve. The central thermodynamic conditions will not be able to break away from this saturated iron vapor pressure curve until the central pressure rises to at least several tens of bars, at which the pressure broadening of the lines of triatomic molecules, such as water vapor and ammonia, produces general opacities comparable to that of the iron in condensed form. Only then can adiabatic compression lead toward temperatures at pressures in the hundreds of bar region at which quite large amounts of the interior hydrogen molecules can become thermally dissociated.

This means that a great deal of mass at the center of a giant gaseous protoplanet will have its condensed solids in the liquid phases, so that tiny droplets will coalesce upon collision, growing in mass until they can rain out toward the center of the protoplanet, forming a molten rocky and iron body of substantial size, probably comparable in mass to one of the terrestrial planets today. It seems inevitable that the formation of a core of this sort should precede any instability against gravitational collapse on the part of the giant gaseous protoplanet. The iron saturation vapor pressure curve lies well below the hydrogen molecular dissociation curve in temperature at a given pressure.

I put forward the hypothesis that the rocky cores produced in this way formed the bulk of the inner terrestrial planets which we have today, and that the giant gaseous protoplanets surrounding these cores were tidally dissipated. I also hypothesize that the outer planets resulted from the collapse of giant gaseous protoplanets, there being more time in the outer solar system for the evolution of the protoplanets free from the danger of tidal dissipation.

Tidal dissipation arises in the following way. With the passage of time, there will be a continued inflow of matter in the inner solar system, with matter adding to and increasing the mass of the object or objects near the central spin axis, and possibly also adding some mass to the giant gaseous protoplanets. The evolution of such a system, with the major bodies subject to a constant specific angular momentum, leads to an inward spiraling of the bodies. There is an inner Lagrangian point, which determines whether matter is under control of the central mass or the protoplanetary mass. With the progressive inward spiraling of the protoplanet, the inner Lagrangian point will eventually pass inside the surface of the giant gaseous protoplanet. The material of the protoplanet will then spill across the inner Lagrangian point at the internal speed of sound, leading to a very rapid tidal dissipation of the protoplanet. Only the precipitated inner rocky core of the protoplanet would survive this process.

The dynamical collapse of protoplanets in the outer solar system is also of great interest and poses a number of fascinating problems. A giant gaseous protoplanet is expected to be spinning. so that when it undergoes a dynamical collapse, the central regions will settle down about the rocky cores which have already formed, but the spinning outer parts, with the greater portion of the mass, can be expected to form a gaseous disk rotating about the central region. The evolution of such a disk must be studied by methods similar to those which I have used to study the evolution of the primitive solar nebula itself. The regular satellites possessed by Jupiter and Saturn are presumably formed in such a disk, and the mechanism by which this may happen needs to be studied. General mechanisms of mass loss from the collapsed protoplanets also need to be studied. One such mechanism is the spreading of the radius of the disk so that matter crosses the inner Lagrangian point for the system. Another possible mechanism is the formation of a vigorous outer convection zone in the central object, with the heating of a coronal layer surrounding the collapsed protoplanetary center and the formation of a protoplanetary wind which will carry mass off into space. The existence of such a process at one time seems to be indicated by the fact that in the presence of a gaseous disk there must be a continous fluid connection between the disk and the central object, so that the central object will rotate with rotational instability at the equator. Jupiter and Saturn now rotate significantly slower than this, so that there must have existed a mass loss process which carried away much of their original angular momentum. In addition, studies by M. Podolak and me, as well as by W. Slattery and W. Hubbard, have shown that Jupiter and Saturn contain a significant excess of heavier elements in their interiors relative to solar composition. The implication is that a mass loss process must have occurred from the outer layers of the collapsed object which does not include materials which would condense at lower levels in the atmosphere of the object. Such a mass loss process could well involve more than half of the original mass of the object, leaving a very substantial excess of the heavier constituent in the interior. At the present time Mr. William DeCampli, a graduate student, is investigating the collapse phases of a giant gaseous protoplanet, utilizing the two-dimensional hydrodynamic code developed by Black and Bodenheimer for studying the collapse of interstellar gas cloud fragments.

Heat, Stretch and Erupt: The Relationships Among Global Thermal Evolution, Crustal Tectonics and Surface Volcanism on the Terrestrial Planets. Sean C. Solomon, Department of Earth and Planetary Sciences, Massachusetts Institute of Technology, Cambridge, MA 02139

The style of crustal volcanism and tectonics on a planet is intimately related to the thermal evolution of the planetary interior. The relationship is most obvious for the Earth, on which creation and destruction of lithosphere is an integral part of the mechanism for transferring heat out of the mantle. Tectonics, volcanism and thermal history are also closely related on planetary bodies like Mars, Mercury and the Moon which lack laterally mobile lithospheric plates (1). Interior warming of such planets leads to global expansion, surface extensional tectonics, and a crustal stress system that aids surface volcanism by maintaining open conduits through which magma can reach the surface. Interior cooling leads to global contraction, compressional tectonics and crustal stresses that act to shut off surface volcanism.

Limits on the sign and extent of planetary volume change for Mercury, Mars and the Moon since the period of heavy bombardment of the inner solar system may be set by observed crustal tectonics. By comparing these limits to the volume change predicted from thermal history models and finite strain theory, the possible initial temperature distributions for these planets may be greatly restricted.

The evidence from the extensive lobate scarp system on Mercury for planet-wide compression (2,3) favors initial temperatures near melting throughout most of the interior and completion of core/mantle differentiation prior to emplacement of the oldest major surface units, because core formation involves significant planetary expansion (4) for which no surface evidence remains (2). The 1 to 2 km contraction in Mercury's radius inferred from lobate scarp geometries (3) can be accomplished by lithospheric cooling subsequent to global differentiation and/or by solidifcation of an inner core of γ-Fe with a radius up to 60 percent of the radius of the outer core.

A long history of expansion for Mars is suggested by the many systems of troughs, grabens, normal faults, and volcanic features of variable age now visible on the Martian surface (5). Thermal models consistent with this inference involve cool initial temperatures for most of the planet and a late date for completion of core differentiation. Core formation on Mars involves less total expansion and less thermal energy release (equivalent to a rise in mean temperature of 150°C) than Mercury (700°C) (4) or the Earth (2300°C) (6).

The absence of large scale compressional or extensional tectonics on the Moon limits the lunar radius to within about 1 km of its present value (7) for the last 3.8 b.y. The only thermal models satisfying this constraint involve initial temperature distributions with near melting conditions in the outer 200 to 300 km (1) and a cold interior ($<$500°C). The nearly constant volume is achieved by a balance between lithospheric contraction and expansion of the interior. Very modest

net expansion is predicted for the first 2 b.y. for such lunar models, followed by a slight contraction.

It may be noteworthy that the extent of early heating in Mercury, Mars and the Moon increases in the order of distance from the sun but is not simply related to planetary mass.

Expansion of a planet is generally accompanied by tensional tangential stress in the crust, a condition conducinve to maintaining open channels for magma to feed surface volcanic flows. Conversely, planetary contraction leads to compressive tangential stress and a tendency for such channels to close. The duration of plains volcanism on a planet may be controlled by the length of an expansion period in the planet's history as much as by the avilability of magma sources. The peak planetary volume is predicted to occur at a progressively later time for the bodies Mercury ($\sim$4 b.y. ago), Moon ($\sim$2.5 b.y. ago), and Mars ($\sim$1 b.y. ago). By inference, the youngest large-scale plains volcansim on these planets should decrease in age in the same order.

References

(1) S.C. Solomon and J. Chaiken, Proc. Lunar Sci. Conf. 7th, 3229 (1976).
(2) B.C. Murray, M.J.S. Belton, G.E. Danielson, M.E. Davies, D.E. Gault, B. Hapke, B. O'Leary, R.G. Strom, V. Suomi, N. Trask, Science 185, 169 (1974).
(3) R.G. Strom, N.J. Trask, J.E. Guest, J. Geophys. Res. 80, 2478 (1975).
(4) S.C. Solomon, Icarus 28, 509 (1976).
(5) M.H. Carr, J. Geophys. Res. 78, 4049 (1973); R.P. Sharp, J. Geophys. Res. 78, 4063 (1973); M.H. Carr, J. Geophys. Res. 79, 3943 (1974).
(6) F.M. Flasar and F. Birch, J. Geophys. Res. 78, 6101 (1973).
(7) G.J.F. MacDonald, Planet. Space Sci. 2, 249 (1960).

The rigid hard crusts of the Moon, Mars, Mercury and Venus: Implications for the role of water in crustal mobility of Earth. G. G. Schaber and J. M. Boyce, U.S. Geological Survey, 2255 North Gemini Dr., Flagstaff, AZ 86001.

Recent analyses of Earth-based radar maps of Venus have shown that the distribution of moderately large (35 to 350 km diameter) (1) to large (> 600 km diameter) (2) impact structures on the older Venus terrain appear to have a density similar to the Moon, Mars and Mercury. Further radar verification of such a heavily cratered surface on Venus would strengthen the contention of Schaber and Boyce (3) that this densely clouded, Earth-size body may have had a similar average crustal viscosity as the Moon, Mars and Mercury over the past 4+ x 10^9 years regardless of its present extreme surface temperature. The Earth underwent the same early heavy bombardment of large bodies (4); however, only a few isolated, and relatively young, impact scars remain because of efficient isostatic compensation, plate tectonics, and other crustal deformation and modification associated with a relatively mobile crust and upper mantle. The image data of Mars, Mercury, and Venus and the Moon contain evidence for substantial isostatic compensation of many large (> 500 km diameter), older craters (5) but there is no indication of plate movement and other crustal deformational processes related to an Earth-like upper mantle-crustal mobility.

Baldwin (6) utilized the equations of Haskell (7) to show that the average crustal viscosity of the Moon must have been in the range of $\sim 10^{26}$ poise over the past 4+ x 10^9 years, increasing from a value of $\sim 10^{24}$ in pre-mare time to a present minimum of $\sim 10^{27}$ poise or greater. A similar average crustal viscosity of $\sim 10^{26}$ poise have been calculated for Mars (8), Mercury (5), and Venus (present study). By contrast the viscosity of the upper mantle crust of the present Earth has been determined (7) to be in the order of 10^{21} poise.

The presence of abundant water on Earth and the absence or relative scarcity of it on the other terrestrial planets may be the major factor contributing to the differences in crustal mobility on these bodies. Tittmann et al. (9) used the exceptionally high Q-factor (internal friction quality) of lunar rocks as derived from seismic data to infer no more than 10-cm equivalents of water trapped in the upper 25 km of the Moon. The role that water has played in magmatic, metasomatic and metamorphic processes associated with divergent and convergent plate boundaries in the new global tectonics has been discussed by Wyllie (10, 11), Lambert and Wyllie (12), and others. Magmatic activity occurs on a large scale at divergent plate boundaries where partial fusion of rising mantle produces lava and generates new lithosphere. This cools, thickens and migrates laterally toward a convergent plate boundary, where the lithosphere moves into the mantle along a subduction zone. The release of water from oceanic crust in a subducted lithosphere slab may play an important role in the plate tectonic model for magma generation. Such water may occur in pore fluids, be structurally bound in hydrous minerals, be dissolved in magma, be juvenile; or be introduced from the oceans. The relative importance of each water source is poorly understood however.

The general weakening effect of water on silicate mineral structures is well known. Griggs and Blacic (13) found that quartz crystals containing small amounts of water in the structure were very weak and ductile at temperatures down to 400°C. Similarly, just a few parts per hundred of water are enough to depress the melting point of basalt by 500°C. The primary source of water from hydrated minerals may be from serpentized periodites that make up a large portion of the terrestrial oceanic crust. During the reaction:

$$\text{Olivine} + H_2O \lesseqgtr \text{serpentine}$$

the increased molecular mobility should increase plasticity, as is well known from the physics of solids. Decomposition of serpentine at about 500°C to forsterite-talc and H_2O takes place (accompanied by embrittlement and weakening) during overriding of crustal and oceanic plates, soaking the crust above the shear plane with water arising from the depths around the 500°C isotherm (11,14,15,16).

There is as yet no evidence that any of the dynamic processes of the new global tectonics is now or have ever operated on the Moon, Mars, Mercury, Venus. Whether the absence of abundant amounts of water is responsible for the hard, rigid crusts on these bodies is, of course, difficult to say without further exploration. However, it is suggested that geologic, geochemical and geophysical models designed to characterize the evolution of the terrestrial planets must take into consideration the evidence implied in the cratering record for similar average crustal viscosities for Mars, Mercury, Venus and the Moon over the past 4+ x 10^9 years.

(1) Saunders, R. S. and Malin, M. C., 1977, Geologicia Romana, in press.
(2) Schaber, G. G. and Boyce, J. M., 1977a, The Moon, in press.
(3) _____1977b, Lunar Science VIII - Abstracts of Papers submitted to the 8th Lunar Sci. Conf., Houston, Texas, in press.
(4) Wetherill, G. W., 1975, Proc. Lunar Sci. Conf. 6th, 1539-1561.
(5) Schaber, G. G., Boyce, J. M., and Trask, N. J., 1977, Phys. Earth Planet. Inter., in press.
(6) Baldwin, R. B., 1971, Phys. Earth Planet. Inter., 4, 167-179.
(7) Haskell, N. A., 1935, Physics, 6, 265-269.
(8) Phillips, R. J. and Saunders, R. S., 1974, J. Geophys. Res., 80, 2893-2898.
(9) Tittmann, B. R., Housely, R. M., Alers, G. A. and Cirlin, E. H., 1974, Proc. Lunar Sci. Conf. 5th, 2913-2918.
(10) Wyllie, P. J., 1971, J. Geophys. Res., 76, 1328-1338.
(11) _____1973, Tectonophysics, 17, 189-209.
(12) Lambert, I. B. and Wyllie, P. J., 1970, Science, 169, 764-766.
(13) Giggs, D. T. and Blacic, J. D., 1965, Science, 147, 292-295.
(14) Orowan, E., 1964, Science, 146, 1003-1010.
(15) Rayleigh, C. B. and Paterson, M. S., 1965, J. Geophys. Res., 70, 3965-3985.
(16) Hess, N. H., 1962, in Engel, A. E. J. et al., Petrological Studies, Buddington Memorial Volume. Geol. Soc. Amer., Boulder, Colorado, 599-620.

Mercury: Evidence for an Anorthositic Crust from Reflectance Spectra.
J.B. Adams, Univ. of Wash. & T.B. McCord, M.I.T. & I.F.A., Univ. of Hawaii

Reflectance spectra of Mercury from 0.335μm to 1.064μm were measured in 1969 (McCord & Adams, 1972 Science 178, 745-747) and in 1974 and 1975 (Vilas & McCord, 1976 Icarus 28, 593-599). The recent data do not show an absorption feature near 0.95μm; therefore, there is no evidence for the presence of pyroxene. The featureless steep continuum of the Mercury curve cannot be reproduced by silicate minerals or by homogeneous glasses. The common Fe^{2+} charge-transition bands that occur in the spectra of terrestrial, meteoritic and lunar rocks are notably absent in the Mercury spectrum. Lunar soil samples, characterized by the presence of heterogeneous inclusion-filled glass, have a continuum slope similar to the Mercury curve. Lunar samples, however, have an absorption band near 1μm which in mature soils is primarily due to an Fe^{2+} charge transition in agglutinitic glass. Reflectance measurements of mineral and agglutinate separates from lunar soils shows that the 1μm band in mature soils deepens as direct function of the FeO content of the bulk soil. The absence of a distinct 1μm band in the Mercury spectrum is only reproduced in the spectra of mature lunar soils having less than 6% FeO such as occur at Apollo 16. Increasing amounts of FeO such as in the Apollo 14, 15 and 17 upland soils (and all mare soils) produce a noticeable Fe^{2+} absorption near 1μm that departs from the smooth continuum of the Mercury curve. If it is correct to model the Mercury spectrum on the lunar soils, we can conclude that much of Mercury is covered by mature lunar-like soil containing 6% FeO. Again by analogy with the moon, it is probable that the surface of Mercury observed telescopically is anorthositic in composition. These conclusions are compatible with Mariner 10 data (Hapke et al., 1975 J. Geophys. Res. 80, 17) which show extensive heavily cratered areas with albedos slightly brighter than the lunar highlands.

Very recent telescopic observation of the Mercury reflectance spectra in the near infrared (0.7-2.5μm) shows again the lack of any absorption band near 1μm. The interpretation made using the earlier spectra remain unchanged.

Data Analysis of Mariner 10 Magnetic Field Observations at Mercury and Venus.

Norman F. Ness, Laboratory for Extraterrestrial Physics, NASA-Goddard Space Flight Center, Greenbelt, MD. 20771

It is the purpose of this task to complete the analysis of the data obtained from the GSFC triaxial fluxgate magnetometers flown on the Mariner 10 spacecraft with planetary encounters at Venus and Mercury. The preliminary and subsequent initial analyses of the data have been completed and published (1,2,3,4,5). These papers have established unequivocally the surprising discovery of a substantial, global, intrinsic magnetic field of the planet Mercury. Direct observations of Mercury's field were obtained during the first and third flybys, very close to the planetary surface.

A modest but well developed magnetosphere, magnetosheath and detached bow shock wave was observed by the magnetic field experiment. Cooperative analyses of data obtained simultaneously with the University of Chicago energetic particle detector and the MIT-LASL-GSFC plasma science experiment are now in progress. The principle objective is to quantitatively compare the characteristics of the Hermean magnetosphere with that of Earth and also to elaborate more fully on the mechanisms responsible for production of intense bursts of energetic particles observed during the encounters. The acceleration mechanism most plausibly resides in the magnetic tail neutral sheet of the planet Mercury and is stimulated by changes in the upstream interplanetary magnetic field configuration whereby the rate at which energy is transfered to the Hermean magnetosphere is abruptly altered.

The flyby trajectory at Venus was not capable of selection so as to elaborate completely the nature of the solar wind interaction with the planet but the data are consistent with the absence of any significant intrinsic planetary magnetic field and simply a direct solar wind-ionosphere interaction. The gravity assist trajectory at Venus did yield unique information on the aft-body portion of solar wind flow past the planet and these data are currently in the process of being studied in detail. These results will be combined with those obtained from the plasma science experiment, but not the energetic particle detector, since the latter observed no additional fluxes in its energy range beyond background during the entire Venusian wake and near planet traversal.

Detailed data utilized in the spherical harmonic analysis of magnetic field observations from the two Hermean flybys and the corresponding trajectory positions are in preparation for submission to the National Space Science Data Center. A similar data set for the interplanetary cruise portion of the prime Mariner 10 mission has already been completed. This will permit other research workers to utilize these data in addition to those who have already done so on the basis of our private distribution (see JGR articles 1976 by Whang (6) and by Beard (7) presenting quantitative models of the Hermean magnetosphere).

Anticipating that future missions to the planet Mercury shall be possible, these data will then permit comparative studies in order to establish whether or not any secular change of the magnetic field exists. The uncertainties in the characteristics of the spherical harmonic coefficients derived from the two Mariner 10 data sets admit only of an upper limit to the secular change of the planetary field of the planet. Identification of a secular change would provide a unique argument in favor of an active dynamo model for the planetary magnetic field. At present, it is not possible to eliminate a paleomagnetic origin for the planetary field due to a sub Curie point mantle or the less plausible situation of a sub Curie point mantle and core.

References

(1) Ness, N. R., Behannon, K. W., Lepping, R. P., Whang, Y. C. and Schatten, K. H.: 1974a, Science, 183, 1301.
(2) Ness, N. F., Behannon, K. W., Lepping, R. P., Whang, Y. C. and Schatten, K. H.: 1974b, Science, 185, 151.
(3) Ness, N. F., Behannon, K. W., Lepping, R. P. and Whang, Y. C.: 1975, J. Geophys. Res., 80, 2708.
(4) Siscoe, G. L., Ness, N. F. and Yeates, C. M.: 1975, J. Geophys. Res., 80, 4359.
(5) Ness, N. F., Behannon, K. W., Lepping, R. P. and Whang, Y. C.: 1976, Icarus, 28, 479.
(6) Whang, Y.C.: 1977, J. Geophys. Res., 82, in press.
(7) Beard, D. B.: 1977, J. Geophys. Res., 82, in press.

A Spin-Orbit Constraint on the Viscosity of a Mercurian Liquid Core. S. J. Peale and A. P. Boss, Physics Department, Univ. of California, Santa Barbara 93106

The Mariner 10 mission has detected an intrinsic magnetic field for the planet Mercury, which is attributed to an internal dynamo involving an electrically conducting and circulating molten core.(1) We show here that the viscosity of such a core might be inferred from the dynamical history. Such constraints are important to thermal history calculations and to theories of planetary dynamo field generation.

Mercury is now in the stable spin-orbit resonance where the spin angular velocity $\dot{\psi}$ is exactly 1.5n, where n is the orbital mean motion. Resonances where $\dot{\psi}$ = 2n, 2.5n, 3n, etc. are also stable to disruption by the tides.(2) If Mercury started with a much higher spin rate, it had to pass through these stable higher order resonances. Without a molten core, the probability of capture into these resonances is very small except for the currently existing 3/2 resonance. However, a molten core of large radius (3/4 R_O) drives the capture probability to unity for a range of core viscosities. This range increases as the order of the resonance decreases, so escape from the $\dot{\psi}$ = 2n resonance places the most severe constraint on the core viscosity. If Mercury passed through the $\dot{\psi}$ = 2n resonance on its way to $\dot{\psi}$ = 3n/2 while it possessed a liquid core, the core viscosity must necessarily be outside that range for which P = 1. Otherwise it would never have reached $\dot{\psi}$ = 3n/2 where we find it today.

The results of the calculations are shown in Fig. (1). The crosshatched region shows the range of forbidden viscosities as a function of several parameters for Mercury to escape the $\dot{\psi}$ = 2n resonance. The ordinate is the tidal Q, where the viscosity range depends on Q because the capture probability depends on how rapidly the resonance is approached. The dependence on (B-A)/C comes from the dependence of the energy dissipation on the relative velocity between the core and mantle, which increases with libration frequency.

The solid crosshatching in Fig. 1 corresponds to the case where the boundary layer remains laminar, whereas the dashed crosshatching corresponds to the extension of that region for a turbulent boundary layer. The vertical lines labeled "Earth" are bounds on the kinematic viscosity of the earth's core estimated by Gans.(3)

The upper range of permitted viscosities preclude sufficient motion for a dynamo and can therefore be ignored. If the boundary layer remains laminar and the earth core values are assumed to be reasonable lower bounds on ν, any set Q, ν in the triangular region on the left side of Fig. 1 will allow escape from the 2n resonance. Although this is a rather restricted range it does allow the reasonable values Q = 100 and ν = 0.01 cm^2/sec.

If the boundary layer becomes turbulent at a critical Reynold's number R_C = 500 and if we can replace ν by a turbulent or eddy viscosity $\nu_T = R\nu/R_C$, the constraints are shifted to (B-A)/C from ν and Q, since the coupling becomes independent of ν for turbulent flow. Then $Q \lesssim 20$ and $(B-A)/C \lesssim 10^{-5}$ for escape to occur. Any additional coupling from, say, magnetic fields, bumps on

the core-mantle interface or from a lower critical Reynold's number would make it very unlikely that Mercury could have passed through the 2n resonance with a core of low viscosity.

The uncertainty in the analysis of the turbulent flow must be emphasized. There is thus a need for the experimental determination of spin-up times for fluids in spherical containers in the turbulent regime in order to make the constraints for a possibly turbulent boundary layer more definite.

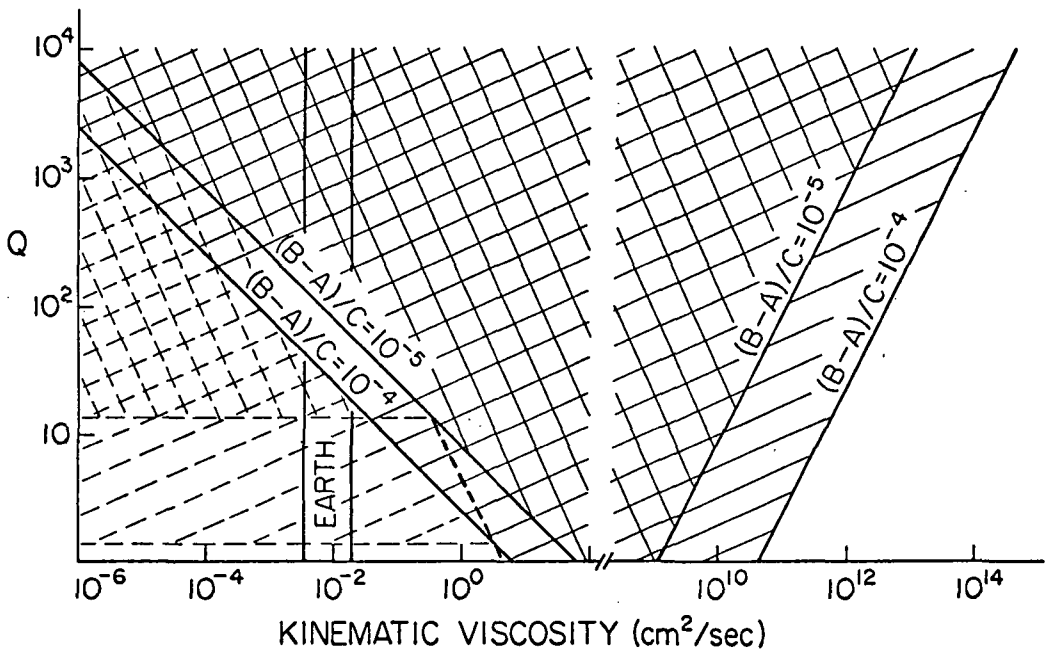

Fig. 1. The crosshatched region includes those values of Q and ν for which capture into the $\dot{\psi}$ = 2n resonance is certain, and values in this region are therefore forbidden if Mercury has escaped this resonance. Solid crosshatching is for a laminar boundary layer and dashed shading is for a turbulent boundary layer with R_c = 500. Region shown is for e = 0.17.

References

(1) Ness, N.F., K.W. Behannon, R.P. Lepping and Y.C. Whang, J. Geophys. Res. 80, 2708-2716, (1975).
(2) Goldreich, P. and S.J. Peale, Astron. J. 71, 425-438, (1966).
(3) Gans, R.F., J. Geophys. Res. 77, 360, 1972.

Mercury's Core: The Effect of Obliquity on the Spin-Orbit Constraints. S. J. Peale and A. P. Boss, Physics Department, Univ. of California, Santa Barbara 93106

In an earlier paper by the authors,[1] rather severe constraints are placed on the viscosity of a Mercurian liquid core and some other dynamical characteristics if Mercury escaped from the spin-orbit resonance where the spin $\dot{\psi} = 2n$, with n being the orbital mean motion. One assumption under which these constraints were established is that the obliquity $\theta \approx 0$ at the time of resonance passage. Here we show that for $\theta \neq 0$, Mercury can easily escape a spin resonance with a large core of low viscosity, and all constraints established with weak coupling between the core and mantle for resonance passage with $\theta = 0$ would vanish. However, the constraints are restored by the fact that θ is rapidly reduced to zero before $\dot{\psi}$ reaches 2n, so it is most likely that $\theta = 0$ as Mercury passes through $\dot{\psi} = 2n$.

The limiting kinematic viscosities ν for certain capture in the strong coupling limit (high viscosity) of core mantle-interaction are only slightly changed by $\theta \neq 0$. But permitted values of ν for escape from $\dot{\psi} = 2n$ are so large in this limit that dynamo action is not possible,[2] so this range of permitted viscosities will not be considered further.

The reduction in the capture probabilities for $\theta \neq 0$ in the limit of low viscosity is illustrated in Fig. 1. It is clear that even for moderate obliquities, Mercury could easily pass through the 2n resonance with a core of low viscosity. Introduction of a turbulent boundary layer does not alter this conclusion.

The core-mantle interaction reduces the capture probability by drastically increasing the rate at which the spin magnitude is reduced. This has the same effect as increasing the magnitude of the tidal torque while leaving the core-mantle dissipation of librations about the resonance unchanged, thereby reducing the capture probability.[3] The spin magnitude decrease follows from the reduction of the component of the spin vector $\bar{\psi}$ in the orbit plane while the component normal to the orbit is conserved as the spin vector of the Mercurian mantle precesses about the orbit normal.[4]

We can now argue that Mercury passed through $\dot{\psi} = 2n$ with $\theta \approx 0$ and our confidence in the core constraints derived earlier can be restored. The same effect which reduces the capture probability so effectively also drives the obliquity to zero very quickly. The time constant for exponential decay of tan θ is

$$\tau_\theta \approx \frac{r_c}{(\nu \dot{\psi}_m)^{\frac{1}{2}}} \frac{(1+C)}{C} \approx 8.9 \times 10^4 \text{ years}$$

where r_c is the core radius and $C = C_c/C_m \approx 1$ is the ratio of the core moment of inertia to the mantle moment of inertia. The numerical value follows with $r_c = 1.8 \times 10^8$cm, $\nu = 0.01$ cm^2/sec and $\dot{\psi}_m = 2n$. With such a short time constant, θ was almost certainly very close to zero (or more properly, close to Cassini state 1[5]) long before it reached $\dot{\psi} = 2n$. Escape of Mercury from this resonance while it had a large core of low viscosity must therefore be consistent with the given constraints of $\nu \approx 0.01$ cm^2/sec and tidal $Q \lesssim 100$ if the boundary layer between the

core and mantle is laminar and with $(B-A)/C \lesssim 10^{-5}$, critical Reynold's number $R_c \gtrsim 500$ and $Q \lesssim 20$-40 if the boundary layer is turbulent subject to the assumptions of the earlier paper.(1)

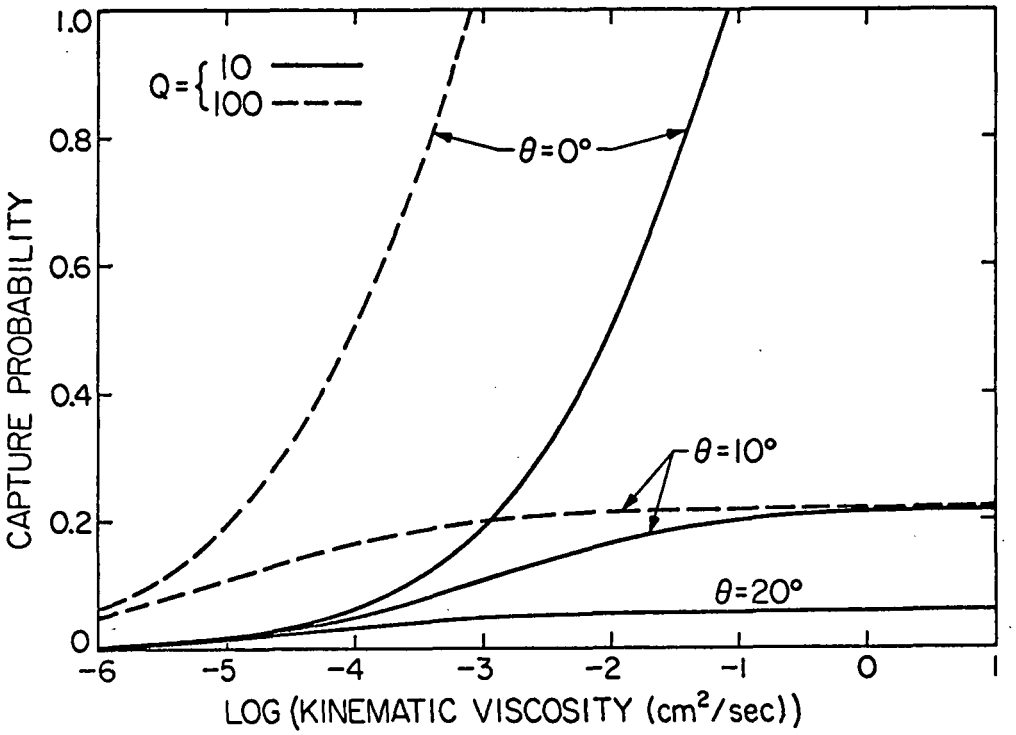

Fig. 1. Capture probability for the 2n resonance in the weak coupling limit, $(B-A)/C = 10^{-4}$. Note the drastic reduction in P with increasing α and the independence of P on ν at larger ν when $\alpha \neq 0$.

References

(1) Peale, S.J. and A.P. Boss, J. Geophys. Res. In press 1977. (See previous abstract.)
(2) Büsse, F. Private communication, 1976.
(3) Goldreich, P. and S.J. Peale, Astron. J. 71., 425-438 (1966).
(4) Goldreich, P. and S.J. Peale, Astron J. 75., 273-283 (1970).
(5) Peale, S.J. Astron J. 79., 722-744, (1974).

Thermal History of Lunar Magma Ocean. Floyd Herbert, Michael J. Drake*, Charles P. Sonett*, and Michael J. Wiskerchen, Lunar and Planetary Laboratory, University of Arizona, Tucson, AZ, 85721. *Also Dept. of Planetary Sciences.

INTRODUCTION. There is a general consensus that the Moon underwent a global melting and fractional crystallization event which commenced at 4.5 ± 0.1AE and resulted in the segregation of a 60-100 km thick plagioclase-rich (ANT) crust and an unsampled mantle of mafic cumulates of unknown thickness. The original depth of this magma ocean is unknown, but minimum estimates indicate a depth of 100-200 km and a maximum depth equal to the radius of the Moon is possible. There is also a consensus that mare and KREEP basalts are produced by subsequent internal remelting of the products of this global differentiation event. The closing of the source reservoirs for a variety of isotopic systems (U-Th-Pb, Rb/Sr, Sm/Nd) at approximately 4.4AE (1-3) for a variety of lunar rock types may be interpreted as representing the solidification of the magma ocean at a depth corresponding to the source of each rock type. Because high-Ti mare basalts and KREEP basalts appear to be derived from shallow depths, perhaps immediately below the ANT crust, the 4.4AE age probably represents the approximate time of solidification of the entire magma ocean. Thus, if we could compute that a magma ocean of greater than a certain thickness would not solidify in ≈0.2AE (4.6 minus 4.4AE), the maximum permissible thickness of the magma ocean would be obtained. With this information, making reasonable assumptions concerning nebular condensation, and assuming homogeneous accretion, an estimate of the bulk composition of the Moon may be computed. To this end we report our preliminary findings concerning the early thermal history of the lunar magma ocean.

EXPLORATORY MODELS. A schematic representation adapted from (4) of what one might expect for the temperature profile of the Moon immediately following rapid accretion is given in Figure 1. The thermal regimes of the Moon are, from surface to interior, (i) a possible small solid crust which would cool by conduction, (ii) a possible small region of crystals plus liquid which would cool by convection, (iii) a convecting liquid region, (iv) a conducting liquid region, (v) a conducting liquid plus solid region, and (vi) a conducting solid region. The boundaries between these regions evolve as cooling proceeds.

There is a basic limitation placed on this starting profile by the fact that convection will begin modifying this profile as soon as the accretion rate diminishes enough to produce a decreasing surface temperature. Thus if accretion decays slowly compared to the convective relaxation time there will never be significant superheat above the liquidus. A consequence of the efficiency of radiative heat loss is that the surface of the Moon will cool to the liquidus temperature on a time scale of a few tens of years regardless of the exact nature of the initial temperature profile if convection were rapid enough to keep the surface molten.

Thus, the key question to be answered concerns the presence or absence of a solid crust, because conduction across such a crust would control the rate of heat loss from the Moon. If a solid crust formed, for typical rock thermal diffusivities of 20 m^2/yr, on the order of 10^6 years are required to thicken to a depth of 10 km, on the order of 10^8 years for 200 km, and on the order of 10^9 years for 500 km. Of course, the solidification history of the magma ocean must have been more complex than the above scenario. The gradients of the liquidus and solidus are probably significantly greater than the adiabatic gradient. Thus if the convection temperature profile resembled the adiabatic temperature profile, and if the magma did become at least partly superheated, solidification would occur at the base of the magma ocean as well as at the top (4) and basal solidification might have been dominant. Further, as fractionation proceeds, density gradients can be significantly modified by

composition gradients, leading to modification or even local elimination of convection. Composition gradients can also modify the local liquidus and solidus temperatures. In particular, local plagioclase enrichment of the magma can raise the persistence temperature of a plagioclase crust. Nevertheless, it should be clear that the most critical factor is the time of and method of formation of an early solid crust.

MECHANISM OF FORMATION OF EARLY CRUST. It has been proposed (5) that a "quenched" crust formed on the surface of the magma ocean. For this event to occur, convection must be inefficient enough to steepen the thermal gradient close to the surface (see dot-dash line, Fig. 1). However, it is not clear that such an overdense crust would persist. The general depletion of volatile elements in the Moon precludes a significant reduction in the density of the chilled crust due to vesiculation (a common agent in reducing crustal densities in terrestrial lavas). Moreover, the possibility of convectional shear and the near certainty of impacts from accretional debris will result in fragmentation and foundering. How, then, could an early crust have formed? We envision a process leading to the formation of plagioclase-rich "rockbergs" as illustrated schematically in Figure 2. The convecting region of the magma will consist of cells whose surface expressions are regions of upwelling (hotter) and subsidence (cooler). In the cooler regions crystallization will occur. At the surface the magma will quench to form a thin sheet. This quenched solid will be more dense than the magma and eventually will founder. Immediately beneath this quenched crust will be a zone of crystals plus melt with the fraction of melt increasing downwards. Plagioclase, which is less dense than the melt ($\approx$2.8 g/cm^3 versus $\approx$3.0 g/cm^3) will exist as separate crystals at temperatures corresponding to $\approx$50-95% solidification. Other phases present will be olivine and pyroxene, both of which are more dense than the magma. We envision differential settling of olivine, pyroxene, plagioclase, and quenched solid, with plagioclase concentrating preferentially higher in column. Whether plagioclase actually floats or simply sinks more slowly will depend in part upon the balance between the rate of convective overturn and the actual density contrast, the latter depending upon the (unknown) bulk composition of the Moon. The end product of this process, regardless of the detailed mechanism, is expected to be a series of plagioclase-rich "rockbergs" occupying the low-temperature regions of the surface. As cooling proceeds, the area occupied by the "rockbergs" will increase until the entire surface is covered by a thickening veneer of plagioclase-rich material. Once the veneer is complete, cooling will continue with conduction across the crust being the rate-limiting process, and the time scale for solidification of the remaining fluid will increase dramatically. We envision solidification continuing at the top and base of the crust, with dense mafic phases settling and plagioclase accumulating beneath and thickening the veneer. This process will continue until a plagioclase-rich crust, a mantle of mafic cumulates, and a shell enriched in incompatible elements between crust and mantle is produced. This proposed thermal history has several possibly important geochemical consequences (4). The task ahead is to model the cooling process quantitatively. Our preliminary calculations suggest that the magma ocean was restricted to the outer few hundred km of the Moon, a result which is consistent with the geochemical requirements of an undifferentiated lunar interior to provide the energy for subsequent remelting of the products of the global differentiation event.

This work is supported by NASA grants NGR 03-002-38, NSG 7020, and NGR 03-002-370.

REFERENCES. (1) Tera and Wasserburg, Lunar Science VI, 807 (1975). (2) Lugmair, "Origin of Mare Basalts", 107 (1975). (3) Shih, Lunar Science

VII, 800 (1976). (4) Walker, Longhi, and Hays, Proc. Lunar Sci. Conf. 6th, 1103 (1975). (5) Taylor and Jakes, Proc. Lunar Sci. Conf. 5th, 1287 (1974).

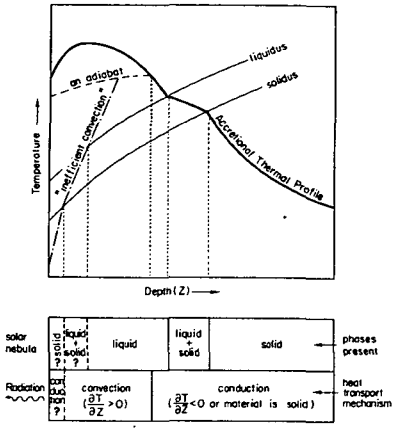

FIGURE 1

Schematic temperature profile immediately following accretion, based loosely on the work of Walker et al. (4). Shown are two possibilities for the convectional temperature profile. Keyed to the graph is a block diagram illustrating the changes of phase and heat transport mechanism with depth.

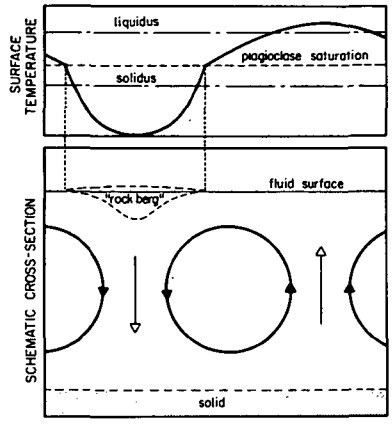

FIGURE 2

Schematic cross-section of lunar magma ocean showing convection process expected to lead to formation of plagioclase-rich floating "rockbergs." Graph at top is plot of surface temperature versus horizonal distance coordinated with horizonal structure of ocean.

Tharsis: Static or Dynamic Support? Roger J. Phillips, Jet Propulsion Laboratory, Pasadena, CA 91103

The Tharsis gravity anomaly on Mars represents support of second and third degree harmonic wavelengths for the order of 10^8 to 10^9 years. We address the question of whether this anomaly can be supported by the finite strength of the interior for this time period.

Stress calculations from a variety of elastic models show that the anomaly must be supported in the lower mantle, shear stresses being on the order of 100 bars. It is assumed that there will be a creep response to this applied stress, and a finite strength of the martian interior would then imply that the time for significant viscous flow exceeds the uplift age of Tharsis. To describe this flow, the simplest rheology to adopt is that of a Maxwell solid, which is dominated by viscoelastic behavior in the short term and by viscous behavior in the long term. The dividing line between these two types of behavior is the "Maxwell time", the ratio of the dynamic viscosity to the rigidity.

The response of the interior to the Tharsis load is most easily understood in terms of viscoelastic load Love numbers (1). Vertical displacement Love numbers have been calculated as a function of the Laplace transform variable, which can be viewed as a reciprocal relaxation time. These Love number spectra clearly show that the relaxation of Tharsis is controlled by the viscosity of the lower martian mantle.

A non-Newtonian flow law (2,3) giving comparatively low strain rates is adopted, since we wish to bias our calculations in favor of finite strength. The diffusion constant in the resulting viscosity relationship can be expressed in terms of T/T_m, the ratio of the actual temperature to the melting temperature. We stipulate that Tharsis has not relaxed more than 1/e in 10^8 years (4), and the resulting value of T/T_m is then about 0.6. For an adopted range of melting temperatures, the actual temperatures fall in the range of approximately 1050° to 1350°C for finite strength of the lower mantle.

The uplift of Tharsis was followed by volcanism that, even if episodic, is distributed through time up to the present or relatively recent past (5). At least part of the mantle must have been at or near solidus temperatures much of the time since the Tharsis event.

For a static support of Tharsis, we conclude then that the magmatic source for volcanism is not in the lower mantle. One can ask, however, if an upper mantle source region is consistent with these lower mantle temperatures. Assuming that $dT/dr \leq 0$; i.e., that temperature does not decrease with depth, then it is possible that the upper mantle is at solidus temperatures at 1350°C. The addition of a small amount of water to upper mantle material will almost certainly allow for solidus temperatures in the interval 1050° to 1350°C, but the solidus will not be realized for temperatures a great deal below this range. Thus, an upper mantle magmatic source region implies that the whole mantle must be nearly isothermal to maintain viscous support of Tharsis in the lower mantle. This thermal state would only seem to be possible through efficient removal of heat by vigorous solid state convection. For convection in the martian mantle, the viscosity implied by $T/T_m = 0.6$ yields a ratio of Rayleigh number to critical Rayleigh number of only about unity (6), precluding such efficient heat removal.

We thus conclude that static support of Tharsis in the lower mantle and continuous magmatic activity at any point in the mantle are in contradiction. In fact, any reasonable temperature for the deep interior and certainly typical thermal model results (6,7,8) yield characteristic second harmonic relaxation times only a small fraction of 10^8 years.

If Tharsis and its surroundings were formed by a flexure in the outer regions of Mars, then in essence this displacement was never supported by the strength of the martian mantle. Alternatively, if the genesis of Tharsis is related to the permanent lateral transfer of mass to this region of Mars, with depletion in other regions, then the deep interior would have rapidly flowed to a hydrostatic state, concentrating shear stresses in the lithosphere. Since there is little evidence for regional crustal failure following the uplift of Tharsis, we are thus led to one of two hypotheses for the support of Tharsis following concentration of stresses in the lithosphere: (a) the lithosphere has finite strength to brittle failure and/or flow, or (b) a dynamic process in the mantle is at least partially responsible for the support of the uplift.

A conservative estimate of lithospheric thickness is 75 to 100 km, which in turn yields a maximum shear stress of approximately 2 kbars. We are led to reject the first hypothesis above for several reasons: (a) The elastic strength of the terrestrial lithosphere does not seem to exceed several kbars over long time periods. (b) A downward elastic flexure of 5 km, for which there is no surficial evidence, would have resulted. (c) The elastic strain of approximately 5% suggests that some type of failure, or at least plastic deformation, would have resulted. (d) Local failure in the Alba region (9) appears to have taken place with lithospheric stresses less than or equal to 1 kbar.

References

(1) W. R. Peltier, Rev. Geophys. Space Phys., 12, 649 (1974).
(2) R. L. Post, Jr., EOS Trans. AGU (abstract), 51, 424 (1970).
(3) R. L. Post, Jr. and D. T. Griggs, Science, 181, 1242 (1973).
(4) R. J. Phillips and R. S. Saunders, J. Geophys. Res., 80, 2893 (1975).
(5) K. R. Blasius, Icarus, 29, 343 (1976).
(6) R. E. Young and G. Schubert, Geophys. Res. Letters, 1, 157 (1974).
(7) D. L. Anderson, J. Geophys. Res., 77, 789 (1972).
(8) D. H. Johnston, T. R. McGetchin and M. N. Toksöz, J. Geophys. Res., 79, 3959 (1974).
(9) D. U. Wise, International Colloquium of Planetary Geology (expanded abstracts), Italian Consortium for Planetary Studies (ed.), 101 (1975).

Page Intentionally Left Blank

Chapter 3

PHOTOGEOLOGIC CONSTRAINTS ON PLANETARY EVOLUTION

Page Intentionally Left Blank

Comparative Studies of the Moon, Mercury and Mars. Verne R. Oberbeck, Theoretical and Planetary Science Branch, NASA, Ames Research Center, Moffett Field CA 94035

A comparative study of craters and plains on the Moon, Mars and Mercury has been carried out during the last year. Our approach has been to use the variable conditions on different planets as an aid to understand the genesis of surface of formations, observed crater populations, crater degradation, crater ejecta dynamics and appearance of different surfaces. Comparative photogeological studies of the inner planets can provide insight into the early history of the solar system and the evolution of planetary surfaces. Such information often cannot be gained by analysis of individual planets. For example, variations in gravitational acceleration atmospheric parameters, and surface conditions on the inner planets provide a natural laboratory for understanding the physics of cratering and its effects on landform development.

The origin of lunar light smooth plains and Mercurian smooth plains were compared and related to crater degradation on the Moon, Mercury and Mars. We then considered a cause for the observed deficiency of craters less than 50 km on certain areas of lunar uplands and on the entire uplands of Mars and Mercury. The deficiency of craters on parts of the lunar uplands and on Mercury and Mars is due to a deficiency in production of primary craters.

During the year we compiled evidence that correlated the degree of degradation of lunar uplands craters with the amount of smooth plains in the area and related this to our model of secondary origin of smooth plains (1,2).

A similar relation was demonstrated for Mercury (1). It was shown that craters around and pre-existing the Caloris basin beneath the peripheral belt of smooth plains were degraded in proportion to the amount of plains materials in the craters. These results in addition to confinement of plains near the basin on Mercury and compression of surface features relative to locations on the Moon are evidence of secondary origin of plains deposits. The question of production of smooth plains as impact melts was examined using a bimodal ejection model for cratering in layered media and the Ries crater ejecta stratigraphy. It was concluded that smooth plains on the Moon and Mercury are probably not impact melts.

The main subject of investigation this year was the question of the nature of the production population of craters on planetary surfaces. Figure 1 shows a summary of the findings. The crater frequency for area C, a typical lunar uplands area contains many basin secondaries. For this reason the observed exponent of the frequency distribution for craters less than 50 km is -2.43, compared to the assumed exponent, -3.5 for craters larger than 50 km. Because the difference is not extreme, the observed differences in population indices has not been emphasized in the past and it has been assumed that one power function characterizes all crater sizes. Thus, the more distinct change in slope of Mars

craters less than 40 km compared to craters larger than 40 km has in the past been assumed to be caused by obliteration of small craters by surface geologic processes (3,4,5) even though we now find similar types of Mercurian crater distributions. Area b is an area on the Moon not covered by ejecta of major basins nor cratered extensively by basin secondaries. It has a crater population like Mars and Mercury suggesting that the population of bodies impacting Mars, the Moon and Mercury was deficient in bodies necessary to produce craters smaller than about 50 km relative to extrapolation of distribution of objects required to produce craters larger then 50 km. Implications are that large episodes of crater obliteration on Mars may not have occurred and differences in slopes of planetary crater distributions do not necessarily signal obliteration events. Preliminary attempts to normalize the assumed production distributions for differences in impact velocity and gravity fields indicate that the lunar and Mercurian data may be brought together but the "density" of Martian craters is still less than either lunar or Mercurian counts, implying a more youthful uplands terrain on Mars.

(1) V. R. Oberbeck, W. L. Quaide, R. E. Arvidson, and H. R. Aggarwal, J. of Geophys. Res., (in press) (1976).
(2) V. R. Oberbeck, F. Hörz, R. H. Morrison, W. L. Quaide, and D. E. Gault, The Moon 12, 19 (1975).
(3) C. R. Chapmen, Icarus 22, 272 (1974).
(4) E. J. Opik, Science 153, 255 (1966).
(5) K. L. Jones, J. of Geophys. Res. 79, 3917 (1974).

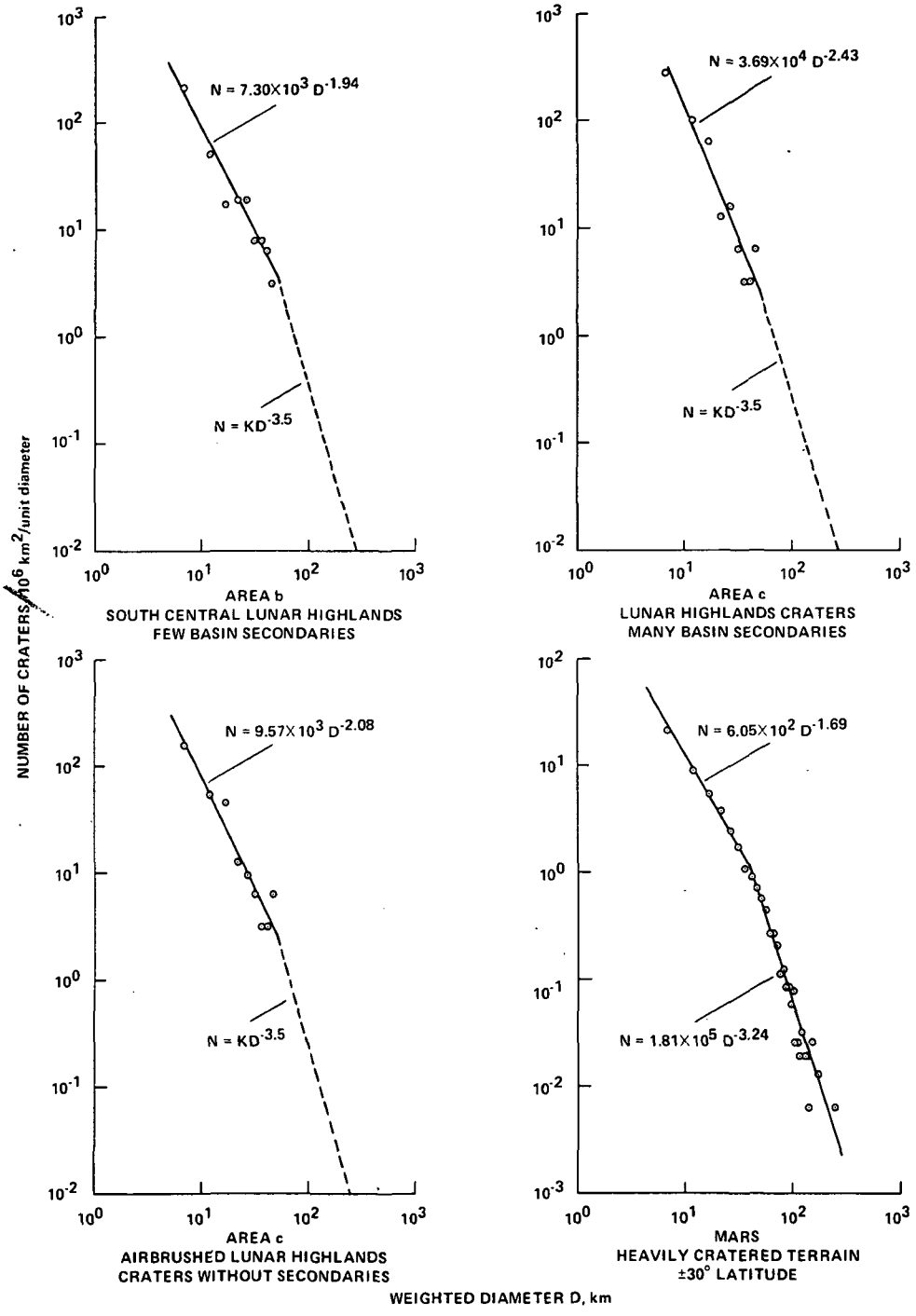

Figure 1. Crater Frequency Distributions for the Moon, Mars and Mercury

Ancient Surfaces of the Terrestrial Planets. Michael C. Malin, Planetology and Oceanography Section, Jet Propulsion Laboratory, Pasadena, CA 91103

Mercury, Mars and the Moon all display features which indicate processes other than impact cratering were operative during their early histories. On Mercury and the Moon, the action of endogenic processes is more easily seen, while on Mars both exogenic and endogenic processes have left their marks.

Study of Mars was initiated during the Mariner 9 mission. Results of preliminary analyses of Mariner 9 data appear in Malin (1) and were reported at the 6th and 8th meetings of the Division of Planetary Sciences of the American Astronomical Society (2, 3). In Malin (1), several characteristics of martian intercrater plains (found within the heavily cratered terrain) which bear on their nature and origin were noted. Specifically, it was observed that the plains consisted of a stratified sequence of competent and incompetent rock units and that the strata were uniform in thickness over large distances. In some areas a distinct, resistant cap rock which displayed mare-like ridges could be recognized. These observations indicated that intercrater plains formation ceased abruptly early in martian history. It was also noted that erosional processes (e.g., channeling, fretting, and chaos formation) presumably involving volatile materials (i.e., water) operated during the period of intercrater plains formation and ceased shortly thereafter. Malin (1) suggested that competent units within intercrater plains are most likely of volcanic origin, and further argued from the uniform thickness over extended distances of less competent units that these were most likely eolian deposits of fine materials (e.g., impact-generated debris, weathering products, volcanic ash). A major, early atmosphere was invoked to explain both the great amounts of uniformly deposited debris and the widespread distribution of erosional landforms whose geneses apparently involved volatiles. The early cessation of intercrater plains formation and the accompanying decline of volatile-related erosion led to the final speculation that the evolution of the martian atmosphere was in some way linked to the early bombardment of the planet. More recent analysis of scarps, ridges and lineaments suggests active tectonic as well as volcanic and atmospheric processes.

Viking results have confirmed many of the observations initially reported in Malin (1), and provide new data for refining the picture of the evolution of early martian surfaces.

Mercury has had a somewhat different history, dominated as well by intercrater plain formation but without obvious volatile or atmospheric activity. This history has been discussed in several publications (4, 5, 6). Intercrater plain formation occurred throughout the period of heavy bombardment and probably reflects both lava extrusion and plastic adjustments crust.

It is suggested that these terrestrial planets record nonballistic processes which acted prior to the formation of the oldest smooth plains and, by analogy with lunar chronology, may have been correlated at least temporally with early bombardment. Whether the processes reflect the composition of the impacting objects (e.g., volatile or radioisotope content), the mode and rate of deposition of heat related to the kinetic energy of the impacting objects, or other phenomena associated with the bombardment has not yet been determined. However, recent research by Ransford (7) suggests impact heating may be the likely explanation.

References

(1) Malin, M. C., Ph.D. dissertation, Caltech (1976).
(2) Malin, M. C., Bull. Am. Astro. Soc. 7 (2) Part II, 369 (1975).
(3) Malin, M. C., Bull. Am. Astro. Soc. (in press)(1977).
(4) Malin, M. C., Geophys. Res. Lett. 3 (10), 581-584 (1976).
(5) Malin, M. C., and D. Dzurisin, Jour. Geophys. Res. 82 (2), 376-388.
(6) Dzurisin, D., Ph.D. dissertation, Caltech (1977).
(7) Ransford, G., Ph.D. dissertation, UCLA (1977).

Origin and Relative Age of Lunar and Mercurian Intercrater Plains. R. G. Strom, Lunar & Planetary Lab., U. of Arizona, Tucson, AZ 85721.

The most widespread terrain type on Mercury is level to gently rolling plains covered by a high density of superposed small craters in the size range 5-10 km. These plains occur between and around clusters of large craters comprising more heavily cratered terrain and have been termed "intercrater plains" (1). The high density of superposed small craters has been interpreted as secondaries from craters and basins of the more heavily cratered terrain which suggests that the intercrater plains are older than most of the heavily cratered terrain and may be the oldest exposed unit on Mercury. If this interpretation is correct then the intercrater plains may be an ancient primordial surface possibly similar to the hypothesized lunar "magma ocean". However, Malin (2) has recognized degraded craters and basins within the heavily cratered terrain which appear to be embayed by intercrater plains suggesting that at least some intercrater plains post-date the later portions of heavy bombardment by large objects. If this is the case then the intercrater plains may represent an early volcanic episode (2) or possibly basin ejecta (3).

On the Moon, a similar type of terrain occurs southwest of the Nectaris basin and is termed the "Pre-Imbrium Pitted Plains" (1 and 4). However, this lunar highlands plains unit has a much more restricted distribution than mercurian intercrater plains. Prior to the Apollo 16 mission which returned impact breccias from a Cayley-type plains deposit, the pitted plains were interpreted as a pre-mare highland volcanic deposit (4). Many investigators now regard this unit to be basin-related ejecta deposits (5). Under this interpretation the deposits' relatively close proximity to the Nectaris basin makes that basin the most likely source.

Since the morphology and stratigraphic relationships of lunar pitted plains and mercurian intercrater plains are so similar, their comparison should provide insight into their origin and relative age. Most previous studies have concentrated on their morphology, stratigraphic relationships, and areal distribution. In this study the crater diameter/density distributions associated with lunar and mercurian highland plains are compared in order to determine the relative age and possible origin of these plains. Only craters in the size range 7-100 km are considered.

Counts of craters ≥7 km diameter were compiled for areas in a strip of lunar highlands extending from the equator to about 70° S latitude and from the central meridian to about 20-30° E longitude. This strip was further divided into blocks consisting of (1) the Albategnius area about 1 to 2 basin radii from the Imbrium basin rim and containing rather large tracts of Cayley material, (2) The Werner area which is rather heavily cratered, and (3) the Cuvier and Manzinus areas containing fairly large tracts of pitted plains. In addition, crater counts were performed in the Clavius region (one of the most heavily cratered regions in the frontside highlands) and in an annular segment adjacent to and south of the Nectaris basin. The annular segment encompasses an area equivalent to the continuous ejecta blanket of a basin this size. Figure 1 is a diameter/density plot of craters in the Albategnius, Werner, Cuvier, and Clavius areas and Figure 2 is a similar plot of the Manzinus area. The crater density (P) is the percent of the area covered by craters of a given diameter. On this type of plot a traditional -2 distribution function on a diameter/frequency plot is a horizontal line, while a -1 distribution is a straight line sloping down to the left at an angle of 45°. This type of plot shows variations in the distribution function much more readily than conventional diameter/frequency plots. Figures 1 and 2 show that the areas containing tracts of pitted plains (Cuvier and Manzinus areas) have a significant deficiency of craters <~40 km diameter

relative to the more heavily cratered areas (Werner and Clavius). This suggests that the pitted plains have obliterated many of the craters <40 km diameter and are therefore younger than much of the heavily cratered terrain. The lunar highlands one basin radius from Imbrium (Albategnius area) show a diameter/density distribution similar to that of the pitted plains. However, contrary to the heavily cratered areas lacking plains units (Clavius and Werner areas) where the density of the more degraded craters (Classes 4 and 5) is significantly less than the fresher craters (Class 3), the Albategnius area shows the density of the more degraded craters is greater than the fresher craters. This indicates that the effect of basin ejecta (Cayley fm.) at one basin radius is to alter the fresher craters (Classes 1-3) to more degraded ones (Classes 4 and 5). Regions of pitted plains (Manzinus and Cuvier areas), on the other hand, display an abundance of fresher craters (Class 3) and a marked paucity of the more degraded types (Classes 4 and 5). This suggests that the mode of emplacement of pitted plains was different from that of the Cayley plains of the Albategnius area. Further, Figure 3 shows that the crater density and population index of the annular segment within one basin radius of Nectaris (Nectaris "Ejecta Blanket") are essentially the same as those of the Clavius area. This indicates that the Nectaris continuous ejecta blanket has been cratered to the same extent as the Clavius region, and that the emplacement of the pitted plains, which caused the loss of craters <40 km diameter, cannot be the result of basin ejecta deposition related to the Nectaris impact. Therefore, the pitted plains probably represent a pre-mare epoch of highland volcanism. Also shown in Figure 3 is the diameter/density distribution of pre-mare craters south of the equator in Oceanus Procellarum and Mare Nubium. The shape of the pre-mare curve and the Manzinus curve are the same, which shows that crater obliteration by volcanic flooding can produce a diameter/density distribution similar to that observed in the pitted plains (Manzinus area).

Figure 4 is a comparison of the crater diameter/density distribution for the lunar Clavius and Manzinus areas, and the south polar region of Mercury (H-15 Quad). The south polar region of Mercury, like many other areas of the planet, contains large tracts of intercrater plains similar to the lunar pitted plains. The slopes of the Mercury curves are steeper than the heavily cratered Clavius area but are similar to the Manzinus area containing pitted plains. This suggests that the mercurian intercrater plains have obliterated craters in a manner similar to that of the lunar pitted plains and were therefore emplaced during the period of heavy bombardment. Furthermore, the curve for the fresher mercurian craters (Curve 1, Figure 4) is shallower than that for more degraded craters (Curve 2, Figure 4), again indicating that the intercrater plains have obliterated some of the original crater population with diameters <40 km. (The turn-up of the mercurian curves at diameters <15 km is the result of the high density of superposed small craters (secondaries) on the intercrater plains).

Therefore, the similarity in the diameter/density distribution between areas containing intercrater plains on Mercury and pitted plains on the Moon suggests that both the mercurian intercrater plains and the lunar pitted plains represent a highland volcanic episode which took place during the period of intense bombardment on each body. The more widespread distribution of intercrater plains on Mercury than on the Moon may be the result of the greater early expansion (more open fracture) of Mercury during formation of its large core than in the case of the Moon (6).

References: (1), Trask, N. J. and Guest, J. E., J. Geophys. Res. 17, pp. 2477 (1975); (2) Malin, M. C., GRL 3, pp. 581-584 (1976); (3) Wilhelms, D.E.,

Icarus 28, 551-558 (1976); (4) Wilhelms, E. D. and McCauley, J. F., USGS Map I-703 (1971); (5) Howard, K. A., et al., Rev. Geophys. Sp. Phys. 12, 309-327 (1974); (6) Solomon, S. C., Ab. Conf. on Comp. Merc. & Moon, p. 32 (1976).

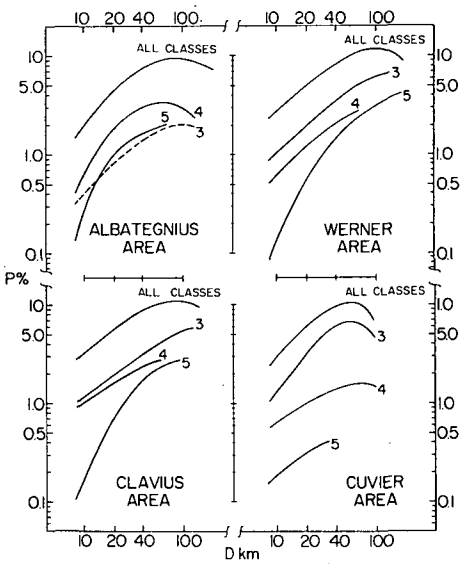

Figure 1

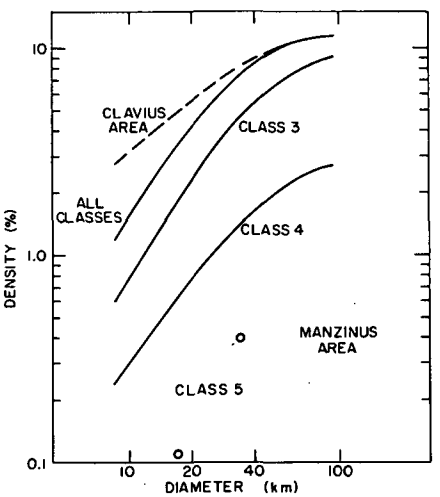

Figure 2

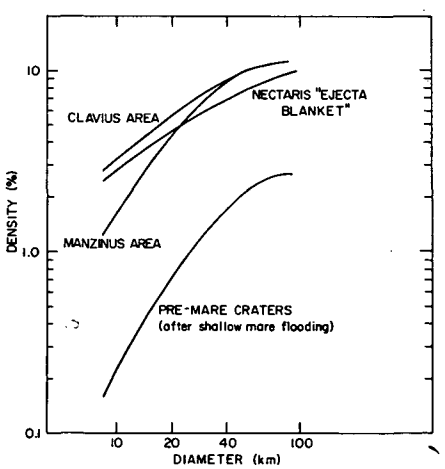

Figure 3

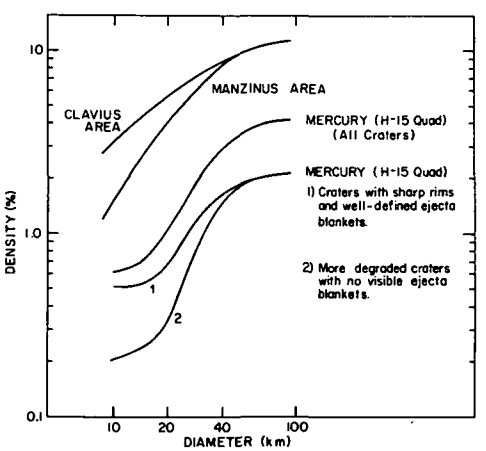

Figure 4

Relative ages of Mercurian plains. Laurence A. Soderblom, U.S. Geological Survey, 2255 North Gemini Drive, Flagstaff, Az 86001.

Measurement of crater density to establish relative ages of geological units is a commonly used technique in planetary geology. Most commonly, observers study small areal samples establishing the size frequency distributions of all the visible craters in those areas. Such diameter-frequency measurements are the most precise (for those small areas), but they are point examples, tediously acquired, and cannot easily be used for mapping tools of relative age.

Crater density can be used as a mapping tool. This requires establishing a "relevant" size range of craters, a narrow diameter range whose density is most likely related to surface age, and mapping the local density of this size range over large regions. Relevant refers to craters that are large enough such that surface processes (such as impact erosion and eolian erosion) are not constantly erasing them and that are small enough so that plains-forming processes obliterated all pre-existing craters when the surface was formed. Or, at least those pre-existing craters were so modified that they are obviously recognized and easily excluded. In order that the mapped density be meaningful the resolution of such a map is necessarily limited by the frequency of craters of the chosen diameter-size range. These limitations are governed by the standard error ($\pm$ N in the statistics ($\pm$ N where N is the number counted). Examples of this mapping technique are given in Soderblom et al. (1974) and Scott and Condit (1977) for Mars.

Using such criteria we have mapped the density of craters in the size range of 5 to 10 kilometers for the available coverage of Mercury excluding those regions where the solar lighting angle on Mariner 10 was greater than 35° (i.e., the solar elevation angle less than 55° - Quadrangle H-7 was excluded). High quality prints of 1:5,000,000 Mercury photomosaics were used as source materials. Areas of smooth plains as described by Trask and Guest (1975) were first plotted on each of the quadrangles. The inter-crater plains, riddled with secondaries were excluded. For each 5° x 5° cell (longitude and latitude) and area of smooth plains was measured and the number of 5-10 km diameter craters was counted. These values were digitized and areal density and statistical uncertainty were calculated for each cell. These data were then smoothed, using standard image processing techniques until the average statistical noise was reduced to 20%; that is the average cell in the running average had more than 25 craters. This resulted in a resolution (cell size) of about 800 km yielding roughly 15 cells for the part of the planet that could be mapped.

Results indicate that the Mercurian smooth plains have a narrow total variation in relative age (crater density) as compared to similar plains on Mars and the Moon which are respectively about 20 to 1 and 5 to 1 (Soderblom et al., 1974 and Boyce et al., 1975). By contrast, the Mercurian smooth plains show a variation of about 3 to 1. Plains in the equatorial and south polar region (including the Caloris planitia) show densities between 2.0 and 4.0 x 10^{-4} craters per km^2 in this size range. The greatest variation in crater density is seen in the north polar region where one area (90°W, 70°N) shows a density of about 1.2 $\pm$3 x 10^{-4}. Photography is poor (oblique) in this area which might account for the discrepancy.

The uniformity of these crater densities is similar to that found by Murray et al. (1974) and Murray et al. (1975) who report variations of about 1.5 to 1. Although obvious swarms of secondaries were excluded from the counts, dispersed fields are very difficult to recognize and may contribute to the variation in crater density (it may be even less than 3 to 1). Compared to the Moon the densities are similar to those seen for the oldest maria and light plains. Scaling a lunar flux to Mercury assuming the same mass flux, higher encounter velocity and gravitational field should yield an upper bound for the Mercurian flux history. This comparison suggests that the Mercurian plains are all ancient (3.5 to 4.5 aeons old) and represent a very narrow span of geologic time.

Boyce, J. M., Dial, A. L., and Soderblom, L. A., 1975, A summary of relative ages of lunar nearside and farside plains: U.S. Geol. Survey, Interagency Rept. Astrogeology 66, 26 p.

Murray, B. C., Belton, M. J. S., Danielson, G. E., Davies, M. E., Gault, D. E., Hapke, B., O'Leary, B., Strom, R. G., Suomi, V., and Trask, N., 1974, Mercury's Surface: Preliminary Description and Interpretation from Mariner 10 Pictures: Science 185, 4146, 11 p.

Murray, B. C., Strom, R. G., Trask, N. J., and Gault, D. E., 1975, Surface History of Mercury: Implications for Terrestrial Planets, JGR, p. 2508.

Scott, D. H. and Condit, C. D., 1977, Correlations: Martian Stratigraphy and Crater Density, abs. this memorandum.

Soderblom, L. A., Condit, C. D., West, R. A., Hermann, B. M., and Kreidler, T. J., 1974, Martian planetwide crater distribution: Implications for geologic history and surface processes, Icarus, 22, 239.

Trask, N. J., and Guest, J. E., 1975, Preliminary Geologic Terrain Map of Mercury, JGR, 2461.

Tectonism and Volcanism On Mercury: Inferences From Morphologic And Photometric Studies. Daniel Dzurisin, Hawaiian Volcano Observatory, Hawaii National Park, P.O., Hawaii 96718

Morphologic and photometric analyses of mercurian surface features, undertaken in support of the author's doctoral thesis and Mercury geologic mapping effort, provide insights into Mercury's tectonic and volcanic history. A scheme for classification of mercurian scarps, ridges, troughs, and other lineaments according to planimetric form was outlined at the 1976 Planetology Program Principal Investigators Meeting (Flagstaff), and will be presented in the literature shortly. Absolute albedo measurements of small areas and relative photometric maps of most of Mercury imaged by Mariner 10 constrain proposed genesis mechanisms for mercurian smooth plains, intercrater plains, and other non-crater landforms. These studies provide a basis for the following speculative tectonic/volcanic chronology for Mercury, which is offered as a working hypothesis subject to test by future topical investigations.

After formation of a solid lithosphere, but before the end of heavy meteoritic bombardment, tidal spindown and global contraction owing to cooling may have combined to produce a global pattern of linear crustal joints on Mercury. Contraction apparently continued after Mercury had been substantially despun, inducing large compressive stresses responsible for development of planimetrically arcuate thrust or high-angle reverse faults. Final movement along these fractures post-dated the formation of most large craters. Details of this proposal, including results of theoretical stress calculations, are provided in a paper in preparation with Dr. Jay Melosh of the California Institute of Technology.

Throughout this early period, intercrater plains formed by extrusion from linear crustal fractures and/or local surface melting. Accumulation of volcanic materials along some fractures created large linear ridges. Erosion subsequently exposed linear dikes which served as feeders for plains-forming fissure eruptions. Superposition of large craters and arcuate escarpments by intercrater plains is rare, suggesting that most intercrater plains were emplaced before the end of heavy bombardment and before most arcuate scarp formation.

The Caloris basin-forming event was a significant milestone in the surface evolution of Mercury. Deposition of, or erosion by, ejected material produced a pattern of linear ridges which radiate from the basin rim. Soon after basin excavation, fluid material covered its floor to form smooth plains. Volcanic extrusion from depth is the preferred mechanism for emplacement of these plains, although impact generated melt and ejecta fallback are plausible alternatives. A system of planimetrically irregular ridges inside Caloris probably formed in response to compressive stresses owing to regional subsidence, perhaps induced by magma withdrawal from beneath to form younger volcanic plains outside the basin rim. Gravitational readjustment to emplacement of plains material outside Caloris may be responsible for scarp and ridge formation there. Finally, continuing isostatic adjustment to basin excavation may have caused central uplift of plains inside Caloris to produce a system of extensional fractures which transect the previously established pattern of ridges. Implications of this scenario for the gravimetric signature of the Caloris region are detailed in a paper (Melosh and Dzurisin) submitted to *Nature*.

At roughly the same time, intense modification of preexisting landforms occurred in a region roughly antipodal to Caloris Basin to produce a distinctive terrain unit characterized by scattered hills and large, linear, open-ended troughs with scalloped walls. Preferential erosion along preexisting lithospheric fractures is the mechanism preferred for linear trough formation.

Planemetrically irregular scarps and ridges developed in smooth plains inside craters are relatively young, tectonic landforms formed in response to local stresses, perhaps induced by subsurface magma movements. The period since smooth plains emplacement on Mercury has apparently been characterized by relatively light cratering and only mild landform degration (1). High reflectivity and anomalous color of several bright patches on crater floors suggest local chemical alteration of surface material during this recent period of mercurian history.

Research supported in part by National Science Foundation Graduate Research Fellowship, and by NASA grants NSG 7155 and W-13, 709 Mod. 13.

1 M. C. Malin and D. Dzurisin, *J. Geophys. Res.*, *82*, no. 2, 376-388 (1977).

Global Tectonics of Mercury. B. M. Cordell, Lunar & Planetary Laboratory, U. of Arizona, Tucson, AZ 85721.

One of the most significant results of the Mariner 10 mission was the discovery of hundreds of lobate scarp-like features widely distributed on the surface of Mercury. Lobate scarps have been interpreted by Strom et al. (1975) as thrust faults caused by a planet-wide compressive stress field, possibly due to thermal contraction of Mercury early in its history. Melosh (1976) has recently suggested that scarps and other lineaments may be a result of loss of angular momentum of the planet by solar tidal interactions during its approach to 3:2 spin-orbit resonance. Planetary lineament systems have also been attributed to 1) despinning due to T Tauri solar wind interactions with planetary magnetic fields, 2) interior convection cells creating surface stresses, 3) polar wandering, and 4) internal redistribution of mass due to variable tidal forces.

For pure planetary contraction, surface stresses would produce thrust faults randomly directed in azimuth. Pure despinning causes a variety of features not observed on the planet (e.g. polar tensional features); however, combinations of despinning and contraction stresses could result in predominantly N-S directed thrust faulting. Surface effects of the other lineament mechanisms are dependent on the particular physics involved but very likely would produce tectonic lineaments nonrandomly distributed in azimuth. These predictions are complicated by local anomalies in rock properties, the plastic nature of a previously faulted crust and observational effects. This paper summarizes the results of a statistical and morphological study of the lobate scarps on Mercury with emphasis on the above problems.

Most of the morphological and transection features of mercurian lobate scarps are illustrated by Discovery and Vostok Rupes. Discovery is over 500 km long and up to 3 km high and its tectonic nature is evidenced by its transection of two large craters; one of which has walls that may show an offset due to the thrust nature of the fault. Vostok Rupe cuts a large crater's walls and shows a clear offset of the crater's walls indicating its compressional tectonic nature. Most scarps are considered to be tectonic because of 1) their height (typically several hundred meters), 2) morphologic similarities to Discovery and Vostok, and 3) consistency of their dimensional parameters with simple models of thrust faulting. A number of geometric and morphologic parameters were measured from the Mariner 10 imagery for each scarp to be used for analysis in this study.

The early inspection of the Mariner 10 imagery by Strom et al.(1975) suggested, and this study has confirmed, three fundamental observations concerning mercurian tectonism: 1) there is no surface evidence for plate tectonics or mantle plumes, 2) there are no exterior concentric graben associated with the large basins, and 3) except for localized regions inside Caloris and the hilly and linear terrain, there are no tensional features at the poles or elsewhere. These observations suggest a tectonic style much more primitive than the earth's, where early global compressive stress fields suppressed the development of tensional features. The lack of polar tension makes untenable the model of pure despinning of Mercury as the origin of the scarps.

The mode (most frequent) lengths of scarps is in the 70-80 km range. Only about 15% of the scarps have lengths exceeding 150 km whereas 85% have lengths between 20 and 150 km. Resolution and illumination effects may hinder identification of smaller scarps.

Figure 1 shows the latitudinal distribution of lobate scarps on the mercurian surface. The plot shows the number of scarps per area (in units of $10^6 km^2$), as a function of latitude, in 10^o increments from the south pole

to +60° latitude. The typical number of scarps per $10^6 km^2$ is about 7-10. However, the latitudes around -20 and -30° which contain the hilly and lineated terrain are deficient in lobate scarps. If Caloris and the hilly and lineated terrain formed simultaneously (Schultz and Gault, 1975), then the assumed destruction of large numbers of scarps at the Caloris antipode implies that most scarps were formed in pre-Caloris time. The lack of evidence for scarps being anywhere embayed by intercrater plains suggests that most scarps are post-intercrater plains. Thermal models of Solomon (1976) provide theoretical evidence against very early lobate scarps because early planetary core formation results in planetary expansion-rift valleys and not thrust faults.

Data on the azimuthal trends of lobate scarp traces is of central importance for a specification of the stress field which caused them. Figure 2 shows four plots of the number of scarps vs. the scarp azimuth for different latitude regions of the planet. The "all latitude" plot includes the latitudes from -90° to +60°. No statistically significant trends are apparent (scarps are randomly distributed), however most scarps appear confined within a sector 60°E and W of north. The remaining plots in Figure 2: ±25°, 25°-40°, >40°, correspond to latitude regions of between +25° and -25°, 25° to 40° and -25° to -40°, and -40° to -90° and 40° to 60°, respectively. For latitudes between ±40° scarp trends display no preferred direction in azimuth, although few scarps have strikes greater than 50° from north. The polar regions(>40°) show no significant preferred azimuth for scarp trends; i.e. scarps are seen trending at all azimuths, including east-west direction.

A possible explanation is that E-W trending scarps are difficult to observe due to lighting effects, and only near the poles would E-W scarps parallel the terminator. Since a region from about 40° latitude poleward would be the only area expected to show comparable numbers of N-S and E-W directed scarps, the conclusion is that scarps seem to be randomly directed in azimuth at all latitudes on Mercury.

The random nature of scarp trends is viewed as strong evidence for the pure contraction model of mercurian tectonism, and as strong evidence against lineament mechanisms resulting in non-random trends. While the proper combination of shrinkage and despinning may cause thrust faulting that is N-S directed at all latitudes, it is considered that the alternate explanation of the data - N-S directed scarps due to planetary despinning were regularly "deflected" of to 50°-60° in azimuth by local irregularities - to be physically unlikely. In general the scarps record no recognizable evidence of the effects of planetary despinning and approach to resonance. While despinning is not ruled out as a tectonic influence on the surface of Mercury, its surface effects are either 1) older than most lobate scarps, 2) have to be subsequently obscured, or 3) never existed. Convection, magnetic and other effects are more difficult to assess, but the non-random nature of their influence does not seem to be recorded in the scarps. It is possible that planetary despinning or other influences may have been responsible for a very early (pre-scarp) set of mercurian lineaments that are rather lunar-like in morphology and trend.

References: (1) Strom, R. G., Trask, N. J., and Guest, J. E., J. Geophys. Res. 80, 2478 (1975); (2) Melosh, H. J., preprint (1976); (3) Schultz, R. H., and Gault, D. E., Moon 12, 159 (1975).

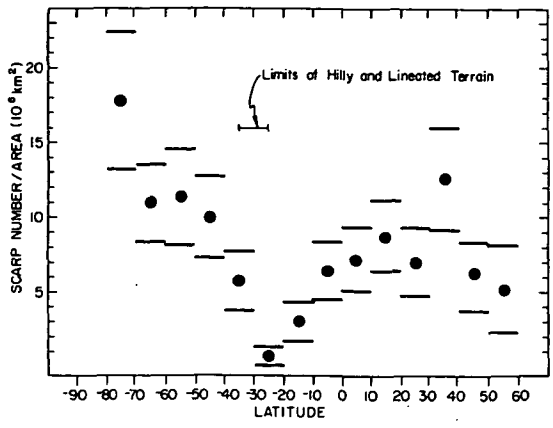

Figure 1

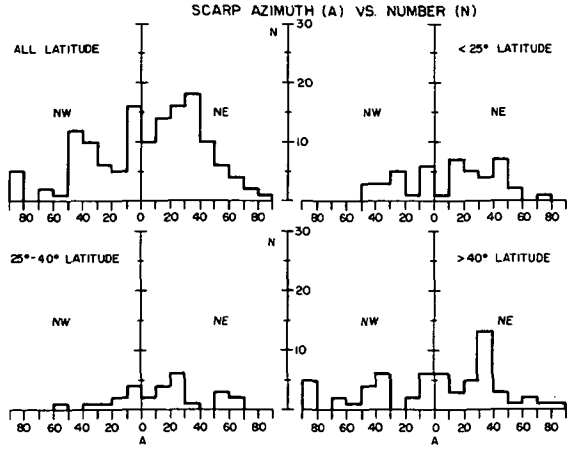

Figure 2

Preliminary Results of Structural Lineament Pattern Analysis of Mercury. Philippe MASSON, Pierre THOMAS, Laboratoire de Géologie Dynamique Interne (bât. 509), Université Paris-Sud, 91405 Orsay Cedex, France.

In order to understand the significance and the origin of lineaments visible on Mercury's surface (near Caloris Basin) four quadrangles (H.1 - Goethe, H.3 - Shakespeare, H.7 - Beethoven, and H.8 - Tir) are studied.

Analysing first the photomosaïcs at 1:5,000,000 scale made at J.P.L. and provided by Henry E. Holt (USGS, Flagstaff Az.), preliminary lineament maps are done. On these maps large lineaments (longer than 500 Km) are drawn. Their geomorphic characteristics are: their extension, their linearity, their intersecting relationships with crater rims and with other lineaments, their horizontal displacements (when some of them are visible).

Two principal lineament directions are seen in these four quadrangles (see Fig.1):

- N.NE/S.SW in H.1, H.3 and H.7,
- W.NW/E.SE in H.7 and H.8.

These two directions seem to be related to Caloris Basin. The lineaments seen in Caloris Basin and cutting its rim, show a radial orientation. The other lineaments located outside and rather far from Caloris Basin (H.7 and H.1 quads) show an orientation parallel to the Caloris radial lineaments.

A more detailed study of each lineament is running, based on Mariner 10 separate frame or stereopair analysis. It comes out that some of these lineaments show horizontal displacements printed in crater rims or in lava flow fronts, and small grabens are seen around Caloris rim, apparently due to some vertical movements.

At that point if the tectonic origin of these lineaments is confirmed, two hypothesis are possible to explain their historical formation:

1) these two directions which seem to be formed contemporaneously, could be related to the Caloris Basin formation.

2) or, they were formed before Caloris (older crustal evolution) and they were rejuvenated during Caloris formation.

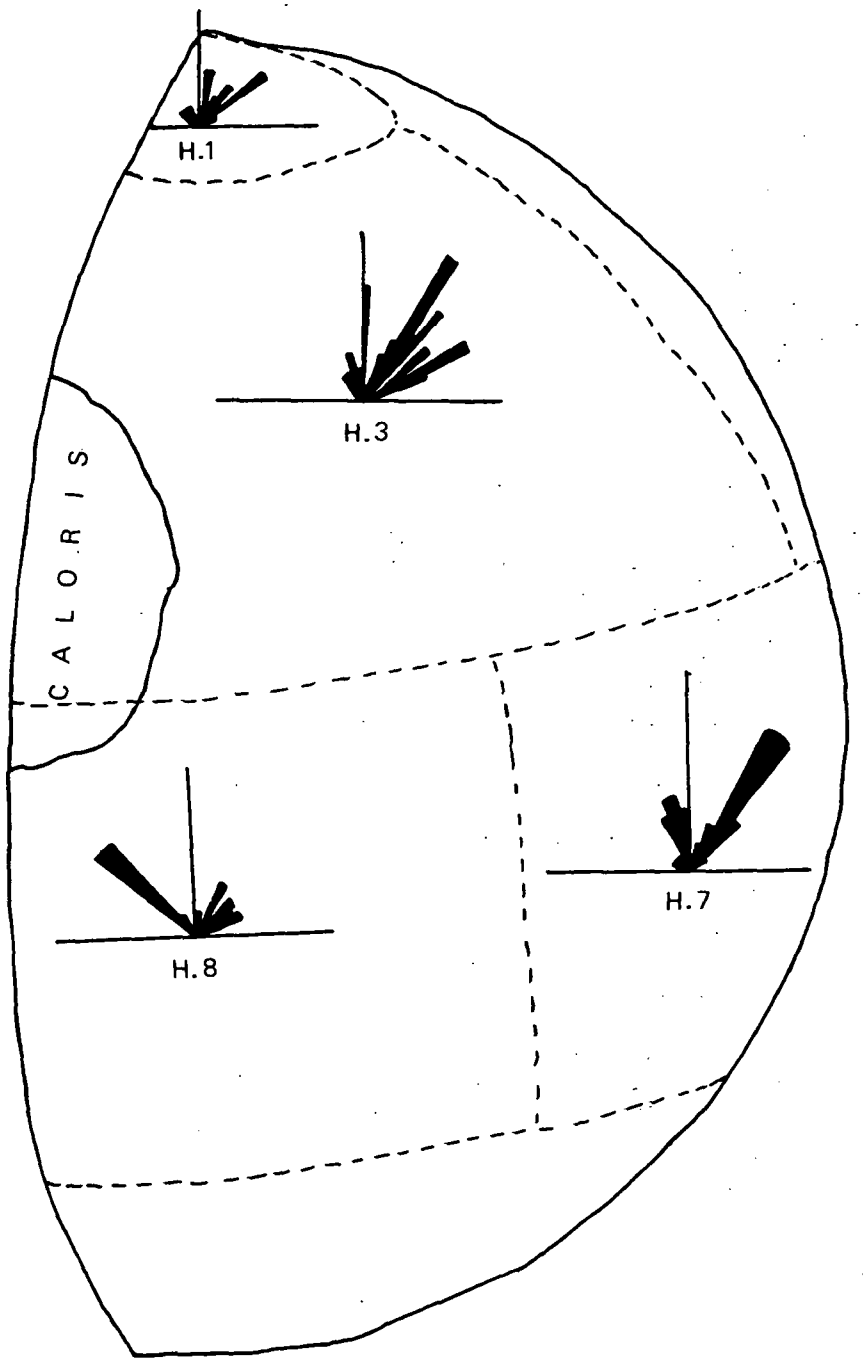

Fig.I: Lineament polar diagrams of H.I, H.3, H.7 and H.8 quads.

Correlations: Martian Stratigraphy and Crater Density. D. H. Scott and C. D. Condit, U. S. Geological Survey, Flagstaff, Arizona 86001

Geologic mapping of Mars (1) established a time-stratigraphic classification of rock units consisting of three major systems, Noachian, Hesperian, and, the youngest, Amazonian. Twenty-five geologic units were assigned to these systems and to positions in stratigraphic sequence using a combination of methods to determine their relative ages. These included overlap and embayment relations of one unit by another, state of degradation of physiographic and structural features, cross-cutting relations of faults, fractures, and channels, superposition relations with relatively dated craters, and differences in the populations of larger diameter craters (>20 km). Some of the rock units appear to occupy relatively narrow niches in geologic time whereas others seem to have been formed over much longer periods.

Subsequent to this mapping, a study was made (2) to determine the intermediate-size (3-10 km) crater density for most of the geologic units on the 1:25,000,000-scale map. The average crater density for the equatorial units was compiled within a zone of approximately $\pm$ 35° latitude. The results of this work show a good correspondence between the inferred stratigraphic positions of most rock units and intermediate-size crater density. Some anomalies were evident, however, as shown in figure 1. The most glaring discrepancy is that of mottled plains material (unit N pm) whose inferred Noachian age is in conflict with its very low density ($33/10^6 km^2$) of intermediate craters. The reason for this becomes clear considering that nearly all of the mottled plains lie far to the north of 35°N latitude, the approximate northern limit of the crater-count study. The few small patches of mottled plains included in the crater counting occur in topographically low areas where they are surrounded and partly mantled by eolian deposits; wind deposition and erosion has effectively obscured a large part of their intermediate-crater populations.

A less obvious anomaly occurs between smooth plains material (unit Aps) and Tharsis volcanic plains (unit Apt). Both units have about the same stratigraphic position, with smooth plains considered even younger in places where it consists of material recently transported by large contemporaneous dust storms. The Tharsis volcanic plains, however, have a much lower crater density than the smooth plains and as the areal extent of both units is large, the statistical relevance of the crater counts is probably good. Thus the reason for the difference between their stratigraphic positions and their crater densities must lie in the nature of the units themselves. The Tharsis volcanic plains occur along an extensive ridge mostly above 5 km in elevation. They are probably dust free and have a high crater retention capacity; crater density should accurately reflect relative age of the unit. The smooth plains occupy low areas near or below datum. It is a composite unit consisting mostly of eolian material that is gradational with cratered plains (unit Apc). Where the smooth plains are thin and cover a relatively featureless substrate, part of this buried material and its crater population may be included in the smooth plains unit. For this reason its crater density may be highly variable from place to place and account for the anomaly shown in figure 1.

Other, smaller differences occur between stratigraphic positions of some rock units and their crater densities. However, the crater density data presented in figure 1 reflect only the mean values and do not show the range of crater densities for each unit. Considering inherent errors in assigning stratigraphic chronologies and in crater counting methods as well as the areal restrictions of the crater density study, the small anomalies remaining do not appear to be significant. Also, some adjustments were made

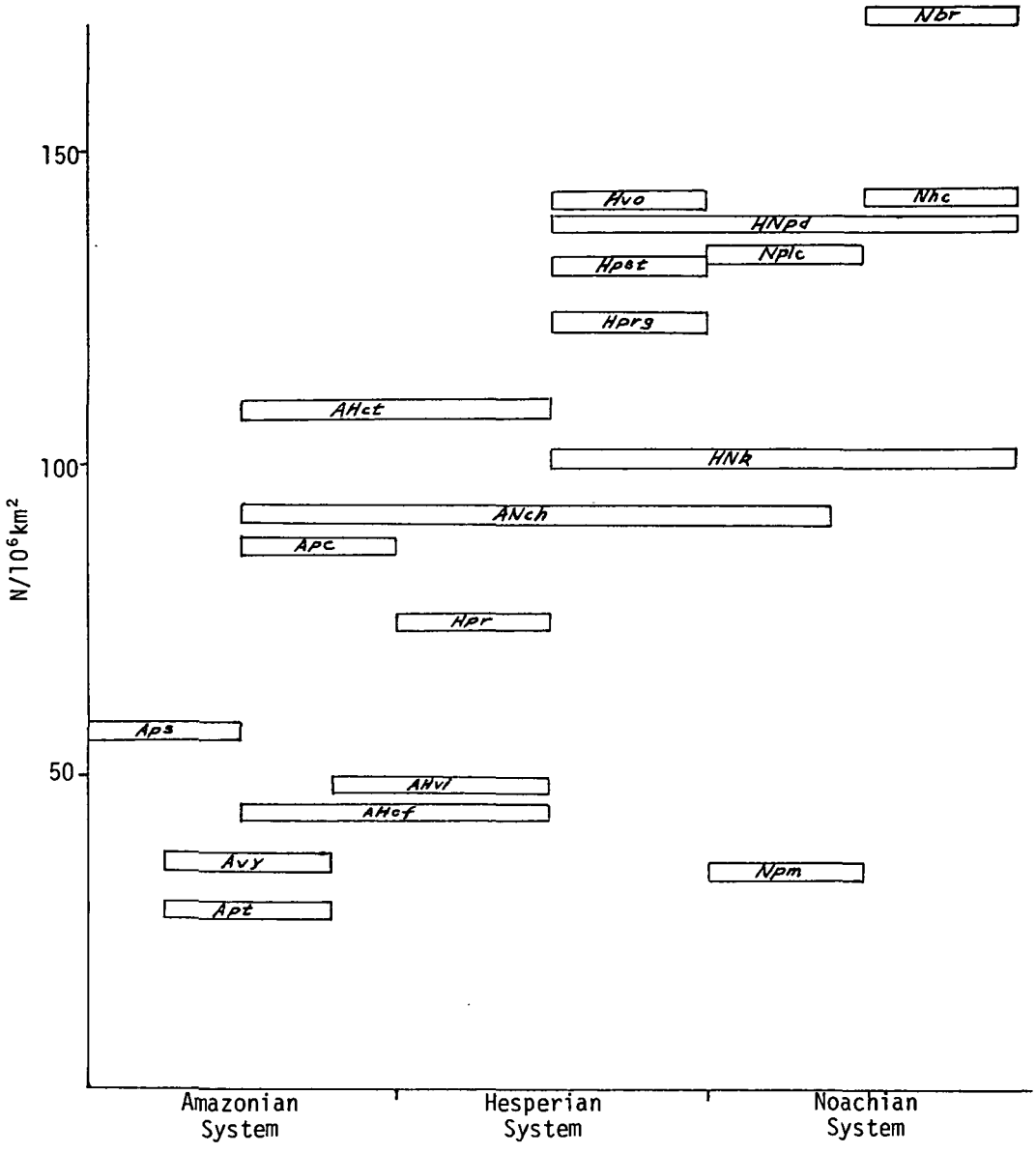

Figure 1.

stratigraphic sequence of martian rock units plotted against number (N) of intermediate-size (3-10km) craters/$10^6 km^2$.

Rock Units

Nbr-basin rim	Hvo-old volcanics	AHvi-intermed. volcanics
Nhc-hilly & cratered	Hpst-streaked plains	AHcf-canyon floor
Nplc-cratered plateau	Hprg-ridged plains	Apc-cratered plains
Npm-mottled plains	Hpr-rolling plains	Avy-young volcanics
HNpd-deflation plains	ANch-channel deposits	Apt-Tharsis plains
HNk-knobby terrain	AHct-chaotic terrain	Aps-smooth plains

in the stratigraphic succession following the crater count study and during preparation of the final map. These changes, however, were minor and involved the extension or retraction of the time intervals occupied by a few units rather than their repositioning in the chronologic sequence.

References

(1) D.H. Scott and M.H. Carr, U.S. Geol. Survey Open File Report No. 76-753 (1976).

(2) C.D. Condit, U.S. Geol. Survey Open File Report (in preparation).

Timing of Deformational Events in the Northern Tharsis Bulge of Mars.
D.U. Wise, Dept. Geology, Univ. Mass., Amherst, MA 01003

The north end of the Tharsis bulge of Mars is a particularly rich area for examining many of the age interrelationships of the planet because of close juxtaposition of many structural age indicators with a number of basic units: ancient cratered terrain, polar-related deposits, lunar appearing plains, and Tharsis volcanics. In evolving an age sequence, traditional relative geologic age indicators were supplemented by strong emphasis on crater density measurements. All homogeneously cratered domains were counted in major map units and in all suitable "B" frames within the Arcadia quadrangle (MC-3) as well as for nearby areas. A standard size frequency curve was used to project these measurements to a 1 km intersection as described by Neukum and Wise (1976a and b). Where "survivor" craters produced a well defined break in the crater curves, intersections for both the older substrate and the younger cover were read. The values at these intersections, namely the cumulative number of craters greater than 1 km diameter per 10^6 km^2, were used as a crater number relative age scale. This scale can be linked to a proposed absolute time scale derived from lunar crater data as described by Neukum and Wise (1976a and b).

The major geologic events from oldest to youngest are: (1) ancient, cratered highland crust (crater number 100,000 = 4.4 b.y.); (2) Lunae Planum lava flows with associated cover of the Tempe plateau and northern plains deposits (crater number 15,000-20,000 = 4.1 b.y.); (3) a period of major fault disruption of the Tempe plateau by the Tempe Fossae system (crater number 10,000-15,000 = 4 b.y.); (4) cover of the Tempe plateau units by a blanket of frost-rich deposits and burial of the south edge of the plateau by oldest cratered plains units (crater number 5,000-10,000 = 3.9-4 b.y.); (5) major geomorphic disection of the western edge of the Tempe plateau; valley wall erosion along Kasei Vallis (crater number 2,500-5,000 = 3.7-3.8 b.y.); (6) construction of Alba Patera, with its associated plains and erosion (crater number 1,000-2,300 = 3.4-3.7 b.y.); (7) splaying fault system of Alba Patera (crater number 500-1,000 = 3-3.5 b.y.); (8) young dunes, eolian plains deposits, thermokarst features.

Broad topographic warpings within the region may have some age limits placed on them. A pseudo-radial lava channel system of Alba Patera has more strongly developed northwest and southeast trending elements suggesting broad arching along a northeast trending axis through the volcano during the outpouring of its flows in the 1,000-2,300 crater number time span. The northwest border of the Tempe plateau is part of a fracture system including the wide valley of Mareotis Fossae. The valley is parallel to the Tempe Fossae fracture system and, like it, lies unconformably beneath etched upland deposits suggesting a similar time of deformation at crater number 10,000-15,000 or about 4.1 b.y. The north-south trending west edge of the Tempe plateau contains the roots of large craters similar to ancient cratered terrains indicating it is an extensively eroded line of anticlinal arching. A swarm of parallel ridges in that area is interpreted as the remains of fracture fillings along the axial zone of the arch. This arching is poorly dated but appears younger than etched upland deposits and older than adjacent plains or about crater number 3,000-5,000 (3.8-3.9 b.y.). Similar or slightly older ages can be applied to the Kasei Vallis deposits and to the cratered plains deposits which either encroach on or cover the tilted south edge of the plateau suggesting the time of that tilting as about crater number 5,000 (3.9 b.y.). A broad subtle NW warping may be indicated across the Tempe plateau to the northwest corner of MC-3 quad-

rangle. Along this line Lunae Planum units and similar aged cratered and fractured plains units are exposed with younger units lapping up onto the structure from the northeast and southwest. The core of the structure is the locus of large exposures of ancient crust of the Tempe plateau and a line of very large old craters on the plains near 55N 80W. The distribution of Lunae Planum aged units over the core of this anticlinorium and the subparallelism of the Lunae Planum mare ridges to it suggest a similar time of arching at crater number 15,000-20,000 (4.1 b.y.). The fact that this arch and Lunae Planum aged units transect the major boundary between cratered uplands of Mars and lower elevation areas of the northern plains means that this fundamental distinction of crustal types predates the Lunae Planum.

The first evidences of the Tharsis arching and stress history begin at crater numbers 15,000-20,000 and extend at least through Alba volcanics of 1,000. The Alba faulting post-dates this but probably ended prior to Olympus Mons with crater number 400. Thus, if the proposed time scale is accepted, Tharsis tectonics involve a complex set of arching, uplift, faulting, and volcanism extending over a period of about 1.5 b.y. from about 4.1 to 2.5 b.y. ago.

References:

Neukum, G., and Wise, D.U., 1976a, Mars: a standard crater size-frequency distribution curve and a possible new time scale: NASA TM X-74316, 27 p.

Neukum, G., and Wise, D.U., 1976b, Mars: a standard crater curve and possible new time scale: Science, vol. 194, no. 4272, p. 1381-1386.

Venus Radar Imaging and Geologic Interpretation. R. Saunders, M. Malin, R. Goldstein, R. Green, and H. Rumsey, Jet Propulsion Laboratory, Pasadena, CA, 91103.

Radar observations of the surface of Venus acquired over the past few years at the Goldstone Tracking Station now cover approximately 6% of the planet at a typical resolution of 10 km per picture element. Reflectivity and altimetry maps (the latter at somewhat lower spacial resolution) are available. As part of a continuing program of mapping the surface of Venus by 12.6-cm microwaves, Goldstein, Green, and Rumsey have reduced additional data taken during the 1975 opportunity. Eight images of the equatorial region, covering about 2% of the planet have been published (1). The latest images include an additional eight equatorial brightness and elevation images and an additional image that includes the β region at 24° N latitude (2). The images have been mosaicked onto an overview radar image of lower resolution but greater coverage. We prepared the mosaic by projecting the larger image to a square latitude-longitude format and then printing the higher resolution images to the same scale. Copies will be made available to planetology investigators.

Some geological observations and interpretations have been derived from the Venus images (3,4). The new images show numerous crater-like depressions, some with raised rims, extensive plains with radar reflectivity that suggest bouldery surfaces, several areas of complex topography reminiscent of martian chaotic terrain, and further evidence of volcanic and tectonic activity. The new image of the β region is particularly exciting. This image provides the first glimpse of what is probably a venusian shield volcano that at least rivals Olympus Mons in size. Except for maximum elevation, the venusian feature β is remarkably similar to its martian counterpart. The main mass of the feature β is approximately 600 km across, compared with 550 km for Olympus Mons. It has a distinct central depression (caldera) approximately 65 km in diameter, almost identical in dimension to the Olympus Mons caldera. The brightness of β in the radar images may be attributed to surface roughness as would be expected from the surface of a shield volcano. The elevation of β is uncertain, but is probably within a few kilometers of 10 kilometers maximum. The observation of such a large shield volcano on Venus, if our interpretation is correct, would decrease the likelihood of Earth-like plate tectonic motions of the venusian lithosphere. However, as more radar images are obtained, the data continue to indicate that Venus is a geologically active planet with diverse landforms and of increasing interest to planetary geologists.

References

(1) R. M. Goldstein, R. R. Green, and H. C. Rumsey, Jour. Geophys. Res., 81, 4807 (1976).
(2) R. Goldstein, R. Green, H. Rumsey, M. Malin, and R. S. Saunders, Bull. American Astron. Soc. (Abstracts of 1977 D.P.S. Meeting), in press (1977).
(3) R. S. Saunders and M. C. Malin, Geologica Romana, in press (1976).
(4) M. C. Malin and R. S. Saunders, Science, in press (1977).

Fracture Domains of Italy - Analogue Study of Brittle Crustal Behavior in a Volcanic-Tectonic Region. D. Wise (1), R. Funiciello (2), M. Parotto (2), F. Salvini (2), (1) Dept. Geology, Univ. Mass., Amherst, MA 01002, (2) Inst. di Geologia, Citta Universitaria, 00100 Rome, Italy.

Curvature of fracture trajectories around Alba Volcano of Mars is among the more spectacular behaviors of the crust of Mars. In an attempt to understand this mechanism of crustal behavior more fully, a terrestrial analogue was sought in the volcanic-tectonic regions of Italy. The results are of considerable interest in the general field of planetary fracturing but have not turned out to be Alba analogues. The volcanic features of Italy are well known and a present day pattern of crustal compression parallel to the axis of that peninsula is beginning to emerge.

Imaging of shadowed relief maps was used to draw fracture traces for all Italy. The resulting 3400 fracture elements were analyzed by a new computer program wherein all data within a given distance of some latitude and longitude were automatically selected for analyses. Up to ten of the most significant peaks on the resulting azimuth-frequency histograms were then automatically fitted with gaussians to provide a smoothing and noise suppression. The gaussians were then recast by computer into windrose form and plotted onto a regional map for all subareas of Italy. Fracture domains for various orientations were drawn and compared with a new brittle fracture map of the Italian peninsula and surrounding seas compiled in conjunction with this study. Some of the fracture domains can be correlated with extensions of offshore fault domains, with known swarms of normal faults of several ages and with broad zones of flexuring along mountain fronts or coastal zones. Nowhere do the systems show obvious pairing or conjugate shear relationships. Nowhere are obvious deflections of fracture trace trajectories related to the modern Italian volcanoes.

In a related study, ground measurements of dikes and minor fault motions were conducted by Wise on the Monte Capanne granite of Elba, one of the youngest (7 m.y.) well exposed circular granite stocks in the world. Northwest trending sigma 3 stress trajectories can be mapped through most of the body without significant deflection. These results, quite unlike the Alba Mars model, support tectonic models of that part of the Mediterranean involving collision of Corsica with the mainland.

This work has developed a technique of fracture domain analysis which will have broad use in planetary studies. It has provided some clues to the origin of the enigmatic topographic linears which seem to characterize all planetary surfaces. For Italy, models producing these features as conjugate shears do not seem to apply. Instead, the fracture traces seem to originate perpendicular to sigma 3 stress trajectories in two different environments: regional compression and sharp flexuring at mountain fronts and basin edges. The lineaments are of a variety of ages and seem to fall into two domain classes: elongate domains of a few hundred kilometers maximum extent and sub-continental domains extending far beyond the limits of Italy. The method has proved useful in delimiting a fracture domain coinciding in location and fracture orientation with the present day seismic energy release pattern of the Apennines. The volcanoes of Italy and the Elba stock, however, cannot be used as simple terrestrial analogues of the splaying Alba stress trajectories of Mars.

Page Intentionally Left Blank

Chapter 4

ASTEROIDS, COMETS, AND MOONS

The Constitution of Cometary Nuclei* Fred L. Whipple, Center for Astrophysics, Harvard College Observatory and Smithsonian Astrophysical Observatory

For many comets the accelerations radially from the Sun have been determined by deviations from gravitational orbits. The radial force per unit area can be calculated on the basis of: a) sublimation equal to absorbed solar radiation divided by the latent heat of vaporization, and b) force radially to the Sun proportional to the momentum of the escaping gas corrected for the geometry of an assumed spherical nucleus.

The calculated radial force is thus proportional to $\pi R^2(1-A)$ where R is the radius and A is the albedo. The acceleration is the force divided by the mass, $4\pi\rho R^3/3$, where ρ is the density, taken as 1.3 gm/cm^3. Equating this theoretical acceleration to the observed non-gravitational acceleration provides a numerical value of $(1-A)/R$.

At extreme solar distances where old short-period comets are usually inactive, photometry provides the well-known quantity area-times-albedo or, as the square root, $RA^{1/2}$. From these numerical values, a solution is then possible for R and A for the nucleus of a comet. The derived quantity from the product is $(1-A)A^{1/2}$, a quantity that maximizes at 0.3849 when $A=1/3$. It provides a limiting check on the basic assumptions and, therefore, on the basic physical properties of the nuclei.

The method is applied to ten short-period comets of perihelion distance, q, less than 1.5 AU, for which the calculations of the non-gravitational forces by Marsden, Sekanina and Yeomans[1] are applicable. The calculated radii range from 0.4 to 1.7 km for $A \leq 1/3$. The results are consistent with water ice as the sublimating material. About half appear to be "spotty," that is, they sublime more slowly than if uniformly covered with water ice. If constituted of a more volatile material they would be even more spotty.

For some comets of a single apparition, H_2O ice is not volatile enough to produce the observed radial accelerations. This, of course, is consistent with the great activity of many comets, both of short and long periods, at solar distances where the vapor pressure of water ice is negligible. For at least one comet, Bennett 1970II, however, the gas production rates, as studied by Delsemme and Rud[2] cannot be reconciled with the observed non-gravitational radial acceleration and the theory of this paper. I suspect that this acceleration is actually spurious, being produced by apparent displacements of the observed nucleus from the true nucleus radially away from the Sun. Such displacements have been observed by Malaise[3]. For C/Bennett I find that the displacements need not exceed some 3300km.

The physical characteristics of comets vary with their orbits and with their age. New comets on their first near solar passage from the Oort cloud are extremely active. The activity appears to fall statistically with increasing age as measured by reduced orbital period. This sequence must represent a corresponding sequence or layering of structure from the surface of a new comet inwards and is described qualitatively in this paper.

I suggest that the excessive activity of new comets such as Kohoutek, 1970XII, at great solar distances, arises from cumulative cosmic-ray damage that activates the outer few hundred gm cm^{-2} from the surface. The total energy input in 4.6×10^9 yr reaches 50,000 cal gm^{-1} near the surface (Fig. 1). This is some 80 times the latent heat of vaporization of water ice. Thus both crystalline structures and molecules are severely damaged if not completely destroyed. Annealing at $T \sim 10$ K must be very small. Hence significant exothermic energy in the form of defects, vacancies and radicals is added to produce the extraordinary activity observed in some new comets. When making this same suggestion earlier Donn[4] concluded that cosmic rays would produce more complicated molecules of carbon but that the volatility of the materials might be reduced rather than increased. The question urgently demands laboratory studies under circumstances relevant to the cometary situation in deep space.

References:

(1) Marsden, B.G., Sekanina, Z. and Yeomans, D.K., Astr. J. 78, p. 211 (1973)
(2) Delsemme, A.H. and Rud, D.A., Astr. Astrophys. 28, 1 (1973)
(3) Malaise, D., "The Study of Comets," NASA SP-393, 740-749 (1976)
(4) Donn, B., "The Study of Comets," NASA SP-393, 611-619 (1976)
(5) Bowen, I.S., Millikan, R.A. and Neher, H.V., Phys. Rev. 53, 855-861 (1938)

* This paper is available as Preprint No. 637 of the Center for Astrophysics, 1976 and is in press: Proceedings of IAU Colloquium No. 39, Lyons, France.

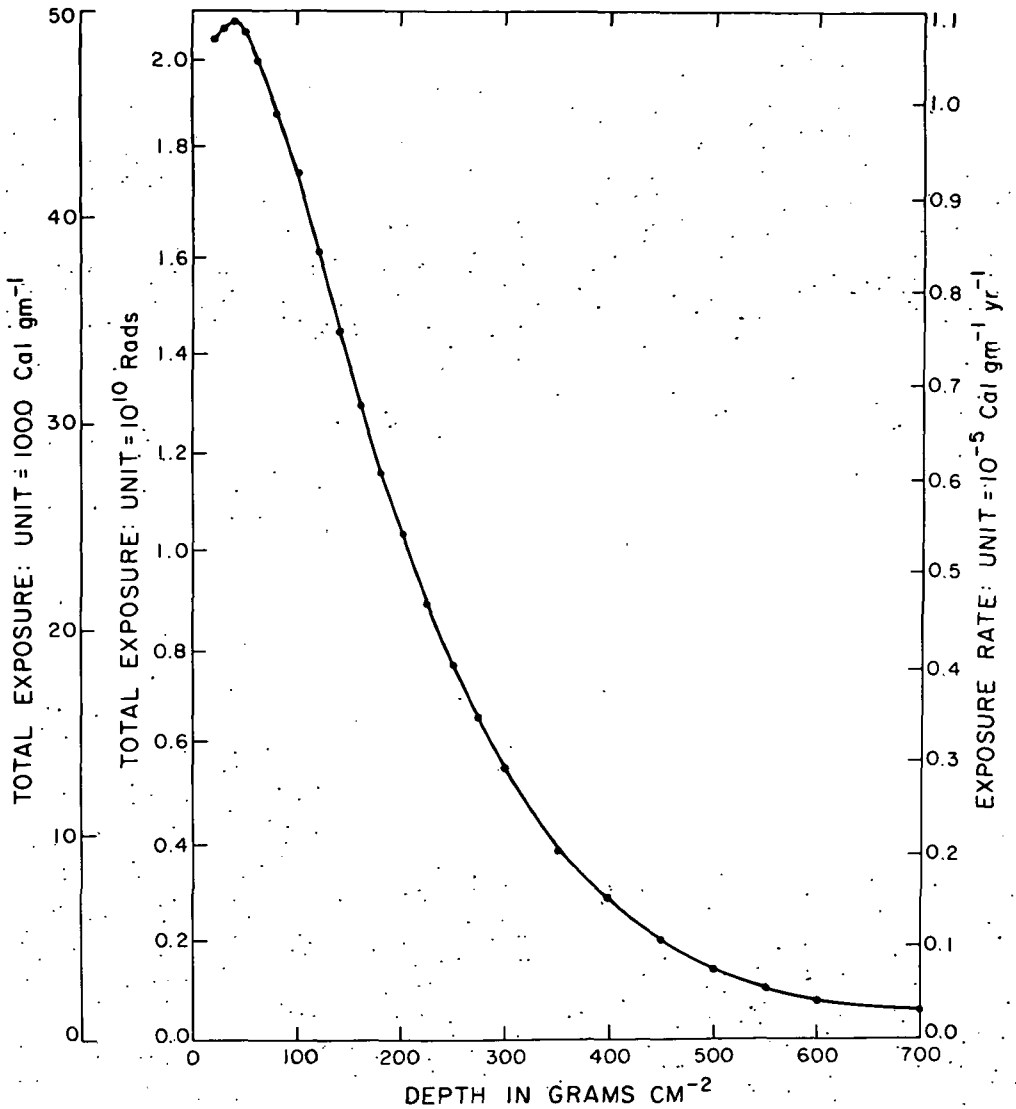

Figure 1. Ionizing Exposure by Cosmic Rays in Comets as Function of Mass Depth: total exposure over 4.6×10^9 yr (left) and exposure rate (right), based on Bowen, Millikan and Neher[5].

Orbit Determination of Nearly-Parabolic Comets and Conclusions Concerning the Oort Comet Cloud. Brian G. Marsden, Center for Astrophysics, Harvard College Observatory and Smithsonian Astrophysical Observatory, Cambridge, MA., 02138.

In continuation of last year's report (1), Table I contains the results of orbit determinations for 25 more long-period comets. The first 12 entries represent new, improved computations for older comets, positions being utilized from the total observed arcs and perturbations by all nine planets being taken into account; the computation for comet 1957 V is by Z. Sekanina, and that for comet 1971 V includes the effects of nongravitational forces. Of the remaining 13 entries, referring to comets that passed through perihelion in 1975 or 1976, three are unperturbed solutions obtained from short arcs. The solution given for comet 1975n refers to nucleus A: similar solutions utilizing the observations of nuclei B or D gave less satisfactory results.

Criteria have been developed for judging orbit quality, and our file now contains 100 first-class orbits and 97 second-class orbits. Together, these orbits comprise less than 40 percent of the observed long-period comets. E. Everhart has revised his computations (2) of the quantities u_b and u_a necessary to reduce the heliocentric osculating values of the reciprocal semimajor axes to the "original" and "future" values, referred to the center of mass of the solar system. A preliminary discussion of these data (3) shows the well-known "Oort effect" to be confirmed and refined in the case of the first-class orbits, although somewhat less so for the second-class orbits. Nevertheless, the effect is still much more pronounced for comets of large perihelion distance (4).

References

(1) Marsden, B. G. and Sekanina, Z., NASA TM X-3364, 34 (1976).
(2) Everhart, E. and Raghavan, N., Astron. J. 75, 258 (1970).
(3) Marsden, B. G. IAU Colloq. No. 39, in press (1977).
(4) Marsden, B. G. and Sekanina, Z., Astron. J. 78, 1118 (1973).

Table I

Recently calculated orbits of 25 long-period comets

COMET	T	Q	E	PERI.	NODE	INCL.	EPOCH
1886 V	86 JUNE 7.8854	0.269803	0.996783	201.2893	193.5059	87.6677	86 JUNE 23
1888 I	88 MAR. 17.5021	0.698772	0.995874	359.9141	246.2570	42.2503	88 MAR. 24
1899 I	99 APR. 13.4781	0.326576	1.000357	8.7040	25.7045	146.2634	99 APR. 16
1908 III	08 DEC. 26.2571	0.945299	1.000672	171.5853	103.7536	140.1775	09 JAN. 15
1911 II	11 JUNE 30.6762	0.683837	0.996296	110.3678	157.9638	148.4265	11 JUNE 13
1911 IV	11 OCT. 10.7638	0.303424	1.000147	71.7046	89.1976	96.4664	11 OCT. 11
1947 VIII	47 SEPT. 4.4310	3.261102	1.002278	73.4524	121.4108	155.0818	47 SEPT.12
1950 I	50 JAN. 19.3128	2.553231	1.000698	40.0965	221.6323	131.3551	49 DEC. 30
1957 V	57 AUG. 1.4373	0.354933	0.999365	40.3135	67.6252	93.9392	57 JULY 21
1970 III	70 MAR. 21.6374	1.719085	0.999125	123.4739	301.0594	86.3089	70 APR. 4
1971 V	71 APR. 17.2497	1.233292	1.000775	152.3562	103.3753	109.6846	71 MAR. 30
1974 XII	74 AUG. 7.8307	6.019048	1.003889	151.7711	225.4027	60.8577	74 AUG. 21
1976C	75 JAN. 15.6855	6.881316	1.001748	193.4386	22.0850	112.0180	75 JAN. 28
1975D	75 APR. 4.5793	1.216939	1.001410	264.1272	157.2120	55.2500	75 APR. 18
1974C	75 AUG. 22.1824	3.011446	0.999593	261.3643	11.6714	50.6422	75 AUG. 16
1975H	75 SEPT. 5.3348	0.425561	1.000095	116.9756	295.6526	80.7779	75 SEPT.25
1975K	75 OCT. 15.3602	0.838047	0.985653	152.0241	216.1091	118.2381	75 NOV. 4
1975P	75 DEC. 21.1813	0.218719	1.000001	358.0972	270.6124	70.6259	75 DEC. 14
1975J	75 DEC. 25.8775	1.603933	0.997450	246.2475	277.9800	91.6061	75 DEC. 14
1975Q	76 JAN. 3.9212	0.863968	1.001214	215.4724	280.7962	93.9534	76 JAN. 23
1976A	76 FEB. 24.636	0.84780	0.99364	313.001	160.095	46.839	
1976D	76 FEB. 25.061	0.67832	1.0	221.755	69.495	147.776	
1975N	76 FEB. 25.2216	0.196626	0.999971	358.4190	118.2313	43.0700	76 MAR. 3
1976K	76 JULY 4.755	5.84532	1.0	118.612	285.455	86.508	
1976G	76 NOV. 3.1544	1.568854	0.999567	193.2555	80.7220	38.8052	76 OCT. 29

A New Model for the Split Comets. Zdenek Sekanina, Planetary Sciences Division, Center for Astrophysics, Cambridge, MA, 02138.

The recognition of a remarkable effect in the configuration of the two nuclei of Periodic Comet Biela in 1846 and 1852 led us to formulate a new model for the motions of the split comets. It is based on the assumption that two fragments of a comet gradually separate at a rate that is determined primarily by a slight difference between the effective solar attractions they are subjected to. The net dynamical effect, which is believed to result from the difference between the momenta transferred to the fragments by outgassing, is of the same nature as the nongravitational forces studied by Whipple (1) and later positively detected in the motions of most of the short-period comets and of some of the nearly-parabolic comets by Marsden (2). The magnitude of the effect in the motions of the split comets depends on the size, density, structure, composition and spin rate of the fragments.

In accordance with the developed formalism (based on an analogy with the effect of radiation pressure on dust particles in cometary tails), we assume that the dynamical force from outgassing is directed away from the sun and varies with heliocentric distance in direct proportion to the solar attraction, so that their ratio is constant. This has been judged to be a reasonable approximation, since the vaporization rate of a volatile substance (as well as the resulting momentum) is known to vary almost exactly in inverse proportion to the square of distance from the sun when the fraction of the solar energy absorbed by the comet is spent predominantly on surface evaporation (rather than on reradiation). The calculations indicate that for water snow, this is true at solar distances up to and somewhat beyond 1 AU and might be a fair approximation even beyond 1.5 and near 2 AU, depending primarily on the degree of contamination of the snow by dust particles.

An iterative least-squares differential-correction procedure has been developed to apply the described model to 33 fragments of 13 split comets, for which angular separations were measured. The basic results of this study, whose details were published elsewhere (3, 4, 5), can be summarized as follows:

(1) The differential force exerted on the fragments by outgassing is typically on the orders of magnitude of 10^{-5} to 10^{-4} the solar attraction.

(2) The magnitude of the differential nongravitational force appears to be inversely correlated with the endurance of the fragments, which is defined as the time from splitting to last observation weighted by the inverse square law of the vaporization rate normalized to 1 AU from the sun.

(3) There is a clear indication that the fainter and less enduring fragments are decelerated relative to the brighter and more persistent ones. The two exceptions to this rule are companion C of Periodic Comet Brooks 2 and fragment A of the sungrazing comet 1882 II.

(4) The times of separation fail to show any characteristic pattern, although some comets split near perihelion (1899 I, 1947 XII, 1970 III, 1975n) and the two sungrazers (1882 II and 1965 VIII) did so in the solar corona, not more than a couple of hours of the perihelion passage. On the other hand, some comets broke up well before perihelion (companion B of P/Brooks 2, 1915 II, 1916 I, probably also 1860 I and 1957 VI) and P/Biela long after perihelion. Companion C of P/Brooks 2 separated near the aphelion of its present orbit, during the comet's very close approach to Jupiter.

(5) The splitting of the sungrazing comets and the primary breakup of P/Brooks 2 might (but do not necessarily have to) be due to tidal forces from the sun and Jupiter, respectively. Other breakups cannot be explained on the basis of this hypothesis and their nature is unclear.

(6) In about 50 per cent of the cases the solution left systematic residual trends that were slight but not negligible. The effects of an impulse at separation, the complicated character of the nongravitational forces (not fully accounted for) and the differential planetary perturbations are suggested as possible sources of the deviations, but their quantitative study is postponed to a future date.

(7) The earth's passages through the orbit planes of the split comets offer rare opportunities to see the fragments "edge-on" and thus to determine their off-plane separations independently of the dynamical model. These correspond to a normal component of the relative velocity of about 1 m/sec or less, or to a normal component of the nongravitational force on the order of 10^{-6} the solar attraction, i.e., 10% of the radial component or less.

(8) The only major drawback of the new approach is its failure to fit the motion of the fragments of Comet Wirtanen 1957 VI, where systematic residuals were comparable to the magnitude of the separation itself. Considering that this is one of the best observed comets, the misrepresentation is clearly of concern and indicates that the model should be doctored up.

References

(1) Whipple, F. L., Astrophys. J. 111, 375 (1950).
(2) Marsden, B. G., A. Rev. Astron. Astrophys. 12, 1 (1974).
(3) Sekanina, Z., Center for Astrophys. Preprint No. 530 (1976). (Icarus, in press.)
(4) Sekanina, Z., Center for Astrophys. Preprint No. 580 (1976). (Astrophys. Lett., in press.)
(5) Sekanina, Z., Center for Astrophys. Preprint No. 616 (1976). (Proc. IAU Coll. No. 39, Lyons, France, in press.)

Asteroid Fragmentation Processes and Collisional Evolution. Clark R. Chapman, Donald R. Davis, and Richard Greenberg, Planetary Science Institute, 2030 E. Speedway, Tucson, AZ, 85719

The asteroids and their fragments are a population of objects in the inner solar system, concentrated between 2 and 4 AU from the sun, which are the remnants of a much larger population of planetesimals that formed the terrestrial planets. Since a large planet failed to form in the asteroid belt, the asteroidal planetesimals have remained to collide with each other and with other planets. The smaller fragments which strike the Earth are called meteorites; the larger ones form craters. Astronomical data obtained during the 1970's have yielded some knowledge about asteroid compositions and, in particular, have strengthened the above hypotheses. These data also have permitted, for the first time, accurate estimates of asteroid sizes. These constraints on asteroid compositions and the new knowledge of asteroid sizes, combined with a knowledge of asteroid orbits and fragmentational physics, permit us to calculate asteroid collision probabilities and the evolution of the size distribution.

Chapman and Davis (1) reported results based on a preliminary computer model of asteroidal fragmentation which demonstrated that asteroids are colliding much more frequently than had been believed before -- sufficiently frequently, in fact, that the asteroids may be regarded as a remnant of a possibly much larger population of objects in the asteroid zone. Further discussion of collisions by Chapman (2,3) developed the hypothesis that one observational type of asteroid (designated "S") are the stony-iron cores of differentiated parent-bodies whose rocky mantles have been stripped away by numerous collisions and that another observational type (designated "C") are the highly fragmented remnant of a vast population of carbonaceous asteroids. Based on this hypothesis, Chapman and Davis (1) estimated that, in fact, the C-type asteroids were roughly 300 times more numerous at an early epoch.

Such models for the collisional evolution of the asteroids seemed to satisfy the available data about the size-frequency distributions of asteroids of the separate compositional classes (4): a power-law distribution for C-type asteroids and a more complicated distribution for S types. More recent data on asteroid size distributions by Zellner and Bowell (5) differ from the earlier data and it is clear that the simple collisional models require revision.

We have augmented our collisional model in several ways to render it more closely representative of actual fragmentational physics. First, our program has been modified to permit the simultaneous collisional interaction of two distinct compositional types, represented by material strengths deemed appropriate for the two predominant types of asteroids (S and C). We have considered cases for strengths close to nominal values for metallic iron (20000 bars) and for carbonaceous meteorites (3 bars), as well as very different values. The second major change is an improved consideration of the size of the largest fragment resulting from a catastrophic fragmentation of an object sufficiently large so that the gravitational binding energy of the object dominates the material strength.

The largest fragment from a catastrophic collision clearly depends on the energy density imparted to the target body. Because of the power-law dependence of the asteroid size distribution, most catastrophic fragmentations (in the absence of a gravity field) involve a collision imparting only marginally enough energy to overcome the material strength of the target; thus the largest fragment is usually a significant fraction of the mass of the target. But for a weak body large enough to possess an appreciable gravitational field, collisions involving sufficient energy to fragment the

body will not in general be sufficient to impart the kinetic energy to the fragments necessary to overcome the body's self-gravity and to disperse the fragments. Thus a catastrophic fragmentation and dispersal of fragments must result from a superenergetic collision, which will certainly fragment the target into many small pieces. The effect will be enhanced by the fact that in general the target body will have been internally fractured by numerous collisions sufficient for fragmentation but insufficient for dispersal. Our improved collisional model incorporates these features.

Numerical experiments simulating the collisional interaction of only weak carbonaceous bodies now yield a size distribution similar to that observed (for diameters greater than 50 km) by Zellner and Bowell (5). In particular, the observed relative absence of 50 - 100 km diameter bodies appears to be due to the infrequent creation of fragments of that size by the catastrophic fragmentation of somewhat larger, gravitationally bound C asteroids.

Numerical experiments simulating the collisional evolution of strong S objects plus weak C objects demonstrate that S objects are surprisingly effective at decimating any population of C objects. Evidently S objects cannot be as strong as 20000 bars; otherwise there would not be so many C asteroids as exist. The observed size distributions of asteroids are best satisfied by simulations in which the S asteroids are not more than two orders of magnitude stronger than C asteroids. However, no simulation has yet been completely successful in producing the current distribution of both C- and S-type objects. Our numerical simulations are being further refined to include the effects of collisional erosion on the size distribution and the mutual effects of size distribution and characteristic impact velocity.

The earlier conclusions of Chapman and Davis (1) that the C asteroids may be a remnant of a much more populous asteroid belt are unchanged by these new considerations. But their argument that the belt was roughly 300 times more populous in the past depends on suppositions about the physical nature of the S-type asteroids which seem to require revision.

(1) C. R. Chapman and D. R. Davis, Science 190, 553 (1975).
(2) C. R. Chapman, Geophys. Res. Lett. 1, 341 (1974).
(3) C. R. Chapman, Geochim, Cosmochim. Acta 40, 701 (1976).
(4) C. R. Chapman, D. Morrison, and B. Zellner, Icarus 25, 104 (1975).
(5) B. Zellner and E. Bowell, I.A.U. Colloquium No. 39 (Lyon, France)(1976).

Present Impact Cratering Rates on the Terrestrial Planets and the Moon.

Eugene M. Shoemaker and Eleanor F. Helin, Division of Geological and Planetary Sciences, California Institute of Technology, Pasadena, California 91125

Present rates of cratering by impact on the terrestrial planets and the Moon can be calculated from estimated populations of planet-crossing asteroids. An upper bound on the contribution of active comet nucleii to the present cratering rates can be obtained from photometric observations of comets by Roemer; it is found that craters produced by active comets are at least an order of magnitude less abundant than the craters produced by asteroidal objects. Hence, cratering rates calculated from population and impact probabilities of the various classes of planet-crossing asteroids should be close to the true rates, provided that the crater scaling laws are adequately known.

Probabilities of impact of Earth-crossing asteroids with the terrestrial planets and the Moon are listed in Table 1. When combined with an estimate of the total population of these objects, based on discoveries in three systematic surveys of the sky, and plausible values of mean albedo and density, the probabilities of impact can be converted to cratering rates (Table 2). The cratering rates shown in Table 2 for Earth and Moon are estimates of the total cratering, exclusive of the minor contribution by active comets. For the other terrestrial planets, account must be taken of asteroidal objects that do not cross the orbit of the Earth. In the case of Mars, the contribution of Mars-crossing asteroids that do not reach Earth can be estimated from direct observation (Table 3). In the cases of Mercury and Venus, there must be a class of asteroids with aphelia inside Earth's orbit that contribute significantly to the cratering rate of these two planets. These Mercury- and Venus-crossing asteroids have been deflected into very small orbits during close dynamic encounters with the two innermost planets; they are virtually precluded from astronomical discovery because the phase angle is never less than 90° and they are always extremely faint. Very roughly, the total crater production rates for Mercury and Venus are at least equal to that shown for Earth in Table 2.

A final correction to the cratering rates on Earth and Venus should be made to account for collapse of crater walls and consequent increase of crater diameters. This effect is not accounted for by the crater scaling relations given in Table 2. On Earth and Venus the correction is estimated to be a factor of 1.8 for the production of craters at 10 km diameter; the correction is negligible at this crater size on Mercury, Mars, and the Moon. When all known factors are taken into account, the relative cratering rates per unit area on the 5 principal objects in the inner solar system are estimated as follows:

	Approximate relative rate of production of impact craters 10 km in diameter
Mercury	1/2
Venus	1
Earth	1
Moon	1/2
Mars	1

TABLE 1

Impact probabilities and velocities of impact of Earth-crossing asteroids with the terrestrial planets and the Moon [1]

Asteroid	Impact on Mercury		Impact on Venus		Impact on Earth		Impact on Moon		Impact on Mars	
	Impact Velocity (km/sec)	Probability of impact (10^{-9}/yr)	Impact Velocity (km/sec)	Probability of impact (10^{-9}/yr)	Impact Velocity (km/sec)	Probability of impact (10^{-9}/yr)	Impact Velocity (km/sec)	Probability of impact (10^{-9}/yr)	Impact Velocity (km/sec)	Probability of impact (10^{-9}/yr)
1566 Icarus	46.8	1.37	37.7	2.72	31.8	1.75	29.9	.11	21.1	0.24
1974 MA	42.5	.26	36.3	1.01	32.7	0.57	30.9	.04	25.0	0.06
1936 CA Adonis	22.2	.57	27.8	7.08	27.3	10.99	25.1	.68	21.6	0.76
1976 UA	13.7 [2]	1.33 [2]	19.5	15.78	23.2	14.84	12.9	.64	--	0
1864 Deadalus	--	0	25.3	2.34	24.8	1.26	22.2	.08	18.3	0.14
1965 Cerberus	--	0	20.6	5.28	20.0	3.12	16.7	.16	11.0	0.39
1937 UB Hermes	--	0	19.6	6.05	21.9	3.47	19.0	.19	17.2	0.34
1973 EA	--	0	32.4	1.53	30.1	0.64	28.1	.04	23.3	0.07
1862 Apollo	--	0	17.5	8.33	20.3	4.29	17.1	.23	15.1	0.41
1685 Toro	--	0	--	0	17.2	4.18	13.3	.18	12.1	0.36
1976 AA	--	0	--	0	15.7	7.98	11.3	.30	--	0
PL-6743	--	0	--	0	17.0	4.20	13.1	.18	13.8	0.31
1620 Geographos	--	0	--	0	16.1	4.46	11.8	.18	9.8	0.41
1959 LM	--	0	--	0	15.1	14.90	10.4	.52	10.2	0.99
1950 DA	--	0	--	0	17.7	2.50	13.9	.11	14.6	0.19
1866 Sisyphus	--	0	--	0	27.8	0.95	25.5	.06	22.0	0.07
1973 NA	--	0	--	0	40.3	0.60	38.8	.04	31.4	0.04
1863 Antinous	--	0	--	0	19.5	1.20	16.2	.06	17.7	0.08
1975 YA	--	0	--	0	35.5	2.46	33.7	.16	25.3	0.25
PL-6344	--	0	--	0	15.8	4.81	11.4	.18	16.3	0.22
rms impact velocity	34.2		27.3		24.6		21.7		19.0	
mean probability of impact		0.18		2.51		4.46		0.21		0.27

1/ Impact probabilities and impact velocities listed here are calculated with the use of the equations of Öpik (1951 and 1976). For a listing of the orbital elements required for these calculations, exclusive of the elements of 1976 UA, see Wetherill (1976).

2/ Impact velocity and probability of impact of 1976 UA with Mercury are based on a statistical model of the secular variation of eccentricity and inclination of Mercury derived from the 10 million year histories of planetary elements presented by Cohen et al (1973).

TABLE 2

Impact rates and rates of crater production by impact of Earth-crossing asteroids with the terrestrial planets and the Moon

	Mercury	Venus	Earth	Moon	Mars
	(10^{-14} km^{-2} yr^{-1})	(10^{-14} km^{-2} yr^{-1})	(10^{-14} km^{-2} yr^{-1})	(10^{-14} km^{-2} yr^{-1})	(10^{-14} km^{-2} yr^{-1})
Rate of impact of Earth-crossing asteroids to absolute visual magnitude 18 1/	0.2 ± 0.1	0.4 ± 0.2	0.7 ± 0.35	0.4 ± 0.2	0.15 ± 0.07
Rate of production of craters 10 km in diameter and larger by impact of Earth-crossing asteroids 2/	0.4 ± 0.2	0.5 ± 0.25	0.7 ± 0.35	0.6 ± 0.3	0.15 ± 0.07

1/ Based on an estimated population of 800±400 for Earth-crossing asteroids to absolute visual magnitude 18 and on the mean probabilities of impact given in Table 1.

2/ Based on adopted mean visual geometric albedo for Earth-crossing asteroids of 0.2 and mean density of 3.3 gm/cm^3; includes corrections for effect of difference of surface gravity on diameters of craters produced on each planet. Diameters of craters have been calculated from the following formula determined from terrestrial cratering experiments

$$D_e = (74\text{m/kt TNT equivalent}^{1/3.4})\ W^{1/3.4} \qquad (3)$$

where D_e is diameter of crater formed on Earth, W is kinetic energy of projectile in kilotons TNT equivalent (Shoemaker et al, 1963); one kt TNT equivalent is 4.185×10^{19} ergs. The diameters given by equation (3) are then scaled for gravitational acceleration at the surface of other planets or the Moon by

$$D_p/D_e = (g_e/g_p)^{1/6} \qquad (4)$$

where D_p is diameter of crater on other planet or Moon, g_e is surface gravity on Earth, and g_p is surface gravity on other planet or Moon (D.E. Gault, personal communication 1976). The cumulative frequency of the craters produced is assumed to be proportional to $D^{-1.7}$, consistent with the observed distribution of post-mare lunar craters larger than 3 km (Shoemaker et al, 1963; Baldwin, 1971).

TABLE 3

Impact rates and rates of crater production by impact of asteroids on Mars

Asteroid Class	Perihelion distance (AU)	Number of asteroids to absolute visual magnitude 18	Rate of impact on Mars to absolute visual magnitude 18 (10^{-14} km^{-2} yr^{-1})	Rate of production of craters 10 km in diameter or larger (10^{-14} km^{-2} yr^{-1})
Earth- and Mars-crossing (Apollo asteroids)	$q < 1.02$	750±300	0.15±0.07	0.15±0.07
Deep Mars-crossing (Amor asteroids)	$1.02 \leq q \leq 1.30$	600±400 [1]	0.08±0.05 [2]	0.06±0.04 [3]
Moderate Mars-crossing	$1.30 < q \leq 1.68$ [4]	15,000±9000 [5]	1.4±0.8 [6]	0.8±0.5 [7]
Shallow Mars-crossing	$1.68 < q \leq 1.73$ [4]	10,000±7000 [8]	0.2±0.15 [9]	0.1±0.1 [9]
Total		26,000±17,000	1.8±1.1	1.1±0.7

1/ Based on discovery of 3 objects in systematic surveys
2/ Based on estimated population and orbital elements for 17 known objects
3/ Based on data indicated in footnotes 1 and 2 and equations 3 and 4 in Table 2.
4/ As noted by Wetherill (1974), secular variations of eccentricity will preclude collision with Mars for many objects with perhelion distances in this range.
5/ Based on discovery of 3 objects in systematic surveys
6/ Based on estimated population and orbital elements for 31 known objects
7/ Based on data indicated in footnotes 4 and 5 and equations 3 and 4 in Table 2.
8/ Based on discovery of 2 objects in systematic surveys.
9/ Rough estimate only.

A Quantitative Comparison of the Surface Roughness of Phobos and Deimos.
P. Thomas and J. Veverka, Laboratory for Planetary Studies, Cornell University, Ithaca, NY 14853

Mariner 9 television images produce the impression that there is less small-scale surface detail on Deimos than on Phobos. It has been suggested that this is an artifact of the processing since Deimos images are magnified more than those of Phobos (Veverka et al. (1974) Icarus, 23, 206). To settle this issue we have pursued two quantitative methods of comparing the surface roughness of the two satellites on scales of 200-400 meters. First, by comparing the roughness of limb profiles (i.e., skylines) on the two satellites; second, by comparing brightness fluctuations in local areas (DN variances). Of the 36 different images obtained by Mariner 9, 4 of Deimos (D25, D111, D149 and D159) and 6 of Phobos (P34, P43, P48, P73, P77 and P80) are suitable for this analysis. Preliminary results indicate that both limbs have similar degrees of roughness on scales of 200-400 meters, and that DN variances are similar in the regions between large craters on both satellites. However, Phobos is rougher than Deimos on scales of several kilometers, and its surface departs more from the triaxial ellipsoid model of Duxbury than does that of Deimos (Duxbury (1974), Icarus, 23, 290; Noland and Veverka (1977), Icarus, 30, 212).

Currently the above techniques are being applied to the recent Viking images of Phobos and Deimos which have a much higher resolution than those obtained by Mariner 9.

Page Intentionally Left Blank

Chapter 5

CRATERING AS A PROCESS, LANDFORM, AND DATING METHOD

LUNAR AND MARTIAN CRATERING STUDIES, AND MARS MARINER 9 GEOLOGIC MAPPING

G. Neukum, Institut für Allgemeine und Angewandte Geologie, University of Munich, and Max-Planck-Institut für Kernphysik, Heidelberg, Fed.Rep.Germany, H. Fechtig and Beate König, Max-Planck-Institut für Kernphysik,Heidelberg, Fed. Rep.Germany, K. Hiller, Institut für Allgemeine und Angewandte Geologie, University of Munich, Fed.Rep.Germany, D.U. Wise, Department of Geology and Geography, University of Massachusetts,Amherst, USA.

I. Lunar Studies

1. The Lunar Impact History in the Last Three Billion Years.

B. König, G. Neukum, H. Fechtig

a) The lunar impact crater production size-frequency distribution in the diameter range 2om-2okm.

The production distribution of primary lunar impact craters was investigated in younger ($\lesssim 3.5.10^9$ years) areas, such as young lava flows, and floors and ejecta blankets of Copernican craters.A strict selection of such counting areas made it possible to exclude most factors of contamination of the primary distribution such as affection by subsequent lava flows, secondary craters,erosion on steep slopes, volcanic craters, etc. The studies resulted in one general distribution for the size range $2om \leq D \leq 5oom$ indicating that the distribution in this size range did not change significantly in the last 3 billion years.

The new measurements have been synthesized with those by (1) for $D \gtrsim 3oom$ and $t \gtrsim 3$ billion years, resulting in one standard size distribution of the primary lunar impact craters (Fig.1). This distribution can be used to refer crater frequency measurements in different size ranges and on differently old areas to a crater frequency value at a standard crater size, preferably D=1km.

The distribution in Fig.1 can be approximated by a polynomial in log D of seventh degree: $\log N = a_o + a_1 \log D + a_2 (\log D)^2 + \ldots + a_7 (\log D)^7$

with $a_o = -2.419$ $a_2 = o.741$ $a_4 = -o.254$ $a_6 = o.o36$

$a_1 = -3.852$ $a_3 = o.958$ $a_5 = -o.349$ $a_7 = o.o46$

(D in km, N per km^2). This polynomial is valid in the size range $2om \leq D \leq 2okm$, but not beyond these limits. Preliminary results by (2) are superseded by these data.

b) The lunar cratering chronology in the last 3 billion years.

In Fig.2 the crater frequency data for the craters North Ray, Tycho, Copernicus, for the terrestrial Canadian Shield (reduced to lunar conditions) and for the A 12 and A 15 LS (3) are plotted versus the corresponding radiometric ages. Cumulative crater frequency curves calculated on the basis of the most reliable North Ray data are inserted for flux half-lives of 1oo, 3oo, 5oo, 1ooo, 3ooo m.y., and for constant flux ($T_{1/2} = \infty$). A constant cratering rate fits the data reasonably well for the whole age range. However, a flux decreasing with a half-life of 3oo-1ooo m.y. for the last 8oo m.y. is also compatible with the data. This means that a slight temporary increase in cratering rate at about 6oo to 8oo m.y. followed by a slow decrease is possible as discussed previuously by (3,4,2). A flux decrease with half-lives of the order of 1oo-2oo m.y. still permitted in (3) can be ruled out now.

c) Absolute ages of Aristarchus and Kepler.

The measured frequencies of superimposed craters for D=1km are $(5\text{-}1o).1o^{-4}$ km^{-2} (Kepler) and $(1.o\text{-}1.4).1o^{-4}$ km^{-2} (Aristarchus). Absolute dating using these data and applying the $T_{1/2} = \infty$ relationship of Fig.2

yields 13o < t < 18o m.y. for Aristarchus and 625 < t < 125o m.y. for Kepler. It is quite clear from morphological and stratigraphical evidences that Kepler is younger than Copernicus so that Kepler's age is probably between 625 m.y. and 95o m.y.

2. Different Ages of Lunar Light Plains.

G. Neukum

The crater populations of 15 lunar light plains show a variation in relative ages by a factor of ≈ 4 in crater frequency of regions in the surroundings of the Orientale resp. Imbrium basin, and by a factor of ≈ 1o for more distant sites (Fig.3). Many light plains are younger than the youngest basin Orientale. Since these plains cannot have been emplaced by any basin event and local impact derived origin can certainly be excluded, an endogenic origin is proposed. Also for the older light plains reconsideration of their genetic origin and of the currently favored hypotheses of emplacement by impact processes (5,6,7) is suggested.

Age determination data by Soderblom and Lebofsky (8) and Soderblom and Boyce (9) (D_L-Values) are shown to be correlated with own cumulative crater frequency measurements for surfaces younger than ≈ $3.8.1o^9$ years (Fig.4). An approximate correlation $D_L \sim N^{0.6}$ can be derived. The correlation $D_L \sim N$ maintained by (9) does clearly not hold. For ages > $3.8.1o^9$ years, the D_L data by (8) and (9), especially those for the light plains, are clearly incompatible with our crater frequency data (Fig.4).

II. Mariner 9 Mars Studies

1. Mars: A Standard Crater Curve and Possible New Time Scale.

G. Neukum, D.U. Wise

The crater size distribution of Mars was studied on Mariner 9 pictures and a possible cratering chronology was derived in linking the martian to the lunar crater data (1o,11). The impact crater production size-frequency distribution of Mars was found similar to that of the moon for crater diameters in the range of o.8 to 5okm, and it appears to have been relatively stable through time. As illustrated in Fig.5, the lunar and martian cater curves can be brought into near coincidence by a diameter shift of a factor of 1.5 appropriate to reasonable impact velocity differences between bodies hitting Mars (8km/sec) and the moon (15km/sec). This indicates that a common population of bodies impacted both planets and suggests the same or a very similar time dependence of impact flux. Constraints on relative lunar and martian fluxes can be obtained by comparing crater frequency data for the lunar and martian highlands and for Mars' satellite Phobos. These cratering constraints provide the basis for a new tentative martian time scale derived from lunar data. The resulting martian crater frequency-age curve is shown in Fig.6 together with previous time scales (12,13) and together with the lunar scale it is based on. Crater frequency data for different martian volcanic-tectonic structures are inserted (data partly from (14)). The previous time scales have painted a picture of a disorderly planetary evolution of Mars punctuated by a strange pulse of Tharsis Ridge tectonic and volcanic activity late in geologic history. The new scale suggests a much more orderly evolution, with Mars like the moon winding down most of its major planetary tectonic and volcanic disturbances in the first 1.5 billion years of its history.

2. Mars Mariner 9: Geologic Mapping of Amenthes MC-14

K. Hiller

As part of the NASA/USGS Mars Mapping Program a geologic map for

interpretation of MC-14 was prepared. The geologic history of the mapping area is concluded as follows: like the moon, high meteorite impact flux has shaped an early crust. Large multiringed impact basins and numerous impact craters in the highland materials are documents therefore. During the subsequent period, the martian surface was modelled predominantly by volcanic processes. Large scale extrusion of low viscosity basalts flooded low parts of the crust including the floors of the impact basins, thus creating vast plains. Concomitant intense erosion took place, denuding the northern edge of the highland complex to mesas and knobs. Later, the consistency of lavas developed to more viscous materials and piled up the Elysium volcanoes (15). The main factures in this area represent tension faults, related to global fracture pattern(16). Contrary to this, Amenthes Fossae are an accumulation of global and Isidis related structures. The only power still active in this part of Mars is considered to be moderate erosion snd sedimentation by an active wind regime.

References

(1) Neukum et al. (1975) The Moon 12, 2o1-229
(2) Neukum and König (1976) Proc.Lunar Sci. Conf. 7th, 2867-2881
(3) Neukum et al. (1975) Proc. Lunar. Sci. Conf. 6th, 2597-262o
(4) Baldwin (1971) Icarus 14, 36-52
(5) Eggleton and Schaber (1972) Apollo Preliminary Science Report NASA SP-315,29-7 to 29-15
(6) Oberbeck et al. (1974) Proc. Lunar Sci. Conf. 5th, 11-136
(7) Head (1974) The Moon 11, 327-356
(8) Soderblom and Lebofsky (1972)JGR 77, 279-296
(9) Soderblom and Boyce (1972) Apollo 16 Preliminary Science Report NASA SP-315, 29-3 to 29-6
(1o) Neukum and Wise (1976) NASA TM X-74316
(11) Neukum and Wise (1976) Science 194, 1381-1387
(12) Soderblom et al. (1974) Icarus 22, 239-263
(13) Hartmann (1973) JGR 78, 4o96-4116
(14) Carr (1976) NASA Tech. Memo. TM X 3364, 152
(15) Scott and Allingham (1976) Geologic map of the Elysium quadrangle of Mars: U.S.G.S. Misc. Inv. Series Map I-935
(16) Binder and Mc Carthy (1972) Science 176, 276-281

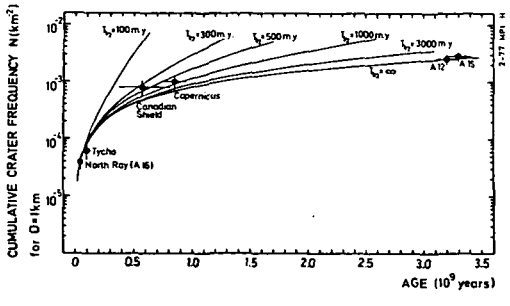

Fig.2

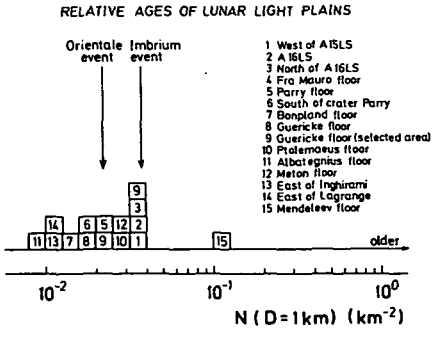

Fig.3

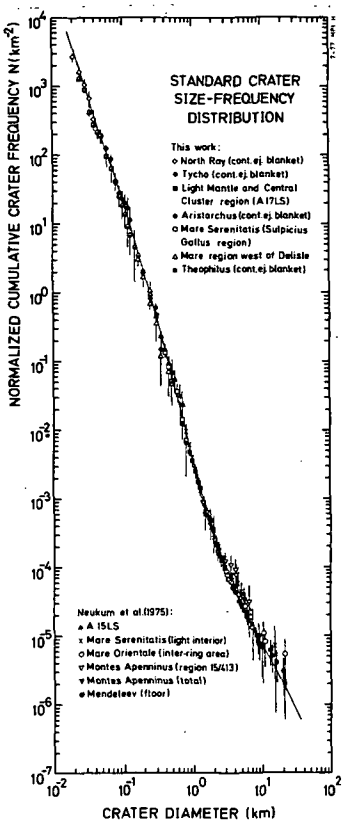

Fig. 1

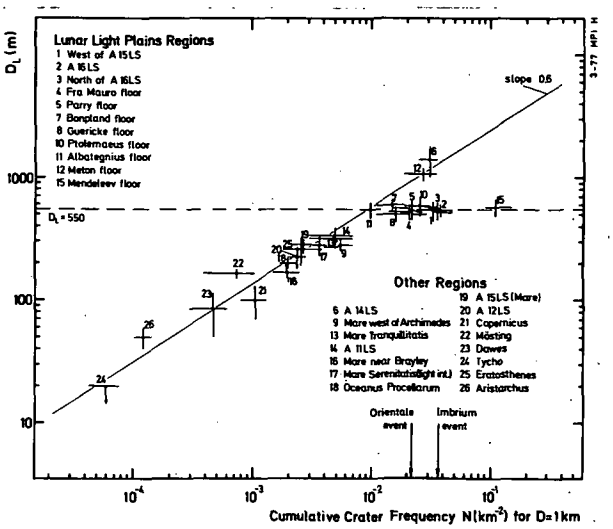

Fig. 4

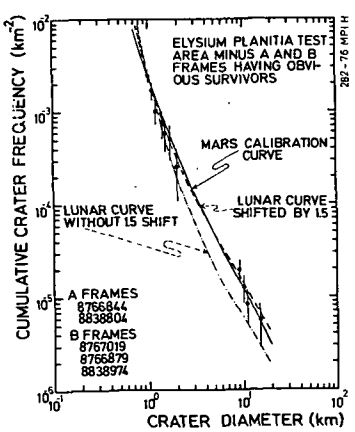

Fig. 5

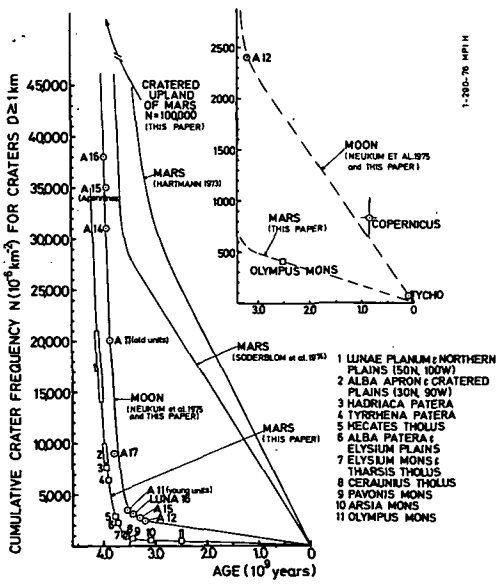

Fig. 6

Rayed Craters on the Moon and Mercury. Carlton C. Allen, Department of Planetary Sciences, University of Arizona, Tucson, AZ. 85721.

Craters with ray systems, common on both the Moon and Mercury, have been investigated. The diameter/density distribution of the rayed craters on each body was statistically compared to the distribution of the freshest recognized crater group on that body, and the rayed crater distributions were compared to each other. Ray formation and darkening processes were assessed and the absolute ages and darkening rates of some lunar crater ray systems were derived.

A diameter/density plot of all rayed craters over 7 km in diameter located on the center 56% of the Earth-facing lunar hemisphere was constructed, using the method of Whitaker (1). The rayed crater curve was compared to the distribution of highland Class 1 craters and to a power-law function with an exponent of -2 (Fig. 1). The Class 1 curve is similar to the -2 power-law distribution, and the rayed crater curve is similar to that for the Class 1 craters, according to the statistical test of Kolmogorov and Smirnov. A similar plot (Fig. 2) compares mercurian rayed craters over 8 km in diameter from the Mariner 10 second encounter, craters which impacted on the Caloris basin fill and surrounding "smooth plains", and a -1.5 power-law distribution. The post-Caloris curve is statistically similar to the -1.5 power-law distribution, and the rayed crater curve is similar to that of the post-Caloris craters.

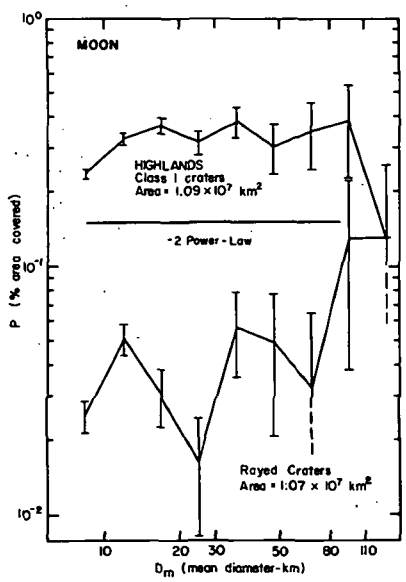

Figure 1

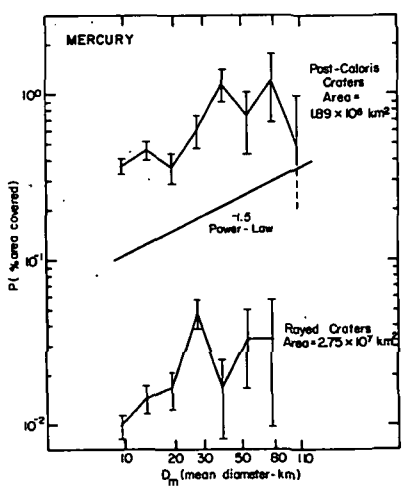

Figure 2

Thus, the rayed craters on both Mercury and the Moon form a representative sample, in terms of diameter/ density distribution, of the freshest group of craters recognized on each body. However, comparison of the two rayed crater curves indicates that they are statistically dissimilar. This dissimilarity

may be due to differences in the mechanisms of production or obliteration of ray systems on the two bodies, or it may be evidence of different populations of impacting bodies in these two regions of the inner Solar System.

Apollo Pan Camera photography was studied in an attempt to understand the process of ray formation. Images of large and small ray systems on Mare Crisium show that these rays are composed of finely-divided material from the primary craters, rather than the bright ejecta blankets of small secondary craters, as described by Overbeck (2). In order to remain bright in a lunar environment wherein surface material is rapidly darkened, the rays must be composed of deposits thick enough that micrometeoroid impact predominantly exposes bright ray material rather than underlying dark material. Studies of regolith turnover (3) lead to the conclusion that lunar ray material occurs, at least patchily, in deposits on the order of 10 cm - 1 m thick, and further that the thinner rays of small craters are darkened faster than the rays of larger craters.

The mechanisms by which rays are darkened are thought to be related to the solar wind and micrometeoroid impact. While both of these processes operate on the Moon, much of the surface of Mercury is shielded from solar wind ions by that planet's magnetic field. It may be possible, however, for these ions to reach the surface at the poles, leading to a more efficient darkening of crater rays in those regions. A plot of the areal density vs. latitude of rayed craters on Mercury's southern hemisphere (Fig. 3) does in fact show a dropoff between 30° and 90°, although no attempt was made to model the change of lighting angle with latitude. The lower areal density between the equator and 30° south latitude is not presently understood.

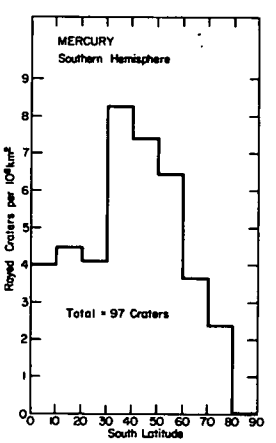

Figure 3

The bright ray system of the lunar crater Lichtenberg, on Oceanus Procellarum, is partially covered by a thin lava flow. The density of subsequent impacts on this flow is not noticeably lower than that on other parts of the same mare, which was dated at 3.3 b.y. at the Apollo 12 site. The strongly faded rays of the crater Theophilus mantle Mare Tranquillitatis, which was dated at 3.7 - 3.9 b.y. Thus, the processes which darken crater rays on the Moon were much more efficient between 3.3 and 3.9 b.y. ago than they have been in subsequent lunar history. This is in qualitative agreement with the inferred changes in the rate of crater formation, suggesting that the rate of ray darkening on the Moon may be dominated by processes related to the micrometeoroid flux.

References:

(1) E.A. Whitaker and R.G. Strom, Abstracts Lunar Sci. Conf. 7th, 933 (1976).
(2) V.R. Overbeck, The Moon 2, 263 (1971).
(3) D.E. Gault, F. Hörz, D.E. Brownlee, J.B. Hartung, Proc. Lunar Sci. Conf. 5th, 2365 (1974).

Large Impact-Crater Production in the Inner Solar System. A. Woronow, Lunar and Planetary Lab., Univ. of Arizona, Tucson, AZ 85721

A computerized Markov Chain technique for simulating large-crater populations provides the following major conclusions: (a) Even the most densely cratered lunar highlands have not attained the saturation or equilibrium limit for craters >7 km diameter. (b) The production function for the lunar craters in the diameter range 7 to 1270 km closely resembles the highly structured size-frequency distribution actually observed, and not a uniform -2.0 slope index as often assumed. (c) The battered and degraded appearance of the lunar highlands' large-crater population is characteristic of the -1.2 to -1.3 production slope index ($7<D<56$), even at subequilibrium crater densities.

In the Markov Chain computer program each crater is represented by eight points on its rim. Subsequent impacts may degrade craters by removing one or more rim points until all eight are gone and the crater is annihilated. For each $\sqrt{2}$ diameter interval a vector and a scalar describe the occupancy of each of the degradation states. The program utilizes 21 different transformation matrices to detail the effects of each new crater on all pre-existing craters as a function of the new crater's size, the old crater's size and degradation state, and the size of the counting surface.

The first application of this model examined the results of the earlier Monte Carlo saturation study by Woronow [1]. The Monte Carlo study could manipulate only four rim points and a dynamic range of only 16x; even so, that study indicated that the most densely cratered lunar highlands had large-crater densities well below the saturation limit, but the short dynamic range available could not simultaneously account for large basin-forming events and smaller scale cratering. Because of the amount of computer time necessary to bring a dynamic range of 64x to saturation, the Markov Chain simulation was stopped short of saturation but at a density well above the "densely cratered lunar highlands" of Strom and Whitaker [2]. At equivalent "model times" the Monte Carlo and the Markov Chain results agree excellently (Figure 1); therefore, this independently verifies the results of the Monte Carlo study and the conclusion remains that even the most densely cratered lunar highlands are not at or near either the saturation or equilibrium density limits.

Two attempts to simulate the observed "average lunar highlands" crater curve of Strom and Whitaker utilized two different production functions, both with ejecta effects included. Because a -2 slope log-log function ($N \sim D^{-2}$) has long been regarded as the progenitor of the highlands craters, this production function was tried first but failed to match the observed curve. Figure 2 illustrates how the production function is imprinted on the surface and eventually surpasses the observed densities with only the slightest bending toward the observed curve. To force the final curve to mimic the observed density at 7 km diameter, 30 new basins would have to form - this would cause a severe mismatch for the rest of the curve and an over-abundance of fresh basins. Because the observed crater densities lie far below the saturation limit, one could assume that they retain the essential characteristics of the production function. The second production function tried consisted of many straight log-log segments joined together to closely emulate the observed highlands crater curve. Figure 3 shows that this production function reproduces the gross features of the average highlands crater curve at the correct crater densities. The slight mismatch of the left-hand portion of the curves indicates that the correct production slope indices must be ~0.1 more negative than the observed slope indices.

Finally, a re-examination of the Monte Carlo results yields an explanation of how the highlands retain a production-function crater population

yet appear highly battered and degenerated. The relative number of craters produced at any two diameters is obviously dependent upon the production function used. The Monte Carlo simulations demonstrate that the relative number of craters obliterated at any two diameters is also dependent upon the production function used. The interaction of these two relationships explains the appearance of the highlands. Figure 4 illustrates the production and obliteration relationships for various production slopes and for two crater diameters differing by a factor of 4 (an arbitrarily selected ratio). A -3.0 slope, for instance, loses 250 craters of size D for every one it loses of size 4D, while producing only 64 of size D for every one of size 4D. This causes an initial population of -3 slope to rapidly change toward a -2 slope. A -1.2 slope (approximately that observed over the diameter range 7 to 56 km), however, loses craters in nearly the same proportions as they are produced. The direct imprint of the production function's size-frequency distribution, in this case, is not readily altered even by substantial losses of craters. Simulations also show that when the total density of craters in the diameter range 7 to 56 km match the observed crater densities, a -3.0 production function has sustained minimal loss of craters while a -1.2 production function lost nearly 30% of all craters formed. Therefore, if the highlands craters resulted from a steep production function they should look quite fresh, but the shallow -1.2 production function will yield a population quite battered in appearance - yet retaining the features of the production function.

For a very simple yet convincing demonstration of this, computer-drawn crater populations with various slope indices were compared to the Cuvier region of the Moon (Figure 5). The battered and confused appearance of the model with a -0.4 production function contrasts with the pristene appearance of the -2.0 and -3.0 production functions. Figures 5a to e all have the same dynamic range specified to the random number generation and roughly the same numbers of craters as in the lunar region of Figure 5f. No difficulty exists in placing the lunar area between the -1.0 and -1.5 production functions.

In summary, these studies indicate that the large-crater population of the lunar highlands will appear quite degraded (as it does), but still have a crater density well below the saturation or equilibrium limits and retaining the essential features of its production function.

References: (1) Woronow, A., J. Geophys. Res., in press. (2) Strom, R. G. and Whitaker, E. A., in preparation.

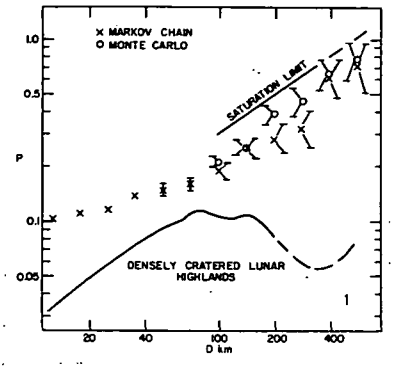

Fig. 1 Comparison of the Monte Carlo and Markov Chain saturation results (production slope = -2) and the observed lunar curve. P is the fraction of surface area in each $\sqrt{2}$ diameter interval (i.e. number of craters in the interval times their mean area divided by the area of the counting surface.

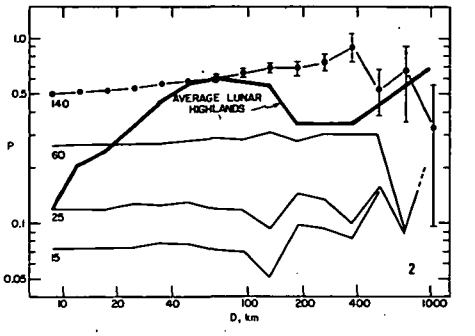

Fig. 2 An attempt to simulate the observed lunar curve with a -2 slope production function. Successive curves are labeled in thousands of craters produced. This model fails to match the observed curve.

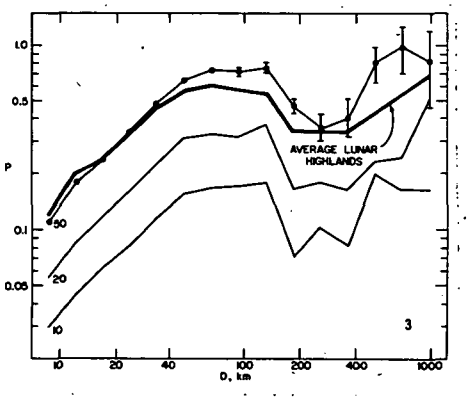

Fig. 3 An attempt to simulate the observed lunar curve with a production function resembling the observed distribution. This model fits well.

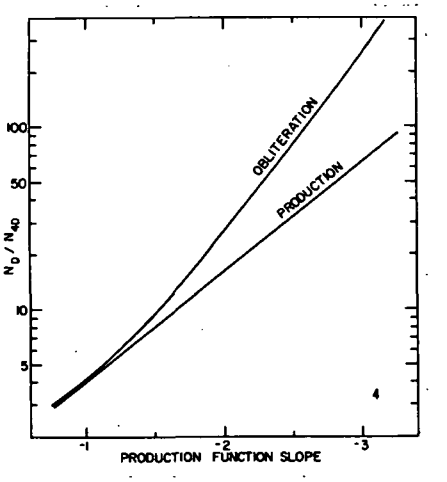

Fig. 4 Relative production and obliteration rates for two crater diameters a factor of 4 different and for various production slopes.

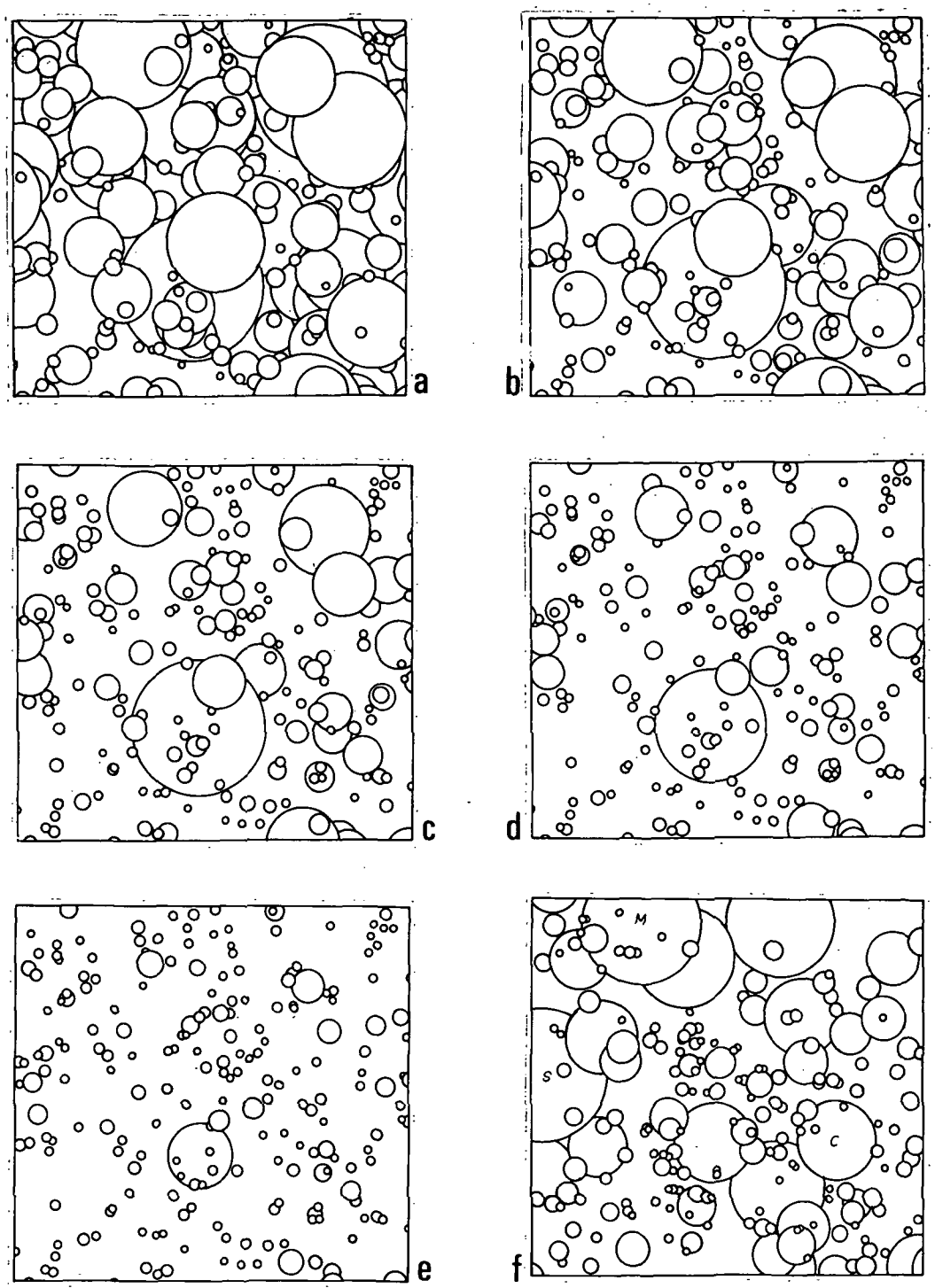

Fig. 5 A through e are computer-drawn crater populations with -0.5, -1.0, -1.5, -2.0, -3.0 production function slope indices respectively. Compare these to the Cuvier-Stofler-Maurolycus lunar area in f.

The Effect of Nongravitational Factors on the Shape of Martian, Lunar and Mercurian Craters: Target Effects. Eugene I. Smith and Jill Ann Hartnell, Division of Science, University of Wisconsin-Parkside, Kenosha, Wi 53140

Valid comparisons of crater shape between planets can not be satifactorily accomplished without evaluating the effects of non-gravitational factors such as target characteristics and substrate properties. In order to determine the influence of target properties on crater shape, we grouped the craters on each planet according to terrain type and determined the frequency-size characteristics for central peaks and terraces for each terrain. Terrain types were adapted from generalized geologic maps of each planet (1,2,3). Briefly, we showed that there are significant differences in the terrace-size and central peak-size relationships for different terrains on Mars and on the Moon. Mercury on the other hand shows no significant differences in the crater shape-size curves between terrain types. Several crater morphologies are unique to Mars and may reflect unique target properties. For example, central pits and flow-like ejecta (4) are associated with many craters. These features may be due to impact into a target containing a permafrost layer.

Mars was divided into four basic terrain types: a) plains units, b) cratered deposits, c) mountainous terrain about the Argyre basin, and d) knobby terrain at the boundary between the plains and cratered units. In detail our data showed: 1. There are significant differences in the frequency of occurence of central peaks and terraces when comparing craters on the plains with those in the cratered terrain. All studied craters in the plains at a diameter (D) greater than 25 km are terraced, whereas on the cratered terrain all craters are terraced at $D \simeq 55$ km. Below a diameter of 25 km a greater percentage of craters on the cratered terrain have central peaks than do craters on the plains, however above a D of 25 km the trend is reversed. This reversal suggests that larger (and older) craters may have been involved in an obliteration event (5,6,7), whereas smaller (and younger) craters formed after this event. Central peaks in craters on the plains ($D < 25$ km) may be obscured by dust or lava infilling. 2. Within the cratered terrain relatively fresh craters occur preferentially on or near topographic highs (above 3 km) and in areas of topographic gradient at the boundary between cratered and plains units. Martian craters also seem to be deeper in these higher areas (8). 3. Central pits are more common in martian craters than in craters on the Moon or Mercury. On the Moon 26% of craters with central peaks have summit pits (9) and occasionally a central pit may form (10). Central pits in craters on Mercury are rare. Pits on Mars mainly occur in the cratered terrain (89%) in craters ranging in diameter from 10 to 70 km. At D=35 km, 31% of fresh martian craters have central pits. The pit normally occurs in craters with no evidence of a central rise or peak; the diameter of the pit averages 11% of the diameter of the enclosing crater. The development of central pits may be related to the process of summit pit formation on central peaks. On the Moon, summit pits probably form by the collapse of the central part of the uplifted central peak soon after crater formation (10). Perhaps on Mars the presence of vaporized ice produced by the evacuation of a permafrost layer may encourage the development of summit pits to the point where they completely obscure the central uplift.

On Mercury there is little difference in morphology-size characteristics between terrains (smooth plains, intercrater plains,

hummocky plains and Caloris terrain, and heavily cratered terrain) suggesting similar target properties for these terrains.

The Moon was divided into five terrain types: a) lunar highlands, b) basin ejecta, c) highlands covered with thin basin ejecta, d) mare toward the central part of the circular basins, and e) mare on the margins of the circular basins and in the irregular basins. In general terraces and central peaks are more abundant in craters < 50 km in diameter on the mare than on the highlands. Also craters with $D < 35$ km that formed on mare in the center of the circular basins are more complex in shape for a given crater diameter than are craters on mare on the margins of the circular basins and in the irregular basins. Here substrate properties may affect crater shape.

In addition we re-examined our crater shape-size data in light of several recent papers on the morphological characteristics of fresh craters on Mars, Mercury and the Moon (11,12) which suggested that there are factors more important than gravity in affecting crater morphology. This study is contrary to the work of Gault et al. (13),and Smith (14) who observed differences in the size-shape data which suggested that gravity was an important factor in influencing crater shape. Comparison of our new terrace-size and central peak-size data which take into account terrain effects on each planet suggests that g is an important factor in affecting crater shape, thus confirming the studies of Gault et al. (13), and Smith (14). Terraces occur with greater frequency in smaller craters on Mercury than on the Moon below a diameter of 30 km (fig. 1), and there is a greater frequency of small (D between 10 and 30 km) craters on Mercury and Mars with central peaks than on the Moon. These differences are clearly observed even when terrain data envelopes (the range of size-shape data for all terrains on a single planet) are compared (figs. 1 and 2).

References:

(1) Wilhelms, D.E., and McCauley, J.F., U.S. Geological Survey, Map I-703.
(2) Carr, M.H., Masursky, H., and Saunders, R.S., Jour. Geophys. Res. 78, 4031 (1973).
(3) Trask, N.J. and Guest, J.E., Jour. Geophys. Res., 80, 2461, (1975).
(4) Carr, M.H. et al., Science, 193, 766, (1976).
(5) Hartmann, W.K., Jour. Geophys. Res., 78, 4096, (1973).
(6) Jones, K.L., Jour. Geophys. Res., 79, 3917, (1974).
(7) Soderblom, L.A. et al., Icarus, 22, 239, (1974).
(8) Burt, J., Ververka, J., and Cook, K, Icarus, 29, 83, (1976).
(9) Allen, C.C., The Moon, 12, 463, (1975).
(10) Baldwin, R.B., The Measure of the Moon, U. Chicago Press, 488p. (1963).
(11) Cintala, M.J., Head, J.W., and Mutch, T.A., Geophys. Res. Letters, 3, 117, (1976).
(12) Wood, C.A., Cintala, M.J., and Head, J.W., Conference on Comparisons of Mercury and the Moon, Lunar Science Institute, p. 38, (1976).
(13) Gault et al., Jour. Geophys. Res., 80, 2444, (1975).
(14) Smith, E.I., Icarus, 28, 543, (1976)

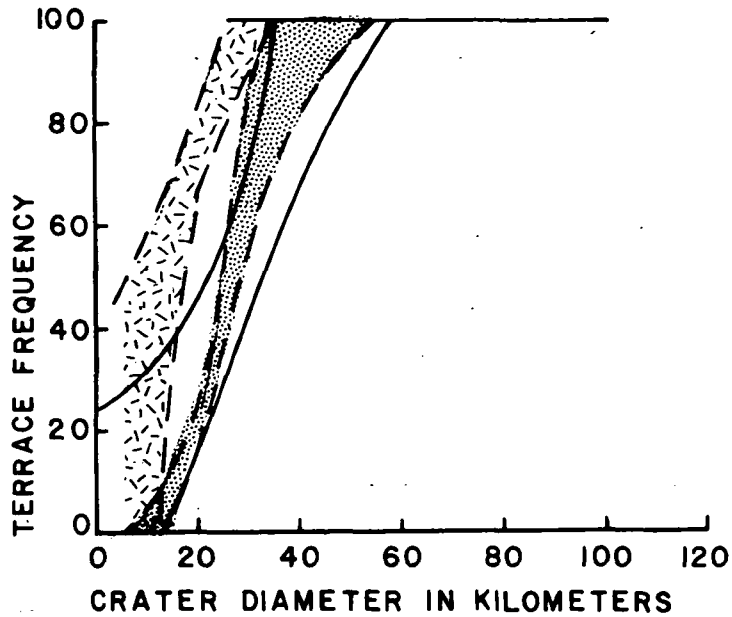

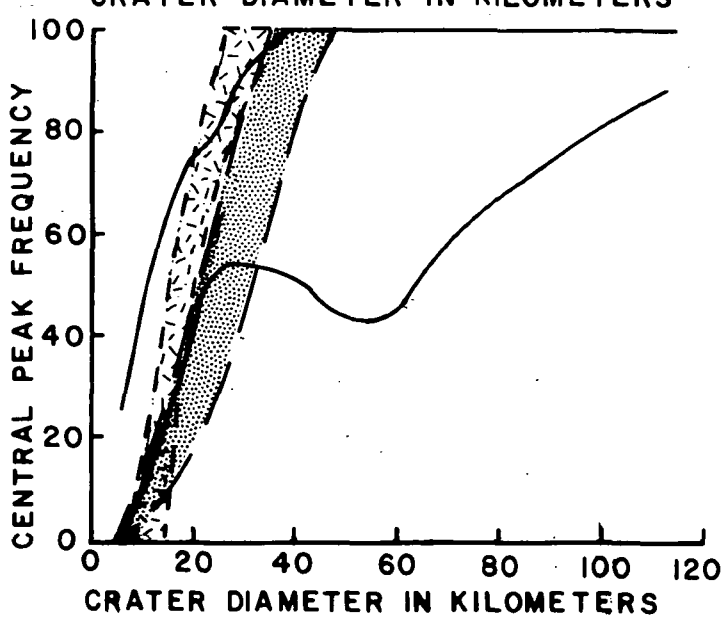

Figures based on a sample of 215 martian, 127 lunar and 71 mercurian craters.

Figure 1 (above) Terrace frequency-diameter plot for craters on Mars, Mercury and the Moon. Plots for each planet are shown as data envelopes. An envelope contains all size-shape data for the various terrains on each planet. The Moon-dotted pattern, Mercury-crosshatched pattern, Mars-no pattern.

Figure 2 (below) Central Peak frequency-diameter plot for craters on Mars, Mercury and the Moon. See explanation to Figure 1 for legend.

Interplanetary Comparisons of Fresh Crater Morphology: Preliminary Results. Mark J. Cintala, Charles A. Wood, James W. Head, and Thomas A. Mutch, Department of Geological Sciences, Brown University, Providence, R. I., 02912

A program is underway to digitize all mercurian craters greater than 5 km in diameter on Mariner 10 photography.[1] The method is very similar to that used to collect data for the Brown University Mars Crater Library.[2] Additionally, an independent catalog of all nearside lunar craters greater than 7 km in diameter has been completed recently at the University of Arizona Lunar and Planetary Laboratory.[3] These catalogs include data on crater location, diameter, morphology, and degradation. In addition, both the mercurian and lunar catalogs contain morphometric data on central peak heights and crater depths. These catalogs, yielding data for over 65,000 craters on the three planets, provide comprehensive bases for detailed crater population studies.[4]

Comparison with previous work - Past studies of lunar[5], mercurian[6], and martian fresh craters[7] have dealt with small, select samples of craters (120, 130, and 193 craters, respectively). We report similar studies for the three planets, utilizing the Brown University and LPL catalogs; the numbers of fresh craters studied through these data sets are 3020 for the Moon, 1665 for Mercury, and 33810 for Mars. Differences in frequency of occurrence of central peaks and wall terraces between the new and previous work are shown in Tables 1 through 3. It appears to be extremely difficult to select small numbers of craters for statistical study without introducing observational bias into the data set, because these selective samples consistently overestimate the frequency of occurrence of peaks and terraces, especially at the smaller diameters. The percentages tend to converge at the larger diameters, probably due to the smaller numbers of fresh craters at this end of the size range.

Fresh Crater Morphologies on the Moon, Mercury and Mars - The frequency of central peaks and terraces, based on the Brown University and LPL catalogs, are presented in graphical form in Figure 1. All craters are fresh (Moon and Mercury: class 1 defined on the basis of rim sharpness[8]; Mars: classified as fresh on the basis of qualitative crater depth and rim continuity[9,10]). No attempt has been made to segregate endogenically modified from endogenically unmodified craters on the Moon and Mercury; obvious calderas have been deleted from the Martian population.

Mercurian craters generally have a greater frequency of occurrence of peaks and terraces than do lunar and martian craters at all diameters, until 100 percent occurrence is attained. Martian craters exhibit a lower rate of frequency increase with diameter than lunar and mercurian craters for both morphologic features; martian central peaks never attain 100 percent

occurrence[10].

Discussion - Differences in the frequencies of occurrence of these morphological features have been associated previously with differences in gravity on the three planets[6,7]. Since Mercury and Mars have nearly equal gravities, more than twice that of the Moon, the trends in Figure 1 tend to weaken this hypothesis.

It has also been suggested that substrate differences may be an important factor in controlling final crater morphology.[4,11,12] Preliminary studies indicate that the morphology/diameter relationships for craters on the lunar maria are very similar to those for craters on the mercurian smooth plains, but that the maria/smooth plains distributions of peaks and terraces differ significantly from both the lunar highlands and mercurian heavily cratered terrain/intercrater plains relationships. If more detailed work, now in progress, upholds these preliminary observations, a number of suggestions can be made. First, there is statistical evidence for substrate control of crater morphology. Second, since similar terrain types do not cover equal areas on the three planets, whole planet morphology/diameter distributions should be compared with caution. Third, similar behavior of the lunar maria and mercurian smooth plains may indicate that the two surfaces have similar physical properties. This would imply that the smooth plains had an origin similar to that of the lunar maria.[13,14] Finally, differences in morphology/diameter distributions for lunar and mercurian cratered terrains indicate that these surfaces have different physical characteristics.

References: (1) Cintala, M. J. et al. (1976) Conf. Comparisons Mercury/Moon, 5. (2) Arvidson, R. E. et al. (1974) The Moon, 9, 105. (3) Wood, C. A. (1972) The Moon, 3, 408. (4) Wood, C. A. et al. (1976) Conf. Comparisons Mercury/Moon, 38. (5) Smith, E. I. and A. G. Sanchez (1973) Mod. Geology, 4, 51. (6) Gault, D. E. et al. (1975) J.G.R., 80, 2444. (7) Smith, E. I. (1976) Icarus, 28, 543. (8) Arthur, D. W. G. et al., (1963)Comm. Lunar Planet. Lab., 2, 30. (9) Arvidson, R. E. (1974) Icarus, 22, 264. (10) Cintala, M. J. et al. (1976) Geophys. Res. Lett., 3, 117. (11) Head, J. W. (1976) Proc. Lunar Sci. Conf. 7th, 3, 2913. (12) Cintala, M. J. (1976) Submitted to Proc. Conf. Planet. Cratering Mechanics. (13) Trask, N. J. and J. E. Guest (1975) J.G.R., 80, 2461. (14) Strom, R. G. et al. (1975) J.G.R., 80, 2478.

MOON

D	Peaks S&S	Peaks LPL	Terraces S&S	Terraces LPL
0-10	0	2	0	0
11-20	26	11	12	0
21-30	53	40	33	40
31-40	79	75	79	68
41-50	87	96	87	88
51-60	100	91	100	91
60+	100	100	100	100

Table 1. Comparison of frequency of occurrence vs. diameter for central peaks and wall terraces for fresh lunar craters, according to Smith and Sanchez[5] (S&S, 120 craters) and the Lunar and Planetary Laboratory (LPL, 3020 craters). In this and the following tables, D=diameter (km); central peak and terraces abundances are in percent.

MERCURY

D	Peaks G	Peaks BU	Terraces G	Terraces BU
0-10	0	0	7	0
11-20	80	12	80	0
21-30	84	60	95	17
31-40	83	97	92	59
41-50	100	100	100	88
51-60	100	100	100	83
60+	100	100	100	100

MARS

D	Peaks S	Peaks BU	Terraces S	Terraces BU
0-10	33	0	0	2
11-20	60	12	9	5
21-30	77	22	12	27
31-40	69	27	50	45
41-50	55	32	70	68
51-60	57	45	93	100
60+	71	65	93	100

Table 2. Comparison of frequency of occurrence vs. diameter for central peaks and wall terraces for fresh mercurian craters, according to Gault et al. (G, 130 craters) and the Brown Univ. Mercury Crater Library (BU, 1665 craters).

Table 3. Comparison of frequency of occurrence vs. diameter for central peaks and terraces for fresh martian craters according to Smith[7] (S, 193 craters) and the Brown University Mars Crater Library[10] (BU, 33810).

Figure 1.

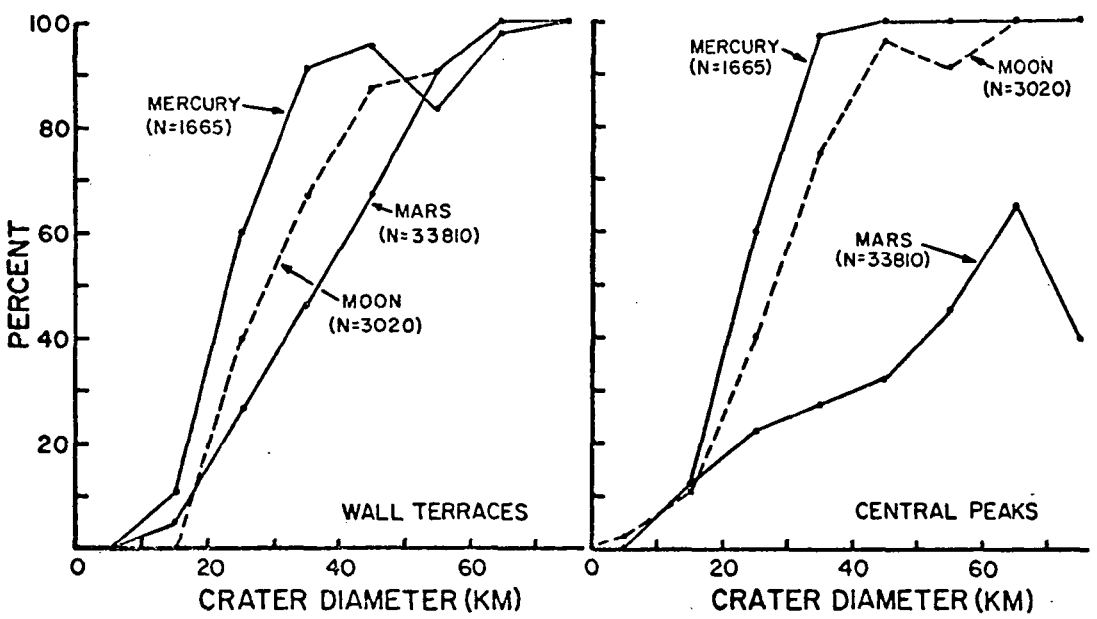

Crater Evolutionary Tracks. Gerald Schubert and Richard E. Lingenfelter, Department of Earth and Space Sciences, University of California, Los Angeles, CA 90024, and Richard J. Terrile, Division of Geological and Planetary Sciences, California Institute of Technology, Pasadena, CA 91125.

A description of crater morphology based on rim height/depth (h/d) and depth/diameter (d/D) ratios provides a quantitative method of assessing the relative importance of competing crater modification processes. Different classes of processes produce distinctive evolutionary tracks on a h/d vs. d/D diagram. We have calculated such tracks for three general classes of crater modification: those processes which add material to the crater (filling), those which redistribute material within the crater vicinity (slumping), and those which remove material from the crater vicinity (erosion). Figure 1 shows evolutionary tracks for simple models of the filling, slumping and erosion processes and also for several combinations of these processes. d_0 and D_0 are initial values of d and D. Σ is the slope of the inside crater wall; in the model, it may be as large as ∞ (a vertical wall), but it can be no smaller than 2d/D. t_e and t_f are characteristic erosion and filling times.

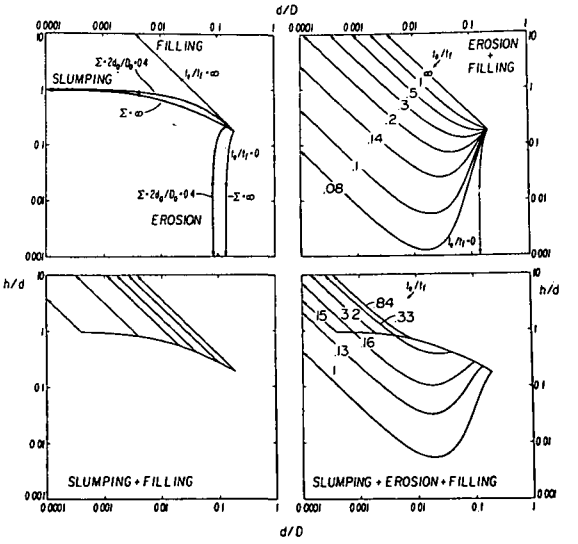

Figure 1. Evolutionary tracks for models of different crater modification processes. The arrows indicate the direction of evolution with time.

Typical evolutionary tracks for the filling, slumping and erosion models are quite distinct from one another, allowing for the discrimination of these classes of processes in crater morphologic data. For example, any crater whose morphology places it above the slumping envelope must have undergone some filling with outside material while any crater below this must have undergone some removal of rim material. The evolutionary tracks of craters being modified by more than one process depend strongly on the relative efficiency of these processes. This relative effectiveness can be characterized by either the relative rates or time scales of the competing mechanisms. For example, the ratio of the characteristic erosion time to the filling time, t_e/t_f, gives a measure of the relative importance of erosion and filling, ranging from $t_e/t_f = 0$ for pure erosion to $t_e/t_f = \infty$ for pure filling.

We have compared h/d and d/D ratios for craters on the Earth, Moon and Mars with theoretical evolutionary tracks for the general classes of crater modification. New morphometric data, from earth-based radar scans and Mariner 9 images of Mars and Apollo metric photography of the Moon, were used to calculate h/d and d/D for martian and lunar craters. Figure 2 shows this comparison.

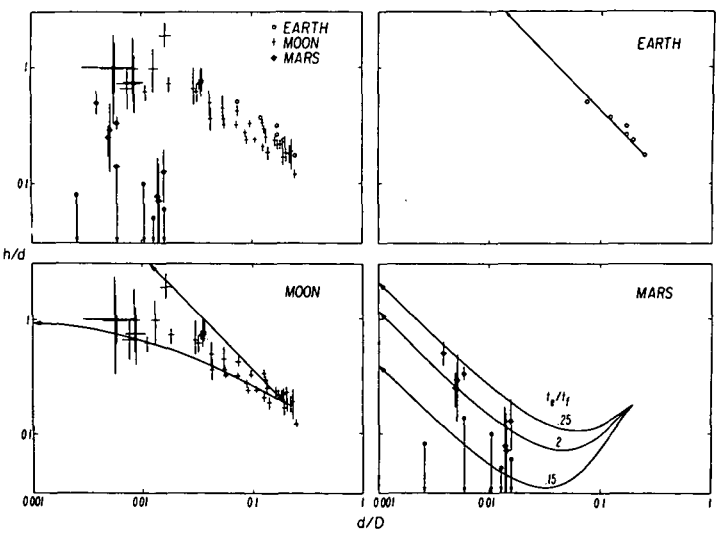

Figure 2. Comparison of model crater evolutionary tracks (solid lines) with lunar, martian and terrestrial data (individual points). The evolutionary tracks for the lunar data are filling and slumping curves. A filling track fits the few terrestrial data points and erosion-filling curves model the evolution of martian craters.

Lunar and terrestrial craters occupy similar regions of the h/d vs. d/D diagram, whereas martian craters lie distinctly apart. This implies that martian craters fall on a different evolutionary track from terrestrial or lunar craters. The evolution of the lunar and terrestrial craters can be modelled by a combination of filling and slumping processes. Martian crater evolution, however, cannot be understood on the basis of these two classes of crater modification alone. Instead, a process such as aeolian erosion which removes material from the crater rims, must have been the principal form of modification, and evolutionary tracks based on such a model coupled with weak aeolian deposition within the crater can indeed fit the martian h/d vs. d/D data. A paper by the authors, "Crater Evolutionary Tracks", is in press in The Moon.

Degradation Trends of Mercurian Craters and Correlation with the Moon. Charles A. Wood, James W. Head, and Mark J. Cintala, Department of Geological Sciences, Brown University, Providence, R. I. 02912

Impact craters are the dominant landforms on Mercury and the Moon. These craters represent standard experiments repeated ad infinitum on each planet and thus provide a statistical tool for examining the cratering process itself, probing the target planet, and gauging the degradation processes effecting the craters. Numerous studies have documented subtle interplanet variation in fresh crater morphology apparently due to differences in physical characteristics of projectiles and planets.[1] The present preliminary study reports changes in morphological characteristics of mercurian craters with increasing degradation, to provide evidence on degradation processes on Mercury and to correlate degradation sequence and style with major geologic time periods and events.

The investigation is based on morphological data for the 650 mercurian craters with diameters > 20 km in the Brown University data bank[2] and is modelled on previous studies of degradation of lunar craters.[3] Degradation states of mercurian craters are classified on a scale from 1 to 5 according to the scheme devised by Arthur[4] for lunar craters, with class 1 having sharply defined rims while class 5 craters are extremely battered and fragmentary. Geologic time runs from class 5 to 1. Figure 1 summarizes changes in morphological features of mercurian crater > 20 km with degradation class/geologic time. Crater rays are the first feature to disappear on Mercury as on the Moon[3], however satellitic craters are associated with much more highly degraded craters on Mercury than is common on the Moon. Our statistical data thus confirm this previously noticed[5] significant difference between craters on Mercury and the Moon. A related anomalous characteristic of mercurian craters is the persistence of raised rims throughout geologic time. This may result from the concentration of ejecta near a crater's rim due to Mercury's large gravitational field as suggested by Gault et al.[1] and Head et al.[6]

Mercurian craters are commonly circular but their circularity decreases from class 2 to 5 as crater rims become poorly defined. Polygonal rim outlines that occur on Mercury are neither as common nor as systematically developed as on the Moon[3], and our data show little evidence for a mercurian grid system. Rim crest continuity falls off rapidly and regularly from class 1 to 3, due to superposition of craters on rims, indicating progressive degradation due to impacts.

There is a smooth decrease from class 1 to 3 in the percentage of craters considered to be deep, suggesting a progressive shallowing with increasing degradation. The distribution by class of terraces in craters has a trend very similar to that

of the depths, and central peak occurrence follows a similar pattern. Thus, crater depth decreases, and continuous rims, central peaks, and terraces all systematically decrease in abundance from class 1 to 3, but at class 3 there is an inflection point and from class 3 to 5 the various morphological features do not decrease at the same rate as before (Fig. 2). Preservation of all morphologic features is more complete for classes 1 and 2 than if degradation had proceeded at the same rate as during the epoch from class 5 to 3. Thus a major change in the rate, and presumably style, of degradation occurred during class 3 time.

Head[3] found that crater degradation on the Moon could also be divided into two time periods based on differing styles and rates of crater degradation processes. Period II degradation has occurred since about 3.9 b.y. ago and is characterized by slow, continuous erosion of crater morphologic features by subsequent impacts. Period I, prior to 3.9 b.y. ago, was characterized by a very high impact rate and the formation of multi-ring basins; these two factors caused rapid destruction of craters. Thus the boundary between lunar crater degradation periods I and II corresponds to the termination of the early period of intense bombardment.

Based on the data in Figure 2 the end of the period of heavy bombardment and basin formation on Mercury occurred between the middle of class 2 and class 3 epochs. Crater class distribution maps show that Caloris basin formed during the class 2 epoch. This closely parallels lunar degradation history, where the end of heavy bombardment occurred between the middle of class 2 and 3 epochs and Imbrium and Orientale formed during class 2 time.

Evidence concerning the time of formation of the smooth plains (SP)[7] which fill and surround Caloris also comes from distribution maps of each degradation class of mercurian craters. Craters formed from class 5 through class 2 time are more abundant on the ancient heavily cratered and intercrater plains terrains than on SP. However, class 1 craters appear to have nearly the same crater density over all of Mercury. This implies that the mercurian smooth plains were emplaced near the boundary between the class 2 and class 1 epochs.

The lunar maria were also formed around the boundary between degradation classes 1 and 2. Thus, major events in the development of the Moon and Mercury-termination of heavy bombardment, basin formation, and smooth plains/maria emplacement-occurred at the same degradational stages in the history of the two planets.

References: (1) Gault, D. E. et al. (1975) J.G.R., 80, 2444; Cintala, M. J. et al. (1976) Geophys. Res. Lett. 3, 117. (2) Cintala, M. J. et al. (1976) Conf. Comparisons Mercury/Moon, 5. (3) Pohn, H. A., and Offield, T. W. (1970) U.S.G.S. Prof. Paper 700-C, C153; Head, J. W. (1975) Moon 12, 299. (4) Arthur, D.W.G. et al. (1963) Comm. Lunar Planet. Lab. 2, 30. (5) Trask, N. J.

(1976) Conf. Comparisons Mercury/Moon 36; Scott, D. H. (1976) Conf. Comparisons Mercury/Moon 30. (6) Head, J. W. et al. (1976) Conf. Comparisons Mercury/Moon, 15. (7) Trask, N. J. and Guest, D. H. (1975) J.G.R. 80, 2461.

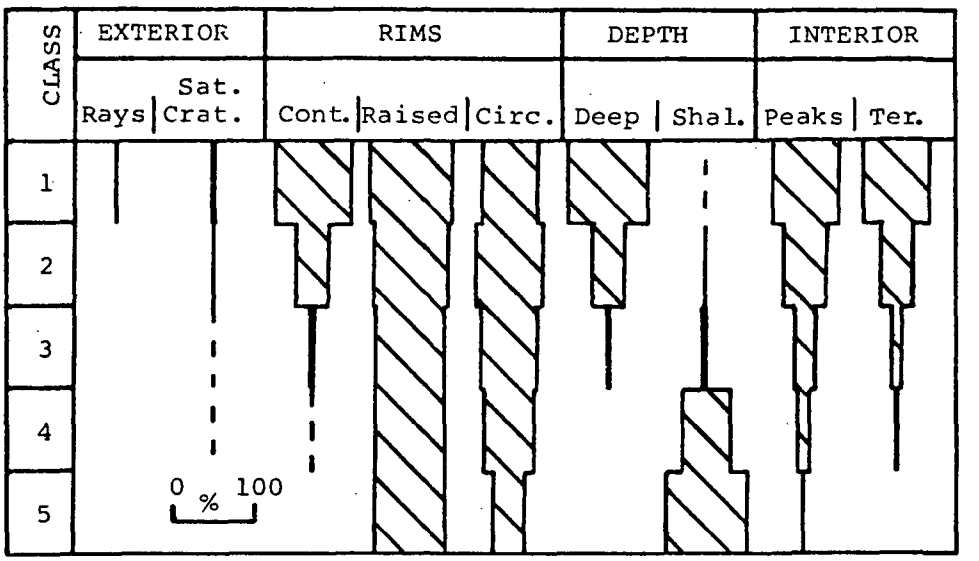

Fig. 1: Changes in mercurian crater morphology with age.

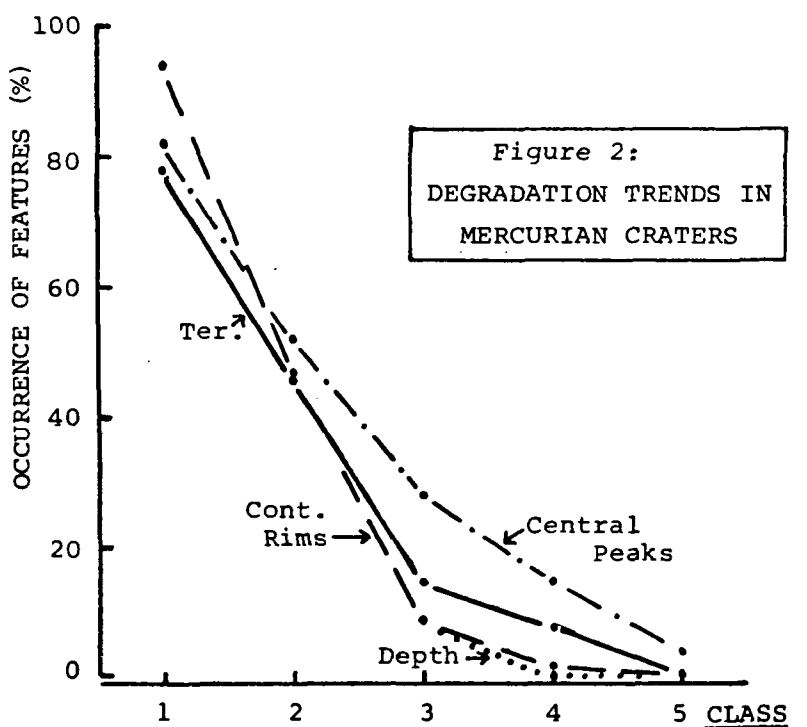

Figure 2:
DEGRADATION TRENDS IN MERCURIAN CRATERS

Formation and Obliteration of Large Craters on the Terrestrial Planets.

Clark R. Chapman, Planetary Science Institute, 2030 E. Speedway, Tucson, AZ, 85719

The craters on the moon, Mercury, and Mars and other terrestrial planets testify to a long history of bombardment by interplanetary objects. The degradation and obliteration of these craters on the cratered terrains of these planets, and the even more complete removal of large craters from the Earth, Venus, and the plains units of the other three bodies, testifies to the large-scale geomorphological processes that have acted during part or all of the history of the terrestrial planets. Studies of these craters, and their stratigraphic relationship to other geological features, can help to address questions in two fundamental areas of solar system science: (i) the distribution and evolution of small-body populations in the inner solar system and (ii) the geomorphological evolution of the surfaces of the terrestrial planets.

This general subject has been in a state of considerable flux during the past couple years as Mariner 9 interpretations of Martian cratering became crystallized and as preliminary hypotheses about comparative planetological cratering were developed based on Mariner 10 imagery of Mercury. Several common assumptions about cratering have been under attack, in particular the once-prevalent belief that the heavily cratered units on the moon (and perhaps Mercury and Mars as well) represent a condition of saturation equilibrium (1,2,3,4). Several important new hypotheses for terrestrial planet cratering have been offered, as well, including the suggestion that the crater populations on the cratered terrains of Mercury, the moon, and Mars are all predominantly due to an intense period (perhaps episode) of bombardment by the same population of interplanetary bodies at some early time in solar system history (roughly 4 b.y. ago).

A recent tendency by many investigators has been to adopt, or even deduce, absolute chronologies for the geologic evolution of the surfaces of the terrestrial planets which places not only the formation of large craters, but also large-crater degradation and formation of plains units, in the distant past (prior to 3 b.y. ago). I have argued elsewhere (5) that absolute chronologies are available only for the moon and the Earth, and that ages are poorly constrained for Mercury and Mars. The recently proposed "possible new time scale" for Mars by Neukum and Wise (4) is, like its predecessors, based on certain controversial assumptions. Neukum and Wise treat Martian and lunar highland crater populations as production functions dating from 4.4 b.y. ago. Their chronology is further based on an assumed age for the present surface of Phobos.

The notion that the lunar highland crater population is unsaturated is at least an arguable proposition (6). Despite the lower spatial density of Martian craters, however, their shallow depths (7,8,9) and spectrum of degraded morphologies rule out their being a production function. Rather the large Martian craters constitute a population that is, or has been, in equilibrium with rather extensive endogenic obliteration processes.

Chapman and Jones (6) have now reconciled their earlier models for Martian cratering and obliteration (10,11). Readers are directed to this review article for what I trust is a clearer exposition of the models than has been previously available. From the morphologies of the largest Martian craters, it appears that they were obliterated by a large-scale, efficient obliteration process -- probably of endogenic orgin, but possibly due to the cratering process itself -- acting contemporaneously with the cratering. Similar conclusions were reached previously by Chapman, Pollack, and Sagan (12) and by Soderblom et al. (13). The morphologies of the middle-sized craters on Mars provide dramatic evidence for a subsequent episode of

obliteration in intermediate Martian history. By "episode" I mean that the ratio of obliteration rate to cratering rate increased and then decreased again. Since this period of obliteration appears, from stratigraphic relationships, to be roughly coincident with the formation of the ubiquitous furrows in the cratered terrains and with the first formation of northern plains (the so-called "cratered plains" units), it is plausible to link this important event in Martian history with both the beginning of major Martian volcanism and with a period of more clement atmospheric conditions on the planet. This further suggests that Martian atmospheric evolution may have been causally connected with volcanic evolution. The distribution of small craters on Mars implies that post-obliterative-episode epochs on Mars have seen surprisingly little net erosion and obliteration.

We cannot state when, in absolute chronology, this obliterative event occurred. But acceptable chronologies (5) place it anywhere from about ½ b.y. ago to the later stages of the intense early bombardment on Mars which probably occurred, as on the moon, about 4 b.y. ago. If this important epoch of Martian geologic evolution occurred in relatively recent history, it would imply that Mars was geologically quiescent following the early heavy bombardment and that it only rather recently became geologically active. If the other extreme chronology is accepted, it would imply that virtually all of the geologically, geophysically, and meteorologically interesting evolution of the planet occurred during and shortly after the period of intense early bombardment (only volcanism in the immediate vicinity of the Tharsis Montes would then have occurred more recently). Intermediate chronologies include those that have major Martian plains units forming throughout the planet's history.

We should be careful about incorporating our preconceptions from terrestrial and lunar experience into our hypotheses for Mars. The relevant geomorphological and geological processes manifest on the surface of Mars are driven, ultimately, by the thermal evolution of the interior of Mars. Plausible scenarios for the thermal evolution of Mars do not yet permit us to choose one chronology over another.

Further understanding of the absolute chronologies for Mercury and Mars must await either (i) substantial improvement in the cataloging of small asteroids and understanding of their orbital evolution or (ii) the return of datable samples from those two planets. Since conclusive results from either approach are not imminent, the best we can do in the meantime is to formulate plausible hypotheses for planetary geological evolution.

(1) A. Woronow, J. Geophys. Res., in press (1977).
(2) R. G. Strom and E. A. Whitaker, NASA Tech. Memo. X-3364, 194 (1976).
(3) V. R. Oberbeck, W. L. Quaide, R. E. Arvidson, and H. R. Aggarwal, J. Geophys. Res., in press (1977).
(4) G. Neukum and D. U. Wise, Science 194, 1381 (1976).
(5) C. R. Chapman, Icarus 28, 523 (1976).
(6) C. R. Chapman and K. L. Jones, Annual Rev. Earth Planetary Science 5, 515 (1977).
(7) M. J. Cintala, J. W. Head, and T. A. Mutch, Proc. Lunar Sci. Conf. 7th, 3575 (1976).
(8) M. C. Malin and D. Dzurisin, J. Geophys. Res. 82, 376 (1977).
(9) J. Burt, J. Veverka, and K. Cook, Icarus 29, 83 (1976).
(10) C. R. Chapman, Icarus 22, 272 (1974).
(11) K. L. Jones, J. Geophys. Res. 79, 3888 (1974).
(12) C. R. Chapman, J. B. Pollack, and C. Sagan, Astron. J. 74, 1039 (1969).
(13) L. A. Soderblom et al., Icarus 22, 239 (1974).

Morphological characterization of the Mercury large craters: statistical behaviour of the craters in H1,H6,H7,H8,H11 and H15 quadrangles.

A. Carusi, M. Fulchignoni, M. Poscolieri - Laboratorio di Astrofisica Spaziale del CNR - P.B. 67,00044 Frascati,Italy.
R. Casacchia - Istituto di Geologia Università di Roma.

A systematic study of the Mercury craters has been carried out on the basis of the Mariner 10 imagery and the maps produced by the U.S.G.S. Astrogeology Center in Flagstaff. The analysis of the whole explored areas of Mercury has been already carried out at a scale 1:25,000,000 by Carusi et al.(1,2) and by Caputo et al. (3). Some preliminary results at 1:5,000,000 have been obtained for polar regions by Caputo et al.(4) and by Carusi et al. (4).

The morphological characterization of the Mercury craters is based on the empirical scale described by Carusi et al.(1): five morphological discrete indices are used for each crater,as indicated in fig.1, where each row contains the reference craters for the values of each index. The five indices refer respectively: i) the presence of terraces in the inner wall (1 no, 2 yes); ii) the degradation of the outer rim (1 ghost, 2 highly degraded, 3 moderately degraded, 4 sharp, 5 rayed); iii) the presence of superimposed smaller craters on the floor (1 no, 2 yes); iv) the floor degradation (1 highly degraded, 2 moderately degraded, 3 with inner structures as ridges or rills, 4 flat); v) the presence of central peaks (1 none, 2 one peak, 3 multiple central peaks, 4 peaks chain, 5 multiring). Since each index is independent, 400 different morphological classes are so obtained. The crater classification is really detailed if all the indices are used, it is possible however to use such criterion at any level, obviously taking into account the parameters of interest only: i.e. if we like to know the distributions of craters with terraced walls and central peak(s), disregarding the other morphological characters, we must pick-up all the craters having 2 as first index and a number greather than 1 as fifth index.

The results of the statistical analysis obtained classifying the craters larger than 20 km in the considered quadrangles can be used to understand the surface history of Mercury. The isodensity maps give informations about the age of the studied areas if some relationships between time and morphology is hypothized. Such relationships can be identified on the basis of comparative considerations among terrestrial planets and/or genetic physical models.

As an example, we discuss the results obtained analyzing the craters in the areas between $\pm$ 60° lat., in comparison with the craters of the polar regions. The statistics has been carried

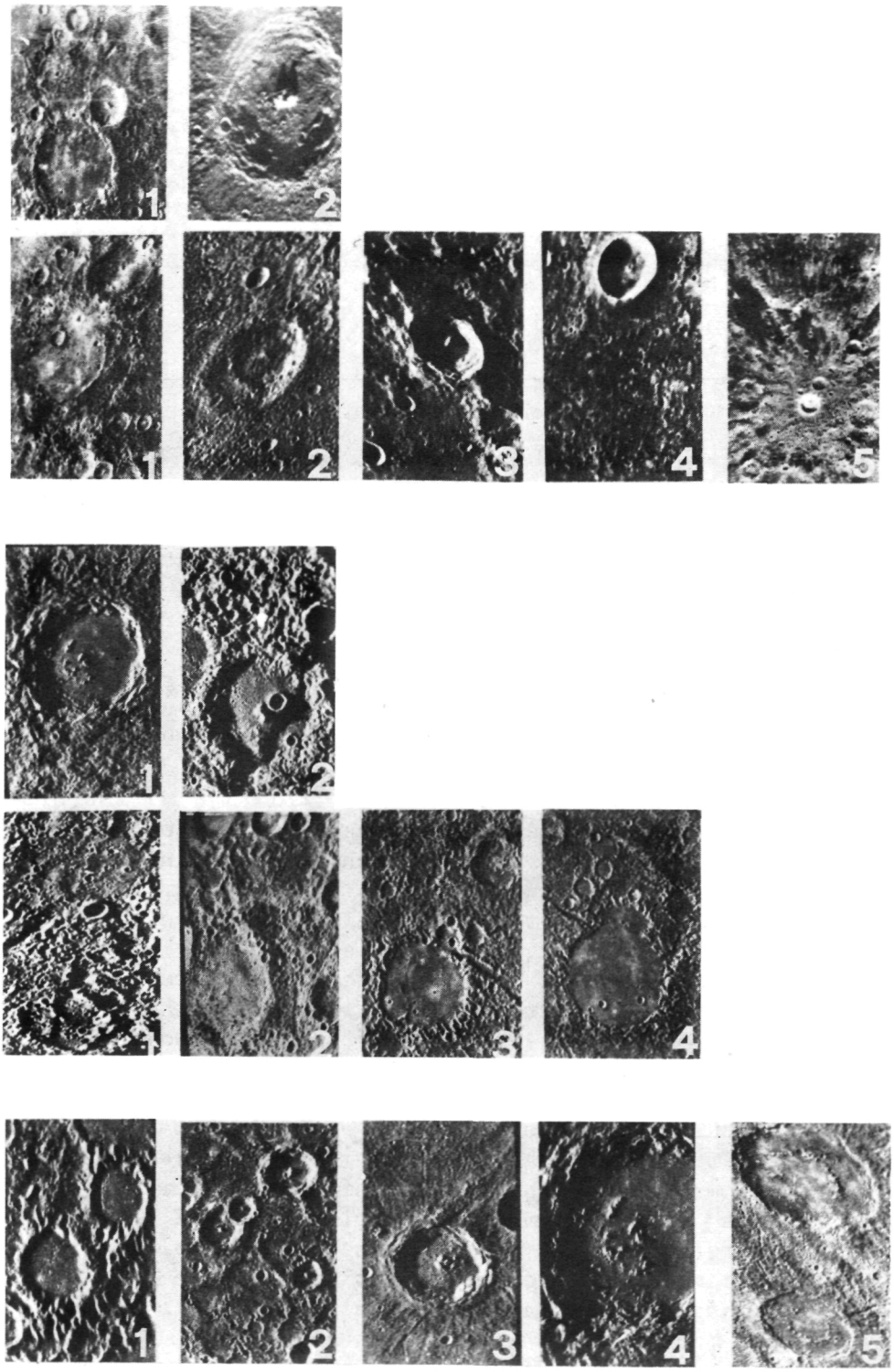

Fig. 1 - Morphological scale

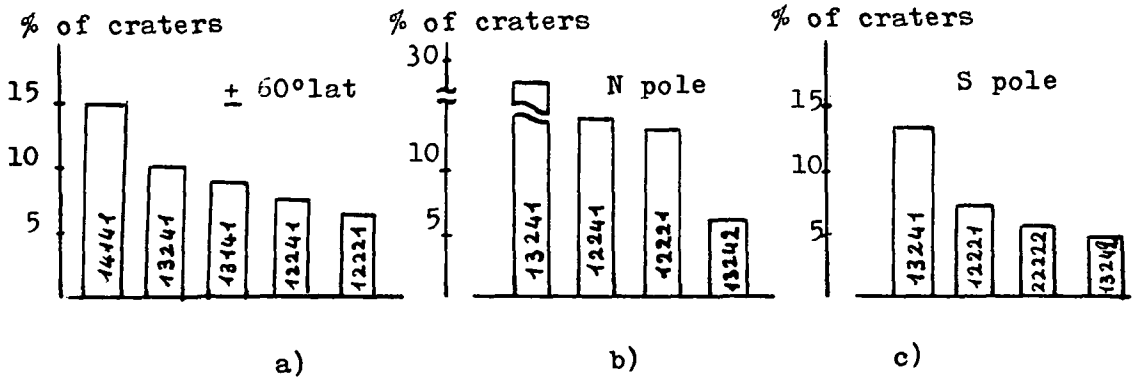

a) b) c)

Fig. 2

out on about 3000 craters in the central belt and, respectively, on 264 and 262 craters in the northern and southern regions.

The morphology of the craters in the whole area between ± 60° lat. is represented in fig.2a; the behaviour of the craters in H1 and H 15 quadrangles is shown in fig. 2b and 2c for the statistically meaningfull classes. Five morphological classes account for the 45 % of the total amount of craters in the central belt, whereas about the 80 % of the craters belong only to 19 classes. The class 14141 represents the small yongest bowl shaped craters, whereas the classes 13241, 13141, 12241 and 12221 contain most of craters that probably were bowl shaped. Such sequence seems indicative of the degradation history of the same kind of craters: the comparison between the areal distributions of these classes can allow to outline the final cratering history of the studied regions.

In the boreal region about the 60% of the craters belong to the classes 13241,13242,12241,12221, showing the same trend that we found in the central region even if the youngest craters are less abundant.

The craters in the austral region have a wider morphological distribution indicating a different more complex surface history where probably tectonism played a fundamental role.

References

1. A. Carusi, M.Fulchignoni, C. Caputo,M. Parotto,Geologica Romana (In press) (1976).
2. A. Carusi, M. Fulchignoni, C.Caputo, R. Casacchia,G.Cavarretta, M. Parotto, Ibid (1976)
3. C. Caputo, M. Parotto, A. Carusi, M. Fulchignoni,Ibid (1976)
4. C. Caputo, R.Casacchia, M. Parotto, A.Carusi,M.Fulchignoni, M. Poscolieri, Ibid (1976)

CRATER AND BLOCK POPULATIONS AT THE VIKING 1 LANDING SITE. R. Arvidson and E. Guinness, McDonnell Center for the Space Sciences, Dept. of Earth and Planetary Sciences, Washington University, St. Louis, Mo. 63130.

(a) Viking Lander 1 touched down on what appears from orbit to be a mare-like plain complete with wrinkle ridges and a population of fresh-looking craters. From the Lander perspective the region appears to be a rolling plain, strewn with volcanic rocks. From orbital imagery the crater population follows a log-log linear distribution ($1km > d > 300m$) down to the image resolution limit of about 300m (Figure 1). That segment of the population between 1km and 300m is consistent in slope with the population tabulated for craters superimposed on Tycho, Copernicus, and Apollo 12 (1). Because the three lunar populations have similar slopes, but cover an age range from 0.1 to 3.3×10^9 years, it is unlikely that any of the three populations is dominated by secondaries (1). The same is true for Mars and the flattening of the size distribution for sizes $\gtrsim$1km is probably due to change in the production function. The population of bodies forming the craters is either not log-log linear in size, or energy-gravity-crater size scaling parameters change in some as of yet unknown fashion. The Chryse Planitia area occupies a larger area than our count areas on the moon and thus provides a good sample of the rarer larger craters (2).

(b) The view from the Viking Lander 1 shows a paucity of craters relative to the moon and yet from orbit the crater size-frequency distribution is log-log linear down to the resolution limit of 300m. We can test the probability that craters of a given size below the orbital resolution limit have been produced but that they cannot be seen from the Lander because of the chance that some random spatial clustering of craters has occurred. The Lander cameras stand 1.3m above the Martian surface. At such a height, assuming a spherical Mars, the horizon is 3km away. The most likely number of craters of a given size range that would fall within the camera field of view is:

$$E = \left[\int_{d}^{d+\Delta d} Ad^{\gamma}\, d(d)\right] * \pi r^2$$

where: E is the number of craters of size d to $d + \Delta d$ to be expected in a circle of radius r, where r is the effective range of the cameras. A and γ are the intercept and slope of the crater size-frequency distribution seen from orbit (Figure 1). Assuming that the impacting population forms in a random manner with respect to location is the same as saying that the population obeys a binomial probability distribution where:

$$\frac{E}{N} = \frac{\pi r^2}{\text{count area}} = p$$

where N is the total number of craters of size d to $d + \Delta d$ within the count area (about $30{,}000km^2$) and p represents the fraction of the total number of craters to be expected within a circle of radius r.

But, E is subject to variations due to random spatial clustering. However, if the population is random with respect to location, then the number observed would surely be within $E \pm 3\sigma$, where σ^2 represents the variance about E. For a binomial distribution:

$$\sigma^2 = Np(1-p) = \left(1 - \frac{\pi r^2}{\text{count area}}\right) E$$

For the analysis, we have chosen r = 500 meters. Such a value of r, with Lander camera resolution, is about the limit at which a 25m diameter crater is just resolvable. For crater sizes between 100-300m, $E \pm 3\sigma$ is $.75 \pm 2.6$; for 50-100m, $E \pm 3\sigma$ is 4.9 ± 6.6; and for 25-50m, $E \pm 3\sigma$ is 35.4 ± 17.9. Since craters larger than about 50m are rare, there is a fair chance they

are not in the field of view. However, for $\leq$ 50m craters the probability of seeing them is high enough that they would be in the Lander field of view if they existed. However, only one crater can be identified with certainty at VL1. That crater is located on the horizon, $\geq$3km away. Topographic maps constructed out to 100m range by utilizing the two cameras in stereo shows that there are no discernible craters of any size (3). Gault et al showed that craters $\leq$50m should in fact be rare to non-existent because of ablation and break-up of projectiles by the Martian atmosphere. Our results are consistent with such theoretical treatment.

(c) The block size-frequency distribution for parts of the Lander 1 site is shown in Figure 2. The population is denser than even the population found on large, fresh lunar craters, noteably Tycho. Tycho is 100 m.y. old and not enough time has elapsed for much block destruction (1). However, in the vicinity of Lander 1, no such crater exists. Because of the atmosphere on Mars, small meteroids are shielded-out and the lunar-impact gardening that destroys blocks does not occur. If wind erosion rates are low, a block population could conceivably accumulate that mimics the fresh populations on the moon. Preliminary estimates of the populations thrown in from a crater population as shown in Figure 1, with a cutoff at 50m, show that there are more blocks present than can be accounted for solely by impact. Rather, the blocks consist of impact material, and blocks weathered in situ out of bedrock. Finally, the group of large (>2m) blocks northeast of the spacecraft appear to represent a separate population (5). They form a cluster that may represent impact of projectiles ejected from some distant cratering event. Because of atmospheric drag, they may have been slowed down enough to have landed, disturbed the regolith, but not to have made a discernible crater.

(d) Preliminary block counts for VL2 are higher than counts for VL1. Lander 2 touched down on the Utopia Plains, about 200km southwest of the 100 km crater, Mie. Conceivably, the block population is from Mie, although the test of this hypothesis is hampered by the fact that the abundance of blocks expected at this distance from Mie is difficult to predict.

(1) Arvidson, R., E. Guinness, C. Hohenberg, Abstracts IIX Lunar Science Conf., in press (1977).
(2) Neukum, G. and D. Wise, Science 194, 1381 (1976), have reached a similar conclusion from MM9 data.
(3) Binder, A., T. Mutch, R. Arvidson, E. Morris, J. Geophys. Res., in press.
(4) Gault, D. and B. Baldwin, EOS 51, 343 (1970).
(5) The blocks are sufficiently large that they have trapped a considerable amount of fine-grained material, as described in Mutch, T. and others, Science 194, 87 (1976).
(6) Shoemaker, E.M. and E.C. Morris, Icarus 12, 188-212, (1970).

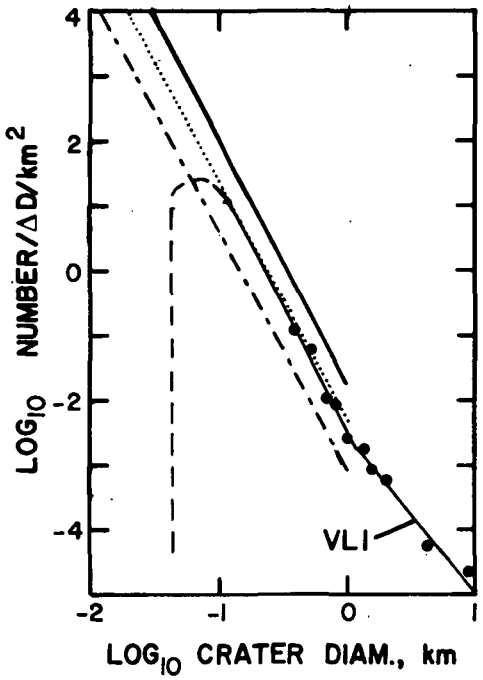

Figure 1
The crater size-frequency distribution for an area of 100km radius around the Viking Lander 1 site is compared to three lunar crater production populations for crater sizes between .1 to 1 km. The dashed-dotted line is for craters superimposed on Tycho, the dotted line is for craters on the floor of Copernicus, and the heavy solid line is for Apollo 12. The Mars data have been fit in a least squares sense. Note that the slopes of all four populations are similar for craters between .1 to 1km. The population in Chryse Planitia appears to be in production down to 100m. The sharp fall-off below 100m, shown by the dashed line, is an inference based on Lander imagery. The fall-off is attributed to ablation and break-up of meteoroids by the Martian atmosphere. Given these results, the integral effect of aeolian activity appears to have been minimal. At most, only a few meters of wind erosion can have occurred over the lifetime of the Chryse Plains.

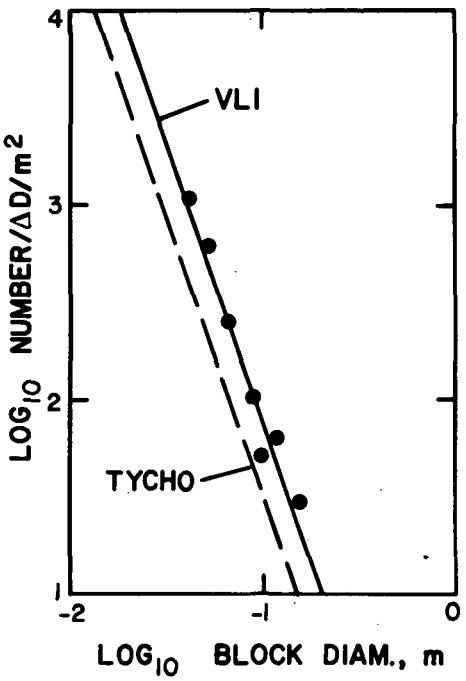

Figure 2
The frequency/area of blocks within 7 to 8m of the front of Viking Lander 1 is actually higher than the block population derived by analysis of Surveyor VII images taken on the ejecta of Tycho. Surveyor data are from Shoemaker and Morris (6). Mars data are fit in a least squares sense. There are more blocks than can be accounted for by integrating the individual contributions from >50m craters surrounding the VL1 site. Other processes, like in situ weathering from bedrock, must have contributed to the observed block population.

MULTI-RINGED BASINS: A MODEL FOR FORMATION IN MULTI-LAYERED MEDIA: R. A. De Hon, University of Arkansas, Monticello, AR. 71655

It is proposed that multi-ringed basins form by meteoridal impact into a multi-layered target and non-isotropic expansion of the radial shockfront in successive layers of target material. Ring spacing and shelf elevations are controlled by the location of discontinuities between layers. The major factors governing crater and basin morphology are the energy of the projectile (mass and velocity), depth of penetration, stratification of the target, and post-cratering modification. The following mechanisms (modified from Quaide and Oberbeck, 1968, Gault et al., 1968 and Head, 1976) are suggested for the formation of multi-ringed basins.

Hypervelocity impact into a target of isotropic material yields a hemispherically expanding shock front, and excavation proceeds by rarefraction along an expanding inverted cone of ejection. The final form of the cavity is a bowl-shaped crater. In layered materials, a bowl-shaped crater is produced when the depth of penetration is small compared to the total thickness of the surficial layer. For meteoroids with higher energy and greater penetration, the pressure of the shock wave reaches the bottom of the layer but the pressure may be less than the dynamic yield strength of the substrate. The shock front is primarily restricted to the surficial layer by refraction and reflection at the boundary between layers. Excavation is restricted to the surficial materials, and the expanding cone of ejection (more correctly a frustum) exists only in these materials. The resulting crater is flat floored and near the level of the layer interface. When the shock wave pressure exceeds the dynamic yield strength of the substrate (penetration near the interface) a bench crater is formed as the substrate material is fragmented and ejected.

When a meteoroid penetrates into substrate material (thin surficial layer or greater penetration depth), two independent shock fronts are initiated. A shock front, its attendant rarefraction, and cone of ejection develop in the surficial material and strip the overlying materials from the interface with substrate as an expanding, shallow flat floored cavity. The energy is primarily restricted to the surficial layer. As the projectile penetrates the substrate, a second shock front and excavation cavity begin to form independent of the first. The resulting morphology is a crater-in-crater structure consisting of a large flat floored basin with an inner crater rimmed by ejecta from the substrate. Modification of the double ringed basin may include terraced walls, radial faults, rebounded or domed interior, and concentric faulting as the basin reaches an equilibrium with its environment.

This model poses several implications for the interpretation of multi-ringed basins and planetary crusts. Some of the implications are listed below:

1. Spacing of rings in multi-ringed basins is a function of layer thickness.
2. The number of rings is dependent on the number of layers penetrated.
3. Shelf elevations are approximately equal to the elevations of the discontinuties.
4. Central peaks probably form by rebound; whereas, inner rings form by excavation and deposition.
5. Rings are composed of different materials from different layers.
6. Inner crater dimensions approximate the depth to diameter relationships of bowl shaped or flat floored craters.
7. The volume of ejecta from a multi-ringed basin is considerably less than that of a normal crater with the same diameter.

This model is capable of being verified by a variety of experiments and observations including:

1. Confirmation of reflection and refraction of the shock wave and confinement to the upper layer.
2. Experimental confirmation of a second cone of ejection as the projectile generates a second shock front in the lower stratum.
3. Experimental formation of bench craters and double ringed craters in layered target materials.
4. Photogeologic identification of the ejecta blanket and of secondary craters of the inner crater overlying wall and rim materials of the outer crater.
5. Orbital geochemical determination of ring compositions.

References

Gault, D.E., Quaide, W.L., and Oberbeck, V.R. (1968) Impact cratering mechanics and structures. In Shock Metamorphism of Natural Materials, Mono Book Corp., Baltimore, p. 87-99.

Head, J.W. (1976) The significance of substrate characteristics in determining morphology and morphometry of lunar craters. Proc. Lunar Sci. Conf. 7th, p. 2913-2929.

Quaide, W.L. and Oberbeck, V.R. (1968) Thickness determinations of the lunar surface layer from lunar impact craters. J. Geophys. Res. 73, 5247-5270.

Multi-Planet, Multi-Ring Basin Studies. John F. McCauley, U.S. Geological Survey, Flagstaff, AZ 86001

Preliminary comparisons between the Orientale and Caloris basins have been completed, and uncontrolled basin-centered geologic maps for each have been prepared. A polar stereographic basin-centered topographic map for Orientale, prepared from Lunar Program Office funding is nearing completion. A similar topographic map for Caloris should be ready in late May 1977. A general geologic analysis of these two basins has been completed and submitted for publication in the Proceedings of the Conference on Comparisons of Mercury and the Moon.

The inner basin scarp of Orientale is thought to be a bench separating the upper parts of the basin from its deep bowl-shaped interior. The elongated and complexly fractured domes of the basin floor formed by centripetal compression in the last stages of the cratering sequence. The Inner Montes Rook are considered a central peak ring. The Montes Rook and the nonlineated knobby and associated smoother materials that overlie the Cordillera scarp around much of its circumference are the uppermost parts of the overturned rim flap which formed early in the cratering event. The knobs and smaller massifs are probably coherent blocks quarried from deep within the Moon. They were among the last materials to leave the basin and had little radial momentum unlike the lineated Hevelius which formed earlier by disaggregation of the rim flap, secondary cratering, and the ground surge. The Cordillera scarp, best seen on the east side of the basin but poorly developed and discontinuous on the west, is a primary feature formed early in the crater excavation process by basinward motions of the walls and the fractured zone beyond the rim of the expanding cavity. The Cordillera scarp is overlain by ejecta over most of its extent, and post-basin internal slumping previously thought to be important must be a subordinate process in development of the scarp.

The basin fill in Caloris has no counterpart in Orientale but the materials between the most prominent scarp and the weakly developed outer scarp appear to be the degraded and possibly mantled equivalents of the massifs and knobs associated with the Montes Rook. The radially lineated terrain that generally lies beyond the outer scarp of Caloris is considered the subdued counterpart of the Hevelius Formation which generally shows the same relation to the Cordillera scarp at Orientale. Thus, the prominent innermost scarp of the Caloris basin is the equivalent of the Montes Rook. Beyond this scarp is the overturned flap covered by large blocks and massifs derived from a deep horizon in Mercury where the bedrock is more coherent than the upper, impact-brecciated layers. The radially lineated deposits, as in Orientale, are earlier-arriving basin ejecta and secondary crater materials mixed with the pre-basin surface all of which were modified by the ground surge.

Orientale and Caloris have more in common than previously realized. The basin fill in Caloris is, however, different from that seen in Orientale. The Caloris fill is thicker and has obscured probable inner ring structures and the late stage compressional ridges of the type present on the bench between the Montes Rook and the Inner Basin scarp. The Montes Rook and the main Caloris scarp are similar structural features. They respectively mark the edge of the crater of excavation at each basin and are composed of the overturned rim flap covered by late stage blocky, fallback from relatively coherent deep horizons. Lineated ejecta derived from shallower horizons is present near and beyond the weakly developed outer Caloris scarp which is the counterpart of the Orientale scarp. This lineated ejecta and lobes of hummocky ejecta like the Alpes Formation at Imbrium are partly buried by

smooth plains deposits that are probably related to the basin-forming event. A well developed field of secondary craters lies at about one basin diameter around Caloris. The textural differences between the material around the main Caloris scarp and the lineated material beyond suggests that Mercury is layered like the Moon and that the Caloris crater excavated coherent materials from one or more of these more competent layers at depth. The difference in spacing between the Caloris rings cannot, however, be related to internal layering. It is more probably a gravitational effect which causes ejecta to travel proportionately shorter distances on Mercury than the Moon as well as inhibiting ground motions and internal deformation.

GLOBAL SEISMIC EFFECTS OF BASIN-FORMING IMPACTS

H. Grady Hughes, Frederick N. App, and Thomas R. McGetchin, Los Alamos Scientific Laboratory, P.O. Box 1663, Los Alamos, NM 87545

Models of the thermal evolution of the moon and the terrestrial planets suggest that basin-forming impacts occurred when the planets had partially molten interiors overlain by thickening lithospheres, comparable in thickness to the basin radii. We are investigating the effects or large impacts on planetary surfaces using a Lagragian computer program which treats shock wave propagation and includes the effects of material strength, elastic-plastic behavior and material failure. In this paper we describe the computer code and some physical details of our numerical techniques, and report the results of several initial calculations. We study the global seismic effects for cratering energies (10^{24} and 10^{25} J) intermediate between the Copernicus and Imbrium events on the moon, and compare the phenomenologies for assumed solid and molten planetary interiors. The principal results are as follows: 1) Far-field effects are largely independent of cratering mechanisms (e.g., simulated impacts vs buried explosion). 2) Antipodal seismic effects are significantly enhanced by focusing and are of substantial magnitude. Vertical ground motion may be on the order of kilometers, and accelerations approach one lunar-g. 3) The most violent activity occurs at significant depth beneath the antipode, considerably after the passage of the initial compressive/rarefactive shock wave, and results from complex interactions with the free surface. 4) Seismic effects are decidedly more pronounced for a molten planet than for a solid one. 5) Tensile failure may occur at depths of tens of kilometers beneath the antipode, and may also occur over the entire surface, although at shallower depths.

These results support the suggestion of Schultz and Gault (1975 a.b) that the unusual terrains antipodal to large planetary basins may have been catastrophically modified by seismicity generated by the basin-forming impacts. We would further suggest that these impacts may in fact have pervasively and repeatedly brecciated the entire lithospheres of the terrestrial planets as these lithospheres formed and thickened.

Gravity Effects on Impact Crater Formation. Donald E. Gault, Murphys Center of Planetology, P.O. Box 833, Murphys, CA 95247. John A Wedekind, NASA Ames Research Center, Moffett Field, CA 94035

Gravitational acceleration is one of the primary parameters that is important to impact cratering processes and the interpretation of the effects of cratering on planetary surfaces. The importance of gravity stems, first, in its role in determining the ultimate size of the crater of excavation, second, as it influences the distribution and effects of ejecta deposited around a crater, and third, in its role in post-cratering modifications of large craters of excavation. We report there experimental results directed toward the first two subjects.

The experiments were performed in the Ames Vertical Gun Ballistic Range facility using quartz sand for the target medium in order to minimize strength effects and, hence, accentuate the effects of gravity-induced stresses at the scale of the tests. The target (60 cm diameter and 20 cm deep) was suspended from springs over a central column support that was constrained to only vertical movement by ball bearings. The springs exerted a constant upward force independent of their extension so that when the target system was "dropped" the target experienced a transient reduced "g" field during which time the impacts occurred and the craters were formed. By changing spring constants, six different transient fields were obtained at nominal values of 0.8, 0.66, 0.5, 0.3, 0.2, and 0.1 "g"; thus providing seven values of acceleration with the target stationary at 1.0 "g". Because of the rapid decelleration at the bottom of the downward stroke of the support column, which destroyed the final crater geometry, all data were obtained photogrammetrically from 35mm movie imagery taken at 60- and 30 frames/sec. Aluminum spheres with diameter 3.18 mm and mass 0.047 gram were launched from a light-gas gun at a nominal velocity of 6.6 km/sec. All impacts occurred from vertical incidence into horizontal target surfaces. Ambient air pressure in the impact chamber was less than 1mm Hg. A guillotine-type shutter was driven by explosives across the projectile trajectory to trap propellant gases uprange and prevent aerodynamic disturbance of ejecta.

Crater dimensions (both diameter and depth) were found to vary with the inverse 1/6 power of gravitational acceleration. Crater formation times varied with the approximately 5/8 power of "g". These experimental values contrast with, respectively, 1/4 and 5/8 power relationships associated with so-called gravity scaling conditions for which the target medium has zero strength. The difference between 1/6 and 1/4 appears to be attributable to a small effective deformational strength of the quartz sand as indicated by the collective results of these experiments and small scale explosive crater studies. Such effects of small, but nevertheless finite, strength have minimal effects on formation times, but seem to suggest that "pure" gravity scaling (or 1/4 root dependence) can never be realized for normal conditions with geologic materials on planetary bodies. One possible exception, however, for an asymtotic approach to 1/4 conditions may occur for large impacts into water, a target medium with minimum strength.

Ballistic Impact Ejecta in a Martian Atmosphere. Peter H. Schultz, Lunar Science Institute, Houston, TX, 77058, and Donald E. Gault, Box 833, Murphys, CA, 95247.

Lunar and mercurian craters provide important clues for ejecta emplacement mechanisms under different gravitational fields. The tenuous martian atmosphere, however, introduces an additional parameter that may complicate direct comparison of crater styles to other planets. As a first step in evaluating the importance of this complication, the effect of aerodynamic drag on ballistic ejecta in a martian atmosphere has been examined.

The martian atmosphere is assumed to be isothermal and in hydrostatic equilibrium, thereby permitting the use of a scale height (8 km) and an exponentially decreasing density with height above the surface. In addition, we temporarily have neglected other atmosphere-impact interactions that might occur. The deceleration of a particle traveling through an atmosphere is simply expressed by

$$\frac{C_D \cdot \rho_{atm}}{d \cdot S} \cdot v^2$$

where C_D is the drag coefficient, ρ_{atm} is the atmospheric density, v is the particle velocity, d is particle density, and S is the particle radius. In order to trace the complete trajectory, three nonlinear differential equations must be solved numerically on a computer.

Several different models of transient crater growth were used. As an upper limit to the dispersion of ejecta from an impact, the ejection velocities decayed as $(R/X)^3$ and the time of crater growth increased as $(X/R)^{\frac{1}{2}}$ where R is the final transient crater radius and X is the radius of the growing transient cavity. This description follows current computer simulations of impact and explosion crater formation (1). However, in contrast to Ivanov (2), ejection velocities are scaled with crater size as $R^{\frac{1}{2}}$ in order to preserve the same mass distribution of ejecta with crater size.

If it is assumed that no particle-particle interactions and no aerodynamic shadowing by leading ejecta occur, then calculations indicate that the tenuous atmosphere has little effect on small-size ejecta (0.5 cm diameter) from a 1 km crater but significantly reduces the scaled ballistic range from a 5 km crater. Ejecta from craters larger than 5 km are affected more drastically, and over 95% of the ejecta impact at significantly reduced velocities within one crater radius from the transient rim of a 10 km crater. Because crater rim collapse will occur in craters of this size range, considerable ejecta should return to the crater interior. Increasing the atmospheric pressure a factor of 2 has little effect on a 1 km-diameter crater but further shrinks the ejecta range for a 5 km-diameter crater to a

distribution similar to a 14 km-diameter crater. Similarly ballistic ranges of particles with sizes smaller than 0.1 cm in diameter are reduced more drastically around larger craters.

Partial correction for ballistic shadowing has been introduced by assuming that no drag occurs as ejecta leave the crater but increases as the sine of the angle of departure from the original ejection angle. This correction disperses the ejecta distribution for 0.5 cm particles but remains effective in reducing the range for 0.25 cm particles.

Several preliminary conclusions can be drawn.

1. Aerodynamic drag under present martian atmospheric conditions will affect significantly ejecta smaller than 1 cm.

2. Significant sorting of ejecta with range by particle size may occur.

3. Considerable amounts of ejecta impact close to the crater rim for craters larger than 1-5 km but little aerodynamic effects occur for craters smaller than 1 km. Even greater effects should be evident if atmospheric pressures had been greater in the past.

4. More conservative models of crater growth involving lower ejection velocities result in even less dispersed ejecta distributions for larger particle sizes.

5. Ejecta from large craters may be trapped within the crater following rim collapse. Such trapping should produce craters shallower on Mars than on Mercury or the Moon, as observed (3).

The sequence of ejecta emplacement for small particles appears to be altered significantly. The close-in arrival of considerable ejecta mass may result in an ejecta flow unlike the emplacement sequence envisioned for the Moon. Moreover, models reveal significant distortions of the classical ejecta skirt and indications of possible particle-particle interactions (4). Much larger ejecta ($> 10^2$ cm) are relatively unaffected by such interactions and by aerodynamic drag, thereby producing secondary craters in a manner similar to that on the Moon. Thus ejecta arrival from martian impact craters may be multi-phased.

If the martian subsurface is composed of relatively small-size particles owing to long-term weathering and depositional processes, then these results indicate that ejecta facies around martian craters could be significantly different from those recorded on the lunar surface.

(1) Cooper, Jr., H. F., The Moon (in press, 1977)
(2) Ivanov, B. A., Proc. Lunar Sci. Conf. 7th, 2947-2965 (1976)
(3) Cintala, M. J., Head, J. W., and Mutch, T. A., Proc. Lunar Sci. Conf. 7th, p. 3575-3587 (1976)
(4) Schultz, P. H. and Gault, D. E., Trans. Amer. Geophys. Union, 57, 948 (1976)

BUNTE BRECCIA: CONTINUOUS BRECCIA DEPOSITS OF THE RIES CRATER, GERMANY. Friedrich Hörz, NASA Johnson Space Center, Houston, TX 77058 and V. R. Oberbeck, NASA Ames Research Center, Moffett Field, CA 94035.

INTRODUCTION: The 26 km diameter Ries Crater was formed ≈15 m.y. ago and is the largest terrestrial impact structure with significant parts of the ejecta still preserved (1). The target consisted of 600 m of Triassic, Jurassic and Tertiary sediments (sands, shales, clays, limestones) underlain by crystalline basement (predominantly granites and gneisses). The resulting deposits display a variety of breccia types including "suevites" (highly shocked crystalline basement), "crystalline breccias" (moderately shocked crystalline basement), the "zone of megablocks" (coarse grained mixture of crystalline and sedimentary rocks) and "Bunte Breccia" (sedimentary components). Bunte Breccia comprises approximately 90% (volume) of all impact deposits beyond the 26 km rim (2,3) and extends to the periphery of the ejecta blanket as do the "continuous deposits" (4) around large planetary craters (Fig. 1). Direct examination of the Bunte Breccia together with the extremely well characterized target stratigraphy allows detailed assessment of the source area(s) of individual breccia components (2,3). As a consequence, a shallow drilling project was performed in these breccias to discriminate between presently competing hypotheses concerning the source area of Apollo 14 and 16 rocks and the associated views of ejecta emplacement mechanism(s) for lunar and planetary continuous crater deposits (4,5,6,7,8). Specifically the Ries offers the opportunity to study the incorporation of "local" materials and thus allows discrimination between the ballistic transportation concepts (4,5, 6) and those favoring a ground hugging flow regime (7,8): a cliff line striking EW (Fig. 1) marks the northernmost invasion of the Miocene sea and its unconsolidated sands. This marine sequence is capped by Miocene freshwater lake deposits (sands, clays, freshwater limestones), patches of which extended into the actual crater area as thin (<50 m), discontinuous and eroded deposits. Thus the marine Miocene sediments were demonstrably absent at the site of the crater cavity and most of the freshwater sediments occurred also south of the cliff line. Therefore the Miocene components, long known to make up significant fractions of the Bunte Breccia (2,3,9) are predominantly, if not exclusively, derived from the local terrain, rather than from within the crater cavity.

Fig. 1 illustrates the distribution of Bunte Breccia and the location of 11 drill sites; locations 1-5 represent a radial traverse; locations 6-11 explore the lateral variation of Bunte Breccia. Core diameter was 101 mm. Table 1 lists geologic and topographic data. The following is an account of field observations; detailed laboratory studies are in progress.

FIELD OBSERVATIONS: The cores consist of megaclasts (>1 m in size), clasts (1-100 cm) and matrix (<1 cm). Large megaclasts (>10 m) of both local and crater derived sources occur, but local components dominate. Many megaclasts are undeformed and primary sedimentary textures display different dip angles, indicating a jumbled, irregular configuration of megaclasts. All size clasts also display irregular orientation and local components, in particular clays, vastly dominate. Crater derived materials are mostly from the upper parts of the stratigraphic column (upper Jurassic), with Triassic and espe-

cially crystalline components being rare. Grain size and lithology of clast populations vary from locality to locality, as well as within any given core. The matrix contains abundant clastic material. The fine-grained groundmass (<1 mm) is almost exclusively derived from local sands and clays. The highly polymict matrix differs between localities as well as within individual cores as evidenced by variable color shades, grain sizes, proportions of clay and sand components and populations of clasts. The transition from one matrix type to another is either gradual or knife edge sharp. Apparently the different matrices were formed at distinctly different locations and/or times before final emplacement. In general, despite considerable clay content, the matrix has a "massive" appearance but on rare occasions shows some lineation indicating laminar flow. The irregular orientation of all clasts, their mode of deformation and the massive matrix character indicate a highly turbulent environment.

"Breccias within breccias" are commonly observed, including up to 3 generations. These features together with the various matrix types indicate an extremely efficient, multiphase mixing process which repeatedly recycled and mixed all components.

The contact of Bunte Breccia and authochtonous country rock (mostly unconsolidated sands or soft clays) is in most cases exceptionally sharp, i.e., <1 cm in dimension (localities 2,3,4,6,10,11). The underlying substrate materials are undeformed. The lack of any weathering horizon at this contact indicates stripping and erasure of the old land surface to considerable depth.

The percentage of local versus crater derived materials was estimated in the field. However, even crude estimates are difficult to make because of the relatively fine-grained and therefore poorly defined matrix which constitutes typically >50% of the cores. Preliminary estimates indicate that local components South of the cliff line may vary from 50 to 80% and cores number 7 and 10 may contain even as much as 90% local materials; there is no doubt that local materials vastly dominate the breccia components at the larger ranges (sites 7,8,9,10,11).

CONSTRAINTS ON EMPLACEMENT MECHANISM:

1. The thick deposits - on occasion >100 m - of the Bunte Breccia (Table 1) and the proponderance of local components necessitate a process that is capable of excavating the local terrain outside the crater rim to depths measured in tens of meters, occasionally >50 m.

2. The contact relationships with in situ materials imply that the breccias were deposited on top of a newly excavated datum plane, rather than on top of an old land surface.

3. Various matrix types and their style of occurrence suggest that they were transported to their final resting place as distinct polymict breccia megaclasts.

4. "Breccias within breccias" and especially the different matrix types indicate a thorough, multistage, mixing and brecciation process, in which both crater derived and local materials participate with the same intensity.

5. Evidence for both relatively energetic forces (e.g., clays lodged in sands) and modest energies (underformed primary textures in clast) is in such close spatial association that a mixing process with dramatically varying particle velocities is necessitated.

6. The irregular and seemingly random orientation of clasts of all sizes together with the massive character of the matrix indicate a largely turbulent environment.

CONCLUSIONS: These constraints are consistent with a ballistic mode of ejecta emplacement. The energy required for excavating local materials, for intense and thorough mixing, and for final emplacement by a debris surge is supplied by ballistic ejecta (4,5,6). Recent observations (10) do not constitute evidence against such an emplacement mechanism, as they indicate only the existence of a debris surge, but not its mode of formation.

Drill Location	Range[1] (km)	(≈r)	Azimuth (N°)	Thickness of Bunte Breccia (m)	In Situ Material
1	28.5	2.2	194	>15	??[2]
2	25.5	2.0	196	52	OSM
3	23	1.8	196	76	OSM
4	19	1.5	195	34	Upper Jurassic Lime
5	16.5	1.3	207	>80	??[2]
6	27	2.1	115	47	OSM
7	36.5	2.8	225	17	Upper Jurassic Lime
8	35	2.7	216	28	OSM
9	32	2.5	206	> 7	??[2]
10	32	2.5	206	21	OSM
11	27	2.1	184	84	OSM

[1]Range: From crater center (crater radius, r = 13 km). [2]No contact; drilling terminated in Bunte Breccia for a variety of geological and economic reasons.

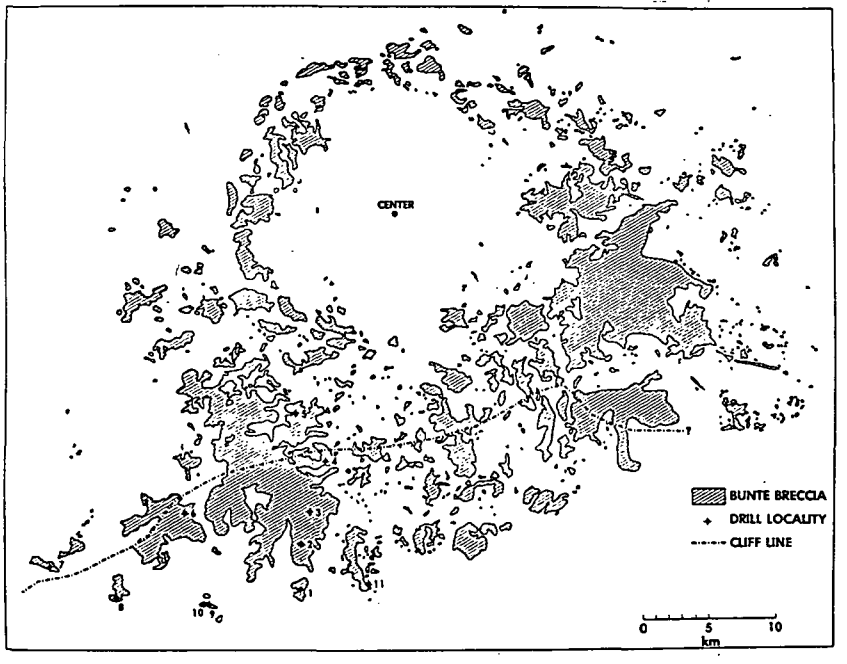

REFERENCES:
1. Pohl, J. et al., The Moon, in press (Flagstaff Cratering Symposium).
2. Hüttner, R. (1969) Geologica Bavarica, 61, 142-200.
3. Gall, H. et al. (1975) Geologische Rundschau, 64, 915-947.
4. Oberbeck, V. R. (1975) Rev. Geophys. and Space Phys., 13, 337-362.
5. Oberbeck, V. R. et al. (1975) The Moon, 12, 19-54.
6. Head, J. W. and Hawke, B. R. (1975) Proc. 6th Lunar Sci. Conf., p. 2458-2501.
7. Moore, H. J. et al. (1974) Proc. 5th Lunar Sci. Conf., p. 71-100.
8. Chao, E.C.T. (1974) Proc. 5th Lunar Sci. Conf., p. 35-52.
9. Schneider, W. (1971) B. Jb. Miner. Abh. 114, 136-180.
10. Chao, E.C.T. (1976) Science, 194, 615-618.

Magnetic Profiles Diagnostic of Maar Craters: Anomalies Associated with Peripheral Ring Dikes. L. S. Crumpler, Jayne C. Aubele and Wolfgang E. Elston, Department of Geology, University of New Mexico, Albuquerque, N.M. 87131.

The lobate ejecta patterns of some martian impact craters have been ascribed to melting of ground ice (Carr, et al., 1977). If this is correct, the presence of ground ice would lead to phreatomagmatic explosions and formation of maars in volcanic terrain. Although terrestrial maars can resemble terrestrial impact craters morphologically, many maars show a diagnostic magnetic signature which may be attributed to the intrusion of deep ring fractures by basalt magma.

Total magnetic field intensity traverses were made across nine recently discovered Plio-Pleistocene maars of the Mt. Taylor volcanic field, New Mexico (Crumpler, 1977), using a portable proton magnetometer. Maars were formed during eruptions of lavas that range from basalt to trachyte. Their eroded profiles range from slightly subdued to breached and strongly subdued. In general, the fresher the maar, the more distinct the associated magnetic anomaly.

The two least degraded craters, the Alejandro maars #1 and #2 (Figs. 1,2) overlap along a fissure and are the result of basaltic phreatomagmatic eruptions which disrupted a pre-existing trachyte terrain (Aubele, et al., 1976). The magnetic susceptibility contrast between trachyte and basalt makes these two maars particularly suitable for modeling. All other basaltic maars have developed in entirely basaltic terrains. Both Alejandro maars are approximately 1 km in diameter. The rims consist of a jumble of trachyte and minor mugearite blocks from a few centimeters to several meters in diameter, including a negligible component of juvenile basalt blocks and cinder. Ejecta extends up to 1/2 crater diameter from the rims. Chert and quartzite pebbles, scattered among the ejecta, were derived from pre-volcanic stream gravel; this gravel appears to have been an aquifer at the time of eruption and provided water for phreatomagmatic explosions. Fine ashes have been winnowed during the 2 to 3 m.y. since formation of the craters and crater floors have been filled by more than 100 m of lake beds, windblown sand, and alluvium.

Total magnetic field profiling of both maars reveals that each crater is characterized by two distinct positive magnetic anomalies, which correspond to the inner crater slopes. Similar vertical magnetic field anomalies are known for Hole-in-the-Ground, Oregon (Lorenz, 1970), and can be duplicated by gravimetric surveys. A terrain effect, which has been postulated as the cause of anomalies found in a few maars in the Pinacate volcanic field, Sonora (Wood, 1974), does not contribute to the observed anomalies in the Mt. Taylor field.

The positive anomalies are best explained by shallow basaltic intrusions along the subsidence ring faults which characterize maars. Ring-fracture intrusions were mapped by Aubele (1976) in a naturally sectioned maar in the Caja del Rio volcanic field, New Mexico, and by Cummings (1968) and Bradbury (1967) at Zuni Salt Lake. The prevalence of positive magnetic anomalies over the lower inner slopes of maar rims suggests that peripheral ring dikes are a common feature of maars.

References

Aubele, J.C., 1976, Montoso maar: A detailed view of internal structure and stratigraphy, central New Mexico: Geol. Soc. Amer., Abstracts w. Programs, v. 8, No. 5, p. 564.

Aubele, J.C., Crumpler, L.S., Loeber, K.N., and Kudo, A.M., 1976, Maare and tuff rings of New Mexico: N. Mex. Geol. Soc. Spec. Publ. No. 6, p. 109-114.

Bradbury, J.P., 1967, Origin, paleolimnology and limnology of Zuni Salt Lake maar, west-central New Mexico: Unpubl. Ph.D. diss., Univ. N. Mex., 247 p.

Carr, M.H., Crumpler, L.S., Cutts, J.A., Greeley, R., Guest, J.E., and Masursky, H., 1977, Martian craters and emplacement of ejecta by surface flow: Proceedings of the Cratering Mechanics Conference, in press.

Crumpler, L.S., 1977, Alkali basalt-trachyte suite and volcanism, Mount Taylor volcanic field, New Mexico: Unpubl. M.S. thesis, Univ. N. Mex., 130 p.

Cummings, David, 1968, Geologic map of the Zuni Salt Lake volcanic crater, Catron County, New Mexico: U.S. Geol. Survey Misc. Geol. Inv. Map I-544.

Lorenz, Volker, 1970, An investigation of volcanic depressions. Part III: Origin of Hole-in-the-Ground, a maar in Central Oregon: Nat. Aeronaut. and Space Adm. Progress Report NGR-38-003-012, Eugene, Oregon, 103 p.

Wood, C.A., 1974, Reconnaissance geophysics and geology of the Pinacate Craters, Sonora, Mexico: Bull. Volcanol., v. 38, p. 149-172.

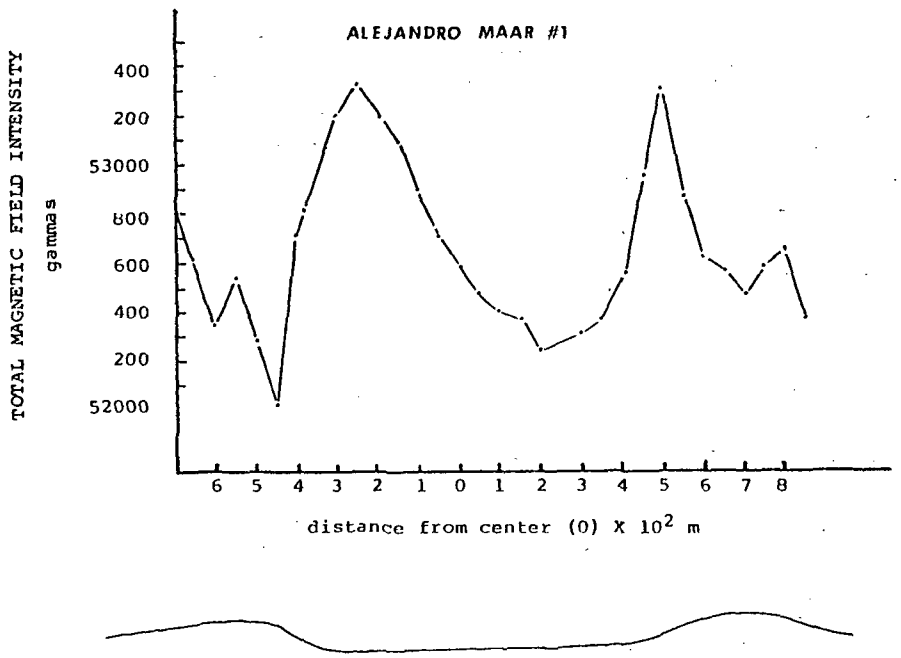

Figure 1. Total magnetic field and topographic profiles of Alejandro maar #1. Vertical scale is 3X horizontal.

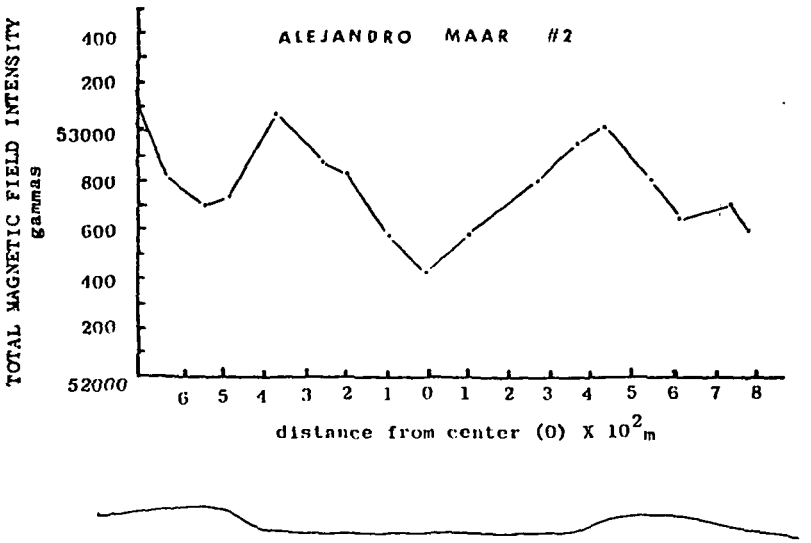

Figure 2. Total magnetic field and topographic profiles of Alejandro maar #2. Vertical scale is 3X horizontal.

Page Intentionally Left Blank

Chapter 6

VOLCANIC PROCESSES

Page Intentionally Left Blank

Structure and Evolution of Mauna Loa Volcano, Hawaii: Inferences Based on Low Oblique Photography and Ground Investigations. Peter W. Lipman and John P. Lockwood, Hawaiian Volcano Observatory, Hawaii National Park, P.O., Hawaii 96718

Color, oblique stereo photography and geologic mapping of the little-studied SW rift zone of Mauna Loa has been undertaken in an attempt to: (1) decipher the sequence of prehistoric volcanic events; (2) identify the locations and geometry of historic vents and flows; and (3) understand the significance of the conspicuous bend in the rift, as well as other major asymmetries of the Mauna Loa shield. Approximately 100 km^2 of the SW rift zone between the 2,000 and 6,000 feet elevation have been mapped, and a remote sensing map of the rift up to the 10,000 foot level has been begun, utilizing an experimental combination of standard black and white air photos, low-altitude aerial observations, and 35 mm color stereo photography.

Preliminary results to date include:

(1) Numerous, young-appearing, prehistoric flows (150-500 years old?) were erupted from the middle SW rift zone, in contrast to published interpretations of an inactive period for Mauna Loa in late pre-written history. Most were from vents relatively high on the mountain, however, and were not sufficiently voluminous to reach the ocean. In contrast, eruptions from the SW rift zone in 1868, 1887, 1919, 1926, and 1950 reached the sea, and together with somewhat smaller activity in 1907 and 1916 from the same part of the rift, constitute exceptionally high-volume activity--at least for the last 500 years or so.

(2) Much and perhaps all exposed rocks on the SW rift upslope of Highway 11 are younger than the Pahala Ash, from which a C^{14} age of 11,780 $\pm$ 300 years has recently been obtained at Kaalualu Bay, south of Waiohinu. If sustained by future work, this interpretation would indicate that only relatively young stages in the evolution of the SW rift can be inferred from exposed rocks.

(3) Many of the young prehistoric vents occur preferentially on the convex (Kona) side of the main rift axis, even though the large-volume historic vents tend to be aligned along the main rift axis defined by older vents. On the concave (Kau) side, there are many open fractures, but few vents. Although no simple pattern of vent migration can thus have occurred in recent times, this distribution suggests a tendency for migration toward the Kona side.

(4) The vent geometry is being studied further in the Kahuku-Ocean View Estates area by detailed gravity measurements. An island-wide study in the 1960's demonstrated a broad gravity high over the SW rift. Preliminary results of the new work indicate that all exposed vents are on the Kona side of this broad gravity high, thus supporting an interpretation of rift migration to the northwest with time.

(5) There is no tendency on the SW rift zone for vents to flare into a pattern radial to the summit of Mauna Loa, as they do on the north side of the NE rift zone, and northwest of Mokuaweoweo.

This work on the SW rift zone, in conjunction with work in progress on the NE rift zone, has led to development of a new volcano-tectonic model that hopefully accounts for many of the distinctive features of Mauna Loa.

These and other aspects of Mauna Loa geology and interpreted as reflecting complex interactions between the growing edifices of Mauna Loa and Kilauea, elaborating on the "edifice effect" concept of Fiske, Jackson, and others. We infer that at an early stage in the development of Mauna Loa, before Kilauea existed as a large volcanic feature, only Mauna Kea and Hualalai were major constraints to growth of the Mauna Loa shield. At such a time Mauna Loa would have had equally long, active, and relatively linear rift zones on both the southwest and northeast sides. The bend in the SW rift

would not have existed and the "Kulani shield" was an integral part of the prehistoric NE rift zone.

The free, ocean-facing sides of Mauna Loa would have been characterized by gravitational, block-slump features similar to the Hilina fault system of Kilauea Volcano. Remnants of these block-slump terranes on Mauna Loa would include the Kaoiki faults and lava-drapped step topography higher on Mauna Loa's south flank. The Ninole Hills, rather than constituting an eroded pre-Mauna Loa volcano, would represent dissected lower blocks of such a slump system. On the Kona side, the relatively inactive Kahuku and Kealakekua fault scarps, as well as lava-drapped step topography in between, are also interpreted as remnants of old block-slump structures. Large-scale submarine features off Milolii also suggest underwater block slumping on this side.

As Kilauea developed into a sizable volcano, it began to serve as a barrier to Mauna Loa's growth. It interfered with gravity slumping on the south side of Mauna Loa and pinned the lower part of the NE rift zone, resulting in greatly reduced rates of volcanism along this part of the rift. The SW rift zone, blocked to the east but open to the west, began to migrate in that direction--gradually developing its conspicuous bend.

The localized distribution of radial vents on Mauna Loa, confined largely to a sector on the north side between radials extending toward Hualalai and Mauna Kea, is considered to reflect the fact that during most of Mauna Loa's growth, it was buttressed only on the north and could expand freely in other directions. In addition, periods of summit inflation and rift injection along the rift zones, would tend to compress the south side of Mauna Loa, closing open fractures, while leaving the north flank free to inflate and distend fractures on that side.

One of the principal keys to unravelling the history of Mauna Loa volcano was the deciphering of the developmental sequence of volcanic events as revealed by low altitude, color stereo photography. Pictures were taken from a light aircraft in a fully automatic mode using a motor-driven, 35 mm camera on repeated, low fly-bys.

Frequency Distribution of Lava Tubes and Channels on Mauna Loa Volcano, Hawaii. Ronald Greeley, Curtis Wilbur, and Donna Storm, University of Santa Clara at NASA-Ames Research Center, M/S 245-5, Moffett Field, CA 94035.

Exploration of Earth, Moon, Mars, and Mercury (?) has shown that basaltic lava flows constitute large parts of the surfaces of the terrestrial planets. Lava tubes and channels appear to be important in the emplacement of certain types of these basalt flows. In order to determine their relative importance in the formation of shield volcanoes, basaltic plains and flood basalt plateaus, photogeological analyses are currently in progress for selected basaltic provinces on Earth. Mauna Loa shield volcano, Hawaii, was the first case examined. Lava flows and associated lava tubes and channels were mapped on aerial photographs of sparsely vegetated parts of the exposed shield for statistical analysis. About 15% of the shield was mapped on stereoscopic photos and an additional 10% on monoscopic photos, representing rift zone and non rift zone areas of the summit, flanks, and distal parts of the shield. Of the flows analyzed, 60.2% had channels (79.4% by flow area), 19.6% had tubes (29.5% by flow area) and 65.6% had either tubes or channels (82.7% by flow area). The figures presented for lava tubes are minimum values, since only collapsed or partly collapsed tubes could be identified. Assuming that the sampling is representative, then at least 82% of the surface area of the shield was emplaced in association with lava tubes and channels. To determine the effect of topography on the formation of lava tubes and channels, their occurrence was compared with local slope; there was, however, no apparent correlation. The conclusion is drawn that knowledge of the geology of lava tubes and channels is essential for understanding the growth and evolution of Mauna Loa shield volcano. Similar analyses have been completed for a small part of the Snake River Plain, Idaho, which show that tubes and channels are less frequent (only 43% of the area involved had either tube-fed or channel-fed flows) than on Mauna Loa. The lower frequency, however, may be attributed partly to the higher state of erosion resulting from the greater age of the lavas in the Snake River Plain. Analyses are currently in progress for Haleakala Volcano, built principally of hawaiite lavas, for comparisons with Mauna Loa and the Snake River Plain.

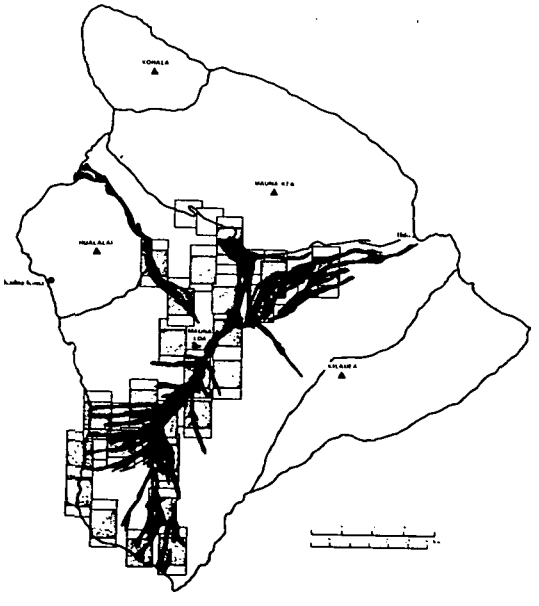

Map of the island of Hawaii and the extent of Mauna Loa shield volcano in relation to the other four shield volcanoes that make up the island. Black areas are historic flows from Mauna Loa; rectangles are "footprints" of the aerial photographs used in this study.

Reference:
Greeley, R., Wilbur, C., and Storm, D. Geol. Soc. Amer. abs. 8 892 (1976)

CONTROLS OF PHYSICAL PROPERTIES OF SNAKE RIVER PLAIN LAVAS ON SURFACE MORPHOLOGIES

John F. Karlo and John S. King, State University of New York at Buffalo
Amherst, New York 14226

Volcanic rocks of the eastern Snake River Plain are dominated by basalts which show a high degree of topographic uniformity. The surface of the eastern plain is made up primarily of coalesced and overlapping lava shields. Individual vents were short-lived and apparently active for short periods of time, commonly for only a single eruption. On the whole, the distribution of vents appears random, although short fracture-controlled vent chains (less than 6 km in length) are common. The vents in any one chain are commonly few in number and evidence of fissure eruption from the chains is not apparent. The basalts of the eastern Snake River Plain are olivine tholeiites which show a narrow composition variation resulting from olivine and plagioclase fractionation, which are the only phenocrysts found in the basalts. This results in a degree of petrologic uniformity which is reinforced by the fact that most basalts are either micro-porphyritic or contain less than 10% phenocrysts.

Early reference to the geology of the eastern Snake River Plain emphasized the low relief and flat topography of the terrain. The low profiles and long slopes of the shields are apparently the result of a combination of low hydrostatic head feeding the eruption coupled with low viscosities of the erupted lava. In the Snake River Plain Province, the top of the asthenosphere probably extends to the base of the crust and is no doubt the site of fractionation as indicated by the composition of cumulate xenoliths. Typical Snake River basalt is phenocryst-poor and most likely erupted at temperatures very near the liquidus. Calculation of magma density at appropriate liquidus temperatures for the range of basalt compositions found on the eastern Snake River Plain yield a range of from 2.68 to 2.82 g/cc. Seismic studies of the Western Snake River Plain and the Basin and Range Province suggest that such values are similar to the average density for the crust of the Snake River Plain. It seems unlikely that the hydrostatic pressure within the magma reservoirs would exceed lithostatic pressure of the overburden, and as the Snake River Plain is in approximate isostatic equilibrium, it follows that because magma and crust densities are very nearly the same, that there is insufficient hydrostatic head to result in typically tall vents. Possibly the abandonment of a single vent in favor of eruption at closely spaced points in a vent chain substitutes for vent elevation.

The typical basalt flow of the eastern Snake River Plain is a "flood" of pahoehoe lava less than 25 m thick. Slopes of the distal flow surfaces range from 0.75 - 2.0 grade per cent and may in some instances increase near the vent to 5 - 6 grade per cent although they often do not. The vents may be marked by central craters, lava lakes or other evidence of late stage activity but many are featureless. The youngest flows cover areas on the order of 10^3 km^2.

Viscosities for the lavas may be calculated from the oxide components of composition at chosen temperatures. For the range of observed composition and liquidus temperatures, the range in viscosities is approximately 300-700 poises with most of the range being due to temperature variation. This low range of fluid values no doubt contributes to most of the uniformity in style of the flows.

Atypical vents showing high relief are present on the eastern Snake River Plain however. One such type of high-relief vent is the result of a pyroclastic phase of activity in the eruption. Pyroclastic activity is identifiable at approximately 25% of the vents in the Hell's Half Acre region

of the Snake River Plain although it is a dominant process in less than 5% of the vents. Pyroclastic vents are striking; they are tall, steep-sided and are often marked by deep, large diameter central craters. Atypical steep-sided flow vents can often be shown to be associated with a dominant period of pyroclastic activity from which they inherited their steep slopes.

Another divergent group of shields with tall vents are characterized by highly porphyritic basalt and the topographic distinction between these vents and those of normal flows are probably the result of viscosity differences due to the contained phenocrysts. Phenocrysts within a melt increase the viscosity. Typical Snake River basalts contain less than 10% phenocrysts whereas the coarsely porphyritic basalts found in association with the tall vents commonly contain more than 25% phenocrysts. This high percentage of phenocrysts increases viscosity by at least a factor of two orders of magnitude.

On a more detailed scale, there is a large degree of variation between flows and within local portions of a single flow. Preliminary results suggest that flows with a higher percentage of phenocrysts tend to be thicker, have rougher surface textures and somewhat different channel morphologies compared with more typical Snake River flows. Within a single flow, the surface can be broken into two portions. The portion near the flow front tends to be very rough and characterized by rapid changes in micro-topography, collapse pits, typical pahoehoe structures, etc. The portions of the flow away from the front are comparatively smooth and may lack all the typical pahoehoe features. Rough calculations of yield stresses and surface tensions based on flow morphologies have been found to be within observed or experimental ranges for lavas. This suggests that the smaller scale features of the flow can be interpreted as dependent on these physical properties. It is postulated that the behavior of Snake River lavas can be treated as that of Bingham materials. Quantitative and semi-quantitative descriptions of Snake River lava flow behavior are in the process of being calculated.

LAVA MOUNDS PERIPHERAL TO THE KING'S BOWL ON THE GREAT RIFT, IDAHO

John S. King and Ronald Papson, State University of New York at Buffalo
Amherst, New York 14226
Ronald Greeley, NASA Ames Research Center, Moffett Field, California 94035

Approximately 100 lava mounds are located in a discontinuous ring around King's Bowl, a prominent volcanic vent on the Great Rift in southern Idaho. King's Bowl is ovoid in plan and about 90 m in length measured along the Great Rift and about 25 m across at its maximum width. The ring of mounds extends nearly 460 m north and south of King's Bowl, up to 520 m east of the vent and 360 m west of King's Bowl. The mounds are of a variety of irregular subrounded outlines, many of which show streamlining outward away from King's Bowl. The mounds are also of a variety of sizes with a minimum dimension of 7.5 m across and a maximum dimension ranging from 12 - 24 m. The average height of the mounds is 3 - 4.5 m.

The typical lava mound consists of a .3 - .6 m high wall of stacked or irregularly oriented plates of basalt from .3 - 1 m across and from 2.5 - 7.5 cm thick. These walls or ramparts are usually discontinuous on that portion of the mound facing away from King's Bowl and give the impression of having been deposited by material moving out and away from the central area. Some mounds lack platy ramparts and instead show low walls of rubbly or scoriaceous basalt. Flow lines and well-defined lava channels are apparent around some of the mounds and almost without exception, the mounds are surrounded at their bases by massive basalt plates which dip away from the mounds.

The lava mounds which are locally called the "Ring of Fire", are apparently related to a lava lake which existed in the location prior to the explosive event which resulted in the King's Bowl crater. Not all of the mounds have similar physical features however and it believed that although they are all genetically related to a source vent at King's Bowl, some of the lava mounds had slightly different histories. Levelling of the mounds established that they were all of nearly the same elevation (average elevation: 1509-1510 m). The distribution, thegeneral morphology and details of minor structures as well as the near uniformity in elevation all suggest that most of the lava mounds were parts of a levee of basalt that retained the lava lake which collected from lava flowing from a vent in the King's Bowl region. The lava erupted from the vent and quickly crusted over. The crust was soon fractured into plates by continuing activity in the underlying molten lava. The general convection of the molten lava probably coupled with withdrawals and resurgence defined the ultimate position of the levee. This levee was irregular in outline with protrusions toward the lake and reentrants away from the lake. However the hydrostatic head of the lava controlled the level of the levee. It is interpreted that either a final resurgence of lava from the vent caused the lava to rise and start to overflow the levee resulting in continuing erosion through the wall or that pressure generated against the wall by resurgence of the lava caused breakthroughs at weak points along the levee. Such points could be positioned at points of reentrants while points of strength (those which were to remain as the mounds) could relate to the convex buttresses in the irregular wall. Whatever the cause, outflow did take place as is clearly seen in the preserved streamlining around some of the mounds. As noted, the mounds are all of similar elevation. However there is a group of mounds arrayed along the east side of the Great Rift which are all of a consistently higher elevation of 1.2-1.5 m in excess of the mean elevation. This suggests that the entire process was repeated and that a lava lake existed at an earlier time at a somewhat higher elevation. The process of eruption, retention, breakthrough and outflow was no doubt short-lived and preceded the King's Bowl event.

Subsequent to the lava lake (or lakes) a phreatic eruption took place from the King's Bowl. This was a violent explosive eruption as evidenced by the field of block ejecta which is especially well-arrayed on the west side of King's Bowl. Projectiles from King's Bowl have repeatedly broken through the lava lake crustal plates as well as through squeeze ups on the crustal surface which forced out at a late stage in the lava lake activity. Ash was also ejected from King's Bowl and this is found primarily along the east side of the crater indicating a prevailing wind from the west at the time of eruption. Ash fills the central depression in many of the mounds on the east side of the Rift.

The King's Bowl itself is believed to be only partially the result of ejection of solid material. The explosive event certainly disrupted rock in the vicinity of the vent and much was thrown out. However withdrawal and subsidence of activity in the vent no doubt allowed gravity adjustment as well and much of the crater as it exists today is believed to be the result of collapse.

BIG SOUTHERN AND EAST BUTTES, RHYOLITIC DOMES ON THE SNAKE RIVER PLAIN IN IDAHO.

Dallas B. Spear and John S. King, State University of New York at Buffalo, Amherst, New York 14226

Three buttes form prominent landmarks on the Snake River Plain between Arco and the Idaho Falls-Blackfoot area in Idaho. Big Southern Butte, the largest of the three, has a diameter of 8 km and rises some 760 m above the Plain. Middle Butte, located 19 km east northeast of Big Southern, is 1.6 km in diameter and 335 m high. Three km east of Middle Butte is East Butte which is 2.4 km in diameter and stands 300 m above the surrounding lava flows. Two of the buttes, Big Southern and East, are rhyolitic in composition whereas Middle Butte is composed of stratified basalt.

The origin of these buttes has long been controversial. Russell (1902) believed them to be steptoes or kipukas, ancient rhyolitic volcanoes surrounded by basalt. Stearns and others (1938) felt they were fault blocks of older rock which had been uplifted and eroded. Recently, it has been suggested that the rhyolitic buttes represent relatively young rocks emplaced as viscous plugs and domes from a remobilized rhyolitic basement.

Preliminary mapping has shown that Big Southern Butte consists of two coalescing cumulo-domes, each of which may have had more than one intrusive center. The division into two primary domes is based on overall morphology and characteristic differences in rock types. The domes are aligned along a west northwest trend with the older dome the more easterly.

The older dome is characterized by a laminated lavender rhyolite which grades in the upper parts of the section to a "sugary" white rhyolite, probably due to hydrothermal alteration. Attitudes of the flow banding generally document flow outward from the center on all sides. Numerous and varied breccias are found on the slopes, most of which are believed to be crumble breccias formed as the dome expanded and grew. Some of the breccias at one outcrop are associated with two thin (5-10 cm thick) ash layers and are thought to have resulted from volcanic eruptions from a vent. This suggests that Big Southern Butte did not grow exclusively be internal expansion. In addition to the breccias, obsidian and minor pumice are present as mappable units.

The younger dome of Big Southern Butte consists of white rhyolite which is very homogeneous and shows but minor flow banding and few associated breccias. Some of the upper part of the rhyolite is hydrothermally altered with intricate caverns and patterns formed by solution and wind action. A few basaltic fragments were found in the rhyolite at one locality.

A north-northwest trending fault separates the white rhyolite of Big Southern Butte from an estimated 230 m section of basalt which dips about 40° in a northeast direction. The bottom of the basalt section is extremely altered but grades into unaltered basalt toward the top.

East Butte has a simpler history than Big Southern. It appears to be a single cumulo-dome made up primarily of a laminated rhyolite with large phenocrysts of sanidine. Also there are numerous inclusions of basalt fragments, presumably torn from the sides of the conduit during the rise of the silicic magma to the surface. Flow banding at East Butte is away from the center in all directions.

A STUDY OF THE TEPHRA DEPOSITS OF SPLIT BUTTE, A MAAR CRATER OF THE SOUTH-CENTRAL SNAKE RIVER PLAIN, IDAHO

Michael B. Womer and John S. King, State University of New York at Buffalo
Amherst, New York 14226
Ronald Greeley, NASA Ames Research Center, Moffett Field, California 94035

Split Butte is a volcanic feature of recent origin located in the south-central Snake River Plain, Idaho. It overlies basalts of the undifferentiated Snake River Group of Pleistocene to Holocene age. Split Butte is west of the young Wapi lava flows which slightly overlap it indicating that Split Butte predates the Wapi.

Split Butte consists primarily of a tephra ring approximately 550 m in diameter with a maximum relief of 50 m relative to the surrounding plain. The tephra, which consists primarily of partially palagonitized sideromelane and small lithic fragments, is thinly bedded and dips radially away from the center of the Butte. A series of en echelon basalt dikes cut tagentially across the ash ring on the northwest. The tephra ring is in disconformable contact with the basalt of a lava lake which was confined by the ramparts. The ring is discontinuous and the lava lake appears to have flowed over a section of it on the southwest. An inner pit crater approximately 20 m deep and 450 m in diameter was formed in the lava lake owing to collapse of the central portion of the lake. A small cluster of spatter cones lies on the circular fracture along which the collapse occurred.

A large split, or declevity, is located on the eastern section of the tephar rim of Split Butte. The split is situated at the point of greatest accumulation of ash and is the result of the removal of a large volume of ash from the outer slope of the tephra ring at this point. The actual mode of formation of the split is as yet unknown.

Over 270 samples of tephra, basalt and soil were collected at Split Butte. The tephrz samples will be petrographically analyzed to determine the variations in composition throughout the eruptive history of the feature. The basalt will be analyzed to determine the relationships, if any, between the samples of the lava lake, en echelon dikes, and the encroaching surface flows. Presence of variations in bulk composition of the erupting magma will be noted and trends plotted.

A grain size analysis is being carried out on the tephra samples and parameters such as mean grain size vs. distance; sorting; type of distribution; etc., will be used as an estimate of eruptive energy and related processes of eruption. An analysis of maximum diameter of basalt throw-out blocks vs. distance from the vent is planned and should give an additional estimate of eruptive energy.

Intense Fumarolic Activity At A Silicic Volcanic Dome: The 1976 Eruptions At La Soufrière De Guadeloupe, F.W.I. Grant Heiken* and Tom McGetchin*, Geological Research Group, Los Alamos Scientific Laboratory, Los Alamos, NM 87545 (*see note 1)

Silicic volcanic domes may be present on the Moon, for example at Rümker and the Marius Hills regions, based on photogeologic studies (e.g., 2, 3, 4). Domes similar in appearance have been described on Mars (5) and if the terrain indicated by recent radar observations of Venus is truely as rough as it is perceived (6), one might speculate that domes are present there as well. On Earth volcanic domes are plentiful in regions of continental volcanism and subduction zones and less common as small volume bodies on oceanic islands.

La Soufrière de Guadeloupe is a 470-m-high, 700-m-diameter, steep-sided dome resting on older volcanic topography (7). The dome is cut by several major fracture systems, with the present (1976-1977) activity centered along SE-NW trending fractures across the SE slope of the dome and a deep, elongate depression at the summit. The present activity began in early summer 1976, with increasing seismic events and occasional summit steam and tephra explosions. The semi-continuous fumarolic activity consists of steam plumes rising from the summit and along the SE fissure. Unless atmospheric conditions are extremely stable, the steam plume rarely rises more than 200 m above the summit; the steam generally carries with it a small amount of fine-grained tephra. Steam explosions, occurring at intervals of 2 to 15 days during the peak activity of fall 1976, lasted up to several hours. Those eruptions which were documented with a sequence camera built up slowly with progressively larger amounts of tephra entrained in the steam cloud. The maximum cloud heights were reached in 10 minutes to over an hour, with 3 to 5 minute fluctuations. Eruption clouds of <50 m to >2000 m were observed. When two separate vents were erupting simultaneously, they exhibited the same fluctuations with time, although cloud volumes were different. Based on these observations, all of the vents appeared to have the same steam source.

Typical activity is well illustrated by the eruptions of October 4. Tephra-laden clouds flowed down valleys west of the dome, rarely rising more than a few hundred m above the summit. These were cool clouds which moved slowly downwind and deposited thin veneers of tephra south and west of the volcano. The fine-grained tephra was wet, forming a grey, sticky deposit containing accretionary lapilli. During and following the larger eruptions, thin streams of light grey, steaming mud flowed down the dome flanks.

The tephra consisted of fine-grained, altered lithic fragments and altered and unaltered mineral fragments in a clay matrix. Lesser amounts of pyrite, hematite and glass were present. The glass particles consist of partly altered, slightly vesicular, colorless dacite. Fresh (juvenile) pyroclasts were not present in the tephra. Plagioclase (An_{55} to An_{77}) and orthopyroxene ($Wo_3En_{62}Fs_{35}$ to $Wo_4En_{52}Fs_{44}$) grains in the tephra are identical to those in rock samples collected from the dome flanks. The lithic fragments in the tephra are also similar to the dome lavas. It is likely that all of the tephra from these eruptions were derived from hydrothermally altered rocks of the dome and no fresh magma has yet reached the surface in the present phase of activity.

The activity at La Soufrière appears to be that of a vapor-dominated geothermal system driven by a localized heat source in the form of a magma body located at relatively shallow depths below the volcano. New magma at depth is suggested by greatly increased seismic activity and shallow epicenters (pers. comm., M. Feuillard). Most vapor dominated systems occur in elevated areas of recharge, where groundwater movement is downward and outward (8). La Soufrière is the highest mountain on Guadeloupe, consists of fractured, highly permeable rock, and is the center of very high rainfall (9).

This geologic setting fits the models of groundwater movement described by Healy (8), in which high temperature fumaroles are present at the summit and warm springs issue from the base of a volcanic dome. It may be that the variation in phreatic eruptive activity with time is dependant on the rate of recharge of meteoric water within the dome, to the decrease in pore pressure during fortnightly tidal minimums, (10, 11) or both. Violent steam eruptions without the actual eruption of magma are relatively common. Examples include the 1956 activity of La Soufrière (7), the eruption of 1.7 x 10^5 m^3 of mud at Lake City Hot Springs, CA in 1952 (12) and the activity at Mt. Baker, WA in 1975 (13).

Activity such as that occurring at La Soufrière will produce deposits, that if identified by remote observation, may be used to infer the presence of a volatile phase. This volatile phase may or may not be H_2O; for example, on Mars the volatiles driving volcanic eruptions might be a sulfur compound or on Venus CO_2. Orbiting planetary missions with high resolution cameras could resolve the presence of distinctive volcanic deposits, such as mud flows and thin tehpra units associated with dome complexes already identified as potential targets for exploration. The spectral signatures of hydrothermally-altered volcanic rocks should be distinctive enough for purposes of identification and mapping. Exploiting these considerations, we feel that Martian volcanic complexes should be of enough interest to rank as primary targets for future exploration of that planet's surface.

(1) The study at La Soufrière was part of an international effort of which the LASL team was a part. The members of the LASL team are too numerous to mention in this abstract, but special recognition must be accorded B. Crowe, R. Peterson, R. West, and J. Eichelberger.

(2) Guest, J. E. and J. B. Murray, Jour. Geol. Soc. London, 132, 251-258 (1976).
(3) Smith, E. I., The Moon, 6, 3-31 (1973).
(4) Baldwin, The Measure of the Moon, U. Chicago Press (1963).
(5) Carr, M. H., Jour. Geophys. Res., 78, 4049-4062 (1973).
(6) Campbell, D. B., R. B. Dyce and G. H. Pettengill, Science, 193, 1123-1124 (1976).
(7) Robson, G. R. and J. F. Tomblin, Cat. of Active Volcanoes of the World, part XX, 18-22 (1966).
(8) Healy, James, Proc. 2nd U.N. Conf. on Geothermal Energy, 415-422 (1976).
(9) Lasserre, Guy, La Guadeloupe, Un. Fr. d'Impression, 1135 pp (1961).
(10) Kienle, J. pers. comm., 1976.
(11) Rinehart, John S., Proc. 2nd U.N. Conf. on Geothermal Energy, 549-551 (1976).
(12) White, D. E., Bull., Geol. Soc. Amer., 66, 1109-1130 (1955).
(13) Eichelberger, J. C. et al., Jour. Volc. and Geothermal Res., 1, 35-53 (1976).

Page Intentionally Left Blank

Chapter 7

EOLIAN PROCESSES

Page Intentionally Left Blank

Fine Particles on the Surface of Mars. Carl Sagan, Laboratory for Planetary Studies, Cornell University, Ithaca, NY., 14853

The Viking Lander Imaging systems have uncovered evidence for fine mobile surface particles in both the Chryse and the Utopia landing sites. Dune-like drifts are more abundant in Chryse; ventifacts -- particularly pitting in rocks, which may be due to aeolian abrasion in materials of differential friability -- may be more common in Utopia. The greatly different states of erosion of rocks in an environment where aeolian abrasion is calculated to be very efficient may be due to very different friabilities of rocks, or to geologically recent exhumation of well-preserved rocks. Image comparison, and single line scan techniques have uncovered no evidence of particle motion since terminal descent maneuvers, consistent with findings by the meteorology instrument that wind velocities have been below saltation thresholds throughout the nominal mission. In Chryse arrays of parallel boulder-associated streaks are evident tending 200° clockwise from North, consistent with the direction of leeward crater-associated streaks in the same region observed by Mariner-9. Observed high cohesion of surface grains confirms that the saltation velocity/particle diameter curve rises sharply towards small diameters, possibly caused by the high oxidation state of the regolith, and that the most readily transported particles on the martian surface have diameters of about 200 micrometers. The apparent absence of sand ripples may be due to the very long saltation skip distance on Mars. An important Viking experiment is scheduled to begin in the spring of 1977, when local saltation thresholds are expected to be exceeded, and the motions of individual surface particles and drift fields will be monitored.

Sedimentary Regimes on Mars. R. Saunders, Jet Propulsion Laboratory, Pasadena, CA, 91103

Two Viking landers, separated by thousands of kilometers on the martian surface, have returned images of surrounding terrains that may be more noted for their similarities than for their differences. Furthermore, while the rock-strewn surfaces appear similar, the chemical analyses of the material at the sites is virtually identical. To what extent have we been able to use these data to estimate the extent or effectiveness of various processes that are believed to operate at the martian surface? Much work remains to be done, but the comments that follow are based on the initial observations.

The mechanical action of particles carried by the wind in the abrasion of rocks or forming of pits, grooves, flutes or ventifacts is minimal. Although the surfaces at both Viking landers has a characteristic windswept appearance, it is likely that fines have been removed but that the net effect has been a very slight (a few centimeters or less) lowering of the surface and formation of local lag surfaces. Pits seen in many rocks do not appear to be the result of differential erosion by wind, or at least they are unlike any terrestrial analogs of that phenomenon. The pits are much more likely to be vesicles in basalt rocks. Angular rocks are far more likely to occur by random breaking up of the parent rock than by wind formation of ventifacts. Rates of erosion by wind activity on Mars are probably extremely low to practically nonexistent. However, particles are transported and deposited by the action of the wind. There is no denying the vast fields of dunes in the north polar region and elsewhere. The drifts seen in the Lander images are also eolian in origin. Although in view of the flow features seen around some young craters, we should not entirely discard the possibility that drifts may be formed by an impact crater event. This author prefers the eolian hypothesis for drifts because it is more in accord with all the observations.

Some discussion of the fine material is in order. Drifts of fine material occur at both lander sites, but are much larger at the Lander 1 site. Drifts should be understood to be distinct from dunes, which retain a characteristic shape and develop a slip-face. It is the development of the slip-face that distinguishes dunes from drifts and provides a certain inherent stability to the dune that drifts do not have.

Some observations of lander and orbiter images have led to the conclusion that fine material is moved by the wind on Mars and provide some physical constraints on the mechanisms involved. The top of the one-meter high boulder near Lander 1 is covered with fine material. It is hypothesized that the material behaves sedimentologically as dust. A critical observation is that, although the boulder has a sizable mantle of sediment, other smaller rocks seen in the near-field have no mantles. Two mechanisms could account for the sediment on the rock. (1) The sediment could be a remnant of a large drift that once covered the rock. (2) The sediment may be produced by the dust storms. By either model, the sediment has escaped erosion that removed surrounding and lower-lying material. This suggests that the sediment is remobilized by the action of saltating grains propelled across the area by infrequent high winds and that the maximum height reached by the saltating grains is less than one meter. Sediment that accumulates on low rocks is effectively removed faster than it can build up again.

The drifts themselves would appear to be composed of particles that move in suspension rather than saltation. Orbital imagery shows areas of dune accumulation; that is, particles that move primarily by saltation. There are the fields of dune forms near the north pole and in smaller patches elsewhere. Although the saltating path is low, as argued previously, the mean path length is longer than on Earth because of the higher wind velocities involved. One implication of this is that the smallest true dune that can form on Mars will be larger than the smallest that can form on Earth. This follows from the fact that dunes become self-perpetuating when they attain enough height to develop a slip-face and thereby trap all the grains that move across them. The minimum size of a slip-face is related to the mean path length of the saltating grains. Another implication is that grain sizes of dune materials may also be larger on Mars. Although the sediment size most easily moved on Earth is about 80 μm, a very small proportion of dune sand is this small. This is because of turbulence. A wind strong enough to maintain saltation can also carry most material as large as 80 μm in suspension and remove it from the area. The mean upward component of the turbulent wind flow exceeds the settling velocity of these particles. On Mars, the settling velocities are typically only slightly greater than on Earth, but the wind velocities required to maintain saltation are much higher. The typical saltating grains that form martian dunes could be nearly one millimeter in diameter compared with 0.25 millimeter on Earth.

There is much "field evidence" to be gleaned from Viking Lander and Orbiter images. This evidence is helping to fine-tune theories of eolian activity and will aid in our understanding of the physics of sedimentary regimes on Earth as well as Mars.

Recent Results from the Martian Surface Wind Tunnel (MARSWIT). Ronald Greeley, University of Santa Clara at NASA-Ames Research Center, M/S 245-5, Moffett Field, CA 94035; J. B. Pollack, NASA-Ames Research Center, Moffett Field, CA 94035; J. D. Iversen, Dept. of Aerospace Engineering, Iowa State University, Ames, IA 50010; and B. R. White, Dept. of Mechanical Engineering, University of California at Davis, Davis, CA 95616.

MARSWIT, the low surface pressure wind tunnel facility established at NASA-Ames, has been in operation for approximately one year. Experiments conducted or in progress include determination of: 1) threshold wind speeds to set particles of various sizes into motion on Mars, 2) effects of adsorbed moisture on wind blown particles, 3) electrostatic charges generated on saltating particles, 4) differences in aeolian erosion under low pressure, and 5) grains trajectories and other parameters of saltating grains. Results and progress from these experiments are as follow:

1) Threshold Determinations: Wind friction threshold speeds (V_{*t}) for particle movement at an atmospheric pressure of 5.3 mb (nominal Mars case) is about 2.5 m/sec, which on Mars implies free-stream winds (a few m above the surface) of 50 to 135 m/sec, depending on the nature of the surface and atmospheric conditions. The particle size most easily moved by winds on Mars is about 160 μm (1).

2) Adsorbed Moisture Effects: Small quantities ($\sim$2-6% by weight) of water adsorbed on particles vaporize at low pressure; in the presence of winds, the vaporization is violent and ejects particles several cm above the surface. If sufficient water vapor is driven a few mm into beds of particles on Mars on a diurnal or other cyclical basis, then slight fluctuations in temperature and pressure may generate similar ejections of particles. This mechanism could be an effective means of setting very small ($\sim$a few μm) particles into motion in comparatively low velocity winds (2).

3) Electrostatic Effects: Interparticle forces have been shown to be important in threshold calculations (3, 4); very little research has been conducted to determine the forces on particles resulting from electrostatic charges built up under saltation conditions at low pressure. Preliminary experiments show the effect is significant and experiments are in progress to determine the magnitude of the forces involved.

4) Erosion Rates: Experiments are underway to compare the effectiveness and rates of erosion under low pressure (martian) for comparisons with terrestrial conditions. Preliminary results conducted in collaboration with D. Krinsley show a higher net erosion at low pressure, as well as mineralogical texture differences; the differences are attributed at least in part to the higher velocities involved in wind blown particles under martian conditions and the comparative lack of "slip-stream" effects.

5) Saltation: Numerical simulations of saltating grains in a martian atmosphere have been carried out (5) which show that trajectory path lengths and terminal grain velocities will be higher on Mars, and that, because the viscous sublayer at low pressure is thicker than on Earth, the particles will be spinning very fast, introducing a significant lift function (Magnus effect).

References cited:

(1) Greeley, R., B. White, R. Leach, J. Iversen, J. Pollack, Geophys. Res. Ltr. 3, 417-420 (1976)
(2) Greeley, R., R. Leach, B. White, J. Iversen, J. Pollack. Desert Dust Symp., AAAS Symp. Proc. (submitted, 1977)
(3) Iversen, J., J. Pollack, R. Greeley, B. White, Icarus 29, 381-393 (1976)
(4) Iversen, J., R. Greeley, J. Pollack, J. Atmos. Science 33, 2425-2429 (1976)
(5) White, B., R. Greeley, J. Iversen, J. Pollack, J. Geophys. Res. 81, 5643-5650

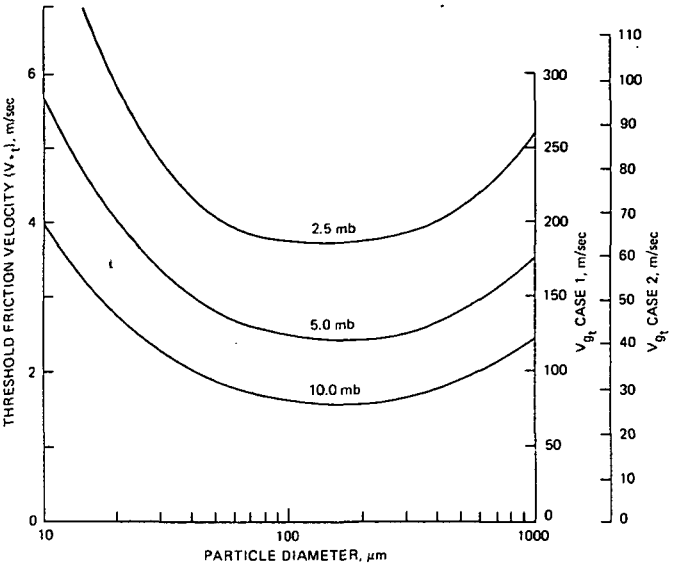

Martian particle threshold curves as a function of particle size at three pressures. Scale on left is V_{*t} in cm/sec, two scales on right are equivalent free stream (above the boundary layer) wind velocities (V_{gt}) based on atmospheric models by Pollack et al (1976); Case 1 is for winds blowing over a flat smooth surface composed of erodible grains, Case 2 is for a surface containing cobbles and small boulders.

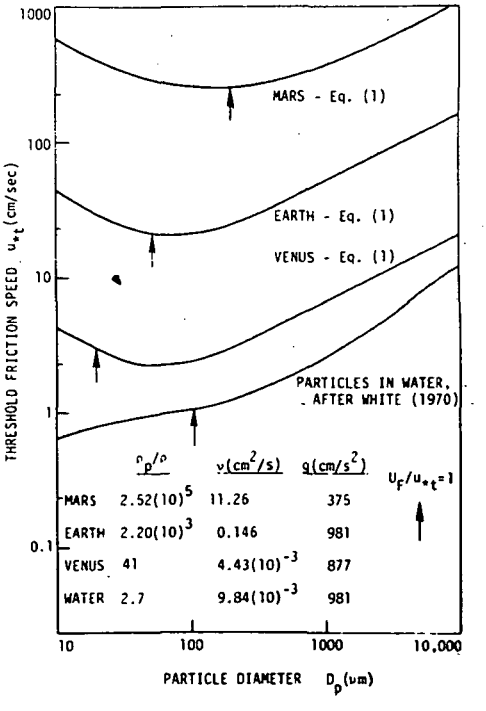

Comparison of threshold friction speed versus particle diameter for Earth, Mars, Venus and in liquid.

Geologic, Topographic, and Meteorologic Influences on Eolian Deposition, Earth and Mars. Alan D. Howard, Department of Environmental Sciences, University of Virginia, Charlottesville, Virginia 22903.

Wind movement of surface material results in sorting by grain size and density. Where rates of sand supply from upwind are low a desert pavement is created. If this pavement contains large roughness elements (such as at the Viking lander sites) large quantities of fine-grained sediment may remain between (and beneath) large boulders. In addition, much sand in transport may be trapped more or less permanently in wind shadows behind large boulders or outcrops. Sand which is too large to be carried in suspension yet is fine enough to be moved by prevailing winds is transported at a slow overall rate by intermittent saltation, and is often piled into bedforms. The saltation load is likely to be trapped in sheltered locations, often as dune fields. Fine material, transported in suspension, may travel on a global scale during individual wind storms. This component of the wind load probably accumulates in large depositional sinks, as discussed below, because once deposited it is difficult to reerode.

The accumulation of eolian deposits requires a sufficient decrease of transport capacity to cause saturation of the sandflow. Such decreases may be due to 1) convergence of flow, 2) downwind decrease in wind shear, or 3) a change in surface conditions. These influences act at scales from a few centimenters to planet-wide. On a synoptic scale deposition of large-scale sand bodies (ergs) occurs where transport rates are high and the resultants of transporting winds (surface winds weighted by direction and transport capacity) converge and/or where the magnitude of the resultants decreases downwind. In most circumstances ergs will grow only until an equilibrium between addition and removal of sand occurs. However, at convergent nodes accumulation will be continuous. On Earth, where surface supplies of sand are renewed by weathering and transport by runoff, ergs are found in most large deserts. On Mars ergs with associated dunal topography appear to be comparatively rare, considering the overall desertic landscape. This might be due to suppression of bedforms in the martian environment (except locally), but it is more likely due to a low availability of transportable material. Weathering by meteorite impact and chemical processes, and addition of fine-grained detritus from volcanic emanations have provided abundant material for wind transport, but most of this has had sufficient time to accumulate in nodal locations, such as (possibly) the polar caps, in sheltered basins where wind velocities are too low to reinitiate motion, or where post-depositional processes, such as formation of ground ice, introduce cohesion. Thus most of the planet is probably covered by an eolian deflation pavement. Occasional local strong winds create planet-wide dust storms and temporary deposition of fine-grained material carried in suspension. Major rearrangements of eolian deposits from the major sites of accumulation may result from changes in the magnitude or direction in transporting winds, or from a decrease in surface cohesion (sublimation of polar ice), that accompany climatic changes.

On a meso- to micro-scale the interaction of winds with topography create local zones of convergence or low shear encouraging deposition in a regime of unidirectional wind. Such deposits are exemplified in the coastal deserts of Peru, including 1) sand sheets, sometimes broken into transverse dunes, 2) ramparts on the windward edges of steep hills, 3) coppice dunes, wings, and tails of sand in the reconvergent wind shadow behind obstacles (lee dunes), and 4) longitudinal dunes on the top of wind-fluted escarpments facing the wind. Isolated dune fields are conspicuously absent. Ridge-top accumulations of sand cover the divides of spurs of the Andes, maintained by upslope thermal winds. With the exception of the latter, similar topograph-

ically-induced deposits occur on all scales from centimeter to kilometer. For example, lee dunes are prominant on Viking lander photos.

Where sand is moved by winds from more than one direction, deposits tend to occur in isolated patches, generally close to, but not abutting against the margins of topographic basins. Dune fields of the Mojave Desert and near the Viking lander sites appear to fall in this catagory, as do crater-floor dune fields. Factors controlling such deposition are topographic funneling and blocking of winds, and possibly the formation of standing (gravity) waves and lee waves in the atmosphere.

On Earth eolian landforms occur on a heirarchy of scales: ripples with a characteristic wavelength determined by the length of grain saltation (1 - 20 cms), dunes with a scale probably determined by the upwind roughness height (50 - 500 m), and draas (1 - 3 km) with a wavelength possibly determined by the depth of the convective boundary layer. Dunes and draas occur as longitudinal or transverse forms, or a mixture of the two. A controversy still exists whether longitudinal dunes are formed along the resultant of bi-directional winds or as a result of helical flow in a unidirectional wind. Scaling of these three forms to Mars is uncertain. Bedforms so far observed on Mars are of the same scale as terrestrial draas. Bedforms of dune size would be difficult to discern on most orbiter photographs. Strictly transverse bedforms are rare on Earth at either the dune or draas scale, because slip-faces are stable only if dunes lose a quantity of sand downwind equal to that gained from upwind. Thus barchanoid, or linguoid forms are common, which pass sand downwind in discrete streamers. The seemingly transverse dunes near the North Polar Cap of Mars are an enigma, and may form in a manner different from terrestrial dunes, for they appear to have very straight crests. They might possibly be more analogous to subaqueous antidunes, forming below a dense near-surface flow of air with standing waves on its upper contact with less dense air. Heavy suspended loads and cold drainage from polar caps could contribute to the density contrast between the surface layer and the upper air. Or, possibly, they may form at very high wind speeds where much sand is carried in suspension beyond the slip face, eliminating the necessity for streamer transport.

Deduction of directions of dominant sand-transporting winds from orientation of dune trends is risky, because oblique trends can result from unidirectional winds due to interaction between longitudinal and transverse elements. In addition, dunes of different grain size respond to different averages of surface winds, and large dunes have longer characteristic times of fomation than do smaller. Isolated barchans are the most diagnostic of wind directions, whereas longitudinal and network-pattern dunes are the most confusing.

High-density flows may have been important on Mars, particularly in the large channels. The buoyancy for such flows can be supplied by particle-to-particle collisions, electrostatic repulsion, or entrained liquid or gas, and the impelling momentum can result from slope failure, downslope gradients, or wind stress.

Experimental Modeling of Wind Erosion Forms. John F. McCauley, A. Wesley Ward, Carol S. Breed, Maurice J. Grolier, U.S. Geological Survey, Flagstaff, AZ 86001, and Ronald Greeley, NASA Ames Research Center, Moffett Field, CA 94035

Preliminary table-top experiments, utilizing a large fan and a variety of materials with low threshold velocities, have given good results on the evolution of different types of landscapes in a unidirectional wind regime. Air flow over the models was mostly turbulent and velocities ranged from 6 to 10 meters per second except in the lees of individual topographic obstacles. Velocities at different points on each model were monitored with a portable hot-wire anemometer. Extensive photographic documentation (including motion pictures) of the evolution of each model with time was acquired. The running times varied from a few hours to as much as six hours in order to obtain an approximation of dynamic equilibrium. The models, ranging from 0.3 to 0.5 meters on a side, were constructed of mixtures of commercial number 60 Ottawa sand, grits, yellow corn meal and used coffee-grounds. Each mixture was slightly moistened to permit molding of desired landforms and allowed to dry slowly. The result was a weakly cohesive, miniature topographic model wherein grains were released slowly into the wind flow, thus simulating the natural weathering process that takes place in various desert environments. Although there are obvious similitude and scaling problems in these experiments, each model was remarkably well-behaved and evolved in an orderly fashion. New insights thus have been obtained into landform development that results exclusively from wind action.

To date four types of models have been studied. The first consisted of a single gentle hill covered with a coarse, cohesive, wind-resistant crust. Under prolonged wind stress, this crust gradually broke up and numerous curvilinear shallow grooves developed in the less resistant substrate on the windward face of the hill. Most of the grain transport was concentrated in these grooves. Local undercutting of the crust produced small, metastable "mushroom rocks." Elsewhere patches of protective crust initiated development of small (2 to 4 cm) streamlined positive features (yardangs) between troughs. The overall pattern developed was surprisingly fluvial in appearance with many of the troughs or wind chutes curving and anastamosing in the upslope direction.

The second model was homogeneous (without a crust), and simulated a fluvial landscape. It consisted of a major "V"-shaped stream valley, oriented into the prevailing wind, and smaller, similarly-shaped, graded tributary valleys, oriented at 45° and 90° to the wind. A small, smoothly rounded hill about 8 cm high was present on one side of the model.

This model evolved very rapidly at first with the main stream channel acting as the major conduit for grain movement. Velocities at the upwind end of the main channel were 30 percent higher than the average air flow over the model. The profile of the main channel gradually changed with time to a broad "U"-shaped depression, and the channel lost its downwind carrying capacity.

The tributary valleys failed to maintain grade with the main channel and were left as hanging valleys early in the evolutionary sequence. These valleys changed profile rapidly, developing a near vertical cliff on the lee sides and a gentle erosional slope on the windward sides.

The top of the rounded hill was remarkably stable throughout the entire run and little grain movement could be observed over its surface. The sides of the hill, however, were steepened by deflation and a tail of coarse particles developed in the lee. Later in the run the main channel was

cut through to local base level (the board on which the model was mounted), blowout depressions developed by the hill, and the tributary valleys assumed the form of shallow elliptical depressions. At this point, representing about a 30 percent loss in volume, almost all traces of the ancestral fluvial landscape had been obliterated and the remaining positive landforms had developed airfoil shapes.

The third model was a simple three-layered block 40 by 30 by 5 centimeters, oriented with its long dimension at right angles to the wind. A weak layer about 2.5 centimeters thick, consisting of coffee-grounds, grits, and sand with a mean diameter of 1.25 mm overlaid a more competent unit of the same thickness, consisting of grits and sand with a mean diameter of 1 mm, which overlaid a highly competent unit 0.5 centimeters thick, consisting of very fine sand and corn meal.

This model, simulating a previously uneroded tectonic block, also evolved rapidly at first with its sides rounding off and the trailing edges narrowing by ablation. The back side of the model failed by slumping at regular intervals to form a series of steep-walled alcoves. The upwind face gradually retreated with progressive lowering of the slopes on each of the units present. Benching on the upwind edges of the model was pronounced and several broad erosional reentrants began to develop. Overhanging promontories formed on the upwind face and were destroyed episodically throughout the run. The top surface was remarkably stable and no topographic irregularities such as blow-outs, wind chutes or streamlined hills were observed. The run was terminated after the whole block had developed an airfoil shape with a curving upper surface, a broad gentle upwind face, and a depositional tail.

The fourth model consisted of three closely spaced, layered and inverted racing sloop hulls 30 cm long, 9 cm wide and 5 cm high, which simulated a mature yardang field like those of the Ica Valley in Peru. The objective was to observe the effects of variations in rock resistance and the flow dynamics over and around these forms of minimum resistance. Two of the hills, consisting of a weak layer over a more resistant one, were oriented with their bows in the upwind direction. The third, with a resistant layer over a weaker one was oriented stern first. The surface on which the hulls sat was weaker than the layers in each.

This model was slow to evolve because it initially approximated a condition of dynamic equilibrium. Grooving of the materials between the hulls, however, proceeded rather rapidly and "U"-shaped troughs developed. The bow-first, soft-over-hard forms did not change appreciably, except for a gain in relative height as the surrounding troughs were deflated. The bows and sterns of these features were, however, modified. The bows became steeper and locally undercut with breaks in slope at the boundaries between original layers. The final profiles of the fronts of these features were like those of bottlenosed dolphins. The sterns developed long tapering tails cut into the softer materials below the hulls. The longitudinal profiles of the backs of these hills did not change appreciably during the run although wind velocities over the tops of the hulls were 30 percent higher than at the bows because of the predictable convergence of flow lines in this region.

The stern-first, hard-over-soft hull was modified more than the others. It was undercut along its flanks and became markedly narrower and higher during the run. It developed a new long downward tapering bow and a long depositional tail. Late in the run, blow-outs developed in the weak surface material adjacent to the bow of the hull closest to the fan, as a result of wind vortices that completely scoured away the surface.

Grain movement in all of the models tested to date was by traction, saltation and suspension with almost all of the motion concentrated in the topographic lows. Individual grains are episodically plucked from the matrix in which they rest to produce a fragile scoured surface in which grains temporarily stand out in relief in the wind stream. Abrasion is not an important process in the evolution of these models although it could theoretically contribute to lowering of the troughs between individual topographic highs. Deflation, or the simple carrying away of grains, is the main mechanism by which wind erosion proceeds. These tests provide verification of earlier speculations, based on field evidence, that the yardangs in the core regions of the major deserts of the world are indeed deflational features (1).

(1) J.F. McCauley, M.J. Grolier, and C.S. Breed, U.S. Geol. Survey Astrogeology Interagency Report 81 (in press).

Comparative Analysis of Fluvial Versus Aeolian Sources for Wind Deposits

Augustus S Cotera & Camilla K. McCauley, Department of Geology, Box 6030, Northern Arizona University, Flagstaff, Arizona 86011

In attempting to define those grain size parameters which discriminate between the source of sediments forming wind deposits, detailed sampling and size analysis has been done and is continuing in the Paiute Point dune field southeast of Cameron, Arizona. Climbing dunes on the west facing slope of the Ward terrace as well as the dune field on top of the terrace have been extensively sampled and grain size distributions calculated. This terrace is an area of unquestionable wind deposition with no fluvial interaction and is thus an ideal site for sampling sand sources restricted to wind systems alone. For comparison, dune fields adjacent to intermittant streams e.g., Cameron dune field, have supplied data for mixed fluvial and aeolian sources of sand.

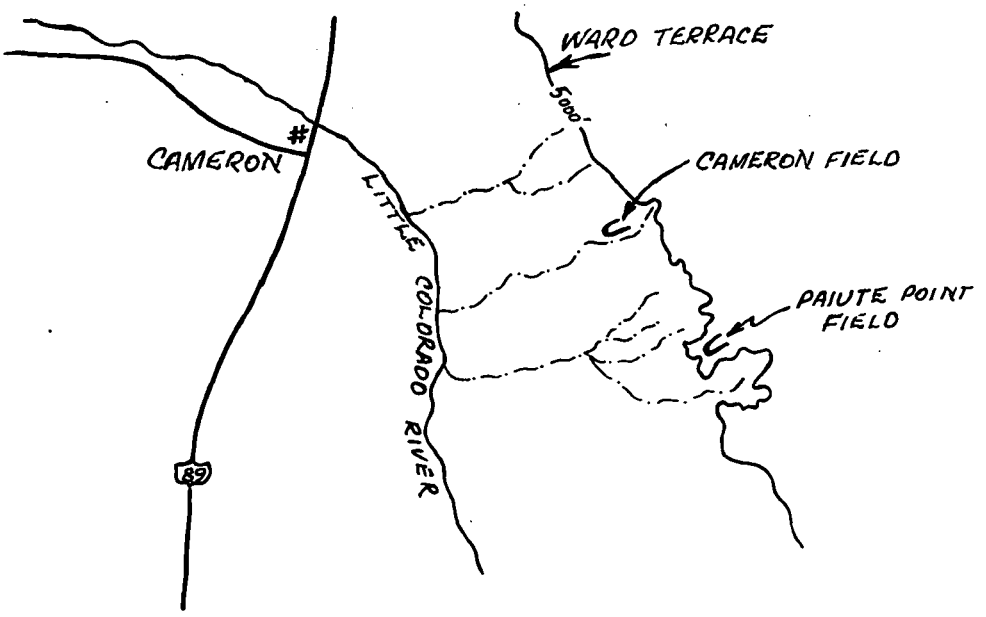

Data for the dune fields in these two environments are given below:

	Cameron Field (Fluvial) (Total # of samples: 20)	Paiute Point Field (Aeolian) (Total # of samples: 27)
Mean Size	2.25	2.34
Sorting	0.74	0.65
Skewness	0.10	0.08
Kurtosis	0.93	1.07

The preceding data was obtained using 8" ASTM seives and calculating the size distributions to estimate the above four parameters, using a combined Method of Moments-Folk & Ward statistic computation. As previously reported in a pilot study, the fourth moment, Kurtosis, appears to be the most reliable parameter for distinguishing between fluvial and aeolian sources of dune sands. Although the average mean size, sorting, and skewness of the distributions does not differ significantly, Kurtosis values are consistently different. The range in individual Kurtosis values for fluvial source samples is from 0.75 to 1.04 with a mean of 0.93, whereas those samples from strictly aeolian sources range from 1.00 to 1.16 with a mean of 1.07.

The ongoing project involves investigation of the dune form and the method of dune emplacement and movement in the existing wind regime. To this end, three instruments are presently in use to develop a long-term wind regime profile. One instrument is a master station recording wind velocity and direction, temperature, humidity, and rainfall. The other two instruments measure wind velocity and direction only but are quite portable enabling a variable horizontal and vertical (up to 35') array of measurements. The future plan of data collection includes monthly small-craft flights over the dune field to obtain precise aerial photographic analysis of changing dune forms and position. In addition, ground photography is also being obtained. Despite several initial problems in wind instrument calibration and data continuity, wind data is now being obtained on a regular basis and will constitute a major input into the project, which will be included in the final report for this study.

On the Nature and Visibility of Crater-associated Streaks on Mars. J. Veverka, P. Thomas, C. Sagan, Laboratory for Planetary Studies, Cornell University, Ithaca, NY 14853

Kuzmin (1975; Russian A.J. Letters, 1, 42) has proposed that all crater-associated wind streaks on Mars are depositional and consist of "unresolved barchan-like dunes." He claims that any streak can appear either light or dark depending on the azimuth of the Sun relative to the streak axis and on the elevation of the Sun above the horizon. Specific claims made by Kuzmin (based on a study of 169 streaks visible in Mariner 9 images) include:
a) streaks appear dark if the Sun's azimuth is less than 90°, and light if the azimuth exceeds 90°.
b) streaks can appear dark for Sun elevations of 15° to 45° (incidence angle i = 75° to 45°), but they can appear bright over a larger range of Sun elevations: 20° to 59° (i = 70° to 31°).

Our study of the entire Mariner 9 picture collection, including over 700 frames showing streaks, lends no support to these statements. In particular we find no merit to the suggestion that a streak can appear either light or dark depending on the illumination geometry. Our data on streak visibility do not support this claim, and there is much evidence that bright and dark streaks differ in both morphology and in character. Most dark streaks are probably erosional, while most bright streaks probably represent accumulations of wind-transportable material. There is no evidence at present that such accumulations have a barchan-like texture.

We find that the visibility conditions for light and dark streaks are identical in M9 images. Both types of streaks are visible for viewing angles $\varepsilon \lesssim 60°$ and illumination angles of $15° \lesssim i \lesssim 75°$. Both types of streaks are visible over the whole range of phase angles covered by Mariner 9 about 15° to 85°). There are numerous examples of dark and light streaks visible at the same solar azimuth, contrary to Kuzmin's claim.

A Statistical Study of Ragged Dark Streaks in the Southern Hemisphere of Mars.

J. Veverka, J. Goguen and K. Cook. Laboratory for Planetary Studies, Cornell University, Ithaca, NY 14853

We have completed a study of dark crater associated wind streaks in the southern hemisphere of Mars, characterized by their ragged, fan-shaped outline and by their rapid variability. A total of 627 such streaks were identified on Mariner 9 A-frames. All lie within a narrow latitude belt: 30 ± 10°S in five isolated areas centered at: (60°W, Mare Erythraeum), (125°W, Daedelia), (220°W, Hesperia), (255°W, Mare Tyrrhenum), and (335°W, Pandorae Fretum). Most of these streaks appeared within an interval of 40 days (between 7 Jan. and 16 Feb. 1972) following the end of the 1971 duststorm, and are most likely erosion scars (Veverka (1975) Icarus, 25, 595). All define a single wind direction: East to West. The average streak area is 1.5×10^2 km^2; the total area of streaks is 9.3×10^4 km^2. Assuming an optically thick layer of duststorm fallout ($\sim$ 1 mm), the formation of the streaks represents the erosion of $\sim 2 \times 10^{14}$ gm of surface material within 40 days or less.

About 25% of all craters in the five areas developed such streaks, the streaks being preferentially associated with craters smaller than 10 km. These southern streaks are morphologically different from the streaks (both light and dark) in the north-equatorial zone of Mars studied by Veverka et al. (1977, Icarus, in press). Examples of the many differences are: (1) the southern streaks show a preferred L/D ratio of about 11 (where L = streak length; D = crater diameter), whereas for the northern streaks the preferred L/D ratio is < 5. (2) The southern dark streaks show a strong tendency to become very wide as L increases, a trend opposite to that displayed by northern streaks. (3) For the southern streaks, there is a strong correlation between crater diameter and streak width: the mean angular width increases approximately linearly with crater diameter up to diameters of 30 km and then drops sharply. For northern hemisphere streaks the angular width was found to be essentially independent of crater diameter.

Many of these differences probably arise because the southern streaks are erosional in character, while the light streaks in the northern survey probably represent accumulations of wind transportable material. It is noteworthy, however, that the characteristics of the southern hemisphere dark streaks studied here also differ from those of dark streaks in the north, possibly indicating a difference in origin.

Viking results are becoming available for several of the areas. In Hesperia the dark streaks appear modified in outline, but unchanged in direction since 1972. In Mare Erythraeum no dark streaks are visible in the Viking coverage, while in Daedelia the dark streaks are present but are changed in outline and in direction (now pointing NE to SW). The high-resolution Viking imagery shows that these streaks are preferentially associated with craters which are surrounded by topographically prominent and rugged ejecta blankets. The images also suggest that the very wide, fan-shaped streaks are built up by successive erosive episodes, each of which contributes a small sector of the final "wind-rose" pattern.

Crater Streaks in the Chryse Planitia Region of Mars: Early Viking Results, Ronald Greeley and Ronald Papson, University of Santa Clara at NASA-Ames Research Center, M/S 245-5, Moffett Field, CA 94035; Joseph Veverka, Laboratory for Planetary Studies, Cornell University, Ithaca, NY 14850.

High resolution images from the early revolutions of Viking Orbiter 1 permit detailed analyses of crater-associated streaks and the interpretation of related aeolian processes. A total of 614 light and dark streaks were studied and treated statistically in relation to: 1) morphology, morphometry, and orientation, 2) "parent" crater size and morphology, 3) terrain type in which they occurred, 4) topographic elevation, and 5) meteorological data currently being acquired by Viking Lander 1. Table 1 shows the distribution by number and percentage of light and dark streaks, their morphology, and their relation to crater morphology. Three factors are apparent: 1) light streaks predominate, 2) most streaks form in association with fresh bowl-shaped craters, and 3) most light streaks are of the "parallel" type, whereas dark streaks are approximately evenly divided between convergent and parallel forms; moreover, very few light or dark streaks are divergent or fan-shaped.

Light streaks have an average azimuth of 218^{o} (corresponding to winds from the northeast), which is nearly the same as the orientation of aeolian "drifts" observed by the Viking Lander imaging team (Mutch et al., 1976) to be $197^{o} \pm 14^{o}$ which lends support to the hypothesis that light streaks are deposits of wind-blown sediment. Dark streaks are oriented at about 42^{o} (nearly in the opposite direction as light streaks), which is nearly the same as the dominant wind direction currently recorded by the Viking meterology instruments (Hess et al., 1976).

Although the size of the sample areas is not uniform among the various terrain types, the high frequency of streaks per unit area is knobby terrain in Chryse Planitia. This is partly explained by the probable production of fine-grained material (weathered from the knobs) to form streaks and other aeolian features, and the higher wind turbulence generated around the knobs. The lowest frequency of streaks is on the elevated plateaus.

The light streaks in Chryse Planitia appear to be relatively stable and to result from deposition of wind-blown material during times of relatively high velocity northeastern winds. Dark streaks are more variable and probably result from erosion by southwesterly winds. Both types will be monitored during the extended Viking mission and the results compared with Lander data.

		LIGHT TONE			DARK TONE	
		Number	Percent		Number	Percent
Fresh, Bowl-Shaped Type I	Co:	80	21.2%	Co:	71	45.8%
	Di:	12	3.2%	Di:	20	12.9%
	P :	284	75.5%	P :	64	41.3%
	Totals	376	99.9%	Totals	155	100.0%
Moderately Degraded Type II	Co:	13	20.0%	Co:	6	33.3%
	Di:	0	0.0%	Di:	3	16.7%
	P :	52	80.0%	P :	9	50.0%
	Totals	65	100.0%	Totals	18	100.0%

Co = convergent; Di = Divergent; P = parallel.

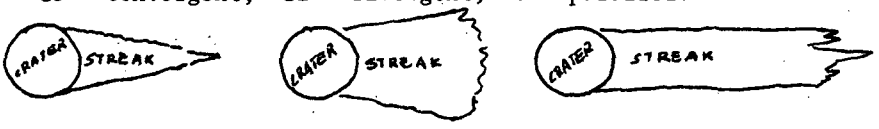

TABLE 1. Distribution of light and dark streaks as a function of parent crater morphology.

Page Intentionally Left Blank

Chapter 8

FLUVIAL AND MASS WASTING PROCESSES

Page Intentionally Left Blank

Evaporation of Ice-Choked Rivers: Application to Martian Channels,
David Wallace and Carl Sagan, Laboratory for Planetary Studies,
Cornell University, Ithaca, NY., 14853

The evaporation rate of water and ice under present Martian conditions has been calculated, and is sufficiently low that at least some Martian channels may have been formed by flowing water even with an atmospheric pressure as low as the present value. While liquid water does evaporate quite rapidly, the evaporative cooling causes a layer of ice to form on top of the water and greatly reduce further evaporation. Under Martian conditions, the ice layer will reach a thickness of about one meter, and the evaporation rate will be reduced to approximately 10^{-6}gm/cm^2 sec. Thus, even a quite modest water discharge can flow for hundreds of kilometers, if it is shielded by an ice layer.

The evaporation calculation involves an equilibrium between solar heating, and radiative and evaporative cooling of the ice layer. The thickness of the ice is governed principally by the amount of sunlight which penetrates the ice layer and then is conducted back to the surface. These calculations differ from those of Lingenfelter et al. (1968) for putative lunar channels in including the effect of the Martian atmosphere. Evaporation from the surface is governed by two physical phenomena: wind and free convection. In the former case, water vapor diffuses from the surface of the ice through a laminar boundary layer, and then is carried away by eddy diffusion above, caused by the wind. The latter case, in the absence of wind, is similar, except that the eddy diffusion is caused by the water vapor being less dense than the Martian atmosphere.

The laminae observed in the polar caps of Mars may also be related to the phenomenon of ice-covered rivers. Ice is a sufficiently poor conductor of heat that sunlight which penetrates it can cause melting to a depth of several meters or more. Because the obliquity of Mars can vary up to about 35°, the increased polar heating at such times could cause subsurface melting of the polar caps, and may possibly lead to the observed laminae.

Entrainment of Sediment by Fluid Flow on Mars. Dag Nummedal, Dept. of Geology, University of South Carolina, Columbia, SC, 29208

INTRODUCTION

Images returned to Earth from Mariner 9 and Viking 1 and 2 demonstrate the existence of large channels commonly held to be of fluvial origin. Streamlined erosional remnants, obstacle scours, and channel bed grooves provide additional evidence for past catastrophic flooding on Mars (Carr, et al., 1976).

With extensive orbital imagery already on hand, photogeology will be a major tool in reconstructing Mars' geologic history. We should, therefore, develop methods which permit quantification of the processes responsible for the observed morphology. Discharge estimates of Mars floods, for example, might provide constraints for planetary outgassing models (Levine, 1976).

While stopping short of hydraulic calculations on specific Mars channels, this paper discusses the applications of two basic relationships, the uniform flow equation and the Shields sediment entrainment function, in an environment with a different acceleration of gravity.

UNIFORM FLOW

Uniform flow in a channel is characterized by a balance between the downhill component of gravity (F_g) and bed resistance (F_r):

$$F_g = \rho gALS = F_r = kV^2PL \qquad (1)$$

where A, L, P and S are the cross-sectional area, length, wetted perimeter and surface slope, respectively, of the channel segment, ρ is the density of water, g is the acceleration of gravity and k is the drag coefficient. Equation (1) yields the Chezy formula:

$$V = C\sqrt{RS} \qquad (2)$$

where $R = A/P$ and $C = \sqrt{\rho g/k}$. The Chezy coefficient (C) is empirically determined when this equation is used in terrestrial channel design. The better-known Manning formula is fundamentally the same, but uses a slightly different power relationship in the hydraulic radius, R. Both the Chezy and Manning equations imply that current velocity depends on the acceleration of gravity. although g is not explicitly mentioned in either formula. With an acceleration of gravity of 3.8 m/s^2 on Mars one finds from eq. (2) that a Martian stream will have a velocity of 0.62 times that of its terrestrial counterpart, i.e. a stream with the same hydraulic radius and slope. Therefore, the slope-area method, the use of compound cross-sections, and other methods developed for flood calculations on Earth (Chow, 1959) can be used on Mars by multiplying empirically determined terrestrial Manning coefficients by 1.60 or Chezy coefficients by 0.62.

SEDIMENT ENTRAINMENT

The energy required to move a sediment particle on a stream bed (W_c) can be expressed as the submerged particle weight times a characteristic distance, e.g. the grain diameter (d):

$$W_c \propto (\rho_s - \rho)gd^3d \qquad (3)$$

where ρ_s is sediment grain density.

Turbulent boundary layer theory states that local mean velocities over a hydrodynamically rough wall are proportional to the shear velocity (Schlichting, 1968). Therefore, energy supplied to a particle of size d, by the turbulent flow, can be expressed as:

$$W_s \propto \rho d^3 u_*^2 \qquad (4)$$

where the shear velocity is expresses by the relation

$$u_* = \sqrt{\tau/\rho} \qquad (5)$$

where τ is the bed shear stress.

Sediment movement requires that the ratio between W_s and W_c equals or exceeds a certain critical value:

$$\frac{W_s}{W_c} \propto \frac{\rho d^3 u_*^2}{(\rho_s-\rho)gd^4} = \frac{\tau}{(\rho_s-\rho)gd} = \text{const.} \qquad (6)$$

For small sediment particles, e.g. sand and silt, the grains do not necessarily penetrate the laminar sublayer. In this case, sediment movement is more due to viscous flow than turbulent action, and the ratio between W_s and W_c is no longer constant but becomes a function of the shear Reynolds number, i.e.:

$$\frac{\tau}{(\rho_s-\rho)gd} = f\left(\frac{du_*}{\nu}\right) \qquad (7)$$

where ν refers to the kinematic viscosity of water. Equation (7) has been tested, and the functional relationship well established, by laboratory flume experiments, first by Shields and subsequently by numerous other workers.

Both parameter groupings in eq. (7) are dimensionless and can be rearranged to give new dimensionless groupings separating d and τ. This modified Shields' relation will read:

$$\tau\left\{\frac{1}{\nu^2 g^2 \rho(\rho_s-\rho)^2}\right\}^{\frac{1}{3}} = f\left\{d\left[\left(\frac{\rho_s}{\rho}-1\right)\frac{g}{\nu^2}\right]^{\frac{1}{3}}\right\} \qquad (8)$$

Equation (8) permits the construction of explicit curves relating the shear stress necessary for initiation of motion, τ, to the particle size, d, for any fluid at any temperature (controlled by ρ and ν) and any rock type (controlled by ρ_s). The dimensionless ratios properly account for variations in g and apply, therefore, to Mars as well as Earth.

Figure 1 illustrates the τ vs. d relation for two minerals of different densities on Earth, and demonstrates also the effect of variations in water temperature. Since temperature only affects the viscosity, only those particles embedded in the viscous sublayer have a temperature-dependent entrainment function. Figure 2 shows the effect on sediment entrainment by reducing gravity from 9.81 m/s^2 to 3.83 m/s^2. For the size range illustrated the temperature effects are negligible. Particles ranging in size from 1 cm to 10 meters will be moved on Mars by a shear stress only 25 per cent of that required to initiate movement on Earth.

CONCLUSIONS

This evaluation of basic hydraulic relationships has demonstrated the following:

(1) Uniform open-channel flow on Mars will have a mean velocity of 0.62 times that of a terrestrial flow for the same slope and hydraulic radius.

(2) The reduced acceleration of gravity on Mars will facilitate sediment entrainment. Gravel and boulders on Mars will be moved by a shear stress only 25 per cent as high as that which is required to initiate movement on Earth.

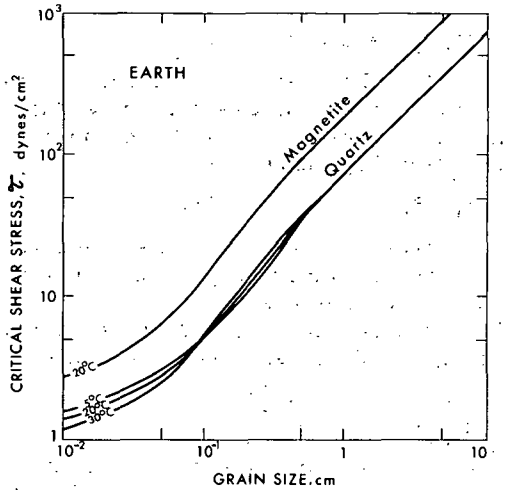

Figure 1

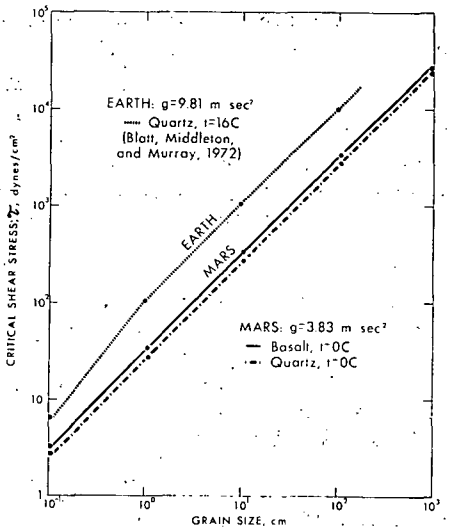

Figure 2

REFERENCES

Carr, M. H., et al., 1976, Preliminary results from the Viking Orbiter imaging experiment, Science, v. 193, p. 766-776.

Chow, V. T., 1959, Open-channel hydraulics, McGraw-Hill Co., New York, 680 p.

Levine, J. S., 1976, The evolution of water on Mars; in Proceedings of the colloquium on "Water in Planetary Regoliths", Hanover, N. H., 5-7 Oct. 1976. U. S. Army Cold Regions Research and Engineering Laboratory.

Schlichting, H., 1968, Boundary-layer theory, McGraw-Hill Co., New York, 747 p.

Martian Channels - Classification by morphology and time of formation, Harold Masursky, J. M. Boyce, A. L. Dial, G. G. Schaber and M. E. Strobell, U.S. Geological Survey, Branch of Astrogeologic Studies, 2255 North Gemini Drive, Flagstaff, Arizona 86001.

The acquistion of recent Viking photographs has allowed us to re-examine the channels originally discovered in Mariner 9 pictures. Fluviatile channels can be grouped as follows: broad, mega-channels that originate in areas of chaotic terrain, e.g. Ares, Simid, and Tiu Valles; large channel arrays, e.g. Maja and Vedra Valles that also originate in collapsed terrain; sinuous channels, intermediate in size, with many tributaries, e.g. Mangala and Ma'adim Valles; short stubby channels with box canyon heads, e.g., Al Quahira Vallis and other unnamed channels along the northern continental border and along Valles Marineris; and channel networks, e.g., Samara, Ladon and many unnamed valles. Lava channels that occur on Elysium Mons become narrow and shallow down stream, like lunar sinuous rilles. Other lava channels that occur on the west side of Alba Patera flow along the crests of ridges and branch downward, acting as basaltic lava distributaries.

The broad channels originate where water flowed out from masses of collapsed terrain that occur within the southern highlands plateau. They record great floods of melt water that emerged from behind melting ice dams. The spacing of the areas of collapsed terrain resembles the spacing of volcanic features in other volcanic centers on the plateau. These relations may indicate that melting of permafrost ice took place over volcanic vents that never reached the surface. Melting occurred spherically outward until a plateau edge was reached; the ice dams were then breached, releasing the impounded water.

The short stubby channels record subsurface water flow and spring sapping along the continental or canyon margins. These channels are part of the "fretting" process that degrades the highland margin. Channels with dendritic networks and multiple tributaries originate at crater rims or within plains units. These must have formed when rainfall fell and collected; they resemble typical terrestrial streams. There is no sign of thermokarst collapse in their headwater areas.

The Ares channel in southern Chryse Planitia is 150 km wide and more than 100 m deep; its gradient is 10 m/km. The quantity of flow in this channel must have reached great flood proportions.

A "degradation index" calculated for channels observed in Mariner 9 photographs was obtained by plotting the differing degrees of degradation of channel margins. Variations in degradation index indicated widely differing ages for the channels studied. However, varying resistance of surface materials to erosional processes may bias the results obtained by this technique.

Standard crater counts have been made from Viking photographs of several channel systems. Crater density determinations of Martian channels vary from a factor of 5 lower to a factor of five higher than density determinations obtained for average lunar mare areas. When the channel crater density determinations are compared to the lunar flux curve derived by Soderblom and others (1973), the ages of formation of the Martian channels also seem to vary widely. Results obtained from these crater counts indicate that several episodes of volcanic heating and climatic warming may have occurred. It is not yet clear whether the episodes of climatic warming coincided with episodes of intense volcanic activity. However, if relative dates can be obtained for the small channels formed by permafrost collapse or spring sapping, and match them to the other channel types, we may be able to correlate episodes of local volcanic heating with periods of planetwide warming.

Characterization of Erosional Forms on Mars by Fourier Analysis in Closed Form. P. Jeffrey Brown, Dag Nummedal, Duane T. Eppler, and Robert Ehrlich, Department of Geology, University of South Carolina, Columbia, S.C., 29208

There has been a great deal of speculation regarding the mode of origin of channel-like features on the Martian surface. One of the most striking aspects of these channel-like features is the presence of numerous well-developed erosional remnants on the channel floors. In a purely qualitative sense, Martian features are not dissimilar to terrestrial features formed by both large and small scale fluvial erosion processes. Fourier analysis in closed form has been used to make detailed quantitative comparisons between the planimetric shapes of Martian remnants in the Mangala, Kasai, and Chryse channels, terrestrial erosional remnants in the Washington scablands, and braided stream bars in Iceland.

The planimetric shape of the Martian features was traced from Mariner 9 imagery, scabland shapes were obtained using topographic maps, and Icelandic bars were traced from low-altitude vertical aerial photographs. The outline of each feature was digitized and the measured points on the periphery were used to express their shape by a Fourier series in polar coordinates of the following form:

$$R(\theta) = R_o + \sum_{n=1}^{10} R_n \cos (n\theta - \phi_n)$$

where $R(\theta)$ is the radius from the center of gravity of a shape to a point on the periphery in direction θ, and R_n is the amplitude and ϕ_n is the phase angle of the n^{th} harmonic.

Although the total number of shapes analyzed in this preliminary study was relatively small (194), three tentative conclusions can be drawn (Table 1):

1. The gross shape of Icelandic features differs markedly from that of other features at the second, third, fourth, and sixth harmonics.
2. Both Martian and loess scabland features differ from basalt scabland features in a statistically significant fashion at the second harmonic.
3. Martian features are similar to loess scabland features--none of the first ten harmonics vary significantly between the two populations at the 0.05 level.

Both basalt and loess scabland features are the product of strictly erosional processes. In contrast, Icelandic forms are the result of fluvial processes of both an erosional and depositional nature. Shape differences between Icelandic features and all other features therefore may imply that Martian remnants formed by purely erosional processes.

Examination of shape frequency histograms for the second harmonic shows that the basaltic erosional remnant population contains relatively large numbers of equant features, that is, shapes with large low amplitude values (Figure 1). In contrast, Martian features and loess scabland features have amplitude values that are uniformly distributed over the full range of the histogram and contain relatively few equant shapes. These differences are thought to be the result of structural control imposed upon the basaltic landforms by underlying joint patterns. Turbulent flow at high angles to the joints in rocks such as the scabland basalt will produce equidimensional forms. Flow at angles more nearly parallel to joint sets will produce a full range of features displaying varying degrees of elongatedness.

At present, the prevalent and most widely accepted theory for the for-

mation of the Martian features is that they were formed by catastrophic floods similar to but of a larger scale than the Lake Missoula flood which formed the Washington scablands 20,000 years ago (1). The results of this study corroborate this theory. Differences in gross shape between loess and basalt scabland features (which were formed by the same series of catastrophic events) result from structural control placed upon the basalt remnants by the fracture patterns in the basalt. The similarity of shape between loess and Martian forms could imply lack of structural control on the Martian surface. However Viking imagery indicates that large scale structural trends do exist on Mars. This suggests that the events that formed the Martian channels were of sufficient magnitude and force to overcome any control imposed by the structure and/or control of the Martian surface.

References

1. Baker, V. R., and Milton, D. J., Icarus 23, 27-41.

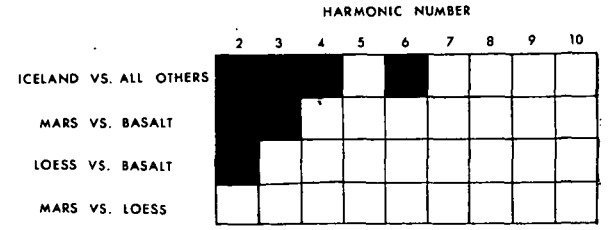

TABLE 1. CHI SQUARE RESULTS. SHADED SQUARES MARK HARMONICS WHERE SIGNIFICANT DIFFERENCES (AT THE 0.05 LEVEL) OCCUR.

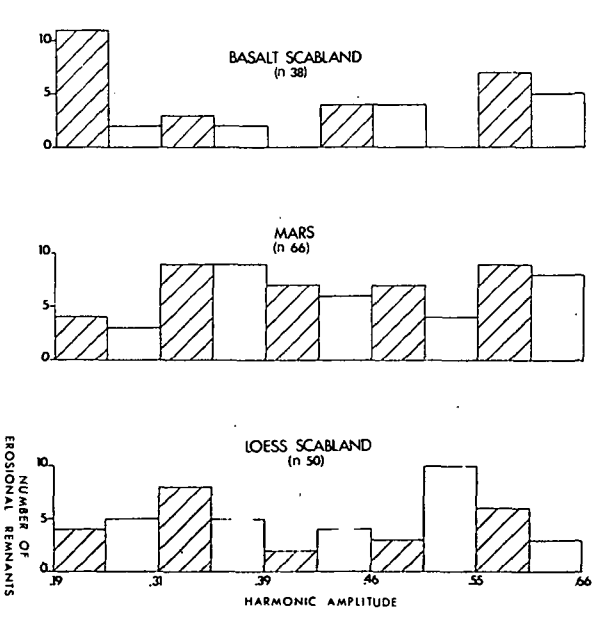

FIGURE 1. HISTOGRAMS OF HARMONIC AMPLITUDE FOR THE SECOND HARMONIC--A MEASURE OF ELONGATEDNESS OF A FORM.

Preliminary Statistical Analysis of Some Martian Channel Networks. D. Pieri, Laboratory for Planetary Studies, Cornell University, Ithaca, NY., 14853

Martian channel networks on the basis of Mariner 9 data were shown(1) to be distributed globally, and to be ubiquitous to the old cratered terrain, perhaps showing a concentration in areal distribution in dark equatorial and subequatorial regions. Detailed global maps of small channel networks based on Mariner 9 data were compiled in addition to which channel maps based on Viking Orbiter data, as they become available, are also being compiled and analyzed. Various parameters are being measured: bifurcation ratio (R6), number and lengths of exterior and interior links (N_e, l_e; N_i, l_i), junction angles (E), gradients (s), and as an analog to terrestrial basins, the area enclosed by the locus of points connecting the ends of first order tributaries (A). It is thought that while the traditional hydraulic parameters may be appropriate to the analysis of the larger channels, where apparently large scale bedforms exist, planimetric network parameters and topologic analysis in the style of Shreve (2,3), Smart (4), and others are more appropriate to channel (valley) networks where channel bed morphology is at present unresolvable. It is hoped that the statistics of these parameters coupled with morphological observations will ultimately allow delineation among the various proposed channel process models. Analogous measurements are being made from ERTS and LANDSAT imaging and are compared to martian channel statistics and published terrestrial values compiled from non-orbital data in order to calibrate the technique.

Preliminary results show the following: 1) Comparable Mariner 9 and Viking Orbiter data have the following relationship, $W_a \geq W_b+1$, where W_a= the highest Strahler network order visible on Viking Orbiter images and W_b= the highest Strahler order visible on Mariner 9 images; 2) $R_{b(1,2)}$ (i.e., R_b between Strahler order 1 and 2 links) is between 5 and 8 for 4th order martian channel systems studied so far, as compared to an average value of between 3 to 5 for most terrestrial river systems. This is indicative of very immature drainage systems (5), if the fluvial process model is correct, although terrestrial/martian scale descrepancies in this context are severe (Qualitatively, one can also infer immaturity by looking at the pictures). Specifically, observation 2 is consistent with a relatively short period of fluvial valley cutting.

(1) Pieri, D., 1976, Distribution of Small Channels on the Martian Surface, Icarus, 27,1, pp. 1-25.

(2) Shreve, R. L., 1966, Statistical Law of Stream Numbers, Jour. Geology, 74, pp. 17-37.

(3) ------, 1967, Infinite topologically random channel networks, Jour. Geology, 77, pp. 397-414.

(4) ------, 1977, personal communication.

(5) Smart, J. S., 1972, Channel networks, Advances in Hydroscience, 8, pp. 305-346.

Viking - Slashing at the Martian Scabland Problem

Victor R. Baker, Department of Geological Sciences, The University of Texas, Austin, Texas 78712

Viking I site selection imagery (1) confirms pre-Viking speculation that the southern Chryse Planitia consists of the expanding reaches of several great outflow channels carved by intense fluvial action (2, 3, 4). Landforms in the vicinity of the proposed A1 landing site (Fig. 1) are clearly analogous to erosional features (Channeled Scabland) created by the passage of late Pleistocene Missoula flood flows across the Columbia Plateau in eastern Washington (5, 6). Most spectacular are the streamlined uplands, termed teardrop-shaped "islands" by some investigators, which are developed downstream from large craters that served as flow obstructions. As with many residual loess hills in the Cheney Palouse scabland of eastern Washington, some of the isolated Chryse plateau remnants are flanked by lineations (erosional grooves?) that conform to the presumed paleoflow streamlines. Terraced margins on the streamlined uplands and irregular depressions occuring in angular patches on the channel floors are analogous to forms produced by differential plucking erosion of the Yakima Basalt in the deep, high-velocity Missoula flood flows. Irregular butte-and-basin scabland often exhibits structural control by faults and joints exactly as occurs on the stripped channel floors in the Chryse region (18.6°N. Lat., 34.8°W. Long.).

Channeling just west of the Viking I landing site (western Chryse Planitia) is analogous to the pattern of Missoula flood erosion on the western Columbia Plateau. Broad ridges transverse to the flood flows in both situations apparently ponded the water on their upstream flanks. Water streaming over low points on these divides scoured deep channels through the downstream flanks of the ridges. Lineations paralleling the presumed flood flow lines abound on the Viking imagery of the western Chryse Planitia. These are probably similar to the longitudinal grooves that locally cover scoured basalt surfaces in the Channeled Scabland. The grooves may form as a result of scour by powerful roller vortices that develop at the base of the flow with their filaments parallel to the flow direction. Craters, sinuous ridges, and polygonal fractures intersect the martian longitudinal grooves implying a considerable time span since channel formation.

The preliminary Viking imagery of the various channels debouching into the Chryse Planitia revealed little morphological evidence of flood deposition. This is also the case on a regional scale for the Cheney-Palouse scabland. There coarse gravel accumulations occur only behind flow obstructions. Even where gravel fills structurally-controlled sedimentary basins, as in the western Channeled Scabland, it was scoured to streamlined or diamond-shaped forms. Morphologically similar diamond-shaped, scoured materials occur in the so-called "braided" reach of Mangala Vallis and near the source locations for the channels entering the southern Chryse Planitia (Fig. 2).

The high-resolution Viking photographs clearly show numerous large crater forms on the eroded floors of some outflow channels. Published crater size frequency distributions appear to confirm suggestions that the channeling is very old, perhaps 10^9 years or older (7). Nevertheless, crater counts in scoured channels will have to be interpreted cautiously. Some crater forms in channels may be exhumed impact-lithified rock that was differentially resistant to flood scour. Circular forms in the Yakima Basalt (dikes surrounding sag flowouts and/or phreatic domes and vents) were preferentially preserved during deep scour by Missoula flooding on the Columbia Plateau of eastern Washington. Flood erosion of martian cratered terrain appears to have been a highly selective process. Viking imagery between

Chryse Planitia and Lunae Planum (17°N. Lat., 55°W. Long.) shows selective erosion of rims on the largest craters. Smaller craters are preserved on residual uplands. Post-channel impact craters are superimposed on some channels. Water pouring over the irregular cratered martian surface, as on the Columbia plateau, was flowing on a sloping surface ungraded by previous fluvial activity. Incision occurred along zones of relative weakness concentrating the water and thereby decreasing flow resistance.

The case for water as the erosive agent in channel formation has been immensely strengthed by the discovery that the residual summer north polar cap is predominantly water ice (8). The association of channel heads with chaotic terrain (Fig. 2) is most consistent with lithospheric water sources, perhaps as permafrost or clathrate in the regolith. However, a volume problem remains. How could the relatively small source areas (chaotic terrain) have contributed the amounts of water required to generate the observed scabland erosion? A working hypothesis is that the channels extended headward by progressive transformation of cratered terrain underlain by water-saturated, fractured rock into chaotic terrain. With continued headward extension, the downstream zones of chaotic terrain were scoured by the most recent flooding. This hypothesis is implied by the remarkable oblique Viking views of the western tributary to Hydraotes Chaos (Fig. 2).

(1) M. H. Carr et at., Science 193, 766 (1976).
(2) V. R. Baker, D. J. Milton, Icarus 23, 4037 (1974).
(3) R. P. Sharp, M. C. Malin, Geol.Soc. Amer. Bull. 86, 593 (1975).
(4) V. R. Baker, P. C. Patton, Geol. Soc. Amer. Abst. Prog. 8, 351 (1976).
(5) V. R. Baker, Geol. Soc. Amer. Spec. Pap. 144 (1973).
(6) V. R. Baker, in Fluvial Geomorphology, M. Morisawa, Ed. (State Univ. N.Y. Publ. in Geomorphology, Binghamton, N. Y., 1973), p. 123-148.
(7) M. C. Malin, J. Geophys. Res. 81, 4825 (1976).
(8) C. B. Farmer, D. W. Davies, D. D. LaPorte, Science 194, 1339 (1976).

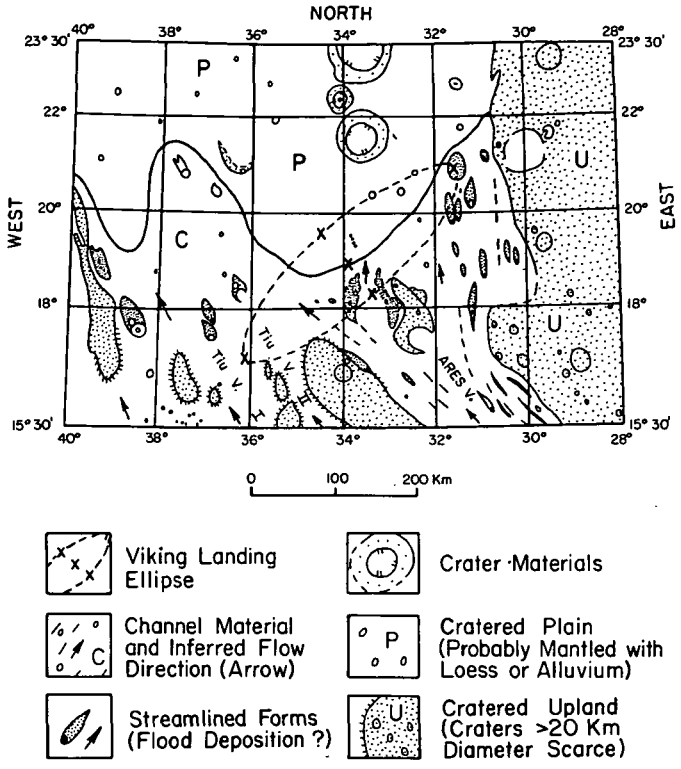

Fig. 1. Local setting of the A1 site where Viking 1 was originally intended to land. The postulated flood-related forms are based on pre-Viking interpretation of Mariner 9 imagery. Much of this interpretation has been confirmed by high-resolution Viking orbiter imagery.

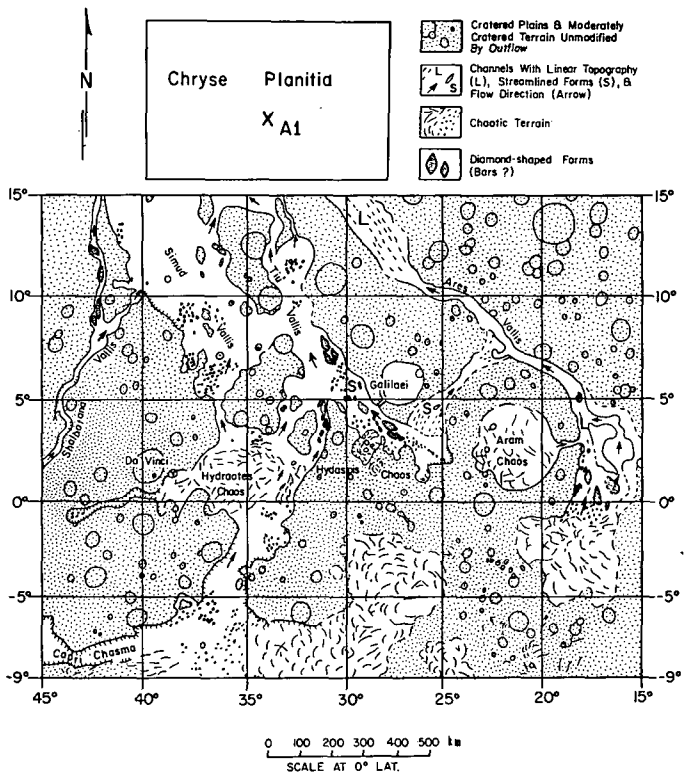

Fig. 2. Upchannel outflow-related features for channels graded to the southern Chryse Planitia. The A1 site shown is the originally proposed location that was abandoned when Viking orbiter imagery revealed excessive terrain roughness. Mapping is schematic and based on an uncontrolled mosaic of Mariner 9 imagery.

EROSIONAL AND DEPOSITIONAL FEATURES OF SOME TERRESTRIAL 'CHANNELS'

Jon C. Boothroyd and Thomas J. Donlon
University of Rhode Island

and

Dag Nummedal
University of South Carolina

A comprehensive study of selected river systems of varying sizes, in various climatic zones on the earth, is being undertaken to gain insight into the morphology and genesis of landforms found within those systems. Concentration is on developing terrestrial analogs of 'bars' and/or erosional remnants observed within the Chryse channels and on Chryse Planitia. A parallel consideration is the assessment of the bed relief of smaller-scale features such as bed material, fluvial bars, and small eolian dunes adjacent to the large-scale landforms. These smaller-scale features are at present unable to be resolved on images obtained by Mariner and Viking orbiters.

Landsat imagery, Skylab, Apollo, Gemini, and vertical aerial photographs, and published material form a primary data base. Our own aerial photos and field work in northern and southern Iceland, northeast Gulf of Alaska, Death Valley, and the channeled scablands of eastern Washington are being integrated with this information to provide some general 'ground truth' for those areas we are unable to visit.

Some parameters to consider are:

1) the climatic zone within which the stream system exists - arctic to tropical;
2) specific meteorology in that zone - humid to arid;
3) overall geometry of the stream system;
4) size of the stream system - 'giant' (one-of-a-kind) to 'small';
5) nature of discharge - perennial, specific extreme-flooding season, or 'flashy';
6) magnetude of discharge - 'giant' (one-of-a-kind) to 'small';
7) geometry of large-scale, within-channel features - size, shape, and relief;
8) origin of the large-scale features - depositional, erosional or polygenetic;
9) composition of the large-scale features - unconsolidated material (principally sand or gravel), sedimentary rock, or igneous and metamorphic rock;
10) nature of small-scale bed relief - erosional (etched bedrock) or depositional (bars, eolian dunes);
11) size of small-scale bed relief - 3 dimensional shape and scale of roughness elements.

In addition to the field areas mentioned above, imagery of the following areas are presently under study:

1) Colville River, north slope of Alaska (70N,145W)

2) Kosi River, India (26^{30}N,87^{30}E)
3) Amu Darya, Syr Darya Rivers, USSR (40N,62E; 45N,65E)
4) southwestern Saudi Arabia (19^{30}-22^{30}N,43-45E)
5) Wadi Hadrawat, PDR of Yemen (16N,50E)

Other localities will be added as the study continues.

The small braided, glacial-outwash streams on the northeast Gulf of Alaska coast contain coarse-gravel (up to 50 cm long axis) longitudinal bars on regional gradients of 3-15 m/km. Aggregates of these 50-100 m long bars form what we call islands. These islands are small, usually < 1 km in length, with a few meters of relief, and below the resolution limit of present Mars imagery. These streams do serve as an example of depositional topography of minor bed relief.

The southern Iceland outwash fans exhibit generally similar bed-relief and gradient characteristics but have a much greater areal extent (up to 800 km^2, Nummedal and Boothroyd, 1876a). Also the Icelandic plains may have glacier-burst flood (jokulhlaup) channels, several hundred meters wide incised up to 30 m below the general plain surface. The floors of these channels contain numerous scour features and anomalously large boulders (Nummedal, et al, 1974). These plains may serve as a 'same size' analog for some of the Chryse debouchment areas, but again, relief is below present resolution capability.

The Copper River, northeast Gulf of Alaska, is a large, interior-draining glacial stream that has large (5-10 km long) diamond-shaped islands that have eolian longitudinal dunes developed on their upstream apices. These dunes are up to 45 m high and are aligned parallel to river flow direction. These islands are examples of depositional features of sufficient size to be resolved on Mariner/Orbiter imagery.

Death Valley arid alluvial fans have much steeper gradients than glacial-alluvial fans (up to 100 m/km), but maximum clast size is similar to the Alaskan fans as are the small-scale longitudinal bars (Nummedal and Boothroyd, 1976a). Degradation of the fan surface by Holocene stream processes has left diamond-shaped erosional remnants up to 3 km long and 15 m high that are clearly visible on Landsat imagery (hence also on Mariner/Orbiter imagery). These remnants consist of unconsolidated fluvial and debris-flow gravels.

The channeled scablands of eastern Washington offer a wide array of erosional and depositional features (Baker, 1973; Baker and Milton, 1974; Boothroyd, Simpson, and Nummedal, 1976). Two points to consider are: 1) that the large-scale streamline features are eroded basalt topography or are polygenetic forms (Palouse Hills), and 2) while some of the small-scale bed relief is depositional (bars and gravel waves), much of the total areal extent of the channel bottom between the erosional remnants is, itself, erosional. This scabland surface contrasts with the depositional outwash plains discussed above.

The Skjafandafjlot valley of northern Iceland contains glacially-smoothed, basaltic, streamline forms up to 30 km long and 150 high. The valley floor is a combination of glacial-outwash plain, and post-glacial basalt flows and spatters cones. Thus the small-scale bed relief has a combination of roughness elements.

The localities discussed above suggest that large-scale streamline features can be formed by a variety of hydrodynamic, aerodynamic, and 'glacio-dynamic' processes, and that small-scale channel-bottom features can be either erosional or depositional with a wide range of bed relief. This further suggests that although the channeled scablands catastrophic flooding model is probably the best we have for the Chryse channels at the present time, similar features can result from lesser magnitudes of discharge under quite different fluvial settings.

Further study will emphasize the relationship of aerodynamic forms, particularly yardangs (MacCauley and Grolier, 1976; Grolier et al, 1976; Grolier et al, 1974), with hydrodynamic streamline forms of similar scale. Attention will be paid to directional trends where the two may occur together, and to similarities and differences of morphology. The Fourier shape analysis technique (Nummedal and Boothroyd, 1976b) will be used in an attempt to discrimate fluvial versus eolian features on earth with an eventual application to Mars.

Deep-Sea Channels: Another Earth Analogy with Martian Channels.

Paul D. Komar and Clare E. Reimers, School of Oceanography, Oregon State University, Corvallis, ORE., 97331; Robert Dolan, Department of Environmental Sciences, Univ. of Virginia, Charlottesville, VA, 22903.

A major sedimentary feature of the deep ocean bottom is the numerous channels which emanate from submarine canyons at the edge of the continental shelf. Each submarine canyon has as a natural extension a channel cut into the deep-sea sediments. These channels bear a striking resemblance to those on Mars, especially the exogenic outflow and runoff channels as defined by Sharp and Malin (1). Like the Martian channels, the deep-sea channels generally lack tributaries or have only minor tributaries, instead consisting of a single pronounced channel extending from its origin at the submarine canyon to the deep abyssal plains, several hundred kilometers in total length. The channels vary considerably in dimensions, but most commonly have widths in the range 5 to 15 km with reliefs of 100 to 200 meters, again similar to the Martian channels.

The deep-sea channels are known to be the product of catastrophic turbidity currents, generated from slumps trapped in the submarine canyons; individual slumps range in volumes from about 10^5 to 10^{11} cubic meters of sediment (2). On the basis of ordered sequences of submarine cable breaks, computations utilizing a Chezy-type equation, and from the competence of the flows to transport gravels and cobbles, it is known that turbidity currents travel with mean velocities up to about 20 m/sec. Densities are thought to range up to 1.30 g/cm^3, and the largest flows sometimes spill from the confines of the channel indicating that they can have thicknesses greater than 200 meters.

The main channel terminates in what is termed the supra-fan area where the channel divides into a number of smaller channels. In this area the turbidity current reduces speed, partially loses its competence, and deposits most of its sediment load. This deposition is spread over a considerable area, so like Martian channels, the deposition area is not as apparent as the channel. In the supra-fan area the smaller channels are braided, although not much is known about the details of the channels there.

The deep-sea channels have much less tendency to meander than do rivers. Where they do meander, the characteristics of the meandering follow different relationships than do river meanders. This may be an indication that meandering characteristics are a function of the effective gravity, and we should be hesitant about applying Earth-based empirical results to the Martian channels.

Although we are not attempting to suggest that the Martian channels are deep-sea channels and the products of turbidity currents, an analysis of the effective gravity and the forces driving the flows indicates that the channelized flow of water on Mars would be intermediate in character between river flow on Earth and turbidity currents in the deep-sea where the effective gravity is reduced. Thus we may better understand the Martian flows by considering both river flows and turbidity currents on Earth.

There is also the possibility that under the adverse conditions presently found on Mars the initial flow of water could be progressively converted to a low-density snow avalanche, a type of density current similar to turbidity currents. During the transition the snow overlying the water would occlude further water loss and would also contribute to driving the flow along the channel. This would be more satisfactory than ice-covered rivers where the ice resists the flow.

P. Sharp and M. C. Malin, Channels on Mars, Geol. Soc. Amer. Bulletin,
. 86, 593-609 (1975).
H. W. Menard, *Marine Geology of the Pacific*, McGraw-Hill Co., New York,
Chapter 9, 191-222 (1964).

A large landslide on Mars. B. K. Lucchitta, U.S. Geological Survey, 2255 North Gemini Drive, Flagstaff, Arizona 86001.

A large landslide on the southwall of Ganges Chasma (lat. 8°S, long. 45°W) issues from a scar that is about 30 km wide and 6 km deep, and forms a curved reentrant in the trough wall. The slide drops a total of at least 2000 m from the top of the scar to the bottom of the trough (1), and is about 70 km long and 60 km wide. The overall slope from crown to tip is 2 degrees. The volume of the slide is at least 120 billion m^3, and the material spread over 2300 km^2 of the trough floor. The landslide mass consists of toreva slump blocks at the head, hummocky deposits farther out, and a vast apron of longitudinally ridged and grooved material in two lobes at the toe. The landslide has no craters on its surface, but an adjacent smaller slide of equal freshness has three craters superimposed that range from less than one to two km in diameter, and their presence suggests that the slides are not recent.

In order to evaluate the origin and mechanism of emplacement of the martian landslide it was compared to many large catastrophic terrestrial slides. Common features of landslides on both planets appear to be 1) the relative order in which layers from the source area are deposited in the slide, 2) fan-like shape, 3) thinness of the debris compared with the horizontal distance traveled, and 4) presence of at least vague lateral and distal rim ridges. The martian slide differs from most terrestrial slides in lacking transverse ridges (2, 3), however, it is similar to landslides in Alaska that have longitudinal ridges and grooves, and that have moved over glacial ice. Those slides had a relatively low coefficient of friction for their respective weights.

Amongst the Alaskan slides, the Sherman slide particularly resembles the martian one. It has been described in detail by Shreve (4) who explained its high efficiency by sliding on a cushion of air and by the inclusion of snow. Even though the martian landslide is also very efficient, it is questionable that it moved on a cushion of air. The present atmosphere on Mars is only about 10 mbar and probably was only 100 mbars in the past (5). A mechanism involving lubrication by a medium other than air seems more likely for Mars. This could be water or steam.

There is some evidence that the Sherman slide was wet when emplaced. This evidence includes 1) resemblance with wet-snow avalanches (6), 2) lack of a marginal dust deposit (6), 3) meltwater deposits on top of the slide (4), and 4) scarcity of percussion marks on the included debris. The Huascaran slide which was cushioned by mud (7) also has few percussion marks on rocks. The water may have been derived from the melting of snow and ice due to the conversion of the energy of the fall into heat, similar to the energy conversion postulated for the Huascaran slide by Erickson and Plafker (8), and for the Hope slide by Mathews and McTaggart (9).

Assuming that the martian landslide had a similar mechanism of emplacement as the strikingly similar Sherman slide, it is suggested that the martian one also contained water. The water could have been obtained from ground ice in the source rock of the landslide. That ground ice is present in the region of the troughs has been proposed previously (10, 11, 12). Some of the water may have been converted into steam, and may have boyed the slide in the manner envisioned by Pautre et al. (13) for the Huascaran slide.

The reason for the occurrence of large landslides can be analysed in terms of a "basic" and an "initiating" cause (14). The "basic cause" for this martian landslide may be found in 1) lithology,--most of the lower trough wall is probably underlain by weak breccia derived from ancient martian craters, 2) stratigraphy,--resistant lava that caps the plateau overlies weak rock, 3) structure,--a circular joint forming the scar may well be a

line of weakness over a buried crater, and 4) topography,--additional stresses are caused on steep slopes by renewed faulting, or denudation from previous slides.

The "initiating causes" for the martian slide may include 1) removal of support by outflow of the lower layer due to the overburden, 2) overloading by additional ejecta or eolian deposits, 3) reduction of friction and cohesion by melting of ice and percolation of water, 4) quakes, and 5) additional stresses due to variations in temperature, pressure, or tidal pulls.

The emplacement of the martian slide may have been as follows: Insolation caused some melting of ice on the steep trough wall; the melting caused an outflow or squeezing out of some material on the wall, followed by wholesale collapse of the wall due to the withdrawal of support. A large part of the interstitial ice in the fallen rock body was converted to water and possibly some steam, and the debris flowed or slid out onto the trough floor at tremendous speeds.

References

(1) U.S. Geological Survey, U.S. Geol. Survey Misc. Inv. Map. I-961 (1976)

(2) Heim, A., Zurich, Fretz and Wasmuth, 218 p. (1932)

(3) Shreve, R. L., Geol. Soc. Amer. Spec. Pap. 108, 47 p. (1968)

(4) Shreve, R. L., Science 154, 1639-1643 (1966)

(5) Owen, T., and Biemann, K., Science 193, 801-803 (1976)

(6) Post, A. S., U.S. Geol. Survey Prof. Paper 544-D., 42 p. (1967)

(7) Plafker, George, Erickson, G. E., Concha, J.F., Seismol. Soc. Am. Bull. 61, 543-578 (1971)

(8) Plafker, George, and Erickson, G. E., Elsevier, Amsterdam v. 1, in press

(9) Mathews, W. H., McTaggart, K. C., Proc. Geol. Assoc., Canada 20, 65-75 (1969)

(10) McCauley, J. F., Carr, M. H., Cutts, J. A., Hartmann, W. K., Masursky, Harold, Milton, D. J., Sharp, R. P., and Wilhelms, D. E., Icarus 17, 289-327 (1972)

(11) Sharp, R. P., Jour. Geophys. Research 78, 4063-4073 (1973)

(12) Lucchitta, B. K., U.S. Geol. Survey Jour. Research, in press

(13) Pautre, A., Sabarly, F. and Schneider, International Society of Rock Mechanics, Proc. 2, pt. B. 859-864 (1974)

(14) Sharpe, C. F. S., Cooper Square Publishers, Inc., New York 137 p.

Page Intentionally Left Blank

Chapter 9

VOLATILES AND THE MARTIAN REGOLITH

Page Intentionally Left Blank

Volatile Evolution. F. P. Fanale, Planetology and Oceanography Section, Jet Propulsion Laboratory, Pasadena, CA 91103

Galilean Satellite Studies:

Recent evidence has provided additional support for our original hypothesis [1] that the surface of J1 (Io) might be largely covered by evaporite deposits. Our original suggestion was based upon (1) the UV, visible and near infrared reflectance spectrum of Io, (2) studies of meteorites, especially studies of salt deposition in carbonaceous chondrites, and (3) our theoretical thermal history for Io. We have since published a far more detailed and quantitative treatment of our hypothesis [2], along with a study of the evolution (especially the surface evolution) of the other Galilean satellites. Observations of neutral Na emission from the cloud around Io [3] are generally supportive of our hypothesis, but are not uniquely supportive since it is almost impossible to gauge the absolute Na abundance on the surface based on the flux from the surface; the flux from the surface from the neutral abundance in the cloud and estimates of the ionization lifetime; the neutral abundance in the cloud from the oscillator strength, resonant scattering parameters, etc. A more specific observation is that the only emission lines thus far observed from the cloud are those of neutral Na, neutral K [4] and S^+, [5], in thorough agreement with our hypothesis. Additionally, the neutral Na:Ca ratio in the supply flux (which we have been able to identify [6] with a flux from Io's surface of neutrals sputtered by Jovian magnetospheric ions) can be shown to be much greater than would be expected from an undifferentiated (e.g. chondritic) source. Observations have been made from earth orbiting satellite of UV line strengths for Mg, Si and Al, but definitive limits on abundance ratios have not yet been set owing to the complexity of corrections for differences in trajectories of Io-originating neutral ejectae which result from mass differences, differences in ionization lifetime, etc. We hope to iron out these theoretical problems very soon. Nonetheless, currently establishable limits on Na:Ca, Na:K etc., together with analysis of possible fractionation occurring during supply or depletion of the cloud seem to eliminate familiar igneous rocks or meteorites as plausible Io surface constituents [7]. Calculation of the extremes of plausible models for preaccretion conditions in the circum-Jovian cloud by other investigators has broadened the range of possible bulk composition models for Io, but our search for plausible accretionary surfaces for that object (which has encompassed examination of scenarios for both homogeneous and inhomogeneous accretion) has failed to reveal a single scenario which runs the gauntlet of the observations nearly as well as the evaporite hypotheses [7].

We have also just completed a very extensive study [8] of the reflectance systematics from 0.3 μm to 2.5 μm of mixtures of various candidate Io surface materials. Our study has included study of the effects of phase proportions, grain size, packing, temperature, irradiation history, annealing history and other variables on the reflectance spectra. Io's spectrum in the region is not overwhelmingly diagnostic; it contains only shallow suggestive bands at ~ .55 μm and ~ 0.8 μm as well as a very sharp conduction drop-off in the UV. Nonetheless, we find that mixtures of various salts with elemental sulfur provide the best match to Io's reflectance spectrum in the visible and UV. These salts include alkalai nitrates, sulfates and carbonates [8]. Several other minerals could be present in reasonable abundance including montmorillonite. There is some suggestion that the salts contain traces of Fe^{+++}. All these observations support the evaporite hypothesis we advanced earlier. Our results suggest the abundance of salts to be higher and that of S to be lower on Io's leading side than on its trailing side, which is in harmony with observations suggesting greater ejection of Na from Io's leading side [8]. The latter observation could,

however, be due to several other causes. Other observations from a variety of disciplines have also peripherally supported our hypothesis, including polarization, radar return and albedo change observations.

A surprising observation has just been reported by D. Cruickshank and C. Pilcher of the University of Hawaii's Institute for Astronomy. They have observed the first deep absorption bands in Io's spectrum. These bands occur in the 3 - 4 μm region and have been interpreted by these workers as being suggestive of the presence of carbonates, nitrates or sulfates [9]. A specific satisfactory identification has not yet been made, so they regard their conclusion as only a tentative one at present. Conversely, however, their results and those of workers at the University of Arizona observing with higher spectral resolution at shorter wavelengths make it seem almost certain that the surface of Io is very anhydrous and is not covered with frosts or ices as previously suggested by other investigators.

Although none of these diverse observations provide definitive evidence favoring the evaporite hypothesis, the totality of their implication is certainly encouraging. In any event it can now be stated with virtual certainty that the surface of Io appears to be unlike known meteorites, igneous rocks or any of the numerous planetary surfaces for which reasonable reflectance data is available, including those of the terrestrial planets, their satellites, innumerable asteroids and the other satellites of the giant planets.

Mars Volatile Studies:

We have measured the adsorption of Kr and Xe on ground basalt, limonite and phyllosilicates of known B.E.T. surface area at a temperature of -78°C (a value close to the disc average mean annual temperature) - assumed to be similar to the average subsurface temperature). We have used these results, together with theoretical considerations, to estimate the effect of regolith adsorption on atmospheric rare gas elemental abundances [10]. We conclude that major preferential depletion of atmospheric Xe and some depletion of atmospheric Kr is likely to have occurred as the result of regolith adsorption. Because of uncertainties in the typical thickness and B.E.T. surface area of unconsolidated regolith material on Mars, together with differences between our experimental conditions and Martian surface conditions, it is not possible to "correct" the atmospheric rare gas elemental composition for regolith adsorption. On the other hand, our work clearly provides a ready explanation for the single major discrepancy between the elemental composition of Martian rare gas and that of "planetary primordial" components of chondritic rare gas: i.e., the much (~4X - 10X) higher Xe:Kr ratio in the latter. Certainly there is no reason for assuming this discrepancy is due to causes other than regolith adsorption. This explanation is similar to the quantitative model that we provided for the analogous discrepancy in the case of the Earth [11]. The difference is that in the case of the Earth, abundant verification of this hypothesis is available in that the rare gas contents of shales can be easily measured and have been found by several groups of investigators to be orders of magnitude greater than those of igneous rocks that contributed to the shales and approximately equal to the quantity that would have to be adsorbed on them (given the total quantity of shale) to explain the Xe "deficiency" in the atmosphere. The Xe:Kr ratio in the shales is also about a factor of ten higher than in the atmosphere as would be required by this hypothesis. Any such "confirmation" on Earth has, of course, only the most tenuous implication for Mars. However, it should be remembered that Mars is thought to have a deep regolith containing fine material comparable in thickness to that on Earth, albeit of different origin (e.g., see summary of evidence in [12]. Also, the

temperature of that regolith is much lower than on Earth. Nonetheless, until some measurements of the ambient heavy rare gas contents of Mars fines and the average depth of Mars' comminuted surface material are made, the case for significant preferential Xe adsorption on the Mars regolith must be based entirely on laboratory measurements and theoretical considerations.

We have recently constructed a quantitative model for regolith-atmosphere CO_2 exchange based on new laboratory measurements of CO_2 adsorption on ground rock at Martian temperatures and CO_2 pressures, and the assumption of conservation of total CO_2 mass in the atmosphere-regolith system [13]. This model may be used to predict the role of the regolith in determining the atmospheric pressure for any given number of CO_2 molecules in the total system and any postulated set of conditions of surface insolation. Some conclusions are:

(1) The arbitrary addition or subtraction of any stipulated amount of CO_2 to the Mars atmosphere plus regolith system without corresponding changes in surface insolation would have only a very highly attenuated effect on the Martian atmospheric pressure. For example, adding an amount of CO_2 equal to that present in the atmosphere would result ultimately (after $\gtrsim 10^6$ years) in a pressure increase of $< 10\%$.

(2) On the other hand, if one keeps the total amount of CO_2 in the system constant and increases the temperature of any regolith column, or of Mars as a whole, by $\sim 40^{\circ}C$, for a period of $\sim 10^6$ years or more, equilibrium pressures of only 25 - 35 mb are likely to result. Still lower pressure variations would accompany similar warming with a 1×10^5 year period (that of the major temperature fluctuations due to obliquity variations). Thus some process other than the exclusive operation of the currently observable obliquity change seems required for major climate change, which may explain why major channel formation was concentrated early in Mars' history as recently suggested by several investigators.

(3) Our model, which predicts the existence of up to 600 g/cm^2 of atmospheric-exchangeable CO_2 in the regolith is also consistent with other estimates of this magnitude of the exchangeable Martian CO_2 inventory based upon the N and O isotope compositions of the Martian atmosphere, as discussed by McElroy and Yung [14].

We consider our Mars regolith-atmosphere model to be a necessary first step in the eventual construction of any realistic Mars climate change model not only because of the strong effect that the long-term buffering by the regolith would have on any given CO_2 inputs postulated to occur because of sublimation of a huge residual CO_2 cap, but also because Viking observations [15] have raised considerable doubt concerning whether such a huge CO_2 cap exists in the first place. Thus we consider the regolith to be the major determinant of any $\gtrsim 10^6$ years change in Mars atmospheric pressure, and we also consider it the only viable source of enough CO_2 molecules to initiate major long-term climate change. In order to produce a realistic climate change model based on our model, long-term major insolation changes must be justified and not merely postulated. Additionally, it would be necessary to take into account any "feedback" mechanisms such as enhanced global heat transport, greenhouse effects, addition of more H_2O to the atmosphere, etc.

References

[1] F. P. Fanale, T. V. Johnson and D. L. Matson, Science, 186, 922-925 (1974).

[2] F. P. Fanale, T. V. Johnson and D. L. Matson, Planetary Satellites, J. Burns, ed., Univ. of Ariz. Press, Tucson, Arizona (1976).

[3] R. A. Brown and F. H. Chaffee, Jr., Ap. J. Lett., 187, L125 - L126 (1974).

[4] G. Münch, J. Tranger, and F. Roesher, Bull. Am. Ast. Soc. (in press).

[5] I. Kupo, Y. Mekler and A. Evintan, Ast. Jour. Lett., 205, L51 - L53 (1975).

[6] D. L. Matson, T. V. Johnson and F. P. Fanale, Ap. J. Lett., 192, L43 - L46 (1974).

[7] F. P. Fanale, T. V. Johnson and D. L. Matson, in preparation.

[8] D. B. Nash and F. P. Fanale, Icarus, in press (1977).

[9] D. Cruickshank and C. Pilcher, Bull. Am. Ast. Soc., Abs. in press (1977).

[10] F. P. Fanale, T. Owen and W. A. Cannon, Abs., Bull. Am. Ast. Soc., in press (1974) (ms. in preparation).

[11] F. P. Fanale and W. A. Cannon, Earth and Planet Sci. Lett., 11, 362-368 (1971)

[12] F. P. Fanale, Icarus, 28, 179-202 (1976).

[13] F. P. Fanale and W. A. Cannon, in preparation (1977).

[14] M. McElroy and Y. L. Yung, Planet. Space Sci., 24, 1107 - 1113 (1976).

[15] H. H. Kieffer, S. C. Chase, Jr., T. Z. Martin, E. D. Miner and F. D. Palluconi.

Climatic Change on Mars: Inferences Based on Viking and Mariner Data.

James B. Pollack, NASA-Ames Research Center, Moffett Field, CA., 94035

Photo reconaissance of Mars conducted from the Viking and Mariner spacecraft strongly suggest that two types of climatic changes have occurred on Mars. First, certain types of channels appear to have been formed by running water. Some of these channels, especially the outflow channels, could have been formed under current climatic conditions if a top ice sheet formed to insolate the water beneath it (1). However, other channels, particularly the gullies, imply a warmer wetter climate in the past with equatorial and mid-latitude diurnally averaged temperatures exceeding the melting point of water. This inference follows from the ubiquitous nature of these features on the older terrain units, which implies they were created either by rainfall or by a warm climate that led to the widespread melting of subsurface layers of permafrost. Age dating of the gullies indicate that they formed close to the time of formation of the oldest volcanic plains unit of the northern hemisphere (2).

Another type of climate change, one that has occurred more recently, is suggested by the laminated terrain found in both polar regions (3). The layering that characterizes this geological unit indicates that there have been periodic fluctuations in the agents responsible for its formation.

In an effort to understand the causes of these climatic changes, we have carried out a series of theoretical calculations. To study the conditions under which the temperature could have exceeded the melting point of water, we have performed a sequence of greenhouse calculations for atmospheres similar to the present one as well as for ones rich in reducing compounds. These calculations were performed with a realistic allowance made for the non-grey nature of the gaseous sources of opacity. The surface temperature was found from a heat balance condition according to which the thermal flux at the top of the atmosphere was made equal to the amount of sunlight absorbed by the atmosphere and ground. A constant albedo of 0.24, a value typical of current conditions, was assumed in all the calculations and the temperature structure of the atmosphere was approximated by a prescribed lapse rate in the troposphere, typically 70% of the adiabatic value, and a constant prescribed stratospheric temperature.

The computed greenhouse effect is a function principally of three variables: the atmospheric composition, pressure, and diurnally averaged amount of incident sunlight. For atmospheres composed principally of carbon dioxide with trace amounts of water vapor, pressures in excess of 1 bar are required to raise the surface temperature above the melting point of water at equatorial and mid-latitude locations. Such large CO_2 pressures lie close to the maximum limit of the total amount of carbon gases outgassed over the lifetime of Mars, as suggested by Viking compositional results (4). Furthermore, the fine grained regolith may have acted as a reservoir for much of this outgassed CO_2. Thus, it appears to be very difficult to obtain the desired greenhouse effect with an atmosphere containing fully oxidized gaseous species.

Much less stringent requirements for attaining the desired warming are found for atmospheres rich in reducing compounds. Such atmospheres apparently are required in the early history of the Earth in order for the chemical steps leading to the origin of life to take place and they may more generally represent the type of atmosphere to be expected soon after outgassing has taken place. Photodissociation of water vapor and exospheric loss of hydrogen causes a subsequent evolution to the current oxidizing atmosphere. For an atmosphere containing methane and ammonia in proportions similar to the Earth's volatile inventory - 30/1 (5), we find that the desired greenhouse effect can be achieved with atmospheres that have about a factor of ten less gas than the corresponding CO_2 dominated atmosphere. Ammonia plays a key role in generating the required atmospheric opacity, with its effect being amplified by the opacity due to water vapor. The latter's abundance is

constrained by its saturation curve and thus some of other gas must supply enough opacity initially to raise the atmospheric temperature to the point where water vapor is abundant enough to make a significant contribution to the total opacity. If much of the ammonia is lost to a surface reservoir or by photodissociation, then much larger pressures are required to obtain the desired greenhouse effect from methane and water vapor opacity. Even larger greenhouse effects may be achieved in partially evolved atmospheres that have a little carbon dioxide, besides methane and ammonia.

In summary, temperatures above the melting point at equatorial and mid-latitude regions on Mars may have been achieved at times when the atmosphere contained reducing gases such as methane and ammonia. A promising time for this to occur was during the formation of the oldest volcanic plains units when much of the atmosphere may have been outgassed, when the regolith may have been less deep, and when the solar luminosity may not have been too much lower than its present value.

Turning now to the polar laminated terrain, we suggest, in accord with Cutts (3), that the polar laminae consist of layers of atmospheric dust and water vapor, but in contrast to Cutts' model, we propose that these layers formed in the polar regions due to the preferential settling of dust and ice particles because they served as condensation nuclei there for large CO_2 particles that formed during winter and fell quickly out of the atmosphere. Furthermore, we suggest that the periodic nature of the layering is due chiefly to obliquity variations, which caused concomittant variations in both atmospheric pressure and summer polar temperatures. The former modulated the atmospheric dust content, while the latter modulated the atmospheric water vapor and hence water ice content. Atmospheric pressure variations are due to a control of this variable by polar and subpolar regolith deposits.

(1) S. J. Peale, G. Schubert, and R. E. Lingenfelter, Science 187, 273 (1975).
(2) D. Pieri, Icarus 27, 25 (1976).
(3) J. A. Cutts, J. Geophys. Res. 78, 4231 (1973).
(4) T. Owen and K. Biemann, Science 193, 801 (1976); M. B. McElroy, Y. L. Yung ad A. O. Nier, Science 194, 70 (1976).
(5) T.Owen, Icarus 28, 171 (1976).

PERMAFROST ON MARS

CORADINI M. and BIANCHI R. - Laboratorio di Astrofisica Spaziale del C.N.R. Frascati and Istituto di Geologia, Univ. Roma
(Italian Consortium for Planetary Studies)

Since the beginning of the Mariner missions and the consequent acquisition of high resolution imagery, Mars has been believed to be a dry planet for at least large part of its history. Only for the early history of Mars, the scientific community has always agreed about the possibility of existence of such an amount of water to determine on the surface tipical erosive feature. Mariner 9 imagery never supported, however, such speculation.

Only after the acquisition of the Viking imagery several water-like erosive features have been observed: accurate analyses also the local geology and the datation - or an least the determination of relative ages - by mean of crater counts, will be of large importance in understanding this problem and in giving better boundary conditions to formulate physical models about formation, permanence and escape of water.

In this context the authors consider the study of permafrost on Mars of large interest both as a mechanism of water trapping and as erosive agent. On Mariner 9 imagery permafrost presence can be only deduced observing particular geologic features as some large grabens with slopes not parallel. These can be an effect of an anisotropic erosion, probably due to the different mixture of water and soil along the strata immediately under the planet surface as well as to the different exposure to the sun of the graben sides (BIANCHI R. and CORADINI M., 1976); on Viking photographs same land slides and collapse features (CARR M.H. et al., 1976) clearly show the presence and the erosive action of permafrost. The primary goal of this paper is the comprehension of the thermodynamics which regulate the formation and the reservation of permafrost on Mars. In this context, taking into account the seasonal variation of temperature and parametrizing the water content in a soil of a given composition and grain size, isothermes - i.e. heat and frost waves - can be computed in the martian underground as a function of the depth. Such computations can give interesting informations on permafrost thickness and consequently on the amount of water which can be trapped in the soil.

Sudden local perturbation of the thermodynamic equilibria caused by large impacts, volcanism, tectonism etc., are also taken into account in checking the possibility of an underground accumulation of liquid water.

References Cited

R. BIANCHI, M. CORADINI, Geologica Romana, in press, (1976)
M.H. CARR, H. MASURSKY, W.A. BAUM, K.R. BLASIUS, G.A. BRIGGS, J.A. CUTTS, T. DUXBURY, R.GREELEY, J.E. GUEST, B.A. SMITH, L.A. SODERBLOM, J. VEVERKA, J.B. WELLMAN, Science, 193, n.4255, (1976)

U. V. RADIATIONAL EFFECT ON: MARTIAN ATMOSPHERIC AND REGOLITH WATER

by

Paul H. Nadeau, Robert C. Reynolds,
Allen R. Tice, and Duwayne M. Anderson

INTRODUCTION

Recent evidence suggests the presence of significant amounts of water on the surface of Mars. Erosional features that are likely of fluvial origin (1,2), the presence of breached craters (3), and the thermal evidence for water ice in the north polar cap (4), all attest to the major role that water may have played on the Martian landscape. The environmental conditions on Mars must first be considered to determine the chemical and physical nature of this water and its interactions with the atmosphere and regolith. In addition to the atmospheric composition, temperature, and pressure, the influence of ultraviolet solar radiation must be assessed. The photochemical formation of oxidizing agents such as O_3 and H_2O_2, by ultraviolet radiation, and their equilibrium and/or kinetic relationships with atmospheric and regolith water are to be determined experimentally. The results should provide information regarding the surface chemistry of Martian regolithic materials, the atmospheric stability, and the likelihood of biologic activity on Mars.

EXPERIMENTAL PROCEDURES

An environmental simulation cell presently under assembly will be capable of regulating atmospheric composition, temperature, and pressure over ranges that include those of Martian conditions. Recent Viking I and II lander results will be utilized to provide reasonable estimates of these parameters for the Martian environment (5,6,7).

A temperature control plate in the chamber is capable of regulating the soil sample temperature from -100°C to +50°C. A high pressure xenon

flashtube equipped with a suprasil window (lower cut off of 1600Å) is utilized to reproduce the solar radiation at the Martian surface. The environmental simulation cell is interfaced with a UTI quadrapole mass spectrometer so that atmospheric composition, photochemical product formation, and evolution of volatiles by the regolith can be monitored.

The simulation will be performed for several earth analog Martian regolith components, in order to obtain information on the manner and the extent of regolith interaction with photochemical reaction products. These materials will cover a wide range of surface properties; they include candidates for Martian regolith components, either observed on Mars or proposed in the literature, such as the clay minerals montmorillonite (8), nontronite (9), as well as limonite (10), basalt (11), magnetite (ferrous iron) (12), and ferric iron compounds. The specific surface areas of these materials have been determined (13) so that their quantitative roles can be assessed for adsorption/desorbtion reactions.

DISCUSSION

The Viking experiments have directly measured some aspects of the physical and chemical behavior of the Martian regoliths. Some of these results will be discussed. The method of sample preparation in the Viking GCMS soil analysis probably removed any free or adsorbed water from the regolith (14). The 0.1 to 1.0% water that was detected, by that experiment, was evolved between 200°C and 500°C, and probably represents the thermal decomposition of mineral hydrates. No H_2O_2 was detected, but the experimental conditions were such that it probably would not have been detected by the mass spectrometer. The primary objective of this experiment was to determine if any organic compounds exist in the regolith. No organic compounds were observed, the detectable concentration limit being 0.1 to 50 ppb. The three biology experiments showed substantial quantities of oxygen evolved by the regolith due either to heating or to contact with water vapor (15).

The labeled release experiment detected evolution of radioactive CO_2 upon introduction of C^{14} labeled nutrients to the regolith (16). The active agents responsible for this behavior in the regolith were stable to 18°C, but inactivated by heat treatment of 50°C for three hours.

A number of hypotheses involving inorganic chemistry have been proposed to explain the results of the biology experiments. They all rely on oxidizing agents in the regolith to explain its chemical activity. The formation of goethite and hydrated clay minerals are suggested as products of the photooxidation of basaltic material (18). H_2O_2 is then formed from water bound to ferric iron produced by photo-oxidation of ferrous iron in the basalt (17). Such a mechanism requires clean, unweathered, ferrous iron-rich minerals, and its applicability to Martian surface conditions is uncertain. Conversely, H_2O_2 could be formed by ultraviolet irradiation of water adsorbed on surface material (19). A surface chemistry model has been proposed also, that involves the presence of metal superoxide, $M(O_2)_2$ that would yield H_2O_2 upon hydration (19a).

Oxidizing agents, photochemically formed, such as O_3, H_2O_2, are known to exist in the Martian atmosphere (20). Since H_2O_2 is formed predominantly from water, atmospheric production would be affected by atmospheric water content. In this respect, Mars exhibits a great asymmetry during the Northern summer, with most of the atmospheric water in the Northern Hemisphere (4). It is interesting that Mars also exhibits a geologic asymmetry, with the older, more primitive surface material in the Southern Hemisphere, and younger, volcanic and aeolian surface material in the north (21). H_2O_2, regardless of its formation mechanism, may be stabilized on clay surfaces. It is well established that H_2O_2 is stabilized in low ph environments (22). The acidic nature of clay surfaces, particularly montmorillonite, has also been established (23). This surface acidity is controlled in part by the degree of water adsorbed on the clay surface. As the amount of water on clay becomes small, the residual water molecules

are highly dissociated (24), enhancing surface acidity (25). Studies of the unfrozen water layer on clay surfaces at Martian temperatures show that thin films, perhaps one monolayer, of liquid water could exist on clay surfaces (26,27). The degree to which acidic clay surfaces can stabilize and store H_2O_2 is uncertain. The high surface areas of clay minerals suggest that it may be quite substantial.

The two major questions this research attempts to answer are:

1) Is H_2O_2 formed in the Martian atmosphere in significant quantities?

2) Is H_2O_2 stabilized and stored by the Martian regolith?

Other related questions are: Could H_2O_2 be transferred from the atmosphere to the regolith, and by what mechanisms? (It is conceivable that diurnal frost precipitation would act as such a mechanism.) Do ferric iron, ferrous iron, or other substances act as catalysts for photochemical reactions? What is the thermal and chemical stability field of H_2O_2 adsorbed on the various minerals of the Martian regolith?

The above questions have implications in many areas. H_2O_2 adsorption by the Martian regolith could explain the preliminary results of O_2 evolution and oxidation of injected nutrients in the Martian soil found by the biology gas exchange and labeled release experiments of Viking I.

A large exchangeable sink of O_2 is necessary to explain observed ^{16}O and ^{18}O isotopic ratios given present Martian degasing and volatile escape models (28). Should significant amounts of H_2O_2 be stored on Martian surface materials, it might provide such an exchangeable sink. The surface chemistry could also play an important role in determining Martian atmospheric stability (20).

The likelihood of earth-type biologic activity and/or the survival of residual organic material on Mars would be greatly diminished if the regolith contained adsorbed oxidizing agents such as H_2O_2. The absence of organic compounds observed by the Viking I and II GCMS soils analysis would indicate that such may be the case.

REFERENCES

1. Milton, D. J., J. Geophys. Res. 78,4037 (1973).

2. Baker, V. R., Milton, D. J., Icarus 23, (1974).

3. Stockman, R. H., Proceedings of Colloquium on Water in Planetary Regoliths, 5-7 October (1976), p. 55.

4. Farmers, C. B., Davies, D. W., LaPorte, D. D., Science 194, 1339 (1976).

5. Kieffer, H. H., Science 194, 1344 (1976).

6. Hess, S. L., Henry, R. M., Leouy, C. B., Ryan, J. A., Chamberlain, T. E., Cole, H. L., Dutton, R. G., Greene, G. C., Simon, W. E., Mitchell, J. L., Science 194, 78 (1976).

7. *Owen, T., Biemann, K., Science 193, 801 (1976).*

8. Hunt, G. R., Logan, G. M., Salsbury, J. W., Icarus 18, 459 (1973).

9. Baird, A. K., Toulmin, P., Clark, B. C., Rose, H. J., Keil, K., Christina, R. P., Gooding, J. L., Science 194, 1288 (1976).

10. Houck, J. R., Pollack, J. B., Sagan, C., Shaack, K. D., Decker, J. A., Icarus 18, 470 (1973).

11. Carr, M. H., J. Geophys. Res. 78, 4049 (1973).

12. Hargraves, R. B., Collinson, D. W., Arvidson, R. E., Spitzer, C. R., Science 194, 1303 (1976).

13. Tice, A. R. (unpublished data).

14. Bieman, K., Oro, J., Toulmin, P., Orgel, L. E., Nier, A. O., Anderson, D. M., Simmonds, P. G., Flory, D., Diaz, A. V., Rushneck, D. R., Biller, J. A., Science 194, 72 (1976).

15. Klein, H. P., Horowitz, N. H., Levin, G. V., Oyama, V. I., Lederberg, J., Rich, A., Hubbard, J. S., Hobby, G. L., Straat, P. A., Berdahl, B. J., Carle, G. C., Brown, F. S., Johnson, R. D., Science 194, 99 (1976).

16. Levin, G. V. and Strant, P. A., Science V 194, p. 1322-1329 (1976).

17. Huguenin, R. L., Presentation at the Colloquium on Water in Planetary Regoliths, Oct. 5-7 (1976).

18. Huguenin, R. L., G. Geophys. Res. 79, 3895 (1974).

19. Oro, J., 1977, Mass Spectrometric Identification of the volatile constituents in the atmosphere and surface of Mars. (In preparation)

19a. Oyama, V. I., Berdahl, B. J., and Carle, G. C., 1977, Preliminary findings of the Viking gas exchange experiment and a model for Martian surface chemistry nature, V. 265, p. 110-114.

20. Liu, S. C., and Donahue, T. M., Icarur 28, 231 (1976).

21. Caar, M. H., Masursky, H., and Saunders, 1973, J. Geophys. Res., V. 78, p. 4031-4039.

22. Schumb, W. C., Satterfield, C. N., and Wentworth, R. C., 1955, Hydrogen Peroxide, Amer. Chem. Soc. Mon 128, 759 pages.

23. Durand, B. and Pelet, R., and Fripiat, J. J., Alkylammonium Decomposition on Montmorillonite Surfaces in an Inert Atmosphere, Clays & Clay Minerals, 1972, Vol. 20, pp. 21-35.

24. Mortland, M. M., Fripiat, J. J., Chaussidon, J., and Uytterhoeven, J. B. (1963), J. Phys. Chem. 67, 248-258.

25. Fripiat, J. J., Jelli, A., Poncelet, G., and Andre, J. (1965), J. Phys. Chem. 69, 2185-2197.

26. Anderson, D. M., Gaffney, E. S., and Low, P. F., 1967, Frost Phenomenon on Mars, Science V. 1551, p. 319-322.

27. Anderson, D. M. and Morgenstern, N. R., 1973, Permafrost: The North American Contribution to the Second International Conference, p. 257-288.

28. Owen, T., Report presented at Viking Molecular Analysis Team Meeting, Feb. 8, 1977.

Superoxides and Liquid Water on Mars, R. Smoluchowski, Materials Laboratory, Princeton University, Princeton, N. J., 08540.

The observed rapid release of oxygen upon addition of liquid water to Martian soil in gas exchange experiments (1) made in both Viking landers led to the suggestion that, as an alternate to a biological reaction, there may be reactions taking place between water and an inorganic superoxide. It is proposed that a ferrate, in particular $CaFeO_4$ which may be formed as a weathering product, is the active compound. The possibility that it could come in contact with liquid water on Mars is evaluated. This crystalline compound is of interest because it could be formed by oxidation of a mineral containing CaO and Fe_2O_3 and because, as all ferrates, it is red-purple in color and it should react with water for instance according to the reaction $2\ CaFeO_4 + 2\ H_2O \rightarrow Fe_2O_3 + 2\ Ca(OH)_2 + (3/2)O_2$. Other reactions involving H_2O_2, which may be formed on Mars by UV radiation, are also possible. In fact Fe_2O_3 is an effective catalyst for the reaction $2\ H_2O_2 \rightarrow 2\ H_2O + O_2$ in an alkaline environment.

Ferrates are cubic crystalline compounds of the general formula $MFeO_4$ where M is either a divalent ion such as Ba or Ca or two alkali metal ions (2) such as K, Rb or Cs. Their stability increases with increasing size of the M ion so that, so far, no Na or Mg ferrates have been reported. Each Fe is in the middle of a tetrahedron of oxygens held by bonds which are partly ionic and partly covalent (3). This tetrahedral group is undoubtedly responsible for the characteristic color of all ferrates. Each Ca is surrounded by 12 approximately equidistant oxygens.

It appears that the Martian soil is a mixture of products of weathering processes (4). One of the possibilities is that on Mars there are basaltic rocks containing some form of augite which lies on the low Ca side of the line of solid solutions of diopside (ideally $CaMgSi_2O_6$) and hedenbergite (ideally $CaFeSi_2O_6$) in the pyroxenes family. In this way one can account approximately for the observed ratios of elements beyond Z = 11 (Si, Fe and Ca) with the exception of Al and S which could occur in other forms. In many of the terrestial pyroxenes of the diopside-hedenbergite series there occur both Fe^{2+} and Fe^{3+} ions in various proportions. Thus a rather small rearrangement of the positions of the oxygens surrounding Ca and Fe ions in pyroxene can lead to the formation of a ferrate molecule and the main question is the required change of valence, and of the nature of the bonds. This reaction could take place on the surface of a suitable pyroxene (or other CaO and Fe_2O_3 or FeO containing mineral) with an adsorbed O_2 (or O_3) in a manner analogous to the Huguenin's photostimulated oxidation of Fe^{2+} to Fe^{3+} ions in the presence of ultraviolet radiation on Mars (5). Because of the difference in bonding and crystalline symmetry one expects the ferrate grains eventually to peel away and expose new layers of the pyroxene. The occurrence of dark reddish coloration on the top surfaces rather than on the sides of rocks seems to support this conclusion. Ferrates are in general quite stable and could exist for a long time in the Martian soil. Because of the low concentration of other elements such classical superoxides as for instance KO_2 probably do not come into consideration.

The rapid release of oxygen upon the addition of liquid water to Martian soil in the Viking experiments raises the question whether a similar reaction does not take place between the ferrate and water contained in the soil in small amounts. Ingersoll (6) pointed out that the evaporation cooling rate of frost condensed at night from the atmosphere is too fast to permit its melting near 0°C because of the thermal convection taking place above an open surface of ice. It is however interesting to reexamine the evaporative cooling of ice present in pores either in the form of permafrost or as ice formed by condensation of vapor originating from permafrost retained at greater depths.

Three factors alter the situation as compared to evaporation from an open surface: 1) the effective diffusion coefficient D_{eff} of H_2O vapor in CO_2 atmosphere can be lowered many orders of magnitude by the onset of Knudsen diffusion and is a function of pore size (7), 2) in pores smaller than a critical size m_o convection does not take place and 3) in a capillary pore closed from above the buoyancy of H_2O vapor in CO_2 atmosphere will slow down rather than accelerate the evaporation of ice. The mass flux of water vapor evaporating from ice in a pore smaller than m_o is given by $E_p = \rho_w (\Delta\rho/\rho) D_{eff}/Z$ where ρ_w is the saturation density of water vapor at the particular temperature, $\Delta\rho$ is the differnece between the densities of the ambient gas and of the gas at the surface, ρ is the density of the latter, and Z is the length of the pore, or rather the thickness of the layer of soil in which pores of a particular size form an interconnecting network. The resulting rate of cooling of ice λE_p, where λ is the heat of evaporation of ice, are given int Table 1 for grain sizes deduced from Viking data (8); porosity of about 0.6 is indicated (9). The minimum size m_o of the pores in which convection can take place, as obtained from $m_o^3 = \nu^2(\rho/\Delta\rho)g^{-1}$ is about 1 mm which is the upper limit of sizes of pores here considered. The data in Table 1 can be compared with 8×10^{-1} cal cm^{-2} sec^{-1}, the solar constant on Mars if the delay and attenuation of the solar heating by the soil itself is taken into account. Since on the landing sites the solar heating and the diurnal variation of temperature decrease exponentially with depth with a constant of about 5 cm it appears that under favorable circumstances the seasonal and diurnal heating rate can be sufficient to overcome the evaporative cooling of ice in pores and lead to its temporary melting in the top layers. Although these amounts of liquid water are very small and are limited to small pores they could lead to localized emission of oxygen if they got in contact with superoxides such as the ferrates discussed above.

Table 1: Evaporative cooling rates of ice in pores on Mars at 0°C. (in cal $cm^{-2}sec^{-1}$)

Grain Diameter (μ)	Porosity			
	.1	.2	.5	.8
0.5	1.9×10^{-5}	3.7×10^{-5}	3.3×10^{-4}	6.1×10^{-3}
10	2.8×10^{-4}	4.7×10^{-4}	3.3×10^{-3}	4.2×10^{-2}
200	3.7×10^{-4}	9.4×10^{-4}	5.2×10^{-3}	5.2×10^{-2}
1000	4.7×10^{-4}	1.2×10^{-3}	5.7×10^{-3}	5.7×10^{-2}

References:

1. Klein H. P., Horowitz N. H., Levin G. V., Oyama V. L., Lederberg J., Rich A., Hubbard J. S., Hobby G. L., Straat P. A., Berdahl B. J., Carle G. C., Brown F. S. and Johnson R. D. Science 194, 99-105 (1976).

2. Audette R. J. and Quail J. W. Inorg. Chem. 11, 1904-1908 (1972).

3. Palenik G. J. Inorg. Chem. 6. 507-511 (1967).

4. Baird A. K., Toulmin P. III, Clark B. C., Rose H. J. Jr., Keil K., Christian R. P. and Gooding J. L. Science 194, 1288-1293 (1976).

5. Huguenin R. L. J. Geoph. Res. 79, 3895-3905 (1974).

6. Ingersoll A. P. Science 168, 972-973 (1970).

7. Smoluchowski R. Science 159, 1348-1350 (1968).

8. Shorthill R. W., Moore H. J. II, Hutton R. E., Scott R. F. and Spitzer C. R. Science 194, 1309-1318 (1976).

9. Baird A. K., Toulmin P. III, Clark B. C., Rose H. J. Jr., Keil K., Christian R. P. and Gooding J. L. Science 194, 1288-1293 (1976).

Carbonate Formation on Mars. Michael C. Booth and Hugh H. Kieffer, Department of Earth and Space Sciences, University of California at Los Angeles, Los Angeles, CA., 90024

A study is presently underway to determine the importance of carbonate formation to chemical weathering phenomena on Mars. Preliminary work has shown that very small amounts of carbonate material are generated in simulated Mars-like environments with or without the existence of an aqueous phase. This study seeks to determine the rate of carbonate growth as a function of environmental conditions, the mechanism by which carbonate is formed in these environments, and, if possible, the composition of carbonate being generated. Environmental parameters being examined for their effect on carbonate growth include the partial pressures of CO_2, H_2O, and O_2, soil temperature, ultraviolet irradiation, the rate of diurnal cycling, and soil composition. Initial results show carbonate formation to be strongly influenced by P_{CO_2} and P_{H_2O}, and the particle grain size of the experimental soil in which carbonate is grown, but to not be related to direct ultraviolet irradiation of particle surfaces.

The environmental system employed is capable of providing the temperatures, atmospheric pressures and compositions, and the high flux UV illumination appropriate to the martian surface. Experimental soil temperatures range between 180° and 298°K, while atmospheric pressures vary from 6 to 200 mb, depending on the experiment. Water, in terms of precipitable micrometers cm^{-2}, ranges in abundance among experiments between 0 and 50 μm. When including oxygen, experiments have a P_{O_2} of $\sim$0.1 mb. The physical state of H_2O is controlled in order to provide surface frosts during cold, nonilluminated ("night") periods and low P_{H_2O} during warm, illuminated ("day") periods without the involvement of an intermediate aqueous phase. Experiments consist of alternating 6-hour periods of "day" and "night" and range in duration from 42 to 114 hours. The experimental soils consist of finely powdered tholeiitic basalt; experiments employing a variety of rock types are also planned.

After exposure, soil samples are analyzed for carbonate on a vacuum system by the analytical acid technique of McCrea(1). Carbon dioxide derived from the decomposition of carbonate during reaction with 100% phosphoric acid in vacuo is measured on a mercury manometer to within 0.01 μmole. Rates of carbonate growth at 100 mb CO_2 pressure are on the order of 10^{13} molecules cm^{-3} sec^{-1} and increase linearly with increasing CO_2 pressure. The presence of H_2O appears to be important to carbonate formation, but an over abundance of H_2O appears to hinder growth. The existence of liquid water in soils does not detectably alter the rate of carbonate formation, but does influence carbonate distribution within the sample; experiments lacking a liquid phase yield a uniform carbonate distribution.

Oxygen is also evolved from soils during analysis for carbonate. This oxygen is thought to be derived from either peroxides or hydroxyl radicals adsorbed on particle surfaces. These oxygen-bearing species are generated by photochemical activity within the environmental chamber and are thought to be the same species that produced oxygen upon the addition of water vapor within the Viking biological experiments (2,3).

(1) McCrea, J. Chem. Phys. 18, 849 (1950)
(2) Klein, H. P., et al., Science 194, 99 (1976)
(3) Horowitz, N. H., Hobby, G. L. and Hubbard, J. S., Science 194, 1321 (1976)

Mars: Surface Mineralogy from Reflectance Spectra. R.L. Huguenin, MIT, Cambridge, MA 02139, J.B. Adams, Un. of Washington, Seattle, WA, and T.B. McCord, Univ. of Hawaii, Honolulu 96822.

Earth-based telescope reflectance spectra (0.3-2.6μm) of numerous small (200-400 km diameter) regions as well as the integral disk of Mars were obtained in 1969, 1973, and 1976 using photoelectric filter photometry (1,2), photometric imaging (3) and CVF IR spectroscopy. Each of the spectra show distinct electronic absorption bands that contain information about surface mineralogy.

Bright areas and dust clouds. The 1973 bright area (fig.1) and dust cloud (fig.2) spectra are very similar between 0.3 and 1.1μm. Each has an intense absorption feature at the blue-UV end of the spectrum with slope changes at 0.50-0.57 and 0.6μm, and a weak absorption band centered between 0.83 and 0.90μm. The blue-UV feature is slightly more intense in the dust cloud spectra than in the bright area spectra, which is probably due primarily to scattering properties of suspended dust vs. surface powder. Also, the weak 0.83-0.90μm band is centered closer to 0.9μm in the dust cloud spectra than in the bright area spectra. The 1969 bright area spectra (0.3-1.1μm) (fig.3, spectra 1-3) are similar to the 1973 bright area and dust cloud spectra, except that the blue-UV absorption feature was not as intense in 1969 and a weak absorption band was centered near 0.93-0.97μm instead of between 0.83 and 0.90μm. Several percent variations in the intensity of the blue-UV feature and the variable appearance of weak bands at 0.83-0.90μm and 0.93-0.97μm have been observed in spectra of the bright area Arabia during previous oppositions (1), and it suggests a temporal variation in surface mineralogy in at least some bright area.

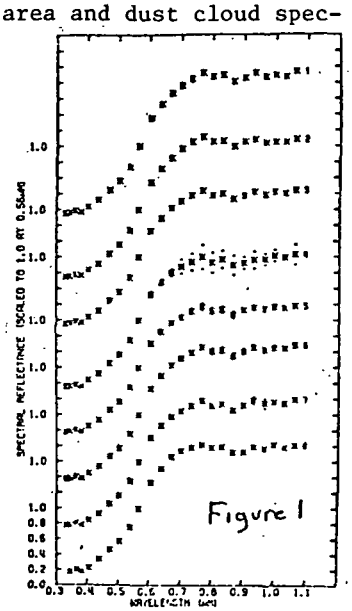
Figure 1

The intense blue-UV absorption feature with slope changes at 0.6μm and 0.50-0.57μm is characteristic of the spectrum of soils containing several percent ferric oxide. The intense blue-UV absorption arises from a pair of $O^{2-} \rightarrow Fe^{3+}$ charge transfer bands centered near 0.34μm ($1t_{1u} \rightarrow 2t_{2g}$) and 0.40μm ($6t_{1u}\ 2t_{2g}$). The slope changes at 0.6μm and 0.50-0.57μm arise from Fe^{3+} interelectronic transitions at ∿0.62μm ($^6A_{1g} \rightarrow {}^4T_{1g}$), and 0.53μm ($Fe_2O_3$) - 0.45μm (FeOOH) ($^6A_{1g} \rightarrow {}^4A_{1g}$, E_g). A third (weaker) absorption band occurs at 0.84μm (Fe_2O_3)-0.89μm (FeOOH) due to the $^6A_{1g} \rightarrow {}^4T_{2g}$ transition in Fe^{3+}. The absence of the $^6A_{1g} \rightarrow {}^4T_{2g}$ band and the strength of the blue-UV feature in the 1969 spectra indicates that the ferric oxide content of the average soil in those areas did not exceed ∿6% (4). The occurrence of a band at 0.83-0.90μm and stronger blue-UV feature in the 1973 bright area and dust cloud spectra suggest that the average ferric oxide content of these soils was a few percent higher than in the 1969 areas. The ferric oxide in the 1973 dust cloud material was apparently more hydrated than the soils on the surface in the 1973 bright areas, as indicated by the differences in the centers of the $^6A_{1g} \rightarrow {}^4T_{2g}$ band (5).

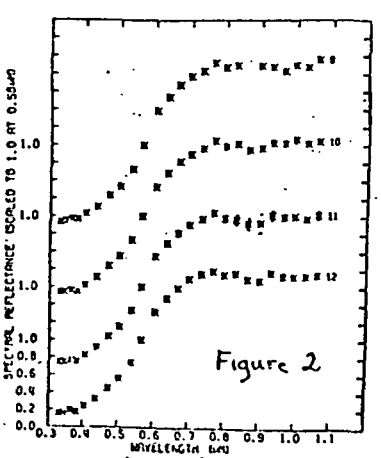
Figure 2

The occurrence of the 0.93-0.97μm band in the 1969 spectra indicates the presence of pyroxene in the surface soil (6). This band is also apparent in some of the 1969 dark area spectra (see below), but not in the 1973 bright area or dust cloud spectra. We interpret these observations as evidence for a multicomponenet soil in at least some bright areas: (1) a fine-grained dust that contains several percent ferric oxide and no detectable pyroxene; and (2) a more coarse-grained pyroxene-bearing soil. The fine-grained component comprised the 1973 dust clouds, and it effectively masked any ferrosilicates that may have been contained in the 1973 bright areas. In the 1969 bright areas the ferrosilicate masking was less effective.

Dark Areas. The 1969 (fig.3, spectra 4-7) and 1973 (fig. 4) dark area spectra differ substantially from the bright area spectra in several important ways. The dark area spectra show a strong broad near-infrared absorption feature that extends from ∿0.8μm longward. The shape of the near-ir feature varies from spectrum to spectrum, indicating regional variations in surface mineralogy. An intense blue-UV feature appears, in the dark area spectra, as in the bright area spectra, but it is significantly less intense. Note that the blue-UV feature is stronger in the 1973 dark area spectra than in the 1969 dark area spectra. The level of atmosphere dustiness was greater in 1973 than in 1969, and the stronger blue-UV feature was probably due to greater contamination by the ferric oxide-bearing dust.

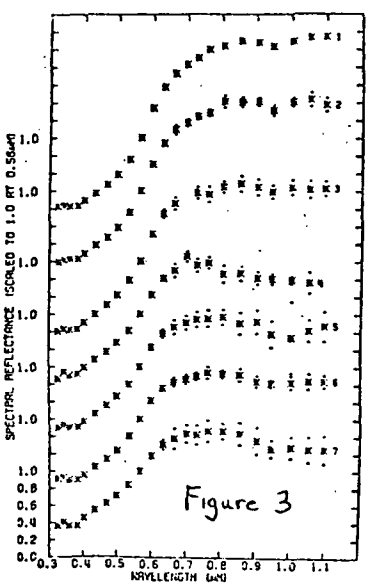

Figure 3

Relative reflectance spectra of the dark area (fig.5) reveal that the near-ir absorption features are composites of bands centered near 0.87μm, ∿0.93μm, ∿0.96μm, and ∿1.05μm in various proportions. The 0.87μm feature appears only in spectra with strong blue-UV features, and it is probably due to contaminant dust. The ∿0.93 and ∿0.96μm features are most likely due to pyroxenes, while the 1.05μm band is probably due to olivine (6). For most of the areas observed, olivine is more abundant than pyroxene. The abundances of magnetite and ilmenite are difficult to extimate, although they probably do not exceed ∿10%.

Infrared spectra. Infrared spectra of the integral disk of Mars taken during 1976 (fig.6) reveal the 0.83-0.90μm ferric oxide band and 0.90-0.96μm pyroxene feature. An absorption band at 1.2201.25μm is tentatively attributed to feldspar. This feature was observed in 1969 infrared spectra of the bright area Arabia and dark area Syrtis Major (fig.7) but the feature was much stronger in the Syrtis Major spectrum, considering the differences in albedo. The coappearance of the feldspar and pyroxene bands in the spectra, and the relative weakness of the feldspar band in the bright area spectrum sug-

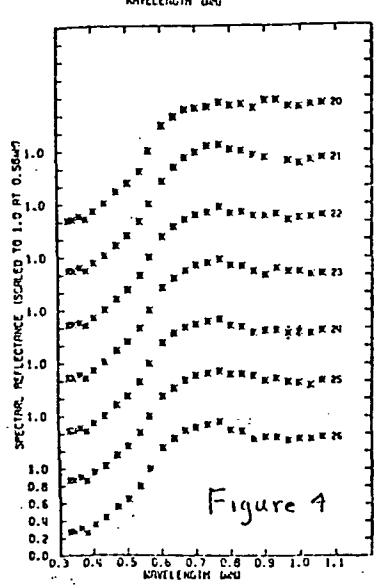

Figure 4

gest that the feldspar is probably contained in the more coarse-grained ferrosilicate soil than in the fine-grained dust. The occurrance of feldspar in the dust component cannot of course be ruled out, however. Future higher-spatial resolution infrared spectra should resolve this. Other features in the 1976 integral disk spectrum (fig.6) are the broad H_2O ice absorption bands at $\sim$1.6μm and $\sim$2.0μm, superimposed on the narrower CO_2 bands at $\sim$1.6μm and $\sim$2.0μm. Higher spatial resolution spectra are neede to determine the origin of the ice features.

The Earth-based spectra reveal that reflectance spectra measured from orbit could provide information on regional variations in petrology and surface ice distribution on a scale of several kilometers.

References

1. McCord,T.B., Elias, J.H., and Westphal, J.A. (1971) Icarus 14, 245.
2. McCord,T.B., Huguenin,R.L., Mink,D., and Pieters, C. (1977) Icarus (in press).
3. McCord, T.B., Huguenin,R.L., and Johnson,G. (1977) Icarus (in press).
4. Adams, J.B., and McCord,T.B. (1969) J. Geophys. Res., 74, 4851.
5. Andersen,K.A., and Huguenin,R.L. (1977) paper presented at 1977 AAS/DPS meeting, Honolulu.
6. McCord,T.B., Adams,J.B., and Huguenin,R.L. (1977) to appear in NASA-SP on Orbital Science.

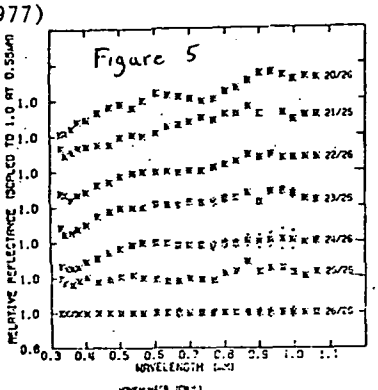

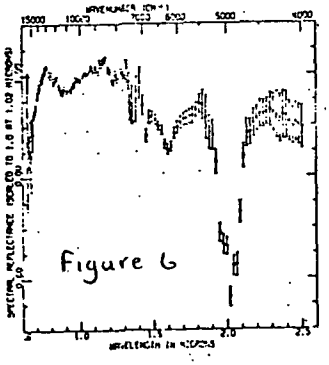

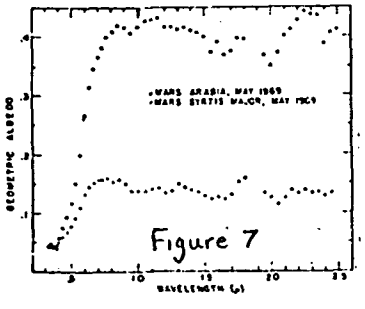

SPECTROPHOTOMETRY OF MARS BY WAY OF THE VIKING LANDER CAMERAS. R. Arvidson and S. Bragg, McDonnell Center for the Space Sciences, Dept. of Earth and Planetary Sciences, Washington University, St. Louis, Mo. 63130.

The Viking Lander cameras are essentially scanning radiometers, where the scene is scanned vertically along a given azimuth, after which the entire camera assembly is rotated in steps about the azimuth plane. This produces an image consisting of successive scan lines. The detectors are silicon photodiodes fit with interference filters. Six filtered photo-diodes can be used for multispectral imaging, covering the wavelength range from 0.4 to 1.1 μm. The responsivity functions for these channels have large band widths (0.1 μm) and irregular shapes due to S/N and design problems. As a consequence, the assignment of a discrete center wavelength to each channel can lead to inaccurate estimates of scene reflectance as a function of wavelength (1). This problem has been overcome by treating the scene reflectance as a linear sum of basis functions, where the basis functions are included in the integral that defines the channel pre-amplifier voltage (2). Such a method produces a reflectance estimate which is nearly as good as the estimate that would be produced by having impulse functions as channel responsivities. The basic limitation in the construction of a reflectance spectrum is the rate of sampling over wavelength space. Absorption features with periods less than about .2 μm, such as some of the Fe^{+3} bands in limonite cannot be reproduced (Figure 1).

Gray patches mounted atop the Landers have known reflectance properties. Adjustment of channel pre-amplifier voltages to make the patches appear gray allows first-order determination of the wavelength dependence of atmospheric transmittance, scattered skylight, and light reflected from the Lander. Relative reflectances for different parts of the scene can then be calculated. Significant results obtained to date for Viking Lander 1 are: (a) Most of the fines, including material exposed in trenches and clinging to the backhoe magnets, fit into a family curves whose differences can be explained solely by lighting and viewing differences, and to textural differences (Figure 2); (b) Most rocks have reflectivities similar to the fines, implying that they are coated or stained with similar materials (Figure 3); (c) The shape of the reflectivity curves for fines is consistent with Fe^{+3} rich weathering products; (d) A group of rocks at the VL1 site (~ 20m from the spacecraft) are distinctly darker than most others, even when differences in lighting and viewing geometry are taken into account. A field of dark fines lies amidst these rocks. The reflectance of the dark fines is distinct and may indicate the presence of FeO; (e) The hard-pan or duricrust exposed underneath the spacecraft by rocket blast has a reflectance that is both higher and of slightly different shape than the other materials. Most likely, this region represents an accumulation of evaporites. This zone has not been properly sampled for x-ray flourescence analysis and as a consequence results from the x-ray experiment cannot be directly interpreted in terms of magmatic or crustal composition without considering materials bound in these deposits; (f) Finally, comparison of the pre-amplifier voltages for parts of the scene covering the gray patches with pre-launch estimates of patch reflectance, demonstrates that one of the three groups of patches on VL1 is covered with a thin layer of dust (Figure 4). The dust was acquired during sampling activities, when material was dumped onto the Lander top, with some of it adhering to the patches. The degree of deviation from pre-launch reflectance data provides a means of determining the rate of dust accumulation. Now that most sampling activity is over, the measurements will allow estimates of the flux of wind-blown materials to be made.

(1) Kelly, L., F, Huck. R. Arvidson, NASA Tech. Mem X-72778, 27 p., (1975)
(2) Park, S., F. Huck, B. Martin, NASA Tech. Mem. X-72773, 18 p., (1975)

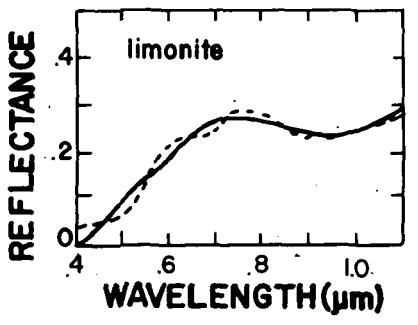

Figure 1
Dashed line indicates the true reflectance of powdered limonite, ratioed to a $MgCO_3$ standard. Solid line is a theoretical reproduction of the limonite curve using the 6 channel Viking system and the basis function approach of Park et al (2). Note that broad absorption features are reconstructed, but, because of sampling limitations, the short period absorptions evident in the limonite spectrum cannot be reproduced.

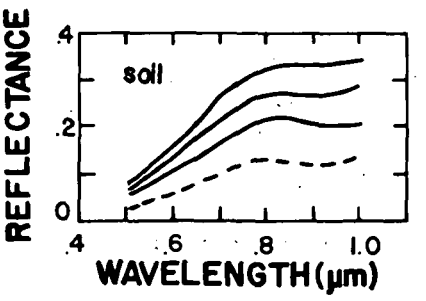

Figure 2
Relative reflectance spectra for 3 undisturbed regions of fine-grained material (solid lines) and 1 region within the sol 8 trench (dashed line) at VL1. The spectra are relative since the reference gray patches to which the spectra are normalized have an as yet unknown contribution of light reflected from the Lander body. Variations in reflectance seem to be due to differences in lighting and viewing geometry, and for the trench material, to textural differences. VL1 frame: (11A147/026, 11A149/026).

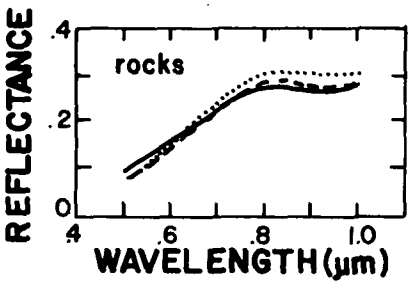

Figure 3
Relative reflectance spectra for 3 of the brighter rocks at VL1. Note that the shape of the reflectance curves mimics that of the undisturbed fines shown in Figure 2, implying that the rocks are coated or stained. Some rocks at VL1 are much darker than those shown. Taken together with textural evidence, the dark rocks are most likely relatively unweathered mafic or ultramafic volcanics. VL1 frame: (11A147/026, 11A149/026)

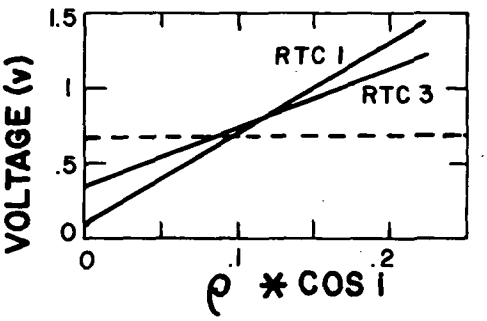

Figure 4
Least squares fits are shown for data from a group of gray patches mounted on the VL1 RTG cover (RTC 1) and near the Lander deck (RTC 3) for a sol 39 image taken in the red light. Pre-amplifier voltages were computed from the DNs for each of the patches and plotted against pre-launch estimates of patch bidirectional normal reflectance, ρ, times the cosine of the solar incidence angle. Since the patches are Lambertian scatters, such plots act as controls to calibrate camera response and to determine if the patches have become covered with dust. As dust thickness increases, slopes of the lines should decrease since patch to patch contrast would have decreased. Eventually, the lines should approach zero slope, with an intercept that corresponds to the voltage derived for the dust alone. The dashed line is the voltage for material clinging to the magnet attached to the RTC 3 assembly. In addition to this information, similar plots for broad band images taken on sols 15, 39, and 186 show that RTC 3 is becoming increasingly dust-coated and that the dust is similar in reflectance to material clinging to the magnet.

Page Intentionally Left Blank

Chapter 10

MAPPING PROGRAMS

Part A

MARS

Mars Geologic Mapping. D. H. Scott, U. S. Geological Survey, Flagstaff, Arizona 86001

The Mars geologic mapping program was started in September, 1972, when quadrangle assignments were announced and a memorandum of agreement was distributed to prospective mappers. At that time each author received an uncontrolled photomosaic base map and Mariner 9 A and B photographs covering the assigned area. The project provided for the systematic mapping of 30 martian quadrangles at 1:5,000,000 scale covering the entire planet. It included 35 investigators representing the U.S. Geological Survey, 12 universities, Ames and JPL research centers, and NASA headquarters. At later stages in the program, mappers were furnished controlled bases; airbrush renditions of photo mosaics were completed in time to be used as bases for several of the geologic maps. During the course of the project, two maps were reassigned and have been completed by new authors.

The status of the geologic mapping in the first quarter of 1977 is shown by figure 1. Twenty-two of the maps are either published, in press, or completed and in advanced stages of processing. Of the remaining 8 maps, 2 were not scheduled to be started until FY '77, 2 others have been partly reassigned with the addition of new co-authors, and 4 are in preliminary or revision stages following technical reviews. In the past there have been long delays between the submittal of a map for publication and its eventual printing. The publications division of the Survey, however, has recently indicated that there will be a substantial reduction in turn-around time from the date of a map's submittal to its printing and distribution.

Mapping styles have varied widely from one quadrangle to another. They have been largely influenced by photo quality but also depend on an author's concept of portrayal, whether to accent the regional geologic picture as opposed to a more detailed one. As a result, a large number of different names have been applied to similar appearing rock units, or parts of the same unit. Even so, boundary contacts of map units between quadrangles have generally shown good agreement and relative age relations have been consistent from map to map. Undoubtedly, some of the maps will need to be revised in light of the Viking orbital images, especially those where new coverage is relatively dense and (or) where previous Mariner 9 A-camera photos are poor and B frames are sparse.

These maps have already directly contributed to the 1:25,000,000-scale geologic map of Mars (1), to the regional evaluation of the Viking prime A (2) and B (3) landing sites, and to a study supporting a penetrator mission to Mars (4).

References

(1) D. H. Scott and M. H. Carr, U.S. Geol. Survey (in press).

(2) D. E. Wilhelms, U.S. Geol. Survey: Misc. Geol. Inv. Map I-895 (1976).

(3) J. R. Underwood, Jr., and N. J. Trask, U.S. Geol. Survey: Misc. Geol. Inv. Map I- (in press).

(4) Paul Spudis and Ronald Greeley, NASA TMX-73, 184 (1976).

MARS GEOLOGIC MAPS

Status – First Quater 1977

MC	Quadrangle	Technicial Reviews	Editorial Review (TRU)	In Press	Published
1	M. Boreum				
2	Diacria				
3	Arcadia				
4	M. Acidalium	▒	▒	▒	
5	Ismenius Lacus	▒	▒	▒	
6	Casius	▒	▒	▒	
7	Cebrenia				
8	Amazonis	▒	▒	▒	
9	Tharsis	▒	▒	▒	▒
10	Lunae Palus	▒	▒	▒	▒
11	Oxia Palus	▒	▒	▒	▒
12	Arabia	▒	▒	▒	
13	Syrtis Major	▒	▒	▒	
14	Amenthes	▒	▒		
15	Elysium	▒	▒	▒	▒
16	Memnonia	▒			
17	Phoenicis Lacus	▒	▒		
18	Coprates	▒	▒		
19	Margaritifer Sinus				
20	Sabaeus Sinus				
21	Iapyqia	▒	▒	▒	
22	M. Tyrrhenum	▒	▒		
23	Aeolis	▒	▒	▒	
24	Phaethontis				
25	Thaumasia	▒	▒		
26	Argyre				
27	Noachis	▒	▒	▒	
28	Hellas	▒	▒	▒	▒
29	Eridania	▒	▒	▒	
30	M. Australe	▒	▒	▒	

Figure 1

The Control Net of Mars. Merton E. Davies, The Rand Corporation, Santa Monica, California, 90406

The most recent report on the control net of Mars was published in May, 1974.(1) A program is now underway to improve the control net by increasing the number of control points and attempting to obtain a more uniform distribution of points. The new spin axis and rotation rate obtained from Viking will be incorporated as well as planetary radii at the control points based on elevations portrayed on the 1:5,000,000 series topographic Mars maps and the Mariner 9 data.(2) Both Mariner 9 and Viking pictures will be used in this work.

The first analytical triangulation of this program was made on January 5, 1977; it included a band of "mapping" Mariner 9 frames encircling Mars at -30° latitude. Table 1 compares this analytical triangulation with that made in May 1974.

Table 1 Mars Control Nets

	May 1974 (Ref. 1)	January 1977
Number of Points	2061	2563
Number of Pictures	762	853
Observation Equations	11678	14014
Normal Equations	6408	7685
Overdetermination Factor	1.82	1.82
Standard Error of Measurements	0.01552 mm	0.01560 mm

References

(1) Davies, M. E., "Mariner 9 Control Net of Mars: May 1974," The Rand Corporation, R-1525-NASA, May, 1974.

(2) Wu, S. C., U.S. Geological Survey, Astrogeology Interagency Report 66.

Mars 1:5,000,000 Mapping. R. M. Batson, U.S. Geological Survey, Branch of Astrogeologic Studies, 2255 North Gemini Drive, Flagstaff, Arizona 86001

Mars 1:5,000,000 mapping program was begun in 1972 under the auspices of the MM71 project (1). Six maps of Mars at the 1:5,000,000 scale were completed under the MM71 project funding. Six maps were completed under funding provided by the Viking Project Office, and two maps were completed of the proposed Russian landing sites under funding provided by the Planetary Programs Office. The remaining sixteen maps were funded by the Planetary Geology Program Office (Planetology Programs)(2).

The 1:5,000,000 mapping series is done in several phases. The first, computation of planimetric map control, was performed under separate contract by M. E. Davies of the Rand Corporation (3). The second phase is cataloging for mosaicking the Mariner 9 pictures. All this phase was completed during fiscal 76. Base mosaics were tied to the Mariner 9 control map provided by Rand Corporation.

The third phase of the mapping effort is final map compilation for publication. In general, television pictures were not suitable for inclusion in formally published maps, because they are frequently taken under a wide variety of illumination and camera alterations. Frequently, pictures had different resolution levels. In some areas, surface details were covered by clouds in some pictures but not in others. A wide variety of computer enhancements can be used to bring out a wide variety of information in the pictures. Only one version of any one picture can be included in any particular mosaic, however. In the 1:5,000,000 Mars mapping project, therefore, skilled photo interpreters were employed to examine all available data in detail and to portray the topography as shaded relief. The portrayal techniques were especially designed to produce a clean cartographic product suitable for formal publication as a general purpose map and as a base map for continuing studies, such as geologic mapping.

A fourth phase of the mapping included compilation of surface elevations based on correlation of a wide variety of data from Mariner 9 and from earth-based observation. The former includes atmospheric pressures (hence surface elevation) derived from the UVS and IRIS experiments, spacecraft occultation measurements, doppler tracking of the spacecraft which provided dynamic information on the figure of Mars. The latter consisted primarily of radar measurements taken at Goldstone and Haystack. The topographic information is expressed in the form of contour lines interpolated and inferred from the value and location of support elevations (4). These contour lines are fitted to the shaded relief for formal publication. This work was completed under the sponsorship of the MM71 project and the Viking Project.

Two versions of each map are published. The first, designated as a shaded relief map of a named quadrangle of Mars, shows the relief and feature names only. The second designated as a topographic map of a named quadrangle of Mars, contains surface coloration (albedo markings), control lines, and nomenclature superimposed on the shaded relief.

As of the beginning of fiscal 78, all work was complete on the project except for ten final shaded relief drawings, and twelve albedo surface coloration overprints. Compilation of all of these products will be complete and the products will be sent to the Publication Division of the U.S. Geological Survey for subsequent publication as "I-Maps" by September 30, 1977. Final publication for distribution of the products should be complete by July of 1978.

References and Notes

1. R. M. Batson, J. Geophys. Res. 78, 4424 (1973).

2. R. M. Batson, Am. Cartog. 3, 57 (1976).

3. M. E. Davies, Mariner 9 Control Net of Mars: May 1974 (Rand, Santa Monica, California, 1974).

4. S. S. C. Wu, Mars Synthetic Topographic Mapping, A Dissertation submitted to the Faculty of the Department of Civil Engineering and Engineering Mechanics in partial fulfillment of the requirements for the degree of Doctor of Philosophy with a major in Civil Engineering in the Graduate College, The University of Arizona, 1976.

Geologic Map of the Mare Australe Area of Mars (1/5m). C. D. Condit and L. A. Soderblom, Br. of Astrogeologic Studies, U.S. Geological Survey, Flagstaff, AZ 86001.

The south polar region of Mars, situated within the heavily cratered hemisphere, is one of the most geologically diverse on the planet. Units exposed in this area range in age from the oldest to the youngest found on Mars. The oldest materials are the rims of large degraded craters, which are surrounded and filled by smooth inter-crater plains. A circular scarp and ridge structure about 875 km in diameter, centered at 83°S, 266°W, forms the great south polar basin and is interpreted to be the largest of these degraded craters. The surrounding smooth inter-crater plains material is apparently a combination of debris eroded from these ancient craters combined with more recent eolian deposits. The ridged plains material, centered near 68°S, 310°W was probably deposited in multiple episodes after the development of the smooth inter-crater plains. The ridged plains material is interpreted as a lava flow unit. The smooth plains material located between 100°W and 340°W and north of 80°S, forms a featureless region of low relief. This unit is probably composed of fine particulate matter, some possibly of volcanic origin that fell from the atmosphere along with or alternating with particles of frozen volatiles (1, 2, 3, 4).

Evidence for a major erosional period following the deposition of the smooth plains material can be found in several areas. Cliff rimmed mesas superposed on the ridged plains material at 68°S, 310°W are interpreted as remains of a much more extensive deposit of smooth plains material which once covered much of the ridged plains, and has since been eroded. A pedestal crater, located within the inter-crater plains material at 76°S, 110°W, may, according to McCauley (5) provide more evidence for erosion. Additionally, numerous cliff rimmed depressions which have been developed presumably by deflation (1) into the smooth plains material at 83°S, 75°W has resulted in etched plains material. The etched plains probably developed during this erosive cycle, because layered plains material, which unconformably overlies the smooth plains material, has been deposited in some areas within the etched material.

The layered plains material, which is composed of 40 or more layers, each 10 to 50 meters thick is thought to consist of eolian debris of global origin and reworked smooth plains material, probably combined with water ice. This complex, which has been eroded into several benches separated by rounded slopes on which the layers outcrop, is transected by two major erosional reentrents radial to the spin axis of the planet. The layered plains material unconformably overlies the smooth plains, inter-crater plains and old crater materials. The erosive benches and reentrents, combined with the common occurrence of linear grooves indicates that the layered plains are in a continuing erosive period. The permanent polar ice cap is the youngest unit in the south polar region. As its farthest retreat during the Mariner-9 mission it covered about 68,800 km^2 and was offset 200 km from the rotational axis of the planet, centered at 87°S, 43°W. Constraints placed on the stability of CO_2-ice dictated by pressure and solar insolation indicate that the permanent South polar ice cap is water ice (4).

1. R.P. Sharp, J. Geophys. Res. 78, 4222 (1973)
2. J.A. Cutts, J. Geophys. Res. 78, 4231 (1973)
3. B.C. Murray, L.A. Soderblom, J.A. Cutts, R.P. Sharp, D.J. Milton, R.B. Leighton, Icarus, 17, 328 (1972)
4. B.C. Murray and M.C. Malin, Science, 182, 437 (1973)
5. J.F. McCauley, J. Geophys. Res. 78, 4123 (1973)

Geology of the Ismenius Lacus Quadrangle (MC-5), Mars. B. K. Lucchitta, U.S. Geological Survey, 2255 North Gemini Drive, Flagstaff, Az. 86001.

The Ismenius Lacus quadrangle includes the northernmost extension of the cratered highlands that occupy a major part of the southern martian hemisphere. It includes three prominent physiographic provinces: cratered highlands in the south, relatively featureless plains in the middle, and mottled plains in the north. The highlands are separated from the plains by a belt of dissected terrain containing mesas and buttes ["fretted terrain" of Sharp (1)].

The highlands are subdivided into six intergradational map units: hilly and cratered material around old, large craters and crater clusters; hilly plains material of irregular topography dominating the eastern highlands; ridged plains material adjoining the hilly plains to the southeast; cratered plains material dominating the western highlands; plateau material along the northern highland margin, and knobby plains material occurring inside old basins and craters. The highlands are traversed by flat-floored valleys which form integrated patterns and widen northward downslope toward the highland-plains border. The eastern highland margin is cut by parallel grooves. Northward, beyond the edge of the highlands, lies the dissected belt that contains mesas, isolated mountains with sharp crests, and areas characterized by hummocky material. The plains material and mottled plains material of the northern map area are seen through haze on the Mariner 9 images.

The southern region of the plateau has a moderate to high density of craters larger than 20 km [15 to 35 percent of surface area, (2)]. The northern border region of the plateau is less densely cratered (5 - 15 percent) and the northern plains have a low crater density (less than 5 percent).

Contours on the map show that the entire region slopes gently from 4 km elevation in the southeast to -2 km in the northwest. Detailed, approximately north-south topographic profiles (3), however, show the plateau to gently rise toward the northern scarp, where it abruptly drops 1.5 - 2 km. Relief on the plateau surface is on the order of 0.5 km, and valley walls measure 0.5 - 1 km.

The geologic history of the area is recorded by an early, high, meteoroid flux forming many overlapping craters similar to the highlands of the Moon; later, outpourings of large volumes of lava buried most of the old cratered surface and created the highland units. Alternatively, isostatic adjustment of a youthful and active martian crust and early volcanism may have eradicated many craters of the period of high flux and created the rimless craters and extensive intercrater plains now seen on the highland surfaces. After formation of the highlands, craters of c_3 age were superposed (c_1 craters are oldest, c_4 craters are youngest). A period of erosion ensued; some fluid material, probably water, carved out canyons and valleys, and the highlands became dissected into mesas and buttes. The dissection proceeded along linear structural trends, which resulted in straight scarps and grooves, and curved trends, which follow the structural imprint of buried craters. The present northern margin of the highlands developed a large escarpment during this time. How far the exposed part of the highland units extended beyond this escarpment before erosion is not known, but at least 500 km is indicated by the dissected belt. After the major dissection was completed, scarps bounding valleys and mesas continued to retreat laterally by mass wasting and possibly wind erosion. A period of late volcanism that began during c_3 time flooded parts of the northern smooth plains and the dissected highland area, and wind deposited sheets of sand and dust on the smooth plains, valleys, intermesa lows, and in the deep interiors of

young craters. An interplay of wind deflation and deposition continues to the present.

References

(1) Sharp, R. P., Jour. Geophys. Research 78, 4073-4082 (1973)

(2) Soderblom, L. A., Condit, C. D., West, R. A., Herman, B. M., Kreidler, J. T., Icarus 22, 239-263 (1974)

(3) Barth, C. A., Hord, C. W., Stewart, A. I., Dick, M. L., Schaffer, S. H., and Simmons, K. E., Laboratory for Atmospheric and Space Physics, University of Colorado, Boulder, 649 p. (1974)

Geologic Map of the Amazonis Quadrangle (MC-8). E. C. Morris, U.S. *Geological Survey, 2255 North Gemini Drive, Flagstaff, Az. 86001*
S. E. Dwornik, NASA Headquarters, Washington, D. C. 20546

The Amazonis quadrangle lies within the northern sparsely cratered hemisphere of Mars (1). The dominant structural and physiographic features of the quadrangle are low featureless plains (Amazonis Planitia) in the center third of the quadrangle, the western flanks of the large volcanic construct, Olympus Mons, and its associated aureole deposits (Solci Olympus) which lie on the eastern slopes of the plains and an area of rough knobby terrain along the western edge of the quadrangle. The central plains descend northward into the circumpolar lowlands (Arcadia Planitia, Vastitas Borealis) and rise southward where they are bounded by the cratered terrains of the equatorial region of Mars.

The oldest material exposed in the Amazonis quadrangle is rough knobby material that forms the western margin of the central plains. The exposures of the knobby terrain are a consequence of elevation and degree of burying by the various plains-forming materials which fill the central plains and cover its margins. The knobby material in the quadrangle is probably partially buried eroded remnants of primitive densely cratered terrain (2). Much of the knobby material is arranged in vague arcuate and circular outlines suggestive of old eroded craters. The density of C_2 and C_3 class craters is the highest of all units within the quadrangle and their size frequency distribution indicates an age comparable to the cratered terrains in the equatorial regions of Mars (3).

The next oldest material is the rolling plains unit that forms the southern margin of the basin. The topography of this material consists of low, rolling elongate highs and indistinct lows trending generally in a northwest direction. The highs in some local areas break up into very irregular trending scarps and fractures. The undulating character of the rolling plains, its elongate highs, ridges and scarps suggest the material is mostly volcanic plains formed from lavas, possibly basalts, with a thin covering of eolian deposits.

The smooth plains form the youngest plains-forming material within the quadrangle and overlies, and buries, or embays all other units and fills the interiors of many craters. At 2 to 3 km resolution the smooth plains material is essentially featureless and sparsely cratered, having very few craters larger than 20 km in diameter. The density of craters appears to increase westward with the least number of small craters (< 20 km diameter) in the plains surrounding Olympus Mons. Because of the increase in crater density westward, an arbitrary division is made between the materials of smooth plains and plains. Plains material, in both high and low resolution pictures, appears identical to the smooth plains unit except for the greater number of small craters.

The plains and smooth plains materials probably include both aeolian and volcanic materials. Aeolian material may be interbedded with the lavas and almost certainly the present surface is partially covered with wind blown debris. The combined deposit appears to thin to the west and south.

Olympus Mons is the youngest feature within the quadrangle. However, the building of the large shield volcano and its associated aureole deposits was probably partly contemporaneous with the formation of the plains and smooth plains material. The large volcano is bounded at its base by a roughly circular scarp 1 to 4 kilometres high. It is proposed that the cliffs bounding Olympus Mons are fault scarps that have been slightly modified by eolian erosion (4). Though roughly circular, the scarp is actually composed of a number of intersecting linear segments some of which appear to have rotational displacement along their traces. The net effect of the

movement along the bounding faults is that Olympus Mons has moved upward in respect to its surroundings.

Aureole deposits, because of their spatial arrangement surrounding Olympus Mons, are clearly associated with the volcanism that produced the large shield volcano. The aureole is interpreted to be a series of very fluid lava flows that were extruded during several episodes prior to the building of the main edifice of Olympus Mons. Transection and superposition relationships exhibited in the southeastern part of the Amazonis quadrangle and also seen in the Tharsis quadrangle (2) indicate that the aureole was deposited after the formation of the rolling plains, but prior to the deposition of the smooth plains material which overlaps and buries some of the aureole deposits. The aureole deposits in turn superimpose one another and each has a different scale of texture of curvilinear troughs and ridges. Also there is a difference in the orientations of these features in relation to overlying and underlying deposits. In the Amazonis quadrangle four aureole deposits are recognized. The deposits are roughly circular with the curvilinear ridges and troughs oriented generally parallel to their margins.

The geologic history of the Amazonis quadrangle, interpreted from the stratigraphic relationships of the exposed rock units, began with the erosion of ancient cratered terrain to form the knobby material. This material probably represents remnants of densely cratered and hilly terrain that developed early in the history of Mars during a period of intense meteorite bombardment. Following the decline of the high impact flux there was a long period of erosion and degradation of the cratered terrain, with subsequent development of the knobby terrain. Many of the rim deposits of the old craters survive only as vague circular arrangements of knobs. The next major event was the flooding of the old cratered and knobby terrain in the southern regions of the map area by a thick series of basalts which form the rolling plains. The undulating character of the rolling plains and some of its ridges and scarps may reflect the buried topography of the old cratered plains. The emplacement of the rolling plains material was followed by a period of intense eolian activity during which the rolling plains and knobby terrain was eroded and buried in places under a blanket of eolian debris which form the plains and smooth plains materials. Prior to the deposition of the smooth plains material and possibly partly contemporaneous with its formation there began an extended period of volcanism along the eastern margin of the basin, centered in the area of Olympus Mons. A succession of very fluid lavas spread up to 1500 km northwestward from the fissures and conduits of the volcanic center. The younger flows were perhaps a little more viscous than the oldest one, extending less distance from their source. The volcanic activity was probably confined more and more to one center of volcanism with the subsequent construction of Olympus Mons. As the huge volcano continued to grow, the surface sagged around the volcano locally forming a shallow basin. A series of intersecting fractures developed around the outer margins of the shield. The last episode of volcanic activity of Olympus Mons probably was preceded by an uplift of the entire volcano along the previously developed fracture system. This uplift possibly was due to an expansion of the magma chamber beneath the volcano, perhaps analogous to the extension of terrestrial volcanoes observed prior to eruption but on a vastly different scale. The scarp that was formed by the uplift has been modified and partly buried in some parts by subsequent volcanic and eolian activity.

References

(1) Carr, M. H., Masursky, H., and Saunders, R. S., 1973, Jour. Geophys. Res. 78, p. 4031-4036 (1973).

(2) Carr, M. H., U.S. Geol. Survey, Misc. Geol. Inv. Map I-893 (1975).

(3) Hartmann, W. K., Jour. Geophys. Res. 78, p. 4096-4116 (1973).

(4) Carr, M. H., Sci. Am., 234, p. 32-43 (1976).

Geology of the Phoenicis Lacus Quadrangle, Mars (MC-17), Harold Masursky, A. L. Dial and M. E. Strobell, U.S.Geological Survey, Branch of Astrogeologic Studies, 2255 North Gemini Drive, Flagstaff, Arizona 86001.

The Phoenicis lacus region includes two of the largest shield volcanoes on Mars, Arsia Mons and the southern half of Pavonis Mons. They rise to about 27 km elevation, towering 16 km above the surrounding Tharsis plateau. Syria and Sinai plana, part of the Tharsis plateau, are about 11 km above Mars mean level. Four sequences of lava flows are seen at Arsia Mons, with younger lava flows lying unconformably on older, wind-eroded flows. The gross shape of the shield and the shapes of the individual flows suggest that most flows are basaltic in composition. Only the third, summit-forming sequence on Arsia Mons may be more silicic in composition; these flows are shorter, thicker, and stubbier than the older and younger flows in the volcanic stack. Similar sequences are seen in the other great shields to the north and west, Ascraeus Mons and Olympus Mons.

Lava flows with flow fronts also cap the high plateau; their morphologic similarity to terrestrial and lunar lava flows suggests that they are also basaltic in composition. Overlap relationships and crater counts indicate that the lava sequences are older to the southeast and southwest; the geometric relationship is like shingles on a roof with successively younger units exposed higher on the plateau.

Limited outcrops of the ancient cratered terrain occur in the south-central part of the region and near the summit of the plateau. Only a thin layer of lava appears to mantle the subjacent ancient rocks on the plateau, indicating that the ancient crust has been uplifted nearly 10 km there. A large positive gravity anomaly over the plateau may indicate that dense mantle rocks have been uplifted also.

Tectonism that raised the crust and mantle to form the plateau probably took place over a long period of time. The faults that bound Valles Marineris, the great graben to the east, and the intersecting faults in the Noctis Labyrinthus area in this region vary greatly in freshness. Because degradation is interpreted to be age dependent, the inferred sequence of faulting can be determined from the varying amounts of degradation, and from intersection relationships. The intersecting faults lie at the apex of uplift and resemble terrestrial fault systems that occur over salt domes and experimentally produced faults over uplifts.

Dark and bright crater tails and irregular bright and dark patches are common and are inferred to be eolian deposits. The 1976 Viking photographs show that these markings have changed deamatically from their appearance in the 1972 Mariner 9 photographs.

Excellent correlations were obtained between radar observations (elevation, reflectivity, root mean square slopes, and peak power) from the Goldstone and Arecibo dishes in 1971, 1973 and 1975, and the topographic and geologic maps drawn from Mariner 9 images and other data. The sharpest reflectivity peaks are observed over areas where little or no mantling materials are inferred to be present; sharp peaks occur in areas where bright halos, presumed to be caused by blocky ejecta blankets, surround small craters, thus implying a very thin regolith. The lowest reflectivity seems to occur where the surface is covered with eolian deposits, in some places reworked to dune forms.

Geologic Map of the Iapygia Quadrangle of Mars. Gerald G. Schaber, U.S. Geological Survey, 2255 N. Gemini Dr., Flagstaff, AZ 86001.

The geologic map of the Iapygia quadrangle of Mars (MC-21) was completed during 1976 and is currently in press for 1977. The Iapygia quadrangle, in the equatorial region (0° - 30°S; 270° - 315°W) of Mars is mainly ancient hilly and cratered upland terrain. The southern one third of the quadrangle is dominated by mountains and knobby materials representing mountains of pre-Hellas material and material related to the Hellas Basin, and mappable in a 500 km wide zone circumjacent to it. The northeastern quadrant of Iapygia contains two large arcuate structural scarps and moderately low-albedo mountain materials and knobby deposits, both associated with formation of the Isidis Basin. The major part of the Iapygia quadrangle is mapped as hilly and cratered upland materials and crater units, with subordinate various plains deposits. A dominant feature of the landscape within Iapygia is the 475 km diameter basin Huygens which has a subtle inner ring structure. The Iapygia quadrangle appears to lie in a large (2000 km diameter), 2+ km deep depression in the equatorial uplands that is well shown on Earth-based radar profiles. Three morphological classes (C_3 freshest - C_1 most subdued) of craters have been mapped in the quadrangle with a lower size cutoff limit of 30 km diameter. Three hundred and six craters > 30 km diameter were recognized within the 3.9×10^6 km^2 of the Iapygia quadrangle.

The mountain and knobby materials mapped on the rim of the Hellas and Isidis Basins are thought to represent the most ancient materials within the quadrangle and perhaps on the entire planet. The absence of recognizable ejecta from the Syrtis Major Basin to the north suggests that strong and complex surface wind regimes and other erosional processes in this area may have completed the destruction of any high-standing rim deposits. Erosion and denudation may have been accompanied by thick mantling of surface materials by post-basin plains deposits. The age relations between Hellas, Isidis and Syrtis Major are uncertain because of intense erosion, plains-forming episodes and the absence of recognizable secondary craters from any of the basins.

The major part of the Iapygia quadrangle forms uplands mapped as hilly and cratered material, exposed primarily in the southern latitudes of the planet, but extend to 40°N around the 330°W meridian. Flat-floored, nearly rimless craters abound on this surface and intercrater areas are locally flat to undulating; scarred by small dendritic erosion channels. Earth-based radar returns from these channeled surfaces indicate substantial roughness at the 20 to 60 m scale. Earth-based radar observations of Mars have also shown that the hilly and cratered unit between 14°-18°S and west of 309°W has sharply reduced rms slopes relative to the hilly and cratered surfaces east of the basin Huygens. This flatter, more subdued (less channeled) surface continues across the Sinus Sabaeus quadrangle (MC-20) to the west.

The cratered plains material mapped in Iapygia is distinguished by the lack of older C_1 and C_2 craters with diameters greater than about 30 km, fewer dendritic channels and the presence of moderately-to-well developed surface wind features (e.g., variable light and dark streaks). The cratered plains are patchy within the quadrangle, and appear to embay the old hilly and cratered surfaces, but are, in turn, overlapped by the younger plains materials. The cratered plains are interpreted as consisting primarily of eolian materials, intermixed in part with local volcanic deposits derived locally or from the general area of Syrtis Major Planitia and Isidis Planitia to the north.

The hummocky plains is found only within the floor of the basin Huygens where they occupy the highest terrain within the basin floor. It is

characterized by a low crater density and rolling hummocky topography; and is interpreted as consisting of volcanic flows mantled by sedimentary and eolian deposits. The ridges' plains are distinguished by lunar mare-like wrinkle ridges and numerous, well developed light and dark wind streaks. The ridged plains are interpreted as basaltic lava flows mantled in part by thin eolian materials.

The youngest plains materials (designated "plains") mapped within the quadrangle is characterized by the lowest crater density of all geologic units, at least down to the 1 km diameter size, and a high apparent albedo. The presence of young plains material throughout topographically low regions, including crater floors and other topographic traps, supports the hypothesis that it consists largely of windblown deposits.

Miscellaneous map units recognized within the Iapygia quadrangle include (a) dark mottled plains and peripheral plains associated with the floor of Hellas, (b) crater dark floor material and crater central peak material, (c) abnormal crater material of probable volcanic origin and (d) channel materials.

The increased number of total craters > 40 km diameter on the Hellas knobby ejecta relative to the hilly and cratered surfaces, confirms the photogeologic observation that no surfaces within the quadrangle are older than those associated with the Hellas impact event. Resurfacing of the hilly and cratered units within the quadrangle could have been brought about by erosion, or more likely, by deposition of sediment and(or) volcanics in early post-Hellas time.

The interpretable geologic history within Iapygia begins with the impact of planetisimals that produced the large Hellas and Syrtis Major Basins, followed soon after by the formation of the Isidis Basin. Subsequent resurfacing and channeling of the hilly and cratered surfaces were followed by deposition of the various plains units and ending with the formation of the variable light and dark wind streaks. The period of intense early bombardment continued throughout the formation of the hilly and cratered surfaces but was greatly reduced by the time of the deposition of the crater plains unit.

Geology of the Aeolis Quadrangle of Mars. D. H. Scott and E. C. Morris
U.S. Geological Survey, Flagstaff, Arizona.

The Aeolis quadrangle is located in the eastern equatorial region of Mars between 0° and 30°S lat and 180°W to 225°W longitude. Two physiographic provinces are represented in the quadrangle: 1) Elysium Planitia in the north, a subdivision of the broad planet-encircling belt of relatively young lowland plains, and 2) ancient cratered highlands in the south forming widespread plateaus and extending to near the polar deposits around the southern ice cap. These two types of terrain are separated by a long irregular scarp trending northwest across the map area. Two large channels transect the highlands and have several features characteristic of terrestrial river beds. Apollinaris Patera, a large shield volcano, projects above the plains in the northeast part of the quadrangle. More than four km of relief occur across the map area from the high plateau in the south and west to the low plains in the north.

The oldest rocks in the quadrangle are hilly and cratered material, old crater rims, and two small mountains near the east margin of the quadrangle (figure 1). Craters up to 50km diameter are common in the hilly and cratered highlands which consist in large part of interbedded ejecta blankets. Other areas of the highlands are partly covered by lava flows and have smooth intercrater surfaces. These rocks are subdivided by their crater populations into a plateau unit and cratered plateau unit which are intergradational. High resolution photos indicate that in some areas differences in crater density result from wind erosion, in others it reflects variations in lava thickness and depth of burial.

Knobby material occurs along or near the boundary between the plains and plateau units. Here, the knobby terrain is produced by erosional retreat of the boundary scarp. Low relief knobs are remnants of rocks in the lower part of the stratigraphic section such as hilly and cratered material. High, flat-topped knobs have plateau material on their upper surfaces.

Plains deposits are widespread in the lowlands but small patches occur within crater floors and other depressions throughout the highlands. The plains are mostly featureless at low resolution but show linear ridges, grooves, hillocks and conical mounds, pits and depressions, light and dark mottling, fractures, and, in places, wrinkle ridges and lobate scarps characteristic of the basalt flows of the lunar maria. Crater densities are low compared to most of the highland rocks.

Two channels within the quadrangle, Ma 'adim Vallis and Al-gahira Vallis, are comparable to some of the other major channels in the Lunae Palus and Oxia Palus regions of Mars. They both show morphologic characteristics of terrestrial river beds including well developed dendritic tributaries that constitute integrated river systems. Topographic contours (1) also suggest that separate drainage basins once existed for each of these large channels. The gradients of each channel are high, about .007 over the central 300 km of their length; this is about twice that of the Colorado River along 300 miles of its upper course. In places, some tributaries and smaller channels are discontinuous, perhaps indicating burial by younger material or, possibly, subsurface diversion through fissures or lava tubes.

The large shield volcano, Apollinaris Patera, is morphologically intermediate in age compared to the young shields of the Tharsis region (2) and those around the Hellas basin (3). The outer flanks of the volcano are relatively gentle but steepen toward the crest; the summit caldera consists of three coalescing collapse depressions. A prominent scarp partly encloses the structure except on the south where, it it once existed, it is now covered by lava flows.

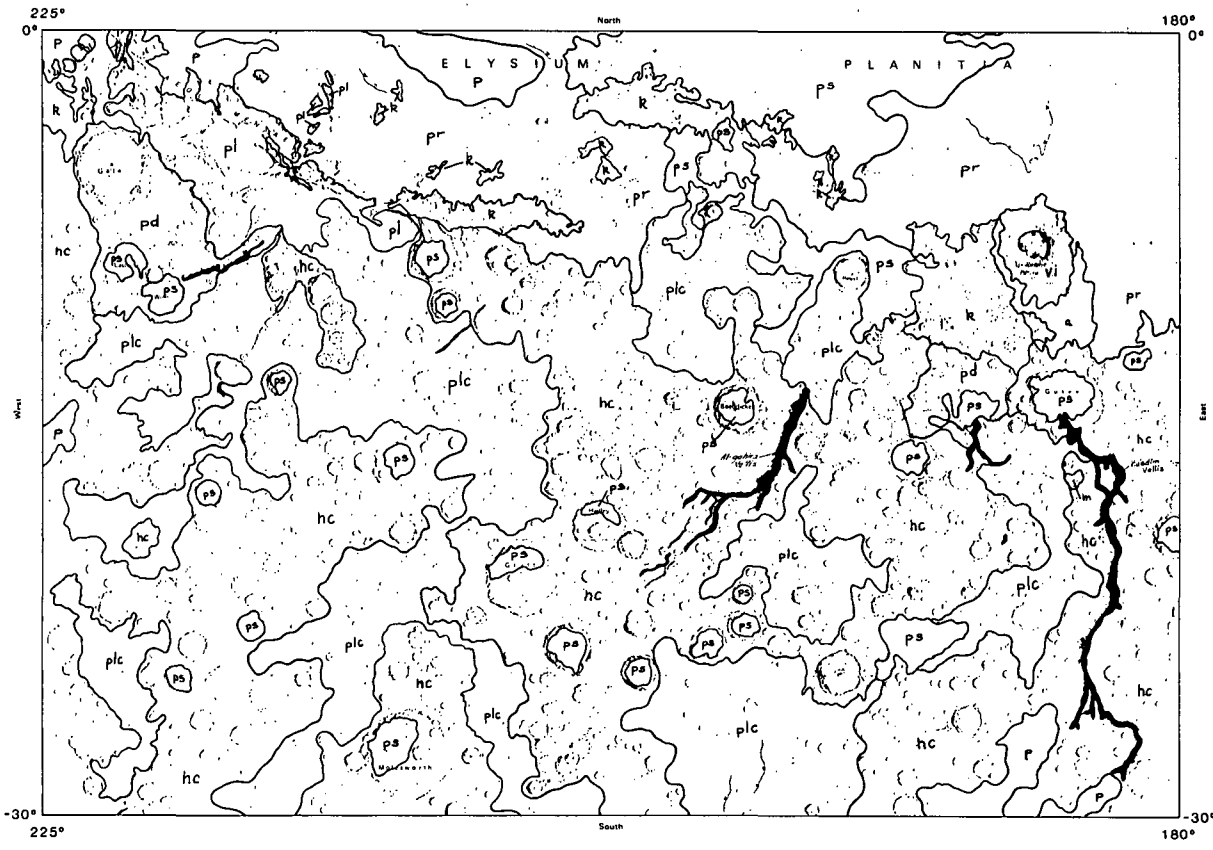

Figure 1. Geologic map of the Aeolis quadrangle of Mars. Major rock units heavy outline: hc (hilly and cratered), m (Mountains), plc (cratered plateau), pl (Plateau), k (knobby), pd (deflation plains), pr (rolling Plains), p (Plains), ps (smooth plains), channels (black), a (aureole around Apollinaris Patera).

An early stage in the geologic history of the Aeolis quadrangle is recorded in the hilly and cratered terrain of the southern highlands. Volcanism on a regional scale followed the period of high impact flux. Large areas of hilly and cratered material were buried, leaving smooth flat intercrater surfaces and the projecting rims of many large craters. Sources of the lava are unknown, probably they were extrusions from fissures. Tectonism during and after this volcanic period uplifted the present highlands along a northwest trending fault system. Initially this fault boundary was farther to the northeast; subsequent erosion and scarp retreat together with stream channeling and dissection of the highlands covered large areas of the lowlands with debris from these processes. Volcanism continued throughout this period but seems to have been mostly confined to the lower regions, producing rolling plains material and the shield, Apollinaris Patera.

Later stages of martian history in the Aeolis region are distinguished only by a light flux of small impacts and continuous erosion and deposition by the wind.

References

1) U.S. Geological Survey, Atlas of Mars, 1:5,000,000 Topographic Series I-1001 (1976).

2) M. H. Carr, U.S. Geol. Survey Misc. Geol. Inv. Map I-893 (1975).

3) D. B. Potter, U.S. Geol. Survey Misc. Geol. Inv. Map I-941 (1976).

Geology of the Phaethontis Quadrangle, Mars. J. Hatten Howard III, Department of Geology, University of Georgia, Athens, GA., 30602

The Phaethontis quadrangle is dominated by densely cratered uplands and plateaus. These terrains are probably primitive Mars crust, reworked and partially emplaced during late stages of planetary accretional bombardment. The below-saturation density of large craters and the flat intercrater areas of these most densely cratered martian terrains may have resulted from erosional obliteration (1) or depositional burial (2). Extensive low-lying areas within the cratered terrains and the floors of large craters are superposed and buried, to different degrees, by plains-forming materials, in which degraded or partially buried crater forms can be seen over most of the quadrangle area. Some topographically higher portions of the crust, not covered with plains-forming deposits, are furrowed by small branching channels, 1-3 km wide, which may be either volcanic or fluvial in origin. This subdued irregular topography probably results from aeolian erosion.

The widespread plains-forming deposits are derived from at least three major martian geologic provinces. Moderately cratered plains occur in extensive low areas of the highly cratered crust to the south, lapping and embaying these terrains and covering floors of craters within the uplands. Rims of large craters project through the plains deposits; rims of other craters are nearly level with the plains, yet the flat floor lies at a level below the plains. This plains-forming unit is within the southern mantled terrain (1) and may, at least in its upper part, be a blanket of aeolian debris from the south polar region.

A lightly cratered plains-forming deposit, which occupies widespread low areas of the subdued plateau terrain and floors of large craters in the north-central and northeastern portions of the quadrangle and which has faint crater outlines within the plains and a gentle hilly surface, may be volcanic ash-flow or lava deposits or aeolian debris deposited over older, cratered crust. A smooth plains deposit, of very low crater density, extends southwestward into the quadrangle from the elevated Tharsis plains. Burial of plateau terrain is so extensive in the northeastern corner of the quadrangle that only high islands of the plateau remain unburied. To the southwest the smooth plains unit becomes thinner, embaying and lapping the plateau terrain and merging imperceptibly with lightly cratered plains. This smooth plains-forming deposit is the youngest in the quadrangle and is probably still being deposited by aeolian activity. Wind directions of the 1971 dust storm, determined from dark wind-formed streaks, suggest that material of the smooth plains deposits, and perhaps of the lightly cratered plains, is derived from the east or northeast.

Some of the most geologically interesting features in the Phaethontis quadrangle are several plains, plateau, and knob-and-mesa terrains which comprise approximately 500,000 km^2 of the Mars crustal surface in the north and northwest portions of the quadrangle (3). Knob-and-mesa material, consisting of bright, rounded to flat-topped hills, occurs in two clusters, of about 10,000 km^2 each, within and rising above surrounding plains units.

Plateau units of this area, thought to be old units superposed on older, densely cratered crustal material, exhibit different morphologies. One plateau terrain bears furrows, some of which are branching, and many areas of the smooth plateau surface are dissected by steep-walled gorges and isolated pits. The bounding escarpment between the plateau and the adjacent, lower plains is crenulated by steep-walled gorges. A second plateau unit also abuts surrounding lower plains with steep escarpments. The third plateau unit has localized topographic surfaces of quasi-parallel and branching furrows, 1-3 km wide, with surface patterns suggestive of sinuous and branching furrows. Some areas of this plateau unit have a more planar

surface, which is cut with parallel grooves and which adjoins lower plains with a steep escarpment.

The escarpments, canyons, pits, and grooves either represent different erosional etching, stripping, or collapse processes, or are several responses of different unit materials to similar processes. The furrows may be primary features associated with formation of the unit which contains them, or they may be the result of erosion.

Few features of volcanic origin have been identified in the quadrangle. Some features in smooth plains to the northeast may be lobate fronts of lava flows, and small branching furrows or channels in the subdued plateau terrain and adjacent low-lying plains may be lava channels or collapsed lava tubes. Two small areas of volcanism may be the dome-like hills and small cones in the plains to the southwest and the local hilly unit superposed on a crater within the subdued plateau in the north.

The major tectonic feature in Phaethontis quadrangle is Sirenum Fossae, a belt of narrow grabens and fault escarpments extending almost 2000 kilometers west-southwest across the cratered plains and plateaus from the Tharsis Ridge. The cratered plains and plateaus in the eastern part of the quadrangle are also transected by northeast-trending grabens and lineaments (interpreted to be eroded or mantled grabens). Sirenum Fossae and these latter grabens are components of the southern fan of fractures produced by crustal upwarp in the Labyrinthus-Tharsis region about 1 b.y. ago (4).

Impact cratering dominated the early history of the Phaethontis quadrangle; a crater-saturated surface of early bombardment may have been removed by some obliterating process and repopulated with the presently observed crater density by the decreasing flux of late-accretionary bombardment (1). Successive, or perhaps coeval, plains-forming events have since filled low areas of the heavily cratered surface. The plains were probably formed by aeolian and volcanic processes, although only the youngest, smooth plains in the northeast show possible volcanic flow features. The origin and time of formation of the small furrows and channels which dissect some of the plateau terrains is uncertain; these channels may represent one or more volcanic or fluvial events. Tectonism, forming the systems of extension fractures, has affected all but the youngest plains.

Wind activity now predominates as the major geologic agent. Dark streaks associated with small craters are common in the northeastern smooth plains and dark patches occur on portions of floors of large craters throughout the area and on the plains at the base of adjoining uplands (48°S, 164°; 58-61°S, 167-170°). At least some of the dark areas are dune fields--one of which is illustrated by a high-resolution frame--which have accumulated in the lee of uplands, mountains, and crater walls, rims, and central peaks.

1. L. A. Soderblom, C. D. Condit, R. A. West, B. M. Herman, T. J. Kreidler, Icarus 22, 239 (1974).

2. D. H. Wilhelms, J. Geophys. Res. 79, 3933 (1974).

3. J. H. Howard, U. S. Geol. Surv. Map, in review; this volume (1977).

4. M. H. Carr, J. Geophys. Res. 78, 4031 (1974).

Knob-and-mesa Terrains, Dissected Plateaus, and Knobby Plains of the Atlantis-Mare Sirenum Region, Phaethontis Quadrangle, Mars. J. Hatten Howard III, Department of Geology, University of Georgia, Athens, GA., 30602.

The northwestern part of the Phaethontis quadrangle--the Atlantis-Mare Sirenum region--is comprised of several plains, plateau, and knob-and-mesa terrains which represent unique crustal units, erosional modification of old crustal material, and burial of low areas. Knob-and-mesa material consists of bright, rounded to flat-topped, steep hills, 1-4 km in diameter. This terrain occurs in two clusters (35°S, 177° and 38°S, 171°), of about 10,000 km^2 each in area, within and rising above surrounding plains units. The knob-and-mesa terrains may be localized units within the crust, differing in composition and erosional characteristics from other crustal units; possibly they are plutonic masses, regionally fractured and eroded by aeolian processes. The close clustering and geographic isolation of each cluster differ from other described areas of knobs (1, 2, 3, 4).

Three plateau units of this area, either old units superposed on or emplaced within older, densely cratered crustal material, exhibit different morphologies. One terrane, a dissected plateau material, bears furrows, often with branching patterns, and areas of the smooth plateau surface are dissected by steep-walled gorges and isolated pits (40°S, 174°). The boundary between the plateau and the adjacent, lower plains is often an escarpment, crenulated by steep-walled gorges (41°S, 169°). This plateau material may be composed of indurated ash-flows or aeolian deposits emplaced in low areas of cratered terrain.

A second plateau unit also abuts surrounding lower plains with steep escarpments (43°S, 177°), some of which correspond to crater outlines. This plateau unit may be either superposed strata or a localized unit within old crust. Subsequent erosion has removed those materials of the plateau material which were brecciated by impacts.

A third unit, subdued plateau terrain, has quasi-parallel and branching furrows, 1-3 km wide, and bears surface patterns suggestive of sinuous and branching furrows. In some areas a more planar surface, which abuts lower plains with a steep escarpment, is cut with parallel grooves (34°S, 148°). The escarpments, canyons, pits, and grooves of the plateau terrains either represent different erosional etching, stripping, or collapse processes, or are several responses of different lithology and structure to similar processes. The furrows may be primary features associated with formation of the unit, or they may be the result of erosion.

Two plains units, adjacent to the plateau and knob-and-mesa terrains, seem to be related, geologically, to the neighboring higher terrains. One plains-forming terrain, from the center of which rises a cluster of knobs and mesas, has as its only relief at B-frame resolution (except for small craters) small ($\leq$ 1 km) bright isolated hills (36°S, 171°); the hills may be volcanic domes or small plutonic masses exposed by erosional stripping of overlying crustal material. The cluster of knobs and mesas may be a large remnant of this stripped unit. The other plains unit, of greater area and extending into the Eridania quadrangle, surrounds one of the plateau units and abuts another; small-scale, low sinuous ridges on these plains may be indicative of lava sheets, subsequently modified by cratering and aeolian activity.

Contiguous coverage of this part of Mars, at A-frame scale, was accomplished during revolutions 103, 105, and 107--early in the Mariner 9 mapping mission--and, unfortunately, even the best computer enhancements of these A frames and their nested B frames permit only vague distinction of the characteristics of these terranes, by which they were mapped (5). Analysis of high-resolution Viking Orbiter pictures is needed to identify processes of scarp formation and erosional stripping, etching, and dissection of plateau

and plains surfaces; to determine the stratigraphic relationship of these terrains to the large fault system, Sirenum Fossae, which transects this region; and to gain a more complete understanding of the complex sequence of events which has produced these surfaces and their underlying materials.

1. M. H. Carr, H. Masursky, R. S. Saunders, J. Geophys. Res. 78, 4031 (1973).

2. M. H. Carr, H. Masursky, W. A. Baum, K. R. Blasius, G. A. Briggs, J. A. Cutts, T. Duxbury, R. Greeley, J. E. Guest, B. A. Smith, L. A. Soderblom, J. Veverka, J. B. Wellman, Science 193, 766 (1976).

3. J. F. McCauley, M. H. Carr, J. A. Cutts, W. K. Hartmann, H. Masursky, D. J. Milton, R. P. Sharp, D. W. Wilhelms, Icarus 17, 289 (1972).

4. D. H. Scott, M. H. Carr, U. S. Geol. Surv. Map, in press.

5. J. H. Howard, U. S. Geol. Surv. Map, in review.

Page Intentionally Left Blank

Chapter 10

MAPPING PROGRAMS

Part B

MERCURY

Page Intentionally Left Blank

Mercury Geologic Mapping Program. Henry E. Holt, U. S. Geological Survey, 2255 N. Gemini Drive, Flagstaff, Arizona, 86001.

A systematic geologic mapping program of the Mercury surface at a scale of 1:5,000,000 was initiated during the summer of 1975. The program is a joint undertaking between the Planetology Program Office of NASA, the U.S. Geological Survey, and NASA supported institutions. The objective of the Mercury Geologic Mapping Program (MGMP) is the publication of a 1:5,000,000 scale Geologic Atlas of Mercury to be producted from Mariner 10 data.

The planet Mercury is divided into 15 quadrangles at a scale of 1:5,000,000 and the Mariner 10 imagery extends over 9 quadrangles, varying from full coverage to as little as 40 percent coverage. Shaded relief maps and controlled photo-mosaics are provided as base maps for compilation of stratigraphic units and geologic structures. Over 900 pictures with surface resolutions of 400 m to 2 kms and 152 rectified and scaled stereo-pairs have been provided for map author's interpretations of geologic features, and processes.

Preliminary geologic maps of 8 quadrangles were presented at the Mercury Geologic Mappers Meeting on November 17, 1976. The photogeologic studies reveal that the Mercurian surface has a deficiency of craters in the 40 to 60 km diameter size range, and in basins larger than 250 km diameter. Fields of secondary craters occur much closer to their primary crater source covering only 1/5 of comparable lunar secondary crater field areas. The erosive effect of these secondary swarms is significant but the secondary craters themselves are well preserved. The plains areas lack volcanic features common the Moon, i.e., domes, sinuous rills, and well-defined lobate flow fronts. The large arcuate scarps which seem to be globally distributed and locally exhibit a reverse fault morphology, suggest a stress field very different from that seen on the Moon and Mars.

The Control Net of Mercury. Merton E. Davies, The Rand Corporation, Santa Monica, California, 90406

The control net of Mercury is established photogrammetrically from measurements of points on Mariner 10 pictures taken during the three flybys. The spin axis of Mercury is assumed to be normal to its orbital plane and its spin rate was confirmed to be two-thirds of its orbital period. By definition, the twentieth meridian passes through the center of the small crater Hun Kal, thus defining the system of longitudes. The horizontal coordinates of the control points are obtained by solving a single large-block analytical triangulation. The method of conjugate gradients is used to solve the normal equations. A planetary radius of 2439 km is assumed at all control points. Coordinates of the camera stations are obtained from the spacecraft trajectory, whereas the camera orientation angles are treated as unknowns in the analytical triangulation. Thus each control point contributes two unknowns (latitude and longitude) and each picture contributes three unknowns (camera orientation angles).

Three published reports reflect the progress in the control net.[1-3] Growth in the amount of data contained in the computations (identified by date) can be seen in Table 1.

Table 1 Summary of Control Net Reports

	2/23/75 (Ref. 1)	12/20/75 (Ref. 2)	9/30/76 (Ref. 3)
Number of Points	1328	1774	2378
Number of Pictures	545	680	788
Observation Equations	11234	16148	25504
Normal Equations	4291	5588	7120
Overdetermination Factor	2.62	2.89	3.58
Standard Error of Measurements	0.05892 mm	0.02836 mm	0.02311 mm

The most recent analytical triangulation contains 435 frames (201 inbound, 234 outbound) taken on Mariner 10's first encounter with Mercury, 333 frames taken on the second encounter, and 20 taken on the third. Reference 4 contains the coordinates of all of the camera stations used in the computation as well as the 12,752 measurements of the 2378 points on the 788 pictures. Reference 5 identifies the craters associated with 1548 control points on 37 figures.

References

(1) Davies, M. E., and R. M. Batson, "Surface Coordinates and Cartography of Mercury," The Rand Corporation, R-1740-JPL, March 1975, and J. Geophys. Res. Vol. 80, No. 17, June 10, 1975, pp. 2417-2430.

(2) Davies, M. E., "The Control Net of Mercury: January 1976," The Rand Corporation, R-1914-NASA, January 1976.

(3) Davies, M. E., and F. Y. Katayama, "The Control Net of Mercury: November 1976," The Rand Corporation, R-2089-NASA, November 1976.

(4) Davies, M. E., F. Y. Katayama, and J. A. Roth, "Control Point Measurements on Mariner 10 Pictures of Mercury," The Rand Corporation, R-2090-NASA, November 1976.

(5) Davies, M. E., and J. A. Roth, "Identification of Control Points on Mercury," The Rand Corporation, R-2091-NASA, November 1976.

Shaded Relief Map of Mercury. R. M. Batson, U.S. Geological Survey, Branch of Astrogeologic Studies, 2255 North Gemini Drive, Flagstaff, Arizona 86001

A set of 1:5,000,000 maps of the planet Mercury was funded during fiscal 76 (1). Compilation of these maps is essentially complete. A final planetwide map of Mercury was funded for completion during fiscal 1977. This map will incorporate appropriate Mariner 10 data and compilations from the 1:5,000,000 series. Two versions of the map will be published at 1:25,000,000. The first will be a shaded relief rendering of the planet with feature nomenclature superimposed. The second will show albedo markings and nomenclature superimposed on the shaded relief.

These maps will be completed by September 30, 1977 and submitted to the U.S. Geological Survey Publications Division for formal publication and distribution.

1. M. E. Davies, R. M. Batson, J. Geophys. Res. 80, 2417 (1975).

The Geology of the Goethe (H-1) Quadrangle of Mercury. J. M. Boyce and M. Grolier, U.S. Geological Survey, 2255 N. Gemini Dr., Flagstaff, AZ 86001.

The Goethe quadrangle (H-1) is located in the north polar region of Mercury (65°N to 90°N). Nearly 40% of the quadrangle has been photographed. The major geologic units include heavily cratered plains, smooth plains (young and old), and intercollated and superposed materials of impact craters and basins. The oldest rocks in the quadrangle comprise the heavily cratered plains units. These materials have moderate relief characterized by numerous overlapping degraded secondary craters, low subdued hills, and old craters; and comprise much of the materials in the western half of the quadrangle.

The basin related materials are located on the western edge of the 328 km diameter basin Goethe centered at 80°N lat., 45° long. These materials comprise moderate to high relief hummocks, hills, and mountains that extend from the basin rim out to $\sim$ 1/2 a basin radius.

The old smooth plains cover most of the eastern part of the quadrangle. These plains have wrinkle ridges, many of which follow the outline of buried craters. The young smooth plains occurring throughout the quadrangle in topographic lows such as craters, have relatively flat surfaces and are generally less cratered than the old smooth plains. The young smooth plains also commonly contain tectonic scarps.

Craters larger than $\sim$ 30 km have been mapped according to their ring morphologies and that of their deposits. The oldest most degraded craters are designated C_1 and generally have narrow subdued rim deposits, flat floors, containing smooth plains, and no associated secondary crater fields. This type of crater is found only superimposed on the heavily cratered plains. The morphologically freshest crater designated in this quadrangle is the type C_3. These craters have steep walls with sharp, fresh-appearing hummocky rim deposits. Secondary crater chains are associated with many of the large C_2 craters. C_2 craters are morphologically intermediate to C_3 and C_1 craters. A possible gigantic basin 1000+ km in diameter (with center coordinates of 75°N lat., 80° long.) may have produced the topographic low filled by the old smooth plains in the western part of the quadrangle.

Structural features such as wrinkle ridges, normal faults and lineaments are common but not abundant. Wrinkle ridges occur only in the smooth plains units, whereas, the lineaments and normal faults generally occur in the cratered terra materials. Obvious volcanic features such as rilles, collapsed depressions, conical and domical mountains and flow lobe scarps are not observed in this quadrangle.

Geological Mapping of Mercury Quadrangle H-3 (Shakespeare) and H-4. Ronald Greeley, University of Santa Clara at NASA-Ames Research Center, M/S 245-5, Moffett Field, CA 94035; J. E. Guest, University of London Observatory, Mill Hill Park, London NW7 2QS, England; D. E. Gault, P. O. Box 833, Murphys, CA.

Mercury quadrangle H-3 and the eastern part of H-4 cover the area between 20°N and 70°N latitude and 90°W to about 190°W longitude. Physiographically, the region includes the eastern half of the 1300 km-diameter Caloris impact basin and vast plains regions which have been subjected to compressional and tensional tectonism. Stratigraphically, the oldest features are ancient craters, basins, and related deposits, all reflecting the terminal stages of heavy bombardment. The east part of the region grades into areas mapped as intercrater plains; the origin(s) and stratigraphic reltions of this unit are of considerable debate. On the one hand, the plain may be very old (post dating even the ancient craters) and represent the early mercurian crust; on the other hand, they may be relatively young deposits resulting from volcanism, mass wasting, or impact cratering processes. Structures and units related to the formation of the Caloris Basin dominate the western region and include the primary rim of the basin, parts of a possible outer rim to the northeast, and hummocky plains and other ejecta units, some of which are similar in morphology and stratigraphic relations to deposits around the lunar Orientale Basin. Smooth plains cover the largest area and, except for young impact craters, are the youngest deposits on Mercury. Smooth plains in the Caloris basin may be volcanic or may be impact melt; crater counts, however, indicate that the plains are significantly younger than the age of formation for the basin, lending support to a volcanic origin for the smooth plains. The origin of smooth plains outside the basin is also in question. Detailed mapping currently in progress will result in differentiation of smooth plains units and should help resolve some of the problems of its origin.

Geologic Mapping of the Victoria Quadrangle (H-2) Mercury.

Elbert A. King, Department of Geology, University of Houston, Houston, Texas, 77004 (Presently Guest Professor, Mineralogical Institute, University of Tübingen, Tübingen, West Germany)

The Victoria Quadrangle (H-2) is located in the Aurora Albedo Province of Mercury between latitudes 20° and 70° North and longitudes 0° and 90°. Two portions of this quadrangle have been imaged by the Mariner 10 Mission. Unfortunately, these areas are separated by a wide gap in surface coverage.

Image coverage of the western margin of the quadrangle is a narrow, contiguous strip of relatively high sun angle imagery that includes the limb and shows abundant albedo markings. The differences in albedo are due primarily to numerous deposits of highly reflective ray material, which are particularly abundant in the northern portion of the quadrangle, and to very low albedo inter- and intra-crater surface units. These very low albedo units may be extrusive igneous rocks or impact melt-rocks. The southernmost portion of this strip contains very rough and irregular terrain units of medium albedo and high crater densities.

Another contiguous area of image coverage is in the central and south-central portion of the quadrangle. This area is more than twice that of the western strip and is bounded to the west and northwest by the limb and by the terminator to the east. This imagery shows excellent surface detail at high resolution in the central portion and near the terminator, but the albedo markings are quite subdued because of the low angle illumination. This area is characterized by flat-floored craters, many with central peaks, abundant secondary craters, and large areas of inter- and intra-crater low albedo units that are relatively smooth. Scarps and lobate igneous flow fronts (?) are common as are some crater chains. One large and prominent scarp of unknown origin is easily visible in the northern portion of this image area on and near the limb of the planet.

A substantial fraction of the image areas in both portions of the quadrangle that are covered by contiguous imagery are low viewing angle presentations of near-limb terrain that are difficult or impossible to use for surface geologic/physiographic mapping.

Geologic mapping of these two portions of the Victoria Quadrangle is proceeding currently on transparent overlays of the individual images. Only informal map unit designations are being used. A total area compilation will be made at a later date when map units have been formalized and described in detail and when base cartographic products are available.

Geologic mapping of the Victoria Quadrangle is being undertaken in collaboration with Dr. George McGill (Univ. of Massachusetts, Amherst).

Geologic Map of the Tolstoj Quadrangle of Mercury. Gerald G. Schaber and John F. McCauley, U.S. Geological Survey, 2255 N. Gemini Dr., Flagstaff, AZ 86001.

The Tolstoj quadrangle (H-8) of Mercury includes the southeast one-quarter of the Caloris Basin and its associated mountainous and lineated ejecta deposits. Large portions of the radially lineated basin deposits have been overlain by younger smooth plains that surround Caloris. Remarkably fresh-appearing secondary craters thought to be derived from Caloris are preserved in the ancient, heavily cratered terrain making up the southeastern one-half of the quadrangle. Prominent large craters with the Tolstoj quadrangle include the extremely degraded (pre-Caloris) basin Tolstoj (485 km diameter - 349 km inner ring) and the post-Caloris crater Mozart (258 km diameter); the latter only partially imaged during the Mariner 10 mission. Mozart is one of the youngest large craters on the currently imaged portion (45 percent) of Mercury and post-dates the formation of the smooth plains surrounding Caloris.

The heavily cratered terrain within the quadrangle is composed of: (a) ancient intracrater plains with a very high density of secondary craters dating back to the oldest basins and (b) craters/basins and their materials. The heavily cratered terrain is also characterized by abundant NW and NE trending lineaments and faults (Figs. 1, 2). Radial lineaments related to the Caloris event are obscured within the area of the Tolstoj quadrangle by the younger plains near the basin and by the planet-wide NW trending fracture system.

At least two distinct types (and ages) of post-Caloris smooth plains materials are recognized within the quadrangle. The first is characterized by abundant small halo craters, mare-type wrinkle ridges and relatively angular contacts with older terrain (e.g., inner crater walls). Several large, irregular patches of the first type plains, superimposed on the cratered terrain, are localized in tectonically controlled depressions. The second plains type is slightly more cratered, has fewer halo craters and mare-type ridges, and forms less distinct contacts with older terrain.

A volcanic origin for the smooth plains within the Tolstoj quadrangle is still in question owing to the lack of any recognizable eruptive vents or lava flow fronts. However, it is entirely possible that virtually all of the smooth plains presently recognized on Mercury are too old and impact eroded to have any vent morphology or flow front scarps preserved. The smooth plains on Mercury have crater densities, at minimum, about as the most cratered, oldest of the lunar mare (1); surfaces on which no recognizable lava flow scarps have as yet been recognized (2,3).

The rather high albedo (0.14-0.15) of the mercurian smooth plains and the spectral evidence for low metallic iron, FE^{+3} and titanium content do not rule out a material of mare basalt composition but limit the chemistry to the most Fe and Ti poor of the Apollo 12 and 15 samples (4). The chemistry, style and rate of effusion of mercurian lava flows may have also played important roles in determining the formation of overlapping, compound flows with few mappable flow scarps as opposed to long, isolated, "simple" flow lobes as described on the lunar surface (2,3,5).

Three large, dark halo C_3 class (relatively fresh) craters (between 3°S and 11°N; 144° to 148°W) within the Tolstoj quadrangle may represent nearly simultaneous impacts of a volatile-rich cometary or chondritic body disrupted before impact by solar gravitational forces.

(1) Murray, B. C., Danielson, G. E., Davies, M. E., Gault, D. E., Hapke, B., O'Leary, B. O., Strom, R. G., Suomi, V. and Trask, N. J., 1974, Science, 185, 169-179.
(2) Schaber, G. G., 1973, Proc. Lunar Sci. Conf. 4th, v. 1, 73-92.
(3) Schaber, G. G., and Boyce, J. M., 1976, Proc. Lunar Sci. Conf. 7th, v. 3, 2783-2800.
(4) Hapke, B., Danielson, G. E., Klassen, K. and Wilson, L., 1975, J. Geophys. Res., 80, 2431-2443.
(5) Moore, H. J. and Schaber, G. G., 1975, Proc. Lunar Sci. Conf. 6th, v. 1, 101-118.

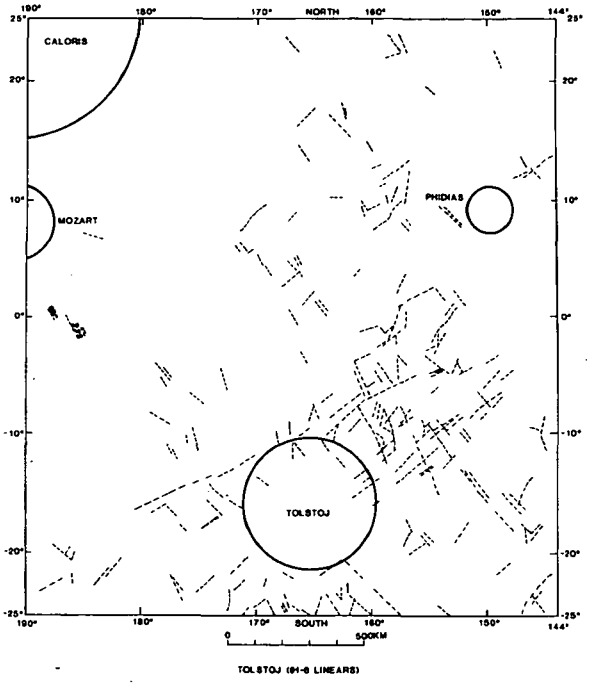

Figure 1

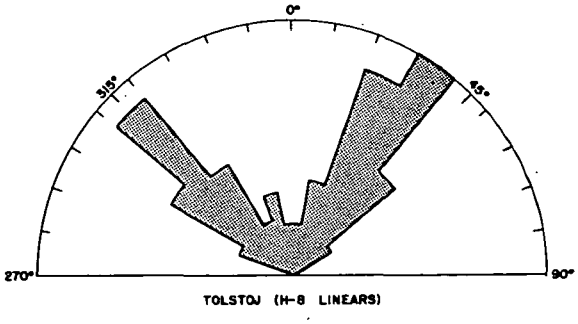

Figure 2

GEOLOGY OF THE KUIPER QUADRANGLE OF MERCURY, R. A. De Hon, University of Arkansas, Monticello, AR., 71655; J. R. Underwood, Jr., West Texas State University, Canyon, TX., 79016; D. H. Scott, U. S. Geological Survey, Flagstaff, AZ., 86001.

The Kuiper quadrangle is located in a heavily cratered equatorial region of Mercury (25°N to 25°S; 0° to 72°W). The region includes the young, 50 km diameter, crater Kuiper (11°S; 31°W), which has the highest recorded albedo on the planet, and the small 0.5-1 km crater Hun Kal (0.4°S; 20.0°W) which is the principle reference point for Mercurian longitude. The geologic map (Fig. 1) is based on photomosaic and shaded relief maps prepared from Mariner 10 imagery. Geologic interpretation is aided by 153 Mariner photographs including 70 quarter-frame photographs and 19 stereopairs. Resolution of the imagery ranges widely but averages 1.5 km. A wide range (more than 50°) of both viewing and illumination angles precludes a high degree of mapping consistency, particularly in an east-west direction. The easternmost 10° of the quadrangle is beyond the evening terminator. West of approximately 55°W longitude most of the geologic units can not be specifically identified because of high sun angles; here mapping is more generalized and fewer units are distinguished.

Major geologic units are smooth and rough terra materials, smooth and cratered plains materials and intercalated and superposed materials of impact craters and basins. The oldest rocks in the quadrangle comprise the smooth terra material (unit ts) and the rim material of highly degraded craters (unit c) and basins (unit b). The widespread smooth terra material has moderate relief characterized by numerous overlapping degraded secondary craters, low subdued hills, and an abundance of old craters and basins. It is similar in many respects to rolling and hilly terra material of the southern lunar highlands. Smooth terra material is gradational in places with cratered plains material (unit pc) which forms relatively flat, densely cratered surfaces with broad ridges and lobate scarps somewhat resembling those of some lunar maria. Cratered plains material embays some of the oldest craters and lies within the outer rings of several ancient basins; they may represent lava flows extruded after an initial phase of high impact flux.

The youngest rock units are rough terra and smooth plains materials. Rough terra material (unit tr) occurs as large young craters and older basins in the eastern part of the quadrangle. The relief appears to be higher than elsewhere in the map area, and the densely clustered secondary craters produce a coarsely textured, hummocky surface. Due to the close spacing and similar age of the craters, it is not possible to distinguish individual ejecta blankets. Smooth plains material (unit ps) covers the floors of numerous craters of all ages and its surface is lightly scoured by secondary craters from craters of a wide range of ages. Thus, this material may have a relatively wide range in age. Smooth plains material exhibits ridges and lobate scarps which more nearly resemble those of the lunar maria. Possibly it is analogous to the Cayley plains that occur within many lunar craters. Although resolution and the abundance of secondary craters are serious constraints to

accurate crater counting, the smooth plains material clearly has a much lower crater density than the crater plains unit. A few patches of very dark material occur in the western part of the quadrangle which is, in part, superposed on bright rays of very young craters.

All craters in the quadrangle are believed to be of impact origin. Young craters (unit c with rim crest symbol) are characterized by sharp rims, well developed ejecta blankets, abundant secondaries and are superposed on most other units. The older craters (unit c) are characterized by degraded rims, less extensive ejecta blankets, and superposed younger materials. At least six multi-ringed basins (unit b) varying from 150 km to 440 km in diameter occur in the quadrangle. There appears to be a regular size progression from large craters with incomplete central rings of peaks to double ringed basins. Secondary crater fields and prominent crater chains are abundant around fresh craters and some large basins.

Structural features such as rilles, mare ridges, and collapse depressions are sparse or unresolved in this part of Mercury. The few faults that cut intercrater areas trend northeast or northwest, but there are several young normal faults which transect the floors of craters. Some scarps may be traced across the walls into the rim materials of the craters. Unrecognized also are high-angle reverse faults that have been identified in other areas of the planet.

The geologic history of the Kuiper quadrangle is primarily a record of the decreasing impact flux and the formation of intercrater plains. Approximately half of the region exhibits the high crater density and multi-ringed basins formed by intense bombardment during the stage of high meteroidal impact flux. As the impact flux decreased, plains materials of possible volcanic origin were deposited in low lying areas resulting in partial burial or embayment of pre-existing craters. Deposition of plains materials was continuous or occurred intermittently into the period of low impact rates. The youngest craters are associated with bright rays similar to those of young lunar craters.

Age relationships of the major map units

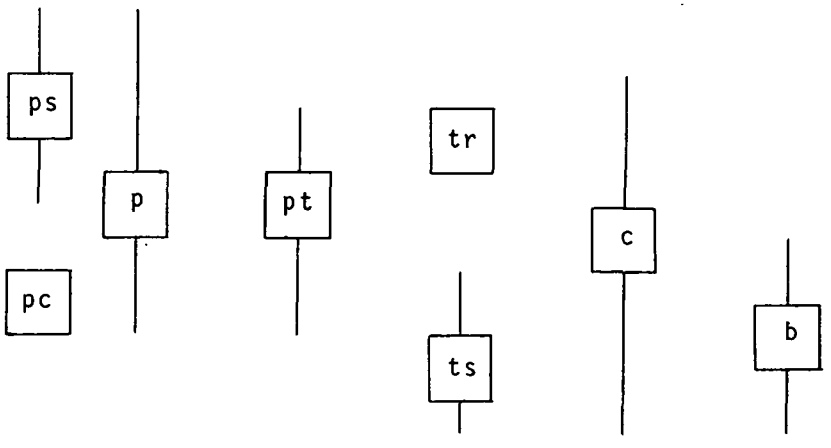

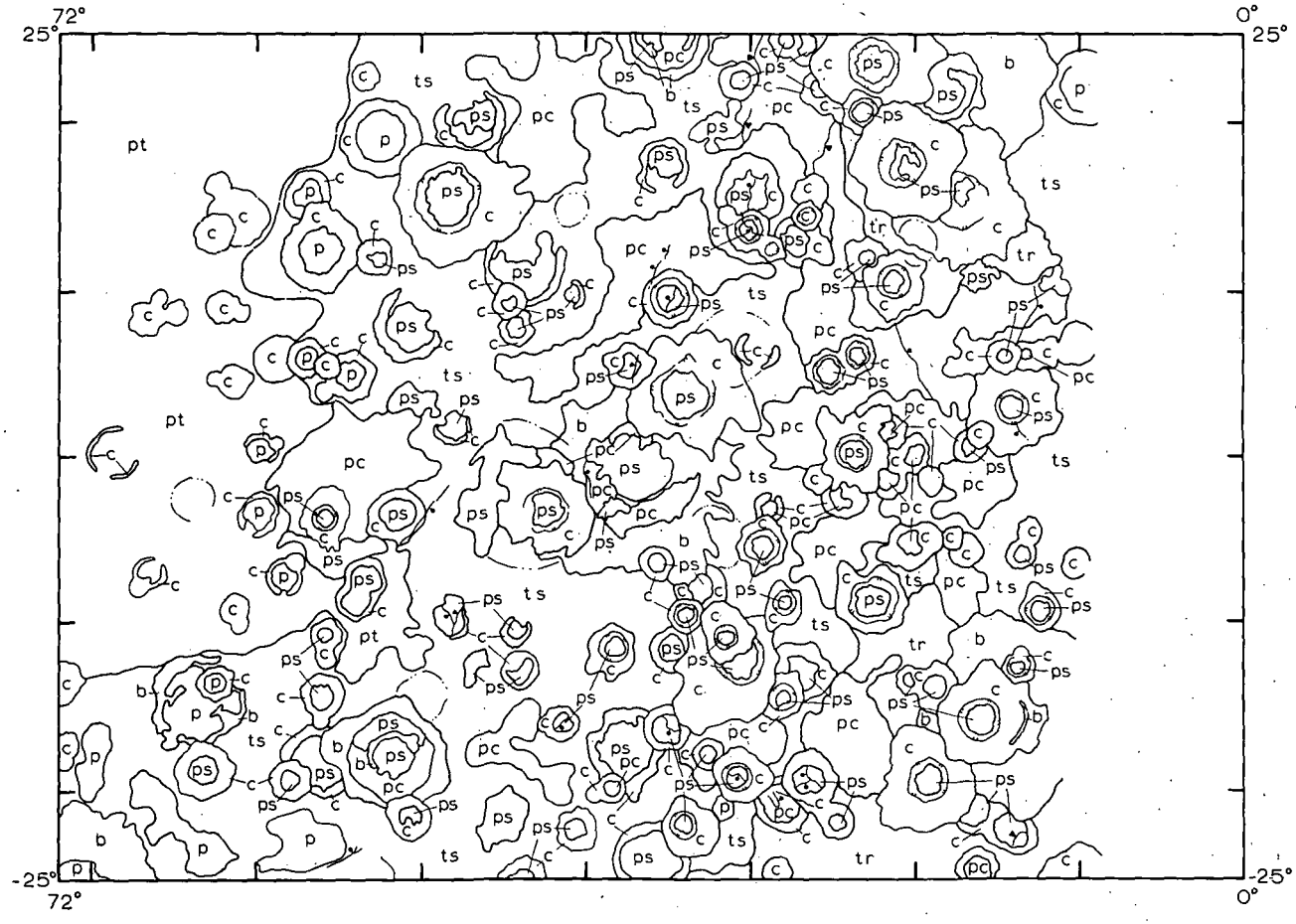

Figure 1. Geologic map of the Kuiper Quadrangle of Mercury. See text for explanation of geologic units.

Geologic Mapping of Michaelangelo Quadrangle (H12) of Mercury: Structural and Topographic Features. Karl R. Blasius, Planetary Science Institute, 283 S. Lake Avenue, Suite 218, Pasadena, California 91101

The Michaelangelo or H12 quadrangle of Mercury extends from 20° S to 70° S between 90 and 180° W. The entire region was photographed at moderate resolution,1 to 2 km, during the second encounter of Mariner 10 with Mercury, and northern portions of the quadrangle were photographed at similar or lower resolution during the first encounter. Abundant overlapping sets of images provide stereo imaging coverage for about 80% of the area of the quadrangle. Albedo variations, other than those associated with rayed craters, are very subtle and terrain types are not highly varied in H12, so it was decided that a reasonable first step in geological analysis of the quadrangle would be a study of the morphology and transectional relationships of scarps, ridges,and crater rims, taking advantage of the enhanced visibility of such features when viewed stereoscopically. This decision was further motivated by the prominent role of tectonics in Mercurian geologic history as interpreted by previous investigators (1,2). In contrast the roles of volcanism and other non-impact depositional processes in shaping the surface of Mercury are not well understood.

Large scarp complexes hundreds of kilometers across, suggesting zones of enhanced crustal faulting, are the most impressive structural features found in the H12 region. The 400 km long arcuate scarp Hero (57°S, 173°W) appears to be part of a larger complex of structural and possible volcanic features spanning a region 1000 km by 300 km. Twelve irregular scarps 25 to 150 km long, a lobate scarp 200 km long, Hero scarp, and two isolated mountains 25 km in diameter comprise this suite of features located in heavily cratered terrain. The two mountains have prominent summit pits, suggesting a possible volcanic origin, however, their flanks are greatly modified by ejecta of a nearby fresh crater, so no primary volcanic features are seen. For the most part scarp faces are rounded and convex upward in profile, the typical arcuate scarp morphology described by Dzurisin (2). In this area the only evidence of offset of surface features yet found is the 20% shortening of the diameter of a 15km crater astride Hero scarp. On average the trends of all scarps in the vicinity of Hero is approximately N50°W.

A 250 km long lobate scarp at 40°S, 140°W appears to be associated with three 100 to 300 km long linear scarps aligned N-S and NW, forming a 1000 km long lobate scarp complex similar to two lobate scarps described by Dzurisin (2) in the H11 and H6 quadrangles to the east and northeast. The lobate scarp has steeper more planar scarp faces than is typical for arcuate or irregular scarps, suggesting a different structural origin.

Two clusters of north trending irregular scarps occur near 135°W, 35°S. Each complex spans an area measuring about 400 km NS and up to 100 km EW. One of these complexes has associated with it a N-S trending ridge about 150 km long and 10 km wide. A scarp in that same complex cuts through the center of a 20 km crater, only half of which is preserved, perhaps due to having been overridden and buried. 600 km to the south an isolated north trending irregular scarp is associated with a similar half preserved crater about 15 km in diameter.

Dzurisin (2) associates arcuate, lobate, and irregular scarps with stresses induced by tidal despinning and global contraction during cooling. Locally strong evidence of crustal shortening of 3 to 10 km along arcuate and irregular scarps in the region of H12 suggests these classes of scarps may represent low angle thrusts caused primarily by global contraction. The lobate scarps tend to be steeper and associate with linear scarp

segments and ridges, suggesting formation by vertical adjustment along global joint patterns possibly ascribable to stresses of tidal despinning.

(1) Strom, R.G., Trask,N.J., and Guest, J.E., JGR 80, n.17, p.2478-2507 (1975)
(2) Dzurisin, D., Ph.D. Thesis Caltech, 179p. (1977)

Geologic Mapping of Bach (South Polar) Quadrangle, Mercury: A Progress Report. Michael C. Malin, Planetology and Oceanography Section, Jet Propulsion Laboratory, Pasadena, CA 91103

A preliminary geologic map of the South Polar region of Mercury is currently in the final stages of completion. In close cooperation with co-mapper R. Strom (University of Arizona), a review version will be prepared during the second and part of the third quarter of FY 1977. A preliminary text is also "in preparation."

Two "new" mapping techniques, which we proposed at the Mercury Mapping Program Meeting held in Houston, Texas as part of the Conference on the Comparison of Mercury and Moon, have been used to convey the temporal and lithologic configuration of surface units on Mercury. The first technique involves the mapping of plains units; the second concerns secondary crater fields.

Previous mapping exercises have designated generally planar surfaces by minor, superposed morphologic features (e.g. smooth plains, hilly plains, fretted plains) or associations (e.g. floor-fractured plains, intercrater plains). While these terms convey morphological or geographical information, alone they provide little insight into the time and rock stratigraphic relationships. In Bach Quadrangle, we have utilized a somewhat different mapping protocol - plains units have been fit within the time stratigraphy established for craters. Specifically, plains within a crater are assigned an age similar to or younger than the crater. Superposition by crater ejecta or secondary craters provides limits on the youth of a surface, whereas embayment of ejecta and eradication of secondaries provide limits on the oldest age. For example, plains within a C_3 crater are classed as P_3 if superposed by C_4 ejecta, as P_{3-4} if superposed by C_5 ejecta, etc. Similarly, plains outside craters which embay C_3 craters but are strewn with crater chains traced to C_4 craters are classed as P_3. "Intercrater Plains," the oldest plains unit, is extremely difficult to divide into subunits, even though occasional, local transectional and superpositional relationships are visible. We are still attempting to evolve a proper technique to handle these plains.

Past mapping efforts have designated secondary crater fields as mappable units, assigning the area within the admittedly poorly located boundaries to the age and rock type of the parent crater. However, many studies of cratering phenomena suggest that most of the material transported and thus surfacing the secondary crater field is mechanically reworked local country rock or regolith. In many instances the material affected by the secondary cratering events would not differ chemically or in physical properties from nearby uncratered material. To make these relationships clearer, we have mapped material units up to their contacts with the continuous crater ejecta and used a light, dotted screen to signify the region disrupted by secondary cratering. In such a manner, the color of the underlying map unit shows through and signifies the physically altered but chemically distinct pre-cratering materials. By using a screen with dots the same color as the primary crater, we indicate both the age of cratering (i.e. the time of disruption of the surface) and the small but perhaps measurable contribution of material from the objects which formed the secondary craters.

Page Intentionally Left Blank

Chapter 10

MAPPING PROGRAMS

Part C

VENUS

Page Intentionally Left Blank

Venus Mapping, Harold Masursky, Mary Strobell and A. L. Dial, U.S. Geological Survey, Branch of Astrogeologic Studies, 2255 North Gemini Drive, Flagstaff, Arizona 86001.

Work has begun on assembling a cartographic base map of Venus from radar images acquired at the Goldstone antenna by Goldstein, Rumsey and Green in 1969, 1972 and 1973-74, and at the Arecibo antenna by Campbell, Rogers, Ingalls and Pettengill in 1969, 1972 and 1975. The landing sites of the three USSR spacecraft, Venera 8, 9, and 10, will be shown also. The low resolution data acquired at Goldstone in 1969, 1970, and 1972, and the locations of the high resolution data recently acquired by the same dish are shown on the index map. The resolution varies from about 10 km/pixel to about 100 km/pixel. Elevation contours will be drawn in areas covered by high resolution images.

A nearly planetwide geologic map will be constructed on this base. The cartographic rendition with the geologic map overlain on it, will serve as a planning base on which the Venus Pioneer 1978 radar elevations and images will be plotted.

(1) Goldstein, R.M., Green, R.R., and Rumsey, H.C., J. Geophys. Res. 81, 4807 (1976).
(2) Goldstein, R.M., and Rumsey, Icarus, 17, 699, (1972).
(3) Rogers, A.E.E., Ingalls, R.P., and Pettengill, G.H., Icarus, 21, 237, (1974).
(4) Campbell, D.B., Dyce, R.B., and Pettengill, G.H., Science, 193, 1123, (1976).

Page Intentionally Left Blank

Chapter 11

INSTRUMENT DEVELOPMENT AND TECHNIQUES

Page Intentionally Left Blank

An X-ray Diffractometer for Mars. A. E. Metzger, J. B. Willett, Jet Propulsion Laboratory, California Institute of Technology, Pasadena, CA, 91103; H. W. Schnopper, Smithsonian Astrophysical Observatory, Cambridge, MA, 02138.

The mineral composition of a rock preserves a record of the physical and chemical conditions under which the constituent phases crystallized. This knowledge, particularly when coupled with direct chemical analysis and other geologic data, will provide an understanding of the sub-crustal, crustal, and in the case of Mars, climatological processes of differentiation and alteration. From this, major inferences may in turn be drawn about both the present physical state of the planet and the primordial material from which it evolved.

X-ray diffraction is the most straightforward, comprehensive and precise method available for the determination of mineralogy. An X-ray diffractometer whose configuration is particularly adapted to planetary application has been constructed and tested as a laboratory breadboard. We will summarize its design and performance up to the present, and then present two innovative ideas, which when demonstrated, will significantly enhance the potential of this instrument.

The instrument has been described in detail in Das Gupta, et al (1). Shown schematically in Figure 1, its design is based on the Seemann-Bohlin focusing principle, in which a line focus target, powdered sample, and a scanning detector all lie on the circumference of a focal circle. The line source is imaged at points appropriate to the various lattice spacings by diffraction from a curved sample. By means of a simple linkage, a detector is made to rotate about the center of the focal circle and point a narrow receiving slit at the center of the sample. The Soller slits are used to limit the divergence normal to the plane of dispersion. The characteristics of this system demonstrated to date include a high diffracted-beam intensity per power input, mechanical simplicity by decreasing the number of moving assemblies to one from the two required by the conventional laboratory Bragg focusing geometry, lattice spacing resolution which is twice that of the Bragg geometry for equivalent dimensions, and relatively light weight and low power requirements.

The performance of this system is illustrated by the quartz diffraction pattern in Figure 2, generated with a chromium-target X-ray tube operating at 25w of power and proportional counter detector scan speed of 4^{o} per/min. Intensity, signal-to-noise ratio and line resolution, comparable to laboratory diffractometers have been obtained.

This instrument is also capable of performing an elemental analysis. Simple to implement since both the X-ray source and sample are stationary, the elemental analysis would be accomplished by adding a non-dispersive detector sensitive to the fluorescence emission from the sample (2). This has been demonstrated on the laboratory breadboard, and will allow a combined mineralogical and geochemical analysis utilizing common samples. A possible alternative would be to share a sample with the combined alpha scattering X-ray fluorescence spectrometer instrument (3).

There remain two areas in which improvements in performance would be welcome, extending the range of the instrument to detect large d-spacing phases, and incorporating a stationary detector system. We now believe both objectives can be realized.

The geometry of the Seemann-Bohlin system limits the range of d-spacings in terms of the minimum source-sample and sample-detector angles. In the present design this is about 7Å and could not be increased beyond 10Å without difficulty. Evidence points to the possible existence of aqueous-related mineral phases on Mars, the sensitive detection of which requires a range to about 20Å. This is the one comparison in which Bragg focusing can

show superior capability. The use of energy dispersive diffractometry has been investigated (4), but the signal-to-background ratios obtained have not been satisfactory.

Our proposed solution is to discard the present cylindrical geometry imposed by the line source in favor of a spherical geometry. The source would become a point rather than a line, the sample holder will be spherical rather than cylindrical, and the diffracted X-rays will focus as segments of small circles. Spherical geometry will permit the elimination of the Soller slits, The resultant decrease in source-sample-detector separation should permit an increase in the range to an estimated 20-22Å.

Our concept for the detection system has evolved from a multiple scanning slit system backed by proportional counters to position sensitive devices which require no moving parts. The first of these was a curved positional sensitive proportional counter which fit the focusing circle (5). The diffraction pattern is accumulated by sensing the position along the wire of each arriving X-ray. This device presented practical difficulties, the primary one being very poor resolution at large d-spacings (small Bragg angles). We now propose to utilize the fact that discrete X-rays detectors in the form of thin (about 100 microns) diffused silicon have been developed. We anticipate an array of 4096 such detectors laid out along the focal circle. Each one will have an associated measurement chain. Data for each diffraction pattern will be collected in parallel and will be stored in a memory prior to read out.

With a successful demonstration of spherical geometry and a partial array of discrete Si detectors, this diffractometer will have become an instrument with no moving parts and a single mode of operation covering a range of 1-20Å. The sample-holder will be able to receive an unlimited number of specimens. Depending on the optimum trade-off between time and power, a diffraction pattern might be obtained in as little as 1 min and should take no more than 10 min, a consideration of importance for a roving vehicle.

This work was supported under NASA contract NAS 7-100 at the Jet Propulsion Laboratory, California Institute of Technology.

References

1. K. Das Gupta, H. W. Schnopper, A. E. Metzger, R. A. Shields, Advan. X-ray Anal. 9, 221 (1966).

2. E. J. Franzgrote, Advan. X-ray Anal. 15, 388 (1972).

3. T. E. Economou, A. L. Turkevich, Nucl. Instr. and Meth. 134, 391 (1976).

4. R. E. Ferrell, Jr., The American Mineralogist 56, 1822 (1971).

5. "Development of a Position Sensitive X-ray Detector for Use in a Light Weight X-ray Diffractometer," Report No. IITRI V6112-1, R. A. Semmler, (IIT Research Institute, Chicago, IL, 1970).

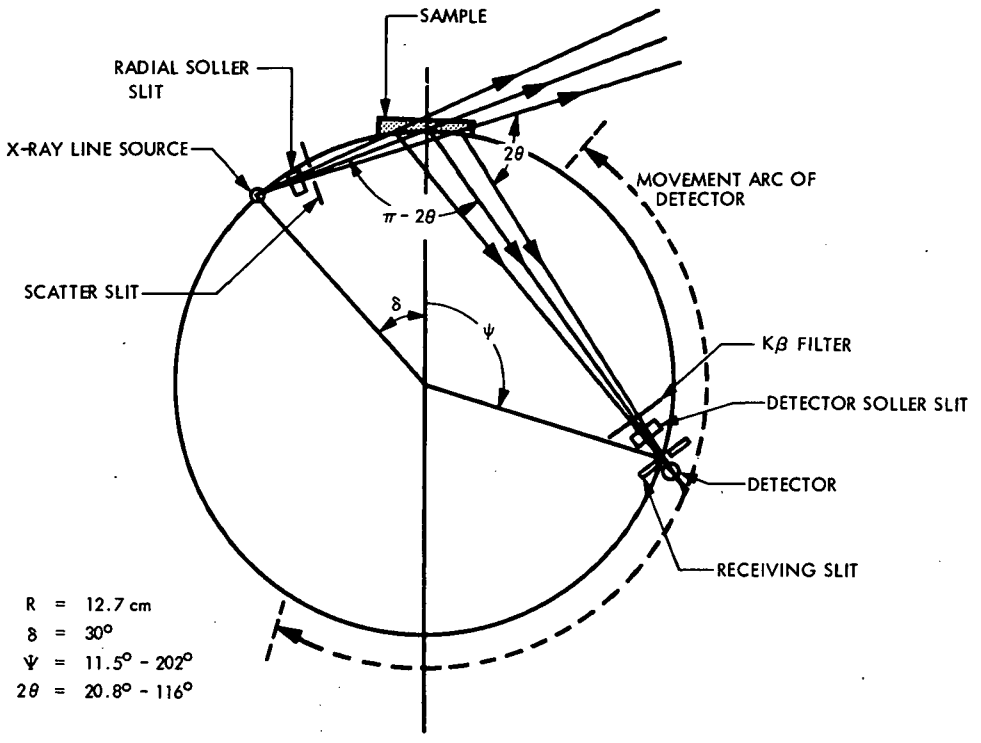

Figure 1: Schematic of the Seemann-Bohlin focusing diffractometer

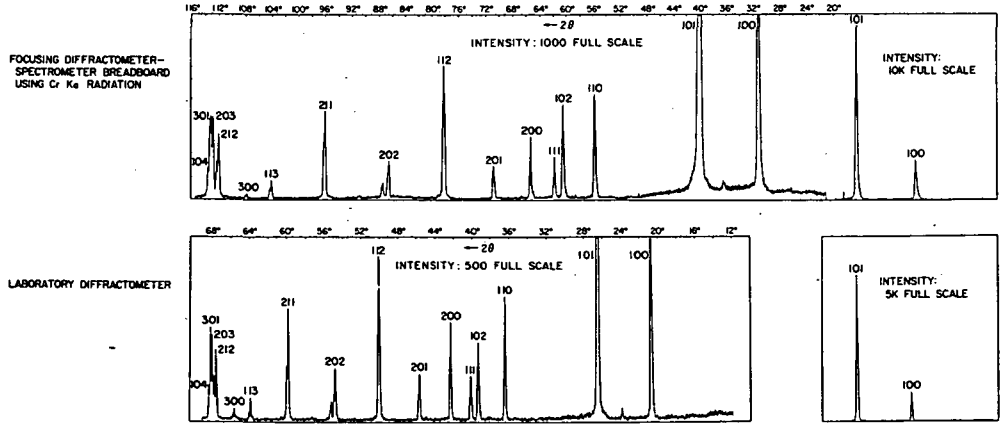

Figure 2: Comparative quartz diffraction patterns

Adaptation of the Alpha Particle Instrument for Penetrator Missions. Anthony Turkevich, Thanasis Economou, Enrico Fermi Institute, University of Chicago, Chicago, Illinois 60637 and Ernest Franzgrote, Jet Propulsion Laboratory, 4800 Oak Grove Drive, Pasadena, California 91103.

In this year the limited effort was directed towards adaptation of the Alpha Particle Instrument (1) for possible Penetrator Missions. The status of this effort is summarized as follows:

1. Miniaturization: A new geometry of detectors and sources in "Micro Alpha", much more compact than in Mini-Alpha is considered for a penetrator mission (2). A breadboard of such an instrument is currently being assembled. Since radioactive alpha sources are not available, the performance of this instrument will be evaluated with a beam of alpha particles from a Van de Graaff accelerator.

2. Shock Tests: Shock tests (up to 3500 g) of several solid state detectors and of source collimators, similar to those proposed for a penetrator instrument, were performed at Sandia Laboratories. The detectors were mounted at various angles up to 45° relative to the deceleration axis. The detectors and collimators passed the tests. More development work is needed on thin films used over the collimators. These tests indicate that the most delicate components of the Alpha Particle Instrument were not affected by the high deceleration.

3. Contamination of the Soil by a Penetrator: Two full-scale drop tests (3) of the Penetrator into loess and basalt revealed serious alteration and contamination of the material immediately outside the emplanted Penetrator. This behavior could seriously affect the results of chemical analysis of the material. In order to be able to examine an uncontaminated sample, a preprototype model of a "Sample Acquisition System" was developed, built and demonstrated.

4. Sample Acquisition System: Figure 1 illustrates, via a cutaway drawing, the operation of the system. This was developed and built in order to demonstrate the concept of a compact system for acquiring a sample from a location up to 2.5 cm from the emplanted Penetrator, and transporting the sample inside the Penetrator where it could be examined by various instruments. The principle involves a drill that, while advancing into the surroundings, carries along a sleeve. The drilled material is brought in by the flutes of the drill inside the sleeve and then deposited into a sample collector.

In the model constructed the drill bit was 0.200", the drill body was 0.165" OD and moved inside a 0.186" OD sleeve. The advancing rate, controlled by a positive feed gear was 0.012" per revolution.

Samples of several hundred mg were delivered by drilling 2.4 cm into the surroundings. The power required was 10-20 W for about 10 seconds, depending on the hardness of the material. The drill was demonstrated to operate in both coarse grained basalt, hard granite and in soft firebrick. With the drill available, multiple uses tended to dull the drill. The main difficulty encountered was occasional clogging of the flutes in the transport phase of the operation.

This drill was exhibited at the 8th Annual Meeting

of the Division for Planetary Sciences of the A.A.S. in Hawaii and performed satisfactorily.

(1) T. E. Economou, A. L. Turkevich, An Alpha Particle Instrument with Alpha, Proton, and X-Ray Modes for Planetary Chemical Analyses, Nuclear Instruments and Methods 134, 391 (1976).
(2) T. E. Economou, A. L. Turkevich, NASA Technical Memorandum TM X-3364, 94 (1976).
(3) M. Blanchard et al., NASA Technical Memorandum TM X-73,181, 188 (1976).

PREPROTOTYPE
SAMPLE ACQUISITION SYSTEM
FOR A PENETRATOR
UNIVERSITY OF CHICAGO

DATE:
1977, JAN.

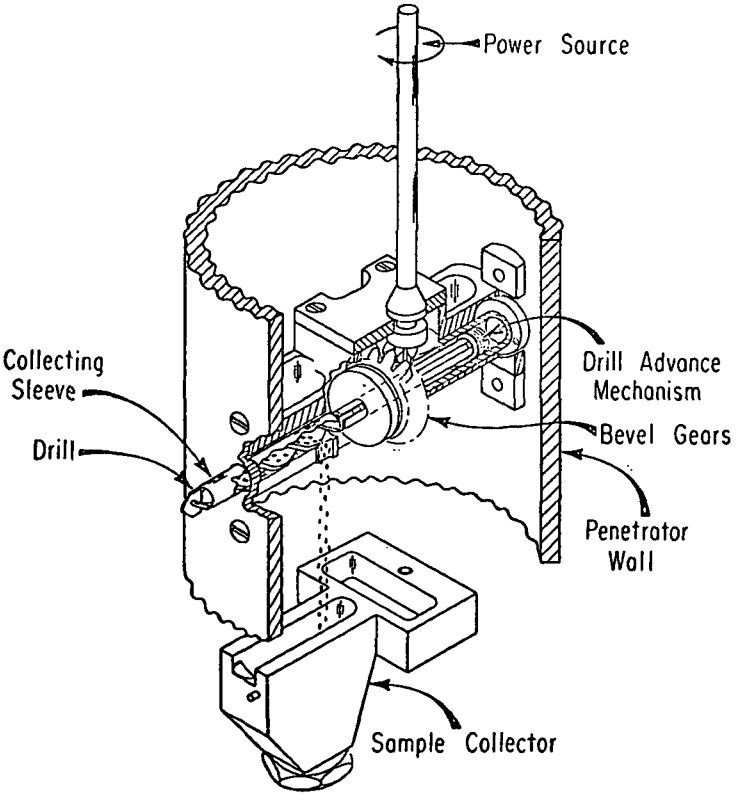

FIGURE 1.

Mars Soil-Water Analyzer: Instrument Description and Status. Duwayne M. Anderson, National Science Foundation, Washington, D.C. James B. Stephens and Fraser P. Fanale, Jet Propulsion Laboratory, Pasadena, CA. Allen R. Tice, USACRREL, Hanover, NH.

For some time there has been no doubt as to the occurrence of water on Mars. It has been confirmed as a constituent of the Martian Atmosphere in quantities roughly corresponding to saturation with respect to ice. The radiometric temperature regime determined by measurements from the Mariner orbiters have established the fact that Mars is a "permafrost" planet where ice and water vapor are the predominant phases of water[1]. The liquid phase can be only temporarily stable, if at all, in localized areas. Other forms of water likely to be found on Mars include various adsorbed phases, interlayer and zeolitic water contained in clay minerals of the regolith, crystalline hydrates, and other combined forms.

The marked interruption in the retreat of the polar ice cap, combined with changes in its radiometric temperature observed by Mariner 9, is consistent with the view that much, if not all, of the underlying Martian polar caps is composed of water ice[2,3]. Observations of what appears to be ephemeral frost and of low-lying clouds having temperatures consistent with water ice crystals add support to the view that water ice may be of common occurrence, particularly in the regolith where it may have created an ice-cemented permafrost.

Terrestrial permafrost is formally defined with reference to ground temperature only. Composition, including relative water and ice contents, is considered only in the classification of permafrost into such categories as unfrozen, ice-rich, ice-cemented, dry, etc. In common usage, however, the term permafrost often is taken to imply the presence of ice. Since it is necessary to make distinctions, in considering

the situation, vis-a-vis Mars, there seems to be little justification for departing from the conventional terminology of terrestrial permafrost. Thus, the temperature regime of the planetary surface and regolith is of primary concern.

Spectroscopic evidence of hydrated silicate minerals among the constituents of the Martian surface[4,5] has been reported and a number of specific minerals, montmorillonite for example, have been postulated as being present[6]. Examination and analysis of sinuous channels visible in the Mariner Mars imagery now augmented by the Viking Orbiter imagery has led to the belief that these channels were formed or subsequently shaped by the movement of a fluid thought most likely to be running water. This implies either atmospheric precipitation or the melting and subsequent run-off of water from ground ice, or perhaps both. Thus evidence for the presence of soil water and perhaps massive ground ice is very strong.

The Viking Lander-1 performed analyses on two soil samples from the Chryse Planitia region[9]. Although the nature of the sample acquisition and processing procedures allowed sublimation and escape of any free water, ice or physical adsorbed water, significant quantities of chemically bound water were detected. Preliminary results of these two analyses are given in Table 1.

Table 1. Surface Water Content at Chryse Planitia
The Viking GCMS Determination.

	Two Samples Heated to Temperatures T_1 and T_2		
	T_1		T_2
	200°C	350°C	500°C
Sample << 1	0.1%	---	0.1 to 1.0%
Sample 2		0.1 to 1.0%	<0.1 to 1.0%

The presence of these quantities of "low temperature" mineral hydrate water is a certain indication that free soil water ice and adsorbed water are intermittently present in the planetary regolith.

The amounts of ice, frost, snow, adsorbed and chemically bound water, ideally, should be determined at various times, locations, and depths in the planetary regolith in order to address the most important questions pertaining to the hydrology of Mars.

A concept that has been advanced recently to measure planetary soil-water involves an assembly of penetrator vehicles. Sample measurements would be taken at the emplacement depth at each site. The soil water detector employed would be:

1) Specific for water

2) Sensitive enough to detect quantities as low as 0.1% by weight

3) Able to discriminate among the various possible forms of water present

4) Relatively direct in concept and implementation and

5) Compatible with a hard landing, planetary penetrator vehicle

Recognizing certain difficulties inherent in the configuration and characteristics of a penetrator vehicle, particularly the acquisition of a measured quantity of undisturbed Martian regolith material, the semiquantitative measurement of the water/ice content in the surrounding regolith is attainable. That is the classification of water contents as: essentially none; a little; or a lot. These catagories would correspond to a site that is completely dry, that contains amounts consistent with the presence of adsorbed water and mineral hydrates; or that contains amounts consistent with the presence of ice-cemented permafrost. This information would be determined as a function of the depth and location of each penetrator vehicle.

A sample acquisition system that has been designed for this purpose is shown diagramatically in Figure 1. The Beckman P_2O_5 integrating water detector meets the essential criteria mentioned above. This detector

Figure 1

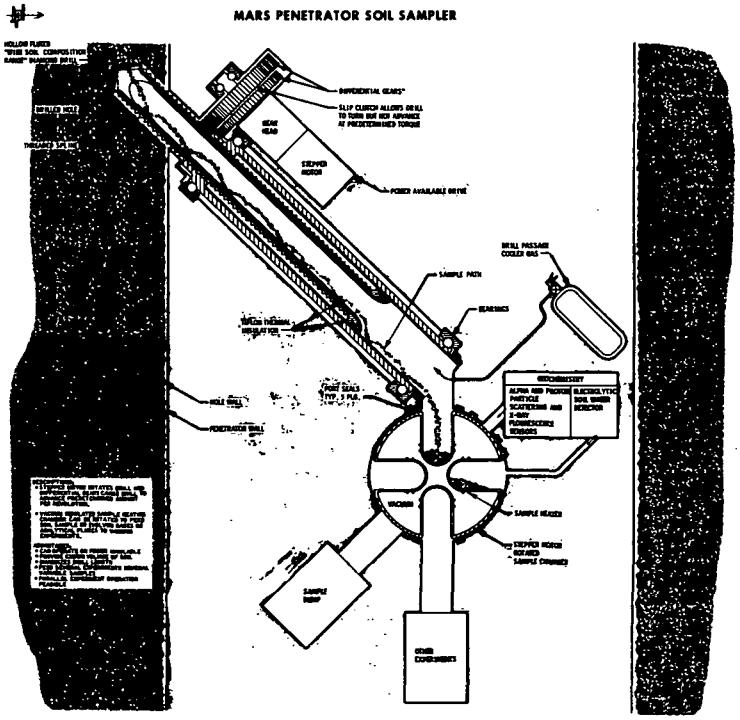

consists of two parallel, unconnected electrical conductors bathed in phosphorous pentoxide-phosphoric acid which functions as an electrolyte. The end of each conductor is connected to a source of EMF sufficient to electrolyze water. The increased current is exactly proportional to the number of water molecules thus disassociated and converted to oxygen and hydrogen gas.

An alternate sensor element consisting of a solid polymer electrolyte (SPE) has also been identified and given a preliminary evaluation. A water detector of either type is capable of meeting the objective.

During the past year, activities have concentrated on demonstrating the survivability of a P_2O_5 sensor when subjected to acceleration pulses at levels expected during typical penetrator impacts on Mars. Part of this work has been accomplished using the 5.5 inch air cannon at Sandia Laboratories. It was also possible during this period to utilize actual drop tests of a penetrator vehicle into loess and basalt targets. A summary of shock test results is presented in Table 2. In every case, the sensor element survived the shock pulse and operated satisfactorily in subsequent tests.

Table 2.

SHOCK TESTS RESPONSE SUMMARY
P_2O_5 ELECTROLYTIC HYGROMETER

	Sensor Element				
	1	2	3	4	5
Description	Standard Beckman P_2O_5 hygrometer sensor, Standard potting in black bakelight case	Bare Beckman P_2O_5 hygrometer tube, standard length, in 5.5 inch air cannon *mount*	Operating shortened Beckman P_2O_5 hygrometer tube in flight prototype *configuration*	Operating shortened Beckman P_2O_5 hygrometer tube in flight prototype *configuration*	Bare Beckman P_2O_5 hygrometer tube, standard length in 5.5 inch air cannon *mount* sealed at about 1.5 ppm water
Maximum shock pulse experienced	2,000 G (air cannon)	21,000 G (air cannon)	17,000 G (air cannon) (also air dropped in basalt at Amboy test 2,500 G)	300 G (Nebraska drop test)	18,000 G (air cannon)
Result	Survived	Survived	Survived	Survived	Survived
Remarks	Survival verified by inspection and electrical continuity test. Calibration shifted, probably due to P_2O_5 displacement.	Survival verified by inspection and electrical continuity test.	Survival and operational performance verified by post shock tests.	Survival and operational performance verified by post shock tests.	Survival and operational performance verified by post shock tests.

Tests of the P_2O_5 sensor is a simulated Mars environment were performed in the following manner. A stainless steel environmental chamber measuring 27 cm long and 10 cm in diameter was used to contain the simulated Martian atmosphere (Figure 2). The top was constructed of plexiglas with a 2.5 cm glass "o" ring sealed finger tube extending through to a depth of 13 cm. Valved lines were installed in the top to introduce water vapor, argon and carbon dioxide gases. Sensor elements

Figure 2.

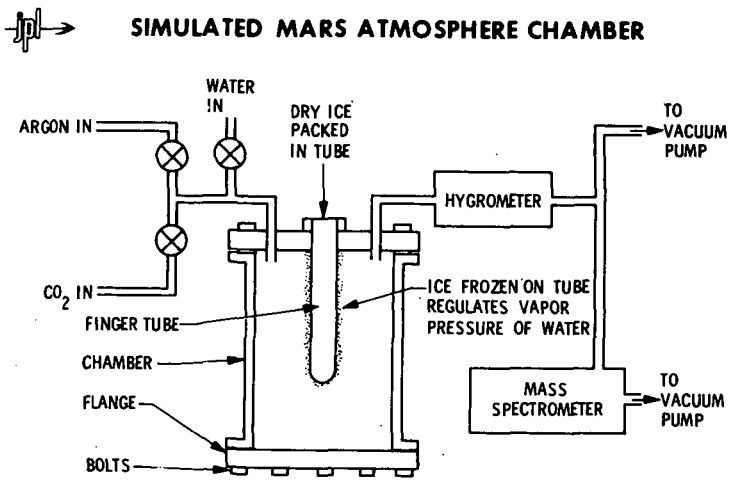

Nos. 3, 4 and 5 (Table 2) were physically mounted on the exterior of the chamber so that interior gases could be directed through it. The lines were valved in a manner that allowed the hygrometer to be isolated from both the vacuum system and the chamber while the system was being either evacuated or purged. A precision metering valve was installed to control the portion of outlet gas admitted into a quadrupole mass spectrometer. Cryogenic pumps were used to evacuate the system and a large capacity ion pump was used to evacuate the mass spectrometer. All the associated stainless steel lines were heated to about 150°C. A quartz Bourdon tube pressure measuring system was used to follow and record the chamber pressures.

A simulated Martian atmosphere was created as follows: The environmental chamber was evacuated to a pressure of about 5×10^{-4} torr. A cold finger tube was then packed with powdered dry ice and a valve was opened to admit water vapor into the chamber. Frost was formed on the finger tube and the water vapor inlet was then closed and the chamber was re-evacuated. Carbon dioxide gas was admitted to a pressure of 7.88 torr and 3.37 torr of argon was admitted, making a total pressure of 11.25 torr.

The testing of sensor element Nos. 3, 4 and 5 proceeded as follows: The valves isolating the hygrometer from the vacuum sink and the simulated Mars atmosphere were opened. The variable leak to the mass

Spectrometer was partially opened until a pressure of 9×10^{-6} torr existed at the ion source. A computer-aided data logger recorded data from m/e 12 through m/e 250 at a scanning rate of 2/min until the initial chamber pressure of 11.25 torr was reduced to about 3 torr, thus simulating the full range of Mars atmospheric pressure.

The mass spectrometer data for m/e 44 (CO_2) and m/e 18(H_2O) obtained with sensor element No. 3 together with chamber pressure vs time are shown in Figure 3. As expected, the CO_2 spectra decreased with pressure until an apparent partial blockage of the sensor tube intermittently reduced the signal level to background. The water peak (dotted line) remained constant at background level throughout the whole run, indicating that the water vapor entering the sensor was quantitatively absorbed and electrolyzed. Similar results were obtained with sensors 4 and 5 indicating nearly flawless performance under Mars conditions.

Figure 3.

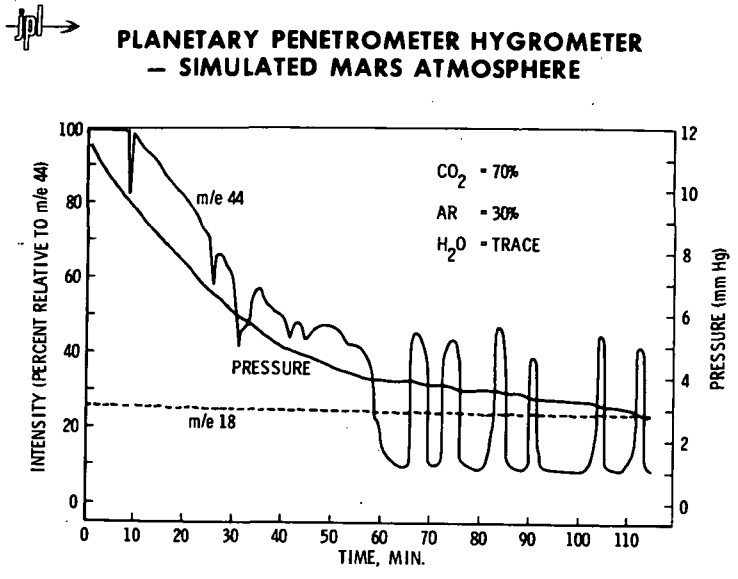

References

1. Kliore, A.J., Fjeldbo, G., Seidel, B.L., Sykes, M.J., Woiceshyn, P.M. 1973, S Band Radio Occultation Measurements of the Atmosphere and Topography of Mars with Mariner 9: Extended Mission Coverage of Polar and Intermediate Latitudes. J. Geophys. Res. 18, p. 4331-4352.

2. Murray, B.C. and Malin, M.D., 1973, Polar Volatiles on Mars-Theory vs. Observations. Science 182, p. 432-443.

3. Soderblom, L.A., Malin, M.D., Cutts, J.A. and Murray, B.C., 1973, Mariner 9, Observations of the Surface of Mars in the North Polar Region. J. Geophys Res. 78, p. 4197-4210.

4. Houck, J.R., Pollack, J.B., Sagan, C., Shaack, K.D., Decker, J.D., Jr., 1973, High Altitude Infrared Spectroscopic Evidence for Bound Water on Mars. Icarus 18, p. 470-480.

5. Primentel, G.C., Forney, P.B. and Herr, K.C., 1974, Evidence About Hydrated and Solid Water in the Martain Surface from the 1969 Mariner Infrared Spectrometer. J. Geophys. Res. 79, p. 1623.

6. Hunt, G.G., Logan, L.M. Salisbury, J.W., 1973, Mars: Components of Infrared Spectra and the Composition of the Dust Cloud. Icarus 18, p. 459-469.

7. Baker, U.R. and Milton, D.J., 1974, Erosion by Catastrophic Floods on Mars and Earth. Icarus 23, p. 27-41.

8. Milton, D.J., 1973, Water Processes of Degradation in the Martian Landscape. J. Geophys. Res. 78, p. 4037-4047.

9. Biemann, K., Oro, J., Toulmin III, P., Orgel, L.E., Nier, A.O., Anderson, D.M., Simmonds, P.G., Flory, D., Diaz, A.V., Rushneck, D.R., and Biller, J.A., 1976, Search for Organic and Volatile Inorganic Compounds in Two Surface Samples from the Chryse Planitia Region of Mars. Science. 194: p. 72-76.

Side-looking airborne radar/photogrammetric analysis of small scale surface roughness. Gerald G. Schaber, U.S. Geological Survey, 2255 N. Gemini Drive, Flagstaff, Arizona 86001.

Photogrammetrically derived, high resolution (< 3 mm) terrain roughness statistics of the Death Valley (CA) Salt Pan were successfully obtained during 1976. These data are currently being reduced with the aid of a sophisticated terrain analysis computer program developed by the U.S.G.S. for Apollo Lunar Rover Vehicle trafficability studies. The data obtained from the program includes: (1) topographic relief, (2) slope angle and slope length between reversals of slope, (3) topographic grain, (4) spectral characteristics (power spectral density plots), (5) hypsometric function (proportion of area lying above a minimum height), and (6) slope angle and slope curvature at various horizontal increments (slope lengths). For all the above categories of data are also included: mean, median, variance, standard deviation, skewness, kurtosis, dispersion coefficient, Elandt coefficient and chi-square. Two additional programs have been written to furnish the probability distribution of vertical/horizontal relief, absolute slopes and absolute curvature (the latter in terms of the radar wavelengths, 3 cm and 25 cm). A total of ten photogrammetric elevation profile traverses have been completed across five distinct roughness units within the Cotton-ball Basin region of Death Valley. Each profile length is a factor of two times that necessary to satisfy statistical requirements for portraying the topographic grain of the surface. Each profile is digitized an equivalent of every 3 mm along the ground surface.

An aluminum template-forming devise designed by us to measure in situ roughness within Death Valley was also evaluated during 1976. This one-half meter-wide instrument contains 64 side-by-side adjustable rods (0.8 cm x 1.2 cm x 120 cm) which mold the surface relief to a resolution of about 1 cm. The in situ template-forming devise was developed as an alternate and cheaper method of calibrating large areas of the Death Valley Salt Pan. The extreme similarities in profiles obtained from the template-forming devise and photogrammetric reduction of Hasselblad photography can be seen in Figure 1. The major difference is the 5 times increase in resolution obtainable with the photogrammetric reduction technique. Both profiling techniques are currently being evaluated in radar backscatter model calculations. Selected roughness statistics for the photogrammetrically derived profile seen in Figure 1 are listed in Table I.

The quantitized roughness data will be utilized during 1977 to derive models for radar backscatter power attributable to "pure" small scale surface roughness. Mathematical modeling of radar backscatter characteristics using idealized (mathematically simple) surface relief has been of limited value for interpreting SLAR image data owing to the complexity of "natural" terrain. For the first time, millimeter scale roughness statistics are available for a natural terrain covered by abundant SLAR images, and numerous other remote sensing image data; along with carefully controlled ground truth.

To date we have obtained a total of 18 flight lines of SLAR image data over Death Valley including X (3 cm wavelength) and L (25 cm wavelength) bands and all four combinations of transmit and receive polarization (HH-HV and VV-VH). These data were collected over the period from 1964 to July, 1976. Usable data include 6 HH polarization X-band images, 9 HH polarization L-band images and 7 VV polarization L-band images. Five VH polarization L-band images and three HH polarization X-band obtained in April 1976 are not usable due to poor quality.

The latest SLAR data to be obtained of Death Valley is a high resolution (3 m) X-band image flown at the request of Gerald Schaber by the Goodyear Aerospace Corp. (Litchfield, Arizona) during a checkout flight of the

sophisticated UPD-4 radar mounted aboard an Air Force Phantom jet. A single flight line was obtained on four separate channels covering an area of 30 km x 90 km. The scale of the original image negative is about 1:100,000; an improvement of about 4 times earlier obtained X or L-band SLAR image data. A portion of these new high resolution image data covering the Cottonball Basin area of Death Valley have been digitized and are currently being computer correlated with a 1964 (15 m resolution) X-band image obtained from the Strategic Air Command. Differences in the backscatter power from the Cottonball Basin on these two images is being portrayed in a color code for geologic analysis.

Additional computer correlations of various radar, aerial photography and Landsat multi-spectral image data sets of Death Valley are concurrently being undertaken by personnel of the Jet Propulsion Laboratory in support of our joint USGS-JPL research into radar backscatter modeling; and as a feasibility study in support of a proposed Space Shuttle (SERGE-Shuttle Experimental Radar for Geological Exploration) radar experiment.

New information gathered to date from our Death Valley radar backscatter modeling studies has generated considerable interest in this region as a test site for analysis of both SeaSat and Shuttle radar image data. Backscatter information gathered from the airborne and terrestrial spacecraft-borne radar sensors will be put to good use in supporting image analysis procedures being developed for use with the Pioneer-Venus and Venus Orbiting Imaging Radar (VOIR) missions.

Table I

Selected Statistics for Photogrammetric surface profile of Quaternary rock salt (rough) unit in Cottonball Basin (see Fig. 1)

General

Max. relief = 40 cm profile length measured ∿ 1.0 m
Topographic grain = 14.1 cm average standard error of a single elevation reading = < .5 mm
Photogrammetric sampling interval = 3.0 mm

ABSOLUTE SLOPE STATISTICS FOR 3 mm SLOPE LENGTH (0.1 x wavelength at X-band)	ABSOLUTE CURVATURE STATISTICS FOR 3 mm SLOPE LENGTH
slope reversals per meter = 84.9	curvature reversals per meter = 196.8
Min. slope = 0.00°	= 0.24°
Max. slope = 89.2°	= 145.59°
Mean = 35.00°	= 26.40°
Variance = 549.70	= 622.84
St. Deviation = 23.44	= 24.96
Skewness = 0.46	= 1.68
Kurtosis = -0.79	= 3.40
Median = 33.56°	= 19.26°
Dispersion coefficient = 1.20	= 1.38
Elandt coefficient = 1.49	= 1.06
Chi-squared = 94.15	= 1245.24

ABSOLUTE SLOPE STATISTICS FOR 241 mm SLOPE LENGTH (∿ 1 wavelength at L-band)

Slope reversals per meter = 0.033
Min. slope angle = 0.65°
Max. slope angle = 46.39°
Mean = 21.58°
Variance = 150.94
St. deviation = 12.29
Skewness = 0.005
Kurtosis = -1.26
Median = 23.68°
Dispersion coefficient = 1.04
Elandt coefficient = 1.76
Chi-square = 235.90

ABSOLUTE CURVATURE STATISTICS FOR 241 mm SLOPE LENGTH

Slope reversals per meter = 1.14
Min. curvature angle = 0.00°
Max. curvature angle = 37.1°
Mean = 1.51°
Variance = 11.44
St. deviation = 3.38
Skewness = 6.63
Kurtosis = 56.48
Median = 0.65°
Dispersion coefficient = 2.45
Elandt coefficient = 0.44
Chi-square = 2556.6

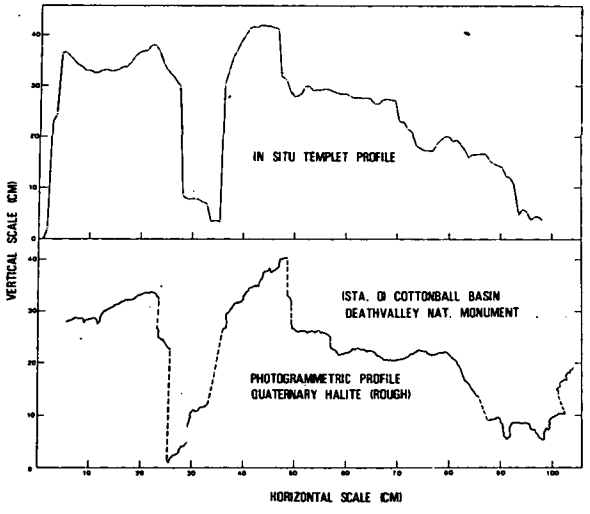

Fig. 1 - In situ templet and photogrammetrically derived profiles of quaternary halite (rough) facies within Cottonball Basin, Death Valley National Monument, CA.

Selection of Viking landing sites based on Viking and Mariner 9 Images and ground based Radar Data. Harold Masursky, G. G. Schaber, Charles Elachi, M. E. Strobell and A. L. Dial, U. S. Geological Survey, Branch of Astrogeologic Studies, 2255 North Gemini Drive, Flagstaff, Arizona 86001.

During Viking site certification the nominal plan called for the first spacecraft to land at 20° north. If the first spacecraft landed successfully, the second spacecraft would go to the B latitude at 44° N; if the first spacecraft failed either at launch or landing, the second spacecraft would go to the C latitude at about 5° south.

Radar observations obtained by the Goldstone, Arecibo and Haystack facilities for the area between 5° and 20° south were studied extensively to determine the safest area for a landing site; observations obtained from 1965 to 1975 were used in these studies. The prime site for the C landing was chosen on the north rim of Capri Chasma where picture, radar and elevation data were optimized.

An area on the high plateau east of Tharsis Montes showed the best radar returns and photographic data, but was disqualified as a candidate C site because it was too high in elevation for a safe landing. Goldstone observations of the site showed unusually strong reflectivity and peak power curves and low root mean square slopes; the Arecibo spectra for the area were sharply peaked. High resolution photographs of the area show many small impact craters with bright halos. These were interpreted to be impact craters in basaltic flow material covered by a thin regolith (unconsolidated mantle material); the halos are caused by ejecta blankets composed of blocky material. At the scale of the lander, this flat smooth area might have been more hazardous because of the ejected blocks.

Low reflectivity returns and attenuated spectra were seen over three types of terrain: 1) Goldstone observations in 1973 of the floor of crater Schiaparelli, where dunes were observed in the Mariner 9 images, showed a dramatic decrease in reflectivity and peak power, and an increase in RMS slope values: Arecibo spectra were low and diffuse. 2) Heavily channeled areas such as those in the cratered uplands of the Iapygia quadrangle (MC-21) returned weak signals compared to those returned by an adjacent smoother less channeled area in the Sinus Sabaeus quadrangle (MC-20). 3) In the Memnonia area, where the surface descends steeply from the Tharsis plateau to the Amazonis lowland, the radar return is markedly low. The abundant lava flow fronts, visible in the Mariner 9 photographs, may indicate a very rough volcanic surface that would diffuse and scatter the radar giving very weak returns. However, this area is the least understood of all the terrains studied.

Radar observations and Viking orbiter photographs were used in the final selection of the landing site for the first Viking spacecraft. Observations obtained by the Arecibo facility on July 5, 6, and 7, 1976 across Chryse Planitia showed very weak returns in the central part of the basin and strong returns to the west on the flanks of Lunae Planum. Photographs of the latter area showed lava flow fronts similar to those seen on the Tharsis plateau. Therefore, the site was moved west of the central Chryse basin to a compromise location between the highly radar

reflective area of Lunae Planum and the area of poorest return in central Chryse; the site also contained fewer fresh impact craters with their attendant abundant blocky ejecta, as verified by crater count data.

In order to better understand the radar observations made of the Chryse Planitia area, photographs and radar data were obtained for the Algadones dunes, west of Yuma, Arizona. A NASA Johnson Spacecraft Center aircraft took the photographs while the radar data of the Algadones dunes (and two playas in central Nevada) were taken with the Jet Propulsion Laboratory breadboard of the Seasat radar instrument, flown on the NASA Ames Research center aircraft. These terrestrial analog sites are similar to areas on Mars that have been intensively studied. In both the dune and playa areas, returned radar echo (peak power) was decreased by a factor of 2 to 4. The playa is covered by unconsolidated sediments of silt and clay with micro-relief mud cracks and shrinkage wrinkles and is characterized by the presence of tiny dunes (less that 1 m high) around the periphery. These areas are analogous to Martian dune areas and the central part of Chryse Planitia, where low returns had also been observed. The stream-dissected mountains in central Nevada also gave low returns; it may be analogous to the channeled uplands on Mars.

Studies made of the radar and picture data for the Viking site selection process have proved that these observations can be powerful tools for geologic mapping and terrain studies. Impact block populations can be predicted presently from the presence of fresh craters in pictures. The greatest hazard on Mars turned out to be the presence of abundant impact ejecta blocks to which the radar is not sensitive or to which the sensitivity of the radar is poorly understood. Predictions of their presence depended on the study of terrestrial and lunar impact craters. Sites were located to be as distant as possible from fresh impact craters visible in the photographs. The radar provided excellent elevation data and RMS slopes allowing the sites to be located in the least rough areas.

Radar Geology. R. A. Simpson, Howard, H. T., Tyler, G. L., Center for Radar Astronomy, Stanford University, Stanford, CA, 94305

Despite their different data base, it is possible for radar astronomers (like photogeologists) to infer geologic properties of planetary surfaces. Radar is sensitive to small-scale (meter-length) surface structure, large scale topography, and dielectric constant of the surface material. These can be inferred quantitatively from dispersion and strength of the radar echo. Once obtained, they can be applied to estimate the origin, age, evolution, density, and (to some extent) composition of the surface in much the same ways as images and photographs can be used.

A radar signal incident on a planetary surface may be visualized as a set of parallel rays which, upon reaching the target, are both scattered back into space and also transmitted into the surface layer (Fig. 1). For a mature surface, having a large population of craters for example, we expect a moderate amount of roughness and the scattered signal will be dispersed over some range of angles. At radio frequencies we find most of the energy being scattered into a small solid angle about the direction of the specular reflection; theoretical models exist by which we can relate the degree of spreading to roughness of the surface.

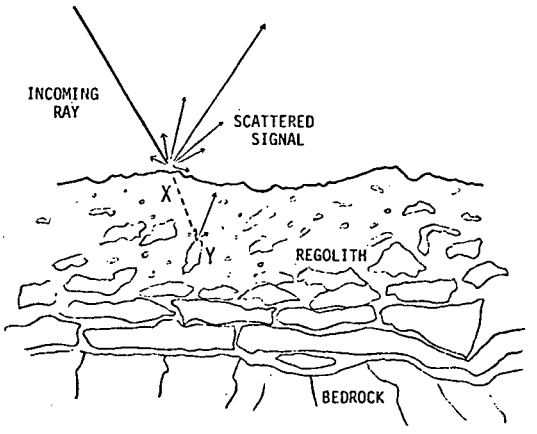

Fig. 1 - Radiowave scattering by a mature planetary surface. Most energy in the echo comes from interaction of the incoming wave with the uppermost surface (X); a lesser amount arises from scattering by buried inhomogeneities (Y).

Part of the energy which reaches the surface (X) is transmitted into the regolith. Being a lossy medium, the regolith attenuates the wave as it propagates deeper into the material. Occasionally the signal will interact with a buried inhomogeneity, such as a rock fragment (Y), causing secondary scattering. Because these tend to be blocky rather than quasi-smooth, as was the upper surface, the inhomogeneities will have a much broader scattering function. The energy scattered by a block returns through the attenuating medium to the regolith-space interface where part is internally reflected. The energy which escapes into space will be both weak and very broad in its angular characteristics. Its detection may be used to infer regolith properties to depths of several meters.

Relatively new surfaces (Fig. 2) are expected to have undergone little meteor bombardment or erosion. If laid down as low-viscosity lava flows, they would be expected to present very nearly mirror-like surfaces to incoming rays. The solid angle into which the scattering takes place will be quite small.

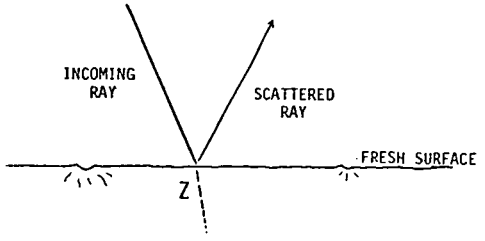

Fig. 2 - Radiowave scattering by a fresh, smooth surface. The reflected ray is expected to be stronger than in Fig. 1 because of higher material density at the upper surface and to be less dispersed angularly because of the smaller amount of roughness. The ray coupled into the planet is dissipated in the material.

Since there has been essentially no regolith development on a fresh surface, the dielectric constant sensed by the ray at Z will be that of solid rock ($\varepsilon \sim 10$) rather than that of a soil ($\varepsilon \sim 3$). The total scattered power will be near 25% of the incident power, compared with approximately 7% for the case shown in Fig. 1. Furthermore, so long as there is no stratification or significant frac-

turing in the first few meters, the 75% of energy coupled into the planet will be entirely absorbed rather than partially scattered back as a contribution to the diffuse echo component.

Clearly the cases illustrated by Figs. 1 and 2 are extremes and we must be prepared to consider intermediates. There are also anomalous scattering surfaces which do not fit the above models:

a. high viscosity (aa) lava flows could be fresh yet extremely rough, giving a very diffuse radar echo;
b. sand dune fields, rather than being isotropic and random surfaces, exhibit periodicities which would appear in radar data with directionally dependent modal signatures;
c. rock-strewn smooth surfaces could have moderate quasi-specular echo components and strong diffuse echoes, without invoking the "buried inhomogeneity" model above.

We believe that the capabilities of and limitations of radar are well enough understood that geologic inferences can be made from the presently available data.

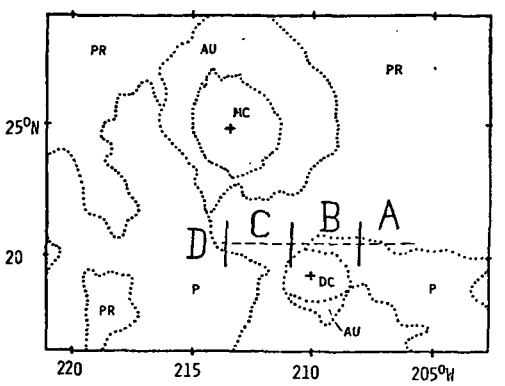

Fig. 3 - Geologic map of Elysium Planitia on Mars. Dotted lines bound units mapped by Scott and Allingham (1); solid lines and bold letters mark units as seen by radar. Radar coverage is limited to perhaps a hundred km on either side of the dashed line.

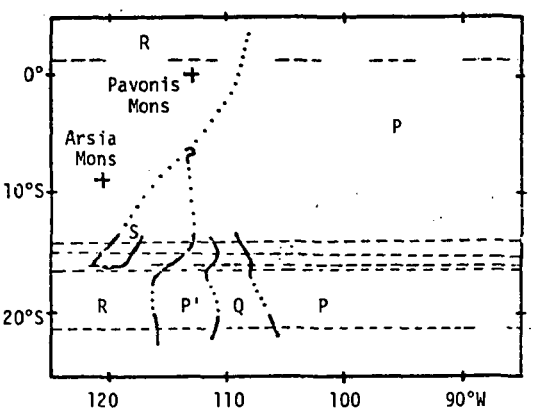

Fig. 4 - Geologic map derived from several radar passes across Tharsis Montes. Dotted lines are boundaries which are uncertain because of missing radar coverage.

Figs. 3 and 4 are examples of the mapping which is possible. Both are derived from Mars radar data, Fig. 3 from 1976 results obtained at Arecibo Observatory and Fig. 4 from 1971 through 1975 operations at both Arecibo and Goldstone Tracking Station. Mapping is limited to a small swath along the radar ground track (dashed lines). In Fig. 4 several parallel tracks have been combined to produce a two dimensional map of the Tharsis region; the single traverse across Elysium Planitia (Fig. 3) gives only the contacts between distinguishable units at 20°N latitude.

Dotted lines in Fig. 3 show the main units as mapped by Scott and Allingham (1). Units DC and MC are the volcanoes Albor Tholus and Elysium Mons, respectively. P is smooth plains having moderate crater density, and is interpreted as eolian deposits. PR is rolling plains showing signs of a flow origin. AU is interpreted as flows originating from dikes around the volcanoes.

Bold letters in Fig. 3 indicate geologic units we infer from radar properties. A is a very smooth unit, one of the smoothest found on Mars. B, however, is extremely rough and may be frothy or aa lava; the contact between A and B is sharp. C may be an extension of B but probably has other components mixed in; the radar echo, though distorted, can be identified here

whereas this was not the case for B. Scattering properties of C gradually improve to the point where unit D (if indeed it can be said to be a separate unit) is typical of Mars' "average" surface.

At Tharsis the geology is more complex. Radar tracks at all latitudes show smooth plains (P) to the east of the ridge with an abrupt change to rough (possibly frothy lava) material at the eastern base of the volcanic cones. The rough material (R) extends several hundred kilometers west of the ridge crest, though here and there it may be mixed with smoother terrain. Tracks south of Arsia Mons respond to Claritas Fossae as a rough surface (Q) splitting unit P from unit P', which is also smooth but has low dielectric constant. Though P and P' have similar roughness, the fracture zone is a very clear divider between average dielectric constant to the east and low dielectric constant to the west, independent of roughness. Unit S, which is also smooth with low dielectric constant, may be a tongue extending down the flank of Arsia Mons.

Similar studies are in progress for other regions of Mars - Chryse Basin being of particular interest - and for the moon. We hope in the near future to be able to define guidelines which can be used to describe planetary surfaces in some geologic sense, based on their radiowave scattering properties.

(1) Scott, D. H., and Allingham, J. W., Geologic Map of the Elysium Quadrangle of Mars, U. S. Geological Survey map I-935, 1976.

Photometry of Planetary Surfaces: Studies of the Validity of a Minnaert Description. J. Veverka, J. Goguen and M. Noland, Laboratory for Planetary Studies, Cornell University, Ithaca, NY 14853

As part of our attempt to describe the photometric properties of planetary surfaces in terms of a unique photometric function we have studied the applicability of the commonly used Minnaert description, according to which the intensity of scattered light from a surface element is:

$$I(i,\varepsilon,\alpha) = B_o(\alpha)\mu^{k(\alpha)}\mu_o^{k(\alpha)-1}$$

where i = arccos μ_o = incidence angle; ε = arccos μ = emission angle; α = phase angle; and $k(\alpha)$ and $B_o(\alpha)$ are the two Minnaert parameters which describe the scattering.

In the first of three related investigations, Noland and Veverka (Icarus, in press) studied the applicability of Minnaert's law to dark, particulate surfaces which scatter according to a generalized Lommel-Seeliger law (Hapke (1963) JGR, 68, 4571; Irvine (1966) JGR, 71, 2931). It was found that this type of scattering, which adequately describes the photometric behavior of dark, intricate surfaces as those of the Moon, Phobos, Deimos, etc., cannot be represented well by a Minnaert law, except near opposition. At any non-zero phase angle, different sets of points on a planet will give different values of the Minnaert exponent k. Points along photometric meridians always give $k = \frac{1}{2}$, independent of phase angle. For points on the photometric equator, k varies between $\frac{1}{2}$ and 1 as a function of phase angle, and at any particular phase angle k varies with the location of the points used on the photometric equator. Specifically,

$$k(m,\alpha) = \tfrac{1}{2}\left\{1 + \frac{1}{1 + m\cot^2\frac{\alpha}{2}}\right\}$$

where $m = \dfrac{\mu\mu_o}{\cos^2\alpha/2}$

Minnaert's description is especially inadequate at large phase angles and at any non-zero phase angle for points close to the limb and to the terminator.

In the second investigation, Goguen and Veverka have extended this work to arbitrarily bright surfaces ($0 \leq \tilde{\omega}_o \leq 1$, where $\tilde{\omega}_o$ = single scattering albedo) and again found the Minnaert description inadequate. It appears to be generally true that for physically realistic scattering laws, a unique Minnaert k cannot be defined on a planet's surface at a fixed α, if $\alpha \neq 0$. For example, at any given phase angle k's determined by using points along a meridian will differ from those determined by using points along the equator. Incidentally, very bright surfaces do not necessarily acquire Lambertian characteristics (i.e., k does not tend to 1, independent of phase angle and position on the disk) as $\tilde{\omega}_o \to 1$.

In the third part of this investigation we studied the traditional article of faith that scattering from glossy surfaces (e.g., glazed frost) can be described in terms of a Minnaert law with $k \gg 1$. Our laboratory measurements show that scattering from glossy surfaces is not well represented by a Minnaert law.

Our conclusion is that analyzing the photometric properties of planetary surfaces in terms of a Minnaert law is an unjustifiable and crude approximation. It cannot yield good results in studies of the detailed photometry of individual areas on a planetary surface.

Planetary Frost Program. Larry A. Lebofsky and James E. Conel, Planetology and Oceanography Section, Jet Propulsion Laboratory, Pasadena, CA 91103

Construction of the laboratory system for the growing of optical quality ices and the measurement of their refractive indices is complete. The problem of growing ice samples against an optically flat surface and removal of the surface from the ice sample has been overcome and work is proceeding with ammonia and methane ice samples. To date, several ammonia ice samples have been grown, but the data obtained have been of limited usefulness because of cloudiness of the samples. We suspect this is due to trace amounts of water present in the ammonia gas used. Work is now progressing with ultrahigh purity ammonia. The results of these latest experiments will be presented.

By redesigning the infrared detection system, we have been able to increase significantly the sensitivity of the system, necessitated by the very weak signals (the ice samples have reflectivities of about 2 - 5%) and spectral features that we are attempting to observe. Because of this we have been carrying out a simultaneous study of the reflection properties of various frosts and other materials in the 1 - 5.5 μm spectral region where stronger spectral features (due to absorption in the particulate material) are used as a guide on system performance. These reflection spectra aid in determining the sensitivity needed in a given spectral region, and what spectral regions will be of most interest.

The data have proven to be valuable in the overall problem of the determination of the composition of satellite and asteroid surfaces. Our laboratory work, along with previous laboratory spectral studies of frosts and hydrated silicates (1, 2) has been used to identify the presence of water frost on the surface of the Galilean satellite Callisto (JIV). This identification has been made possible by the resolving of the 3 μm water frost absorption feature in the spectrum of Callisto (see Figure I).

FIGURE I

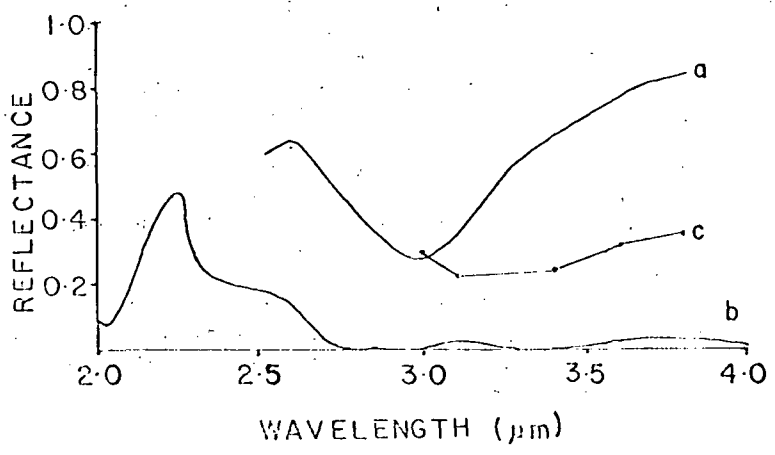

a. Montmorillonite
b. Water frost (1)
c. Callisto, normalized to 1.0 at 1.25 μm

As can be seen from Figure I, hydrated materials also have a strong absorption feature at about 3 μm. Therefore the absorption feature in the spectrum of Callisto may be due solely to the presence of water frost on the surface of Callisto (about 10% surface coverage), or it may also be due in part to the presence of some hydrated siliceous or carbonaceous material. Work is progressing on this question and will be discussed.

These preliminary investigations have demonstrated the importance of the study of the 3 - 4 μm spectral region for the determination of the composition of planetary surfaces. The major expected frosts (water, ammonia, and methane), and hydrated silicates and carbonates, have diagnostic spectral features in this spectral region. These features are in general stronger than ones at shorter wavelengths, and are therefore less likely to be suppressed by the presence of other material (as is the case with the 1.4 and 1.9 μm absorption features due to water frost in the spectrum of Callisto).

(1) Smythe, W. D., Icarus 24, 421-427 (1975).
(2) Salisbury, W., personal communication.

Photometric Analyses of Spacecraft Planetary Images. Bruce Hapke, Department of Earth and Planetary Sciences, University of Pittsburgh, Pittsburgh, PA, 15260

1. Mariner 10 Vidicon Calibration

Since vidicons are inherently nonlinear, it was necessary to show that the photometric decalibration procedure adequately removes the nonlinearities. The linearity of the camera/processing system was checked in space by applying the Helmholtz reciprocity principle to Mariner 10 images of Venus taken through the orange filters. The reciprocity principle states that for a surface illuminated at angle i and viewed at angle e, through phase angle g, so that the radiance is R(i,e,g), if the source and observer are interchanged, so that the radiance is R(e,i,g), the two radiances are related by:

$$R(i,e,g)/\cos i = R(e,i,g)/\cos e$$

Although this relation rigorously applies only to a single surface, if Venus had perfectly uniform optical properties, it would also apply to reciprocal areas near the limb and terminator of the planet. In the orange, local brightness variations on Venus are less than 2%, so that any camera nonlinearity should manifest itself as reciprocity failure. Approximately 100 areas were measured on both A and B camera images. The nonlinearity was expressed as the coefficient b in the expression:

$$R_o = R_a\ (1 + bRa)$$

where R_o is the observed radiance and R_a is the actual radiance. The results of the test are: A camera: $b = 0.000096 \pm 0.00028\ DN^{-1}$

B camera: $b = 0.000021 \pm 0.00045\ DN^{-1}$

Thus the cameras appear to be linear to better than 1% for brightness levels around 100 DN. These results have been published (1).

A second calibration objective is to ascertain whether the photometric decalibration program for the warm cameras can also be used for the cold camera images of the second and third Mercury fly-bys. For this purpose we are intercomparing equivalent images of Mercury taken on Mercury I and II. Although this work is still in progress, results to date are very encouraging, and indicate no substantial temperature effects exist. (Figure 1).

2. Mercury Photometry

One of the objectives of this project is to produce an albedo map of Mercury. In order to accomplish this, the differential photometric function of Mercurian surfaces must be known. For preliminary albedos an average lunar photometric function was assumed. However, this function did not take multiple scattering or latitudinal effects into account.

Images of both Mercury and the moon taken at phase angles near 90^o show pronounced polar darkening. It is known that the moon does not exhibit any systematic dependence of albedo on latitude, implying that the apparent polar darkening is due to the photometric function. An obvious cause is shadowing in craters. We are presently working on a computer program to calculate the effects of slopes and shadows in craters shaped like cones or spherical caps. However, this program is relatively complicated. As an interim measure, the photometric function of a square box of depth d and side D was calculated. The calculated latitudinal profiles were found to agree with the observed profiles quite satisfactorily for d/D = 15-20%. Exact calculations should not change this result appreciably. A number of earth-based photographs of Mercury (courtesy of the Las Cruces, New Mexico Observatory) are being examined, but no evidence supporting polar darkening has been found.

These results imply that on Mercury albedos do not decrease with latitude. However the magnetic field of Mercury should prevent the solar wind from reaching the equatorial regions, but sub-storm-type phenomena will allow

the solar wind to hit the polar regions. If the solar wind were necessary for Mercurian surface darkening processes, polar darkening would be expected. The lack of polar darkening implies that the darkening process is not solar wind dependent, and is most likely due to impact vaporization and redeposition. These results were presented at the Conference on Comparisons of Mercury and the Moon, Houston, Nov. 7, 1976, and will be published in the conference proceedings.

The applicability of the lunar photometric function is also being checked by calculating apparent albedos at different phase angles using Mercury II images. Preliminary results are that the calculated albedos decrease with phase angle. Most of this effect can be accounted for by multiple scattering. Although this topic is being actively investigated, preliminary indications are that the albedos of the bright areas listed in earlier Mariner 10 reports (2) are about 30% high, while albedos of dark areas are about 10% high.

3. Venus Photometry

It should be possible to estimate the departure of Venus cloud particles from isotropic scatterers by measuring the brightness of the cloud tops at different phase angles in orange light. Mariner 10 images of Venus have been chosen and are currently awaiting processing by IPL.

4. Mars Photometry

The principal investigator took part in the activities associated with the Viking 1 and 2 landings on Mars during the summer of 1976. A preliminary photometric function for the surface was calculated from Viking Lander 1 camera data and was found to be more like the moon than like previous functions obtained from above the atmosphere. The reason for the discrepancy may be the rather thick atmospheric haze. These results were subsequently incorporated into the preliminary report of the Viking Lander Imaging Science Team and published (3).

In order to obtain a better photometric function for the Martian surface a detailed photometric sequence was planned and taken by Viking Lander 1, but the data were not processed by IPL until recently and so have not yet been reduced. The reduction will be complicated by scattering from the atmospheric haze. Measurements on the calibrated photometric targets on the Lander indicated that an appreciable part of the illumination on any surface is due to the haze.

5. References Cited

(1) Hapke, 1976, Jour. Atm. Sci., 33, 1803.
(2) Hapke, et al, 1975, Jour. Geophys. Res., 80, 2431.
(3) Mutch et al, 1976, Science, 193, 791.

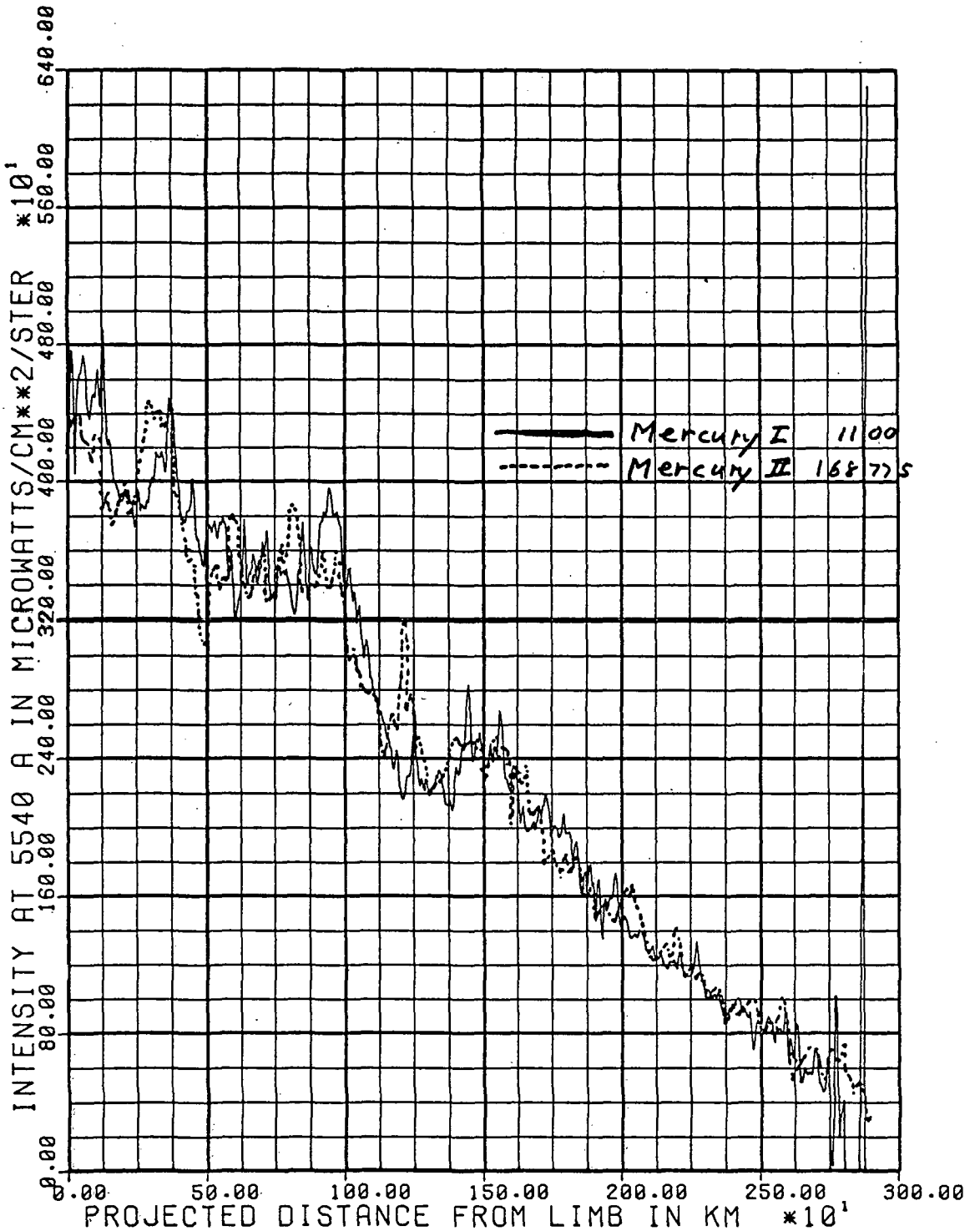
INTENSITY AT 5540 A IN MICROWATTS/CM**2/STER *10¹
0.00
80.00
160.00
240.00
320.00
400.00
480.00
560.00
640.00
0.00
50.00
100.00
150.00
200.00
250.00
300.00
PROJECTED DISTANCE FROM LIMB IN KM *10¹
Mercury I 1100
Mercury II 1687 75

Figure 1.

Development of a Seismometer for Viking. D. L. Anderson, California Institute of Technology, Pasadena, California 91125

SUMMARY

The seismometer has continued to work well since our last report which covered the first 60 Sols of the nominal mission (Science, v. 194, No. 4271, 1976). The present report covers the period of conjunction and the Extended Mission through Sol 131. The main results are as follows:

1. Although the noise background repeats from day to day in general terms, it can be quite variable when looked at in detail. Some days are exceptionally noisy (windy) and some days are exceptionally calm.
2. We seem to have entered a period of higher noise and also noise at night. This change correlates with rapid change in the temperature and opacity of the atmosphere.
3. Sol 131 and to a lesser extent Sol 119 were periods of continuous background activity.
4. A 30-minute long event was seen on Sol 60 in the normal mode. This is not an optimal mode for seismic data but it occurred during the normally quiet period of the evening. If due to a Marsquake it indicates a large event (M > 6.0 - 6.5) at a large distance (> 7000 km).
5. An event having all the characteristics of a local seimic event occurred on Sol 80 in the early morning hours. This would have a magnitude of 2.5 - 3.0 and a distance of 100 to 120 km. It has a signature almost identical to local events recorded on a test instrument at Caltech (in the Event Mode).

CONJUNCTION DATA

The background noise is extremely low from 1800 each evening to 0700 the next morning. The background picks up slightly starting between 0630 and 0700.

The afternoon gusty period starts between 1018 and 1230 each day, usually close to local noon. Peak gusts are usually near 1430 and 1520. There are typically 8 - 12 gusts between noon and 1800, 8-15 minutes in duration and about 40 minutes separation. The gusts range from 5-19 mm in the normal mode. The noise and, by implication, the wind velocity can vary rapidly in the order of a minute or less.

Details of the noise background (winds) are highly variable from day to day. It is only when average values are considered that one gets the impression that the Meteorology repeats daily.

The calibration signals are not changing. This indicates that the Lander has not tilted or jumped.

One important result of the seismic experiment is the discovery that a supersensitive seismometer, an instrument more sensitive than the Viking instrument, can operate on the surface of Mars. All sources of noise that we have identified are internal to the Lander or wind induced vibrations of the Lander, and, possibly, heating and cooling of the Lander.

We have established a good correlation between wind velocity and seismic background. The seismometer output is proportional to $(\text{wind velocity})^2$ indicating that the boundary layer, as expected, is in the turbulent regime. There is a distinct correlation, not only with wind speed, but also with wind direction. We expect that temporal correlations will allow us to determine the time and length scales of microturbulance and to establish the characteristics of the boundary layer.

The Sol 80 event has distinct later arrivals which we interpret as multiple S reflections from a layer at about 15-18 km depth. This may be the thickness of the crust at the landing site of VL-2.

EXTENDED MISSION DATA

Winds are generally less than the seismic threshold (∿3 m/sec) from about 1800 hrs LLT to sometime between 0600 and 1030 LLT. Winds generally average from 2.5 m/sec to 4.9 m/sec from 1000 to 1800 LLT with maximum peaks from 6.4 to 11.5 m/sec.

Unusually high seismic background was recorded on Sol 119 between 1100 and (120) 0100. The noise is continuous and unlike the usual afternoon windy periods. Average winds in this period were unusually high, particularly after 1800 which is usually quiet. Winds averaged greater than 7.5 m/sec during the entire period from 1200 - 1800 with peak gusts of 11.6, 13.2 and 15.1 m/sec. The wind between 1800 and 2400 averaged 6.1, 6.4, 5.8, 5.2, and 4.7 m/sec for successive 1-1/2 hour modules with peaks of 11.36, 10.72, 9.49, 10.71, and 8.86 m/sec through this normally quiet period.

Continuous, although lower level activity, also occurred in the early morning hours on Sols 118, 121, 128, 129, and 130. Exceptionally high activity was continuous from at least Sol 131 1319 to Sol 132 0200. It should be pointed out that somewhere between Sol 110 and 120 the optical depth increased by an order of magnitude. This seems to be haze rather than dust (Mutch, personal communication). Average temperatures dropped rapidly on Sol 119 - 120, 128, and 131. All of this is suggestive of an unusual Meteorological disturbance.

From Sol 110 - 118 the seismic data is characterized by quiet nights, relatively quiet mornings, and slight gustiness in the afternoon. This all changes on Sol 118/119 through Sol 121. Activity picked up again on Sol 124 and on Sols 128 - 130. On Sol 131 all hell broke loose. The activity is higher and more continuous than ever seen before. This indicates higher wind velocities than any previously reported, probably much greater than 22 meters/sec.

Page Intentionally Left Blank

Chapter 12

UNCATEGORIZED

Page Intentionally Left Blank

Results From A Planetary Geology Short Course. Peter H. Schultz* and Ronald Greeley, NASA Ames Research Center and University of Santa Clara, Moffett Field, CA, 94035.

On April 11-14, 1976, the Planetary Geology Program Office, the University of Santa Clara, and the Fairfax County Public Schools sponsored a workshop-style short course in planetary geology for selected high school educators at Skyland, Virginia. The goal was to provide participants materials and background, thereby permitting the introduction of planetary geology at a high-school level (see Schultz and Greeley, 1976). Twenty-one educators participated in the short course. In addition, Dr. Harry B. Herzer, III attended the course as an observer from the NASA Space Science Education Project.

Several researchers active in the field of planetary geology donated time to relate the fundamentals of their particular field. This approach permitted diversity in approaches and first-hand contact between researcher and educator. The final course outline and contributors are given below.

SUNDAY, APRIL 11: INTRODUCTION

Evening

Registration	
Introductory Remarks	P. Schultz, R. Greeley
Missions through the Solar System: Past, Present, and Future	S. Dwornik

MONDAY, APRIL 12: THE PRIMORDIAL PLANETS

Morning

Origin of the Solar System	J. Wood
Introduction to Planetary Surfaces	P. Schultz

Afternoon

Laboratory Exercise: impact cratering	
The Impact Process	D. Roddy

Evening

Laboratory Exercise: impact cratering	

TUESDAY, APRIL 13: THE EVOLVING PLANETS

Morning

Planetary Volcanism and Tectonism	K. Howard

*current address: The Lunar Science Institute
3303 NASA Road 1, Houston, TX, 77058

Laboratory Exercise:
introduction to photo-
interpretation

Afternoon

Geologic Mapping of the
Planets — N. Trask

Laboratory Exercise:
geologic mapping

Evening

The Primordial Earth — H. Masursky

WEDNESDAY, APRIL 14: THE PLANETARY ATMOSPHERE

Morning

Planetary Climatology — G. Briggs

Laboratory Exercise:
atmospheric circulation

Afternoon

Laboratory Exercise:
martian aeolian processes

Closing Remarks.

Student activities were stressed through six laboratory exercises developed for this course. Impact cratering exercises introduced the factors that control crater size including projectile mass, velocity, and target strength. In addition, an evening session was scheduled to allow photographing an impact event with a Polaroid camera and strobe light. Photo-interpretation was introduced through the comparison of lunar and mercurian impact craters. The geologic mapping exercise used global views of Mercury, Mars, and the Moon for an introduction to mapping problems and a segment of the Caloris Basin for detailed mapping. With a turntable, airpuck, and polaroid camera, educators demonstrated the Coriolis Effect and applied it to the direction of wind streaks on Mars. Finally, home-made wind tunnels graphically illustrated the styles of aeolian modification that were compared to martian features from Mariner 9 images.

The majority of educators elected to attend the course for credit through the University of Santa Clara, which required the submission of a paper describing their application of the short-course materials in the classroom. Teachers were generally successful with their applications and one noted that even the "dead heads" became involved. In order to permit wider use of short course materials, a publication similar to A Primer in Lunar Geology by Greeley and Schultz (1974) is planned. In addition, a curriculum guide has been developed jointly with two high school educators from the Fairfax County School District.

Greeley, R. and Schultz, P., A Primer in Lunar Geology, NASA Tech. Mem. 62359.
Schultz, P. and Greeley, R., NASA Tech. Mem. X-3364, p. 277-278 (1976).

The Space Imagery Center at the University of Arizona. G. Georgenson, Lunar & Planetary Laboratory, U. of Arizona, Tucson, AZ 85721.

Lunar and planetary photography acquired from spacecraft and earth-based telescopes has provided a wealth of new information about planetary surfaces and atmospheres. These new data are changing many old concepts and adding new ones regarding the origin of surface features and the history of the Moon and planets. Important new insights into atmospheric dynamics are also being obtained through the study of photography. The flood of new imagery, particularly during the past 10 years, requires cataloging and retrieval techniques unique to imaging data of the Moon and planets. Therefore, facilities are needed to house, catalog, and efficiently retrieve imagery and support data for investigators who use this type of data.

During the past 17 years the University of Arizona's Lunar and Planetary Laboratory has acquired one of the world's largest and most complete collections of lunar and planetary imagery. Because of inadequate storage space and lack of cataloging, most of the material was virtually inaccessible for study. To solve this problem the Space Imagery Center is being established to house both existing and future acquisitions. The Center is located in the Kuiper Space Sciences Building on the campus of the University of Arizona. It constitutes an organized and cataloged collection of imagery. Our facility is open to University faculty and students as well as outside investigators who use such material in their research programs.

The Center's total number of negative and positive images (both earth-based and spacecraft) is close to ½ million items. These data have a variety of formats ranging from 35-mm films to 48-inch prints. The primary lunar material consists of photography derived from the Lunar Orbiter and Apollo missions. The Lunar Orbiter collection comprises about 6200 images, or two full sets. In addition, there is a selection of very high quality 24-inch film positives of the more important Lunar Orbiter pictures. The Apollo material consists of ~9500 8 x 10-inch prints, ~14,500 70-mm film positives, ~20,000 5 x 5-inch metric camera film positives and prints, and ~8000 5 x 48-inch panoramic camera prints and positive films. In addition, we have an extensive collection of high quality earth-based lunar photos taken under lighting conditions not available on the higher resolution Orbiter and Apollo material. Our lunar map collection consists of about 2400 orthophoto, topographic, geologic, albedo, and tectonic maps.

Planetary imagery includes Mariner 6, 7, and 9 photos of Mars, Viking Orbiter photography, Mariner 10 photos of Mercury and Venus, and earth-based imagery covering a 10-year period. The Outer Planet collection consists of earth-based photography of Jupiter and Saturn, and a selected set of Jupiter from Pioneers 10 and 11. We will acquire the imagery of the Jupiter and Saturn systems from the two Mariner Jupiter/Saturn spacecraft.

Work and study areas are available to the user including large layout tables, a light table, and stereoscopic equipment. The Center is not a facility for the production of photographs for outside users. In special cases it may be possible for the Center to reproduce a few photographs at the requester's expense.

The primary retrieval tool of the Space Imagery Center is a computer-linked microfiche viewer containing most of the mission-oriented imagery. These photographs are retrievable by using any of several parameters such as surface coordinates, sun angle, time, etc. The viewer eliminates the need to comb through thousands of prints and films in search of only a few pertinent images.

In the near future, the photography will be indexed according to the geologic and/or topographic features they contain. This will be an extremely valuable means of access to the collection.

Page Intentionally Left Blank

AUTHOR INDEX

Page Intentionally Left Blank

NASA-Langley, 1977

NATIONAL AERONAUTICS AND SPACE ADMINISTRATION
WASHINGTON, D.C. 20546

OFFICIAL BUSINESS
PENALTY FOR PRIVATE USE $300

SPECIAL FOURTH-CLASS RATE BOOK

POSTAGE AND FEES PAID
NATIONAL AERONAUTICS AND SPACE ADMINISTRATION
451

U.S.MAIL

POSTMASTER: If Undeliverable (Section 158 Postal Manual) Do Not Retur

"The aeronautical and space activities of the United States shall be conducted so as to contribute . . . to the expansion of human knowledge of phenomena in the atmosphere and space. The Administration shall provide for the widest practicable and appropriate dissemination of information concerning its activities and the results thereof."

—NATIONAL AERONAUTICS AND SPACE ACT OF 1958

NASA SCIENTIFIC AND TECHNICAL PUBLICATIONS

TECHNICAL REPORTS: Scientific and technical information considered important, complete, and a lasting contribution to existing knowledge.

TECHNICAL NOTES: Information less broad in scope but nevertheless of importance as a contribution to existing knowledge.

TECHNICAL MEMORANDUMS: Information receiving limited distribution because of preliminary data, security classification, or other reasons. Also includes conference proceedings with either limited or unlimited distribution.

CONTRACTOR REPORTS: Scientific and technical information generated under a NASA contract or grant and considered an important contribution to existing knowledge.

TECHNICAL TRANSLATIONS: Information published in a foreign language considered to merit NASA distribution in English.

SPECIAL PUBLICATIONS: Information derived from or of value to NASA activities. Publications include final reports of major projects, monographs, data compilations, handbooks, sourcebooks, and special bibliographies.

TECHNOLOGY UTILIZATION PUBLICATIONS: Information on technology used by NASA that may be of particular interest in commercial and other non-aerospace applications. Publications include Tech Briefs, Technology Utilization Reports and Technology Surveys.

Details on the availability of these publications may be obtained from:

SCIENTIFIC AND TECHNICAL INFORMATION OFFICE

NATIONAL AERONAUTICS AND SPACE ADMINISTRATION

Washington, D.C. 20546